Cool flames, a reactor for low-temperature combustion kinetic studies: Flame stabilization, chemical structure and laminar burning velocities

Thomas Panaget

▶ **To cite this version:**

Thomas Panaget. Cool flames, a reactor for low-temperature combustion kinetic studies: Flame stabilization, chemical structure and laminar burning velocities. Chemical Sciences. Université de Lille, 2022. English. NNT : 2022ULILR075 . tel-04139454v1

HAL Id: tel-04139454

https://hal.science/tel-04139454v1

Submitted on 19 Feb 2024 (v1), last revised 23 Jun 2023 (v2)

HAL is a multi-disciplinary open access archive for the deposit and dissemination of scientific research documents, whether they are published or not. The documents may come from teaching and research institutions in France or abroad, or from public or private research centers.

L'archive ouverte pluridisciplinaire **HAL**, est destinée au dépôt et à la diffusion de documents scientifiques de niveau recherche, publiés ou non, émanant des établissements d'enseignement et de recherche français ou étrangers, des laboratoires publics ou privés.

THÈSE DE DOCTORAT

Préparée à l'université de Lille par

Thomas PANAGET

Soutenue publiquement le 12 Décembre 2022 devant la Commission d'Examen

En vue de l'obtention du grade de Docteur en Énergétique, Thermique et Combustion

Les flammes froides, un réacteur pour l'étude cinétique de la combustion aux basses températures : Stabilisation, structure chimique et vitesses de propagation laminaire

Cool flames, a reactor for low-temperature combustion kinetic studies: Flame stabilization, chemical structure and laminar burning velocities

Composition du jury :

BATTIN-LECLERC Frédérique	Directrice de Recherche CNRS, Laboratoire Réactions & Génie des Procédés, ENSIC, Université de Lorraine	**Rapporteure**
FIORINA Benoît	Professeur des Universités, Laboratoire EM2C, Centrale Supélec	**Rapporteur**
STARIKOVSKAIA Svetlana	Directrice de Recherche CNRS, Laboratoire de Physique des Plasmas, Ecole Polytechnique	**Présidente du jury**
DIAS Véronique	Maîtresse de Recherche, HDR, Institute of Mechanics, Materials and Civil Engineering, Université de Louvain-La-Neuve	**Examinatrice**
LECORDIER Bertrand	Chargé de Recherche CNRS, Laboratoire CORIA, INSA Rouen/Université de Rouen	**Membre invité**
FAROUK I. Tanvir	Associate Professor, College of Engineering and Computing, University of South Carolina	**Membre invité**
PILLIER Laure	Chargée de Recherche CNRS, HDR, Laboratoire PC2A, Université de Lille	**Co-encadrante de thèse**
VANHOVE Guillaume	Maître de Conférences, HDR, Laboratoire PC2A, Université de Lille	**Directeur de thèse**

« […] nous sommes comme des nains assis sur des épaules de géant. Si nous voyons plus de choses et plus lointaines qu'eux, ce n'est pas à cause de la perspicacité de notre vue, ni de notre grandeur, c'est parce que nous sommes élevés par eux »

Metalogicon III, Jean de Salisbury (1159)

Nomenclature

(µ)GC	(micro) Gas Chromatography
(µ)TCD	(micro) Thermal Conductivity Detector
(FS)IDT	(First-Stage) Ignition Delay Time
(P)LIF	(Planar) Laser Induced Fluorescence
(Q)MS	(Quadrupole) Mass Spectrometer
CAD	Crank-Angle Degree
CEM	Controlled Evaporator Mixer
DEE	DiEthyl Ether
DME	DiMethyl Ether
ECN	Equivalent Carbon Number
EGR	Exhaust Gas Recirculation
EI	Electron Ionization
FID	Flame Ionization Detector
HAB	Height Above Burner
HCCI	Homogeneous Charge Compression Ignition
ICCD	Intensified Charged Coupled Device
IE	Ionization Energy
IWS	Interrogation Window Size
JSR	Jet-Stirred Reactor
KHP	Ketohydroperoxyde
LBV	Laminar Burning Velocity
LDV	Laser Doppler Velocimetry
LTC	Low-Temperature Combustion
MBMS	Molecular Meam Mass Spectrometry
MFC	Mass Flow Controller
Nd:YAG	Neodynium-doped Yttrium Aluminium Garnet
NTC	Negative Temperature Coefficient
OME	OxyMethylene Ether
PFR	Plug-Flow Reactor
PID	Proportional-Integral-Derivative controller
PIV	Particle Image Velocimetry
PPCI	Partially Premixed Compression Ignition
RCCI	Reactivity Controlled Compression Ignition
RCM	Rapid Compression Machine
RMS	Root-Mean Square
ROP	Rate Of Production
SACI	Spark-Assisted Compression Ignition
ST	Shock Tube
SVUV	Synchrotron Vacuum Ultra-Violet

Introduction

2022, year during which this thesis manuscript is written, is marked by the war triggered by Russia's invasion of Ukraine. European economic sanctions against Moscow ended up in an important rise of the imported natural gas price. In addition, an exceptional situation of high-energy demand is caused by the recent post COVID-19 world trade resumption, as well as stress on the French electricity market due to the planned and unplanned maintenance of more than half of its nuclear reactors. These coupled elements lead to an uncommon energy crisis, which impacts most of our economic sectors, and consequently our daily lives. This serves as a reminder of the key role of energy in our modern societies.

The 71th edition of the BP Statistical Review of World Energy [1] starts by mentioning that fossil fuels still accounted for 82% of the primary energy use in 2021 (including coal, natural gas, oil). These fossil fuels are known to be one of the main sources of greenhouse gases, responsible for climate change. In 2015, during the COP 21, 193 Parties (192 countries and the European Union) signed the 'Accord de Paris' that pursues several objectives, the most important one being to limit the global warming of the atmosphere to + 2°C. In practical terms, such objective implies a 5% yearly decrease rate of greenhouse gases emissions, the main contributors being carbon dioxide, CO_2, and methane, CH_4. Reaching such an objective calls for coupling energy conservation to massive decarbonization of our primary energy sources, which can be achieved by developing more efficient and 'clean' energy production and technologies. And combustion chemistry has an important role to play.

The energy released during combustion is used for transportation, electricity generation, among others. As pointed out by Professor Kohse-Höinghaus during her Hottel lecture at the 38th International Symposium on Combustion [2], a better knowledge of molecular properties and associated reaction pathways of conventional, bio-based or synthetic fuels is crucial in the design of efficient, low-emission combustion processes. And this is especially true for the development of high-efficiency combustion processes operating in the low-temperature combustion regime, where the fuel structure highly impacts its reactivity. A systematic understanding of these phenomena requires a variety of experimental diagnostics, allowing to develop robust detailed kinetic models that can be validated in a wide range of conditions. It is the purpose of my work performed at the PC2A laboratory (University of Lille), which consisted in the development, validation and exploitation of a new stagnation plate burner dedicated to low-temperature combustion kinetic studies through the extensive analysis of cool flames. This experimental platform offers the unique opportunity to measure both global and detailed parameters regarding the cool flame structure. Moreover, fundamental parameters such as the laminar burning velocities of a cool flame could possibly be inferred, as commonly done for hot flames. The development of such an innovative experimental configuration faces a number of fundamental and technological issues, that are described, discussed, and most of the time solved, in this work.

The first chapter of the present manuscript locates my work in its context. First of all, the history of cool flames, from their discovery two centuries ago until now, is briefly reminded. Then, the fundamentals of combustion kinetics are discussed, with a focus on the low-temperature regime and plasma/ozone-assisted combustion. Further on, fundamentals on laminar flame combustion are briefly addressed, highlighting the scarcity of experimental data concerning the measurement of cool flames propagation speeds. Finally, the last section of the first chapter is dedicated to an overview of past studies of the different fuels studied within this work, respectively dimethyl ether (DME), diethyl ether (DEE) and oxymethylene ether-2 (OME-2).

The second chapter introduces and details the experimental setup that was developed and used for the study of cool flames. It includes several sections that describe the following aspects of the burner and associated diagnostics: the stagnation plate burner and gas supply, CH_2O*-chemiluminescence, CH_2O-PLIF, thermometry, gas sampling and analysis using gas chromatography and mass spectrometry, and finally PIV. While none of these techniques is new, some of them were applied to cool flame analyses for the first time and required some developments that were also investigated.

The third chapter begins by the presentation of the cool flame stabilization procedure. Then, the theory behind numerical simulation of these flames is described. Finally, some aspects regarding the feasibility of modelling such flames using one-dimensional codes, either Chemkin-Pro or Cantera, are discussed. The discussion focusses on the influence of external forces on the cool flames that may interfere experimentally, but that are not computed.

The fourth chapter presents the main scientific lessons learned from the detailed analysis of the chemical structure of cool flames. The low-temperature combustion of the different fuels inside cool flames is investigated through CH_2O-PLIF measurements, as well as temperature and species mole fraction profiles measurements. The importance and influence of ozone on the reactivity of cool flames and their products distribution is also discussed.

The fifth and final chapter of this manuscript presents an experimental measurement campaign that aims to provide the first measurements of laminar burning velocities of cool flames at atmospheric pressure. It allows to shed some light on the kinetics governing the propagation speed of cool flames in the presence of ozone.

This work was funded by the Ministère de l'Enseignement Supérieur et de la Recherche (MESR) through a 3-year grant delivered by the Ecole Doctorale SMRE (Sciences de la Matière, du Rayonnement et de l'Environnement), and is a contribution to Laboratoire d'Excellence CaPPA and Climibio CPER project.

Chapter I. Bibliography

I. Bibliography

This first chapter aims to introduce my work performed during these three years at the PC2A laboratory, by highlighting the different studies that were performed these last years on cool flames. It is divided in four sections: The first one is a quick overview of the knowledge that was gained on cool flames from their first discovery, two centuries ago, until now. The second section is dedicated to the kinetics of low-temperature combustion and plasma or ozone-assisted combustion. The third section presents a brief introduction to premixed-laminar flames theory, including an overview of different techniques used to measure the laminar flame speed of hot flames, and their potential use for laminar cool flame speed determination. Finally, previous kinetic studies on the different fuels used in the context of this work are presented. All of these fuels are ethers, namely dimethyl ether, diethyl ether and oxymethylene ether-2.

I.1. A brief history of cool flames through time

As briefly mentioned in the introduction, the combustion community needs to look into new combustion strategies considering every aspect of energy generation. The recent development of advanced combustion strategies, as well as their observation onboard the International Space Station (ISS), shed light on cool flames as never before. However, their discovery dates from centuries ago. The next chapter aims to retrace the history of these cool flames, from their first mention in the scientific literature in 1817 to their study at the university of Lille as part of my research project. A considerable amount of work was achieved in this domain, this is therefore not an exhaustive review but a general overview throughout the years.

I.1.1. 1817 – 1930: Cool flames discovery

Two centuries ago, in 1817, the British chemist Humphry Davy, member of the Royal Society of Chemistry, made the following comments after igniting ether vapour with a heated platinum wire: '*When the experiment on the slow combustion of ether is made in the dark, a pale phosphorescent light is perceived above the wire […]. This appearance is connected with the formation of a peculiar acrid volatile substance possessed of acid properties.*' [3]. This study is, to the best of our knowledge, the first experimental observation of the existence of cool flames reported in the scientific literature. The apparition of such a phenomenon was allowed by the low heat conductivity of the platinum wire, which limits the power transferred from the wire to the mixture, thus avoiding the ignition of a conventional 'hot flame'. The study discusses the conditions enabling the existence, or not, of these cool flames using various metal wires and different combustible mixtures. It does however not provide important insight into the chemical structure of such flames, except the formation of acidic compounds in the flame.

A few decades later, in 1882, an article authored by William Henry Perkin, British scientist and member of the Royal Society, was published in the literature [4]. It reports the existence of 'pale blue flames' when impinging a combustible mixture on a heated copper ball at temperatures around 250°C.

These blue flames were obtained using different combustible materials, ranging from alkanes and alkenes to aldehydes, alcohols, ethers and fatty acids. In the tested conditions, the luminosity of the flames varied as the combustible mixture changed. The study lacks in detail concerning the conditions in which the experiments were performed. It is however suggested that the intensity of this 'incomplete combustion' depends on the chosen fuel, the brightest one being obtained with diethyl ether. These flames were designated as 'phosphorescent flames' by the author, as they closely resembled the faint luminescence emitted during the imperfect combustion of phosphorus. Two other interesting observations are reported in this study. On a first hand, when the blue flame is initiated in a confined environment, the temperature rapidly increases and a hot flame is formed. On the other hand, the author attempted the measurement of CO_2 concentration in the fumes of the blue flame formed with ether vapours. It was found out that, using ether (diethyl ether, $C_2H_5OC_2H_5$) as fuel, only 0.133 gram of CO_2 was formed when 1.313 gram of O_2 was consumed, leading to a molar CO_2 on O_2 ratio equal to 0.07. For the total combustion reaction of $C_2H_5OC_2H_5$ with O_2, the theoretical ratio is equal to 0.6. This means that there was 10 times less CO_2 formed in the blue flame compared to a hot flame. Moreover, analysis of the condensed gas phase after the blue flame showed that reaction products were mainly aldehydes and ethers.

Late in the 1920's, Harry Julius Emeléus studied the light emission of 'phosphorescent flames' of various combustible mixtures, namely ether [5], acetaldehyde, propionaldehyde and *n*-hexane [6]. Surprisingly, it was observed that the obtained emission spectra were identical whatever the employed combustible mixture, which all consisted of a series of bands between 5000-3600 Å. Later in 1935, a study authored by Alfred Ubbelohde [7] compared the emission spectra of the phosphorescent flames recorded by Emeléus with the fluorescence spectra of formaldehyde [8]. It showed that the excited - 'activated' is the term employed in the cited study- formaldehyde, CH_2O^*, was responsible for the blue colour of the 'phosphorescent flames' studied by Emeléus, and thus that formaldehyde was one of the major product of this incomplete combustion.

These studies form the very beginning of academic research on cool flames which were only, by the time, motivated by pure scientific curiosity. As a matter of detail, William H. Perkin and Harry J. Emeléus were both honoured by the Davy medal, reinforcing the tied relationship between these three scientists and the discovery of cool flames.

I.1.2. 1930 - 1980: Engine knock and first insight into the mechanisms

While cool flames consisted, at their beginning, of an intriguing phenomenon without major repercussions, it was soon found out that the chemistry behind such flames was closely linked to engine knock. This phenomenon takes place when auto-ignition occurs ahead of the propagating premixed flame inside a spark-ignition engine. This usually results in engine damage and reduced efficiency.

Firstly, following the study of Perkin presented above, it was observed that combustible mixtures forming 'phosphorescent flames' promoted knock, which hinted a potential correlation between cool flames and knock. Considering the work of Townend & Mandlekar on the spontaneous ignition of *n*-butane [9] and of *n*-pentane [10], it was shown that the cool flame phenomenon was associated with the auto-ignition of the fuel, and that the pressure possessed an important influence on the temperature at which the ignition occurred. In the case of pentane-air mixtures, it was observed that the ignition at atmospheric pressure started between 550 and 600°C, while the onset temperature dropped at values around 370°C when the pressure reached 15 atmospheres.

By implementing a rapid camera on an engine, allowing the observation of the flame front evolution as a function of the crank-angle degree, Withrow & Rassweiler were able to observe the origin of the knock event in the engine [11]. Knocking and non-knocking explosions were obtained by changing the fuel inside the chamber, a blend of gasoline and benzene being used for the non-knocking condition, while a fuel with an octane number equal to 48 was used for the knocking-condition. Images of the knocking condition showed that spontaneous ignition occurred in the unburned gases, at a point well separated from the flame front.

Knowing that cool flames and knock were two correlated processes, numerous studies investigated the low-temperature oxidation of different fuels. A crucial phenomenon in the low-temperature combustion process of hydrocarbons, the Negative Temperature Coefficient (NTC), was first introduced by Pease in 1929 while studying the oxidation of propane in a flow reactor [12]. It was observed that, when increasing the temperature of the reactor at which rich mixtures of C_3H_8/O_2 were introduced, the conversion of oxygen decreased. It was therefore concluded that the mixture reactivity decreased as the temperature increased. This non-Arrhenius behaviour, that will be presented in more detail later in this manuscript, is typical of the low-temperature combustion regime. In its review, Townend showed that every paraffin containing three or more carbons (i.e., excluding methane and ethane) produced a cool flame between 310 and 370°C when the pressure was sufficient [13]. The assumption that smaller paraffins do not produce cool flames was however proved wrong later on, as it was demonstrated that methane could exhibit a cool flame in the appropriate conditions [14].

In their study on the oxidation of *n*-hexane in the cool-flame region, Bailey & Norrish proposed that the oxidation of hydrocarbons at low-temperatures, typically in the range 200 – 300°C, proceeds through the formation of peroxy radicals, which are relatively stable at these temperatures [15]:

$$RH \xrightarrow{+\dot{O}H} \dot{R}\,(+H_2O) \xrightarrow{+O_2} RO\dot{O} \xrightarrow{+RH} ROOH\,(+\dot{R}) \xrightarrow{1)\ dec.} R\dot{O} + \dot{O}H \text{ or } \xrightarrow{2)+O_2} RO\dot{O} + H\dot{O}_2$$

One can note that, whatever the fate of the ROOH molecule, two radicals will be formed after its dissociation, leading to an indirect chain-branching pathway. This is responsible for the increase of the reactivity with the temperature in the low-temperature range. It was however later shown that ROȮ

radicals could undergo an internal H-atom migration reaction, also called isomerization, forming ȮOOH radicals. A more up-to-date mechanism describing the low-temperature oxidation process will be detailed in Section I.2.2.

Before the 60's, most of the studies of the low-temperature oxidation of hydrocarbons were performed in static or flow reactors. The development of new experimental configurations allowed the study of these mechanisms in different conditions. The stabilization of two-stage flames, i.e., a hot flame preceded by a cool flame, was successfully realized by Agnew & Agnew on a flat flame burner using diethyl ether as fuel [16]. The combined use of spectroscopic, chromatographic and mass spectrometric techniques allowed the identification and quantitative measurement of intermediates and products through the two-stage flame. Besides, in order to gain better insight into the first stage ignition of fuels and its influence on the hot flame, experiments in a Rapid Compression Machine (RCM) were performed by Fish and co-workers [17]. It was found out that the delay between the cool flame and the hot ignition was related to the pressure rise during the cool flame event. In the nearly adiabatic environment of a RCM, the temperature increase is directly correlated to the pressure rise after the first stage ignition delay, i.e., cool flame ignition delay. Therefore, the cool flame heat release controls the hot ignition process during two-stage ignition.

I.1.3. 1980s: Genesis of homogeneous compression ignition

In a constant effort in improving the performances of Internal Combustion Engine (ICE), either through reducing the pollutant emissions or the fuel consumption, innovative combustion strategies have been developed.

In 1979, a study published by Onishi and co-workers [18] reported the development of a new combustion process for ICE, called ATAC (Active Thermo-Atmosphere Combustion), which differed from the well-known conventional gasoline and diesel engine combustion processes. Based on the auto-ignition of a lean fuel/air mixture, the main objective was to increase the fuel conversion in the combustion chamber while decreasing the formation of pollutants. Originally applied in a two-stroke combustion engine, this method showed an important improvement in fuel consumption and exhaust emissions, especially regarding the emissions of nitrogen oxides and soot, which are important atmospheric pollutants. As the combustion was realized in lean premixed conditions, the main challenges lied in the control of the auto-ignition as well as the uniformity of the mixture. The same year, Noguchi and co-workers [19] compared the spark-assisted and auto-ignition, called TS that stood for 'Toyota-Soken', of gasoline in a two-stroke cycle gasoline engine. Using a high-speed camera, they observed that the auto-ignition occurred at numerous points in the combustion chamber, resulting in an overall shorter combustion duration when compared to spark ignition, in which a flame front is formed very near the spark plug and propagates radially through the chamber.

This combustion mode, based on the Compression-Ignition of a Homogeneous Charge (CIHC), was successfully applied to a four-stroke cycle engine [20]. As a major finding in this study, it was demonstrated that the self-ignition process was controlled by the low-temperature oxidation (< 950 K) kinetics, while the heat release process was controlled by the high temperature hydrocarbon oxidation (above 1000 K). The HCCI term, acronym of Homogeneous Charge Compression Ignition, was later introduced by Thring in 1989 [21]. Its study differed from the previous ones as a four-stroke engine was used, and as the geometry of the apparatus was different from the one used by Najt and Foster. Conclusions from this study stated that HCCI combustion was able to achieve fuel economy comparable to a diesel engine (when compared to a gasoline engine) and produced very low cyclic irregularity. High Exhaust Gas Recirculation (EGR) rates were however required, as well as high intake temperatures (> 600 K).

From these first publications on HCCI, extensive research was performed in order to better understand the response of this combustion mode to a variety of parameters: the compression ratio [22], the fuel characteristics [23], the mixture inhomogeneity [24], etc. However, difficulties encountered in the ignition timing control remain an open question. A recent review from Duan and co-workers [25] offers an overview of the different techniques developed in that purpose. Derived from the HCCI combustion mode, different other engine technologies were developed, aiming at simpler ignition timing control. In the Spark-Assisted Compression Ignition engine, SACI, a spark produces a propagating flame front which consumes part of the charge in the combustion chamber. The heat released by this partial fuel consumption heats the remaining unburned gases in the chamber, triggering an earlier auto-ignition [26]. The commercial Mazda e-Skyactiv X engine is based on the SACI technology, with a claim of reduced CO_2 and NO_x emissions, and improved combustion efficiency [27]. Partially Premixed Compression Ignition, PPCI, is also considered as a solution in decreasing the pollutant emissions, especially NO_x and particulate matter. This combustion mode can be achieved by modifying the exhaust gas recirculation rate or the fuel injection properties. Compared to a conventional diesel engine, Zhang and co-workers showed that soot and NO_x emissions could be greatly reduced, but observed a slight decrease of the engine efficiency [28]. Furthermore, Reactivity Controlled Compression Ignition, RCCI, also demonstrated its efficiency in controlling the ignition timing. By using dual fuels with very different reactivity, or a fuel and an additive [29], the auto-ignition delay of the mixture can be controlled [30]. Reactivity control by ozone-adjunction in HCCI engines was also studied by different groups, and is discussed in Section I.2.3.2.

I.1.4. 2000s: Recent findings on cool flames

I.1.4.1. Cool flames observation onboard the ISS

Cool flames were recently observed aboard the International Space Station (ISS), in an experimental apparatus called FLEX, standing for FLame EXtinguishment. The objectives of this research are to investigate the behaviour of flames in microgravity, and to explore the effect of different

fire suppressants in reduced gravity environment. A *n*-heptane droplet burning in micro-gravity is pictured in Figure I.1. The spherical propagation of the diffusive flame front differs from diffusion flames under standard gravity, because of the absence of convection in these conditions.

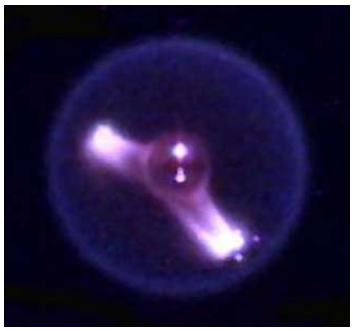

Figure I.1. Burning *n*-heptane droplet in the FLEX apparatus, image from [31].

An anomalous observation was reported during the combustion of *n*-heptane droplets. After the droplet ignition, a relatively large *n*-heptane droplet first underwent radiative extinction caused by the radiative heat loss. But then the droplet continued to vaporize during an extended period according to a quasi-steady burning law, ending in a second-stage extinction. The publication that showed these first observations [32] hypothesized that the burning characteristics of this 'invisible' combustion were closer to cool flames than to conventional hot flames. Numerical simulation of this phenomenon by Farouk and co-workers [33] confirmed the presence of a cool flame, i.e., low-temperature reactivity, that dictated the two-stage ignition behaviour. Tests with *n*-octane and *n*-decane showed a similar behaviour of the droplet combustion under micro-gravity conditions [34]. Further insight into the establishment of cool flames under such conditions was obtained in June 2021, under the program CFI-G (Cool Flames Investigation with Gases). Using an intensified camera, it was possible to capture the faint light emissions of the cool flame after the hot visible flame extinction, as presented in Figure I.2. After roughly 60 seconds, the hot diffusion flame extinguishes due to the radiative heat loss. At 63.04 seconds, a faint trace of chemiluminescence appears on the camera, produced by the cool flame. This observation was not possible using conventional cameras, because of the weak light emission of cool flames [35].

While these experiments performed in the ISS shed some light on the cool flame phenomenon, and more precisely the conditions in which cool flames can take place under reduced gravity, numerous questions still remain on the chemical kinetics behind such flames. Trying to gain some further insight into the mechanisms governing cool flames, different experimental configurations enabling the formation and stabilization of cool flames emerged in academic laboratories. This is the object of the next section.

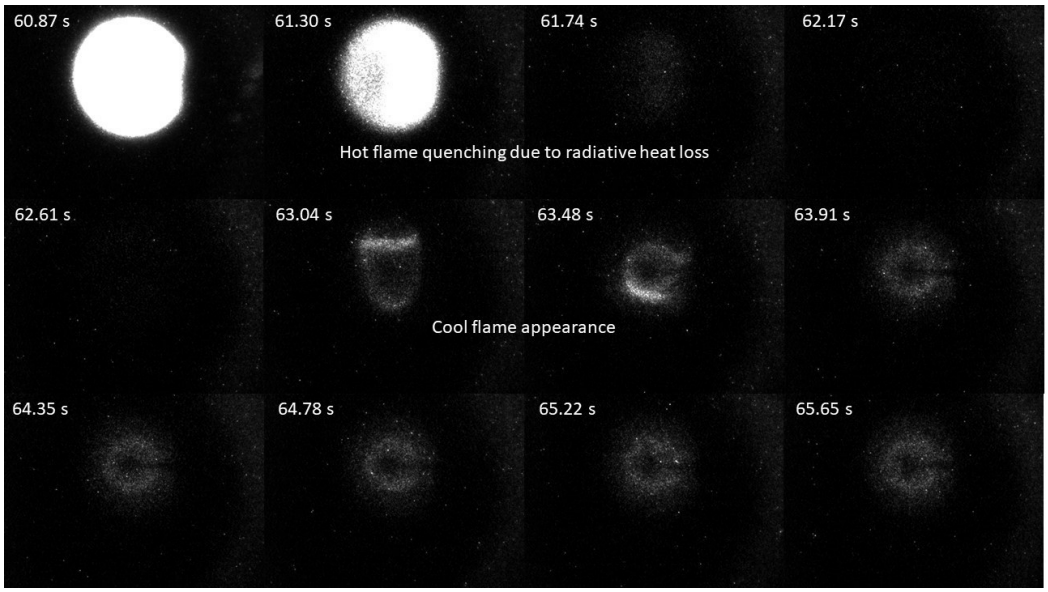

Figure I.2. Hot flame quenching and cool flame appearance under the CFI-G program [35].

I.1.4.2. Recent cool flames academic studies

Different apparatuses can be used in order to study low-temperature combustion kinetics, which are synthetized in Figure I.3. Depending on the chosen experimental configuration, different conditions regarding the temperature domain and dilution can be reached. When operated at steady-state, Jet-Stirred Reactors (JSRs) permit the study of low-temperature combustion kinetics by following the mole fraction evolution of the reactants, intermediates and products as a function of the temperature with a fixed residence time [36]. Reactive mixtures are generally diluted in a neutral gas, such as Argon, Helium or Nitrogen, in order to inhibit the exothermicity caused by the combustion reactions taking place in the reactor. One of its main advantages is the ease of implementing analytical techniques such as gas chromatography, or advanced mass spectrometry techniques, allowing the measurement of highly reactive species [37]. Plug Flow Reactors (PFRs) operate in similar conditions, they however allow to reach higher temperatures than JSRs. It is noteworthy that flow reactors can also be used in non-diluted conditions. It is the case of the micro flow reactor operated by the Maruta group at Tokohu University [38,39]. Using a controlled temperature profile along the reactor, stabilized three-stage oxidation of fuel/air mixtures was successfully observed. On the other hand, RCMs can be used to study the low-temperature oxidation of fuels via the measurement of ignition delay times, i.e., the time necessary for the reactive mixture to ignite after the end of the compression. The typical temperature range of RCMs is 400 – 1200 K, and the pressure range from 5 to 80 bar [40]. While rapid compression machines possess many advantages in measuring valuable data linked to the autoignition chemistry of fuels, few limitations exist. Firstly, their transient nature restrains the variety of analytical techniques that can be developed. Furthermore, temperature non-uniformity due to the presence of roll-up vortex induced by piston motion can greatly affect the interpretation of acquired data using such setup. To avoid this phenomenon, RCMs use creviced pistons to mitigate fluid motion after compression, allowing part of

the mixture to transfer to the crevice during the first-stage ignition and therefore reducing the relevant pressure increase. The heat release of the first-stage ignition is therefore altered, reinforcing the need for experimental setups in which the heat release can be accurately quantified. Finally, shock tube facilities are also widely used within the combustion community. Compared to RCMs, shock tubes allow to reach higher temperatures, the short ignition delays measured at elevated temperatures generally ensuring precise and reliable measurements. As the temperature decreases, ignition delay time increases, which limits measurements in the low-temperature domain. Shock tubes are therefore usually used for high-temperature combustion kinetic studies.

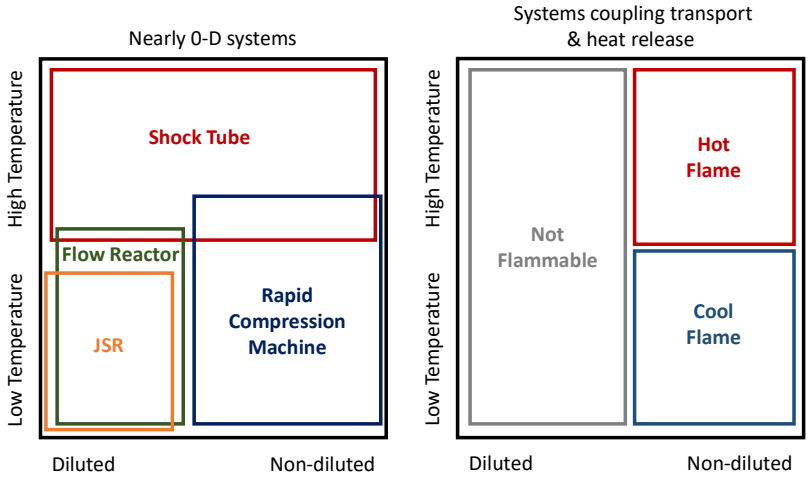

Figure I.3. Study domains of low-temperature combustion kinetics, reproduced from Ju and co-workers [41].

Diluted reactors, rapid compression machines and shock tubes present many advantages, but it was previously highlighted that accurately quantifying the cool flame heat release was either difficult or impossible. As the cool flame is a complex phenomenon coupling the chemistry, thermodynamics and transport aspects of combustion, it was necessary to develop experimental configurations that allow the study of such parameters. Burners adapted to cool flame studies were therefore developed in different laboratories and are presented below.

- **The counter- (or opposed-) flow burner (Princeton University)**

The counter-flow burner is frequently met in flame studies, as it allows flame stabilization in a wide range of conditions with well-defined boundary conditions. The first stabilized, lean, cool flames of dimethyl ether (DME, CH_3OCH_3) were reported by Reuter and co-workers during the 53rd American Institute of Aeronautics and Astronautics (AIAA) Aerospace Sciences Meeting [42]. Following recent studies about the impact of plasma or ozone on combustion, it was observed that adding ozone to a DME/O_2 mixture extended the flammability limits of the flame, and eventually allowed the formation of a self-sustaining cool flame. It is known that when ozone, a compound that tends to quickly

decompose when exposed to relatively high temperatures, is added to the mixture, its decomposition will form O-atoms. This species is very reactive and enables the low-temperature reactivity to take place. Thereby, in the work of Reuter and co-workers, cool flames were stabilized in a counterflow burner, a $DME/O_2/O_3$ mixture impinging a nitrogen flow heated at 600 K. Cool flames were obtained in lean conditions, the equivalence ratio in these experiments varying from ~ 0.08 to ~ 0.25. The necessary ozone mole fraction to stabilize such flames ranged from 3.1 to 3.4% of O_3 in the oxidizer flow. The authors also numerically studied the formation and dynamics of dimethyl ether cool flames using detailed kinetic mechanisms in counter-flow and freely-propagating configurations, with and without ozone-sensitization [43]. It was found out that the flammability limits of the DME/O_2 mixture with regards to hot flames were greatly affected by the presence, or absence, of a cool flame. Further experimental work was achieved by the same group by intensively studying the structure of cool and hot flames in the same mixture conditions in the counterflow configuration [44]. An image of a $DME/O_2/O_3$ cool flame, stabilized in the counterflow burner at Princeton University, is presented in Figure I.4, along with a simplified scheme of the burner. Planar Laser Induced Fluorescence (PLIF) measurements in both flames showed that the production of formaldehyde, CH_2O, was significantly higher in the case of the cool flame when compared to the hot flame. Furthermore, measurements of the flame location, using the maximum of the LIF signal, in both conditions also hinted that the cool flame position, and by extension the cool flame propagation speed, were almost insensitive to equivalence ratio variations in the tested conditions, opposite to hot flames that are known to be significantly impacted by this parameter. Finally, Reuter and co-workers [45] used the counterflow burner configuration to study ignition characteristics of $DME/O_2/O_3$ partially premixed cool flames. Cool flames were ignited following different methods, respectively i) auto-ignition, ii) laser-induced ignition and iii) hot flame extinction. Cool flame auto-ignition is the most straightforward way to stabilize cool flames under favourable conditions, i.e., a relatively low strain rate so that the low-temperature induced chemical time scale does not exceed the flow time scale. Laser-induced ignition using the fourth harmonic, λ = 266 nm, of an Nd:YAG laser also allowed cool flame stabilization by O_3 photo-dissociation, forming O-atoms. The laser beam energy necessary to establish a cool flame was found to be dependent on the inlet flow rate.

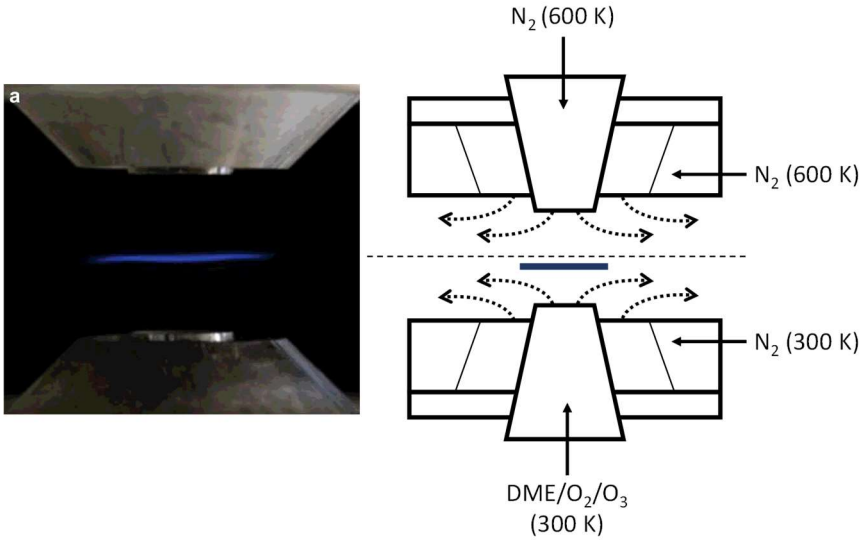

Figure I.4. Image of a cool flame, $\phi = 0.114$ (left-hand side) and simplified schema of the counter-flow burner configuration (right-hand side) [44].

It should be noted that the ozone-sensitization is not absolutely necessary, as the stabilization of cool flames without ozone was reported by Reuter and co-workers [46] for diffusion flames and by Zhao and co-workers [47] for premixed flames. In the first case, the fuel/oxidant ratio had to be greatly increased in order to reach such an objective, as pictured in Figure I.5, which represents the measured extinction strain rate as a function of the DME mole fraction in the inlet flow, with and without ozone. The fuel mole fraction was increased by an order of magnitude to obtain a cool flame without ozone at comparable extinction strain rates than with ozone. In the premixed configuration, the authors had to increase the equivalence ratio until $\phi = 1.5$ to stabilize a cool flame in the counter-flow burner without ozone-sensitization.

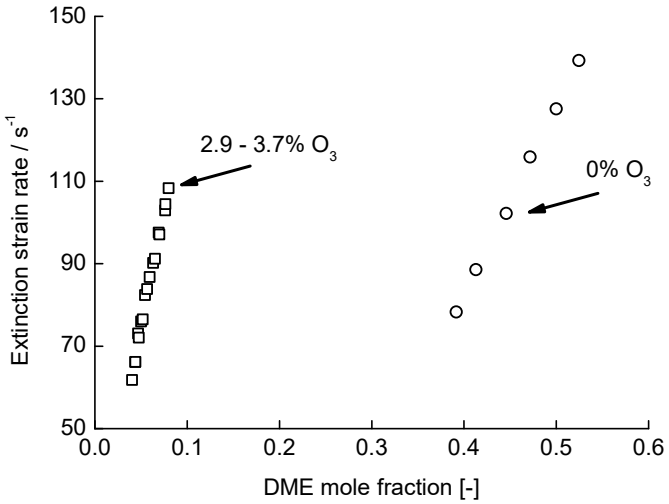

Figure I.5. Extinction strain rates of DME/O_2 cool diffusion flames with and without ozone-sensitization, reproduced from [46].

- **The Hencken burner (University of Wyoming)**

The second recent experimental configuration used for cool flames studies is the so-called Hencken burner. It is composed of 100 capillary fuel tubes, each one being surrounded by six air flow passages within a squared honeycomb matrix. The fuel/oxidizer flow is surrounded by an inert co-flow that limits interactions between the flame and its environment. An image of the Hencken burner, coupled with the corresponding scheme, is shown in Figure I.6.

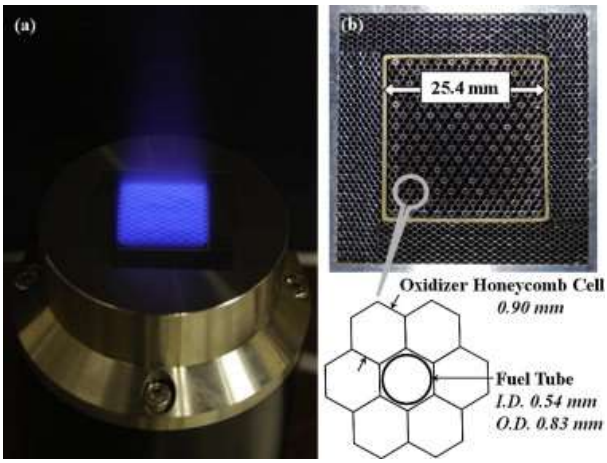

Figure I.6. Image (left-hand side) and scheme (right-hand side) of the Hencken burner, taken from [48].

Premixed ozone-seeded cool flames at sub-atmospheric pressure were studied in this original apparatus, using dimethyl ether [49], propane [50], *n*-heptane [51,52] and *n*-decane [53] as fuels. Operating at low pressure was necessary to ensure a rapid mixing of the fuel and the oxidizer at the surface of the burner. One important feature of this configuration is that the hot flame ignition downstream the cool flame is avoided as an inert gas, Argon in these studies, is used as curtain flow and mixes with the burnt gases above the cool flame. Temperature and species mole fraction profiles were extracted from the stabilized quasi-freely propagating cool flames. One of the major benefits of the Hencken burner is that by working in steady, laminar, nearly one-dimensional, minimally curved, weakly strained, and nearly adiabatic conditions, the measurement of unstrained laminar flame speeds was made possible [48]. Details on cool flame speed measurements will be given later in this manuscript (section I.3.3.2).

- **The stagnation plate burner (University of Tokyo)**

The autoignition characteristics of DME/O_2 mixtures under a heated plate were studied by Lee and co-workers [54,55]. The influence of different parameters on the cool flame ignition, respectively the surface material (Al_2O_3, SiO_2, Fe and Pt were tested), the plate temperature, the inlet equivalence ratio and velocity, were assessed. Using CH_2O-PLIF, which allowed the detection of formaldehyde (one of the major combustion products at low temperatures) even at very low concentrations, coupled with

temperature measurements, permitted the observation of the cool flame ignition. Spontaneous ignition of DME/O_2 mixtures at equivalence ratios as low as 0.03 was detected.

In this context, the aim of this work is to introduce a newly developed burner dedicated to the study of cool flames structure, bringing original datasets for different fuels, thus allowing to gain better insight in the low-temperature combustion kinetics of these fuels.

I.2. Fundamentals on combustion kinetics

I.2.1. Temperature domains in combustion mechanisms

When dealing with combustion, the first thing we think of is the flame of a candle burning in the dark, or the flame propagating in an engine, releasing the necessary energy to move a vehicle. Therefore, it is of common belief that combustion only occurs at the highest temperatures. However, from the presented information in the previous section, it is now clear that combustion does not only occur at high temperature, but that some chemical mechanisms occur at lower temperatures, both of them being very different. Following the Arrhenius law, it is supposed that the global rate of a chemical system increases with the temperature. However, it was experimentally observed that in some cases, while following the oxidation of a fuel in an isothermal reactor over a large range of temperatures (typically 500 to 1100 K), the fuel reactivity undergoes a first step of oxidation, but then its reactivity decreases (the conversion of the fuel decreases as the temperature increases) before increasing again at higher temperatures. This behaviour is illustrated in Figure I.7, in which the evolution of the *n*-heptane mole fraction as a function of temperature is represented in a jet-stirred reactor [56]. As one can see, between 500 and 625 K (**zone 1**), the fuel is oxidized in the reactor, and its mole fraction decreases. Between 650 and 775 K (**zone 2**), the fuel mole fraction in the reactor increases, meaning that the rate of consumption of the fuel decreases as the temperature increases, which imposes a negative activation energy in the Arrhenius correlation. Then, after 800 K (**zone 3**), the fuel conversion increases monotonically until 1100 K, the maximum temperature at which this experiment was performed.

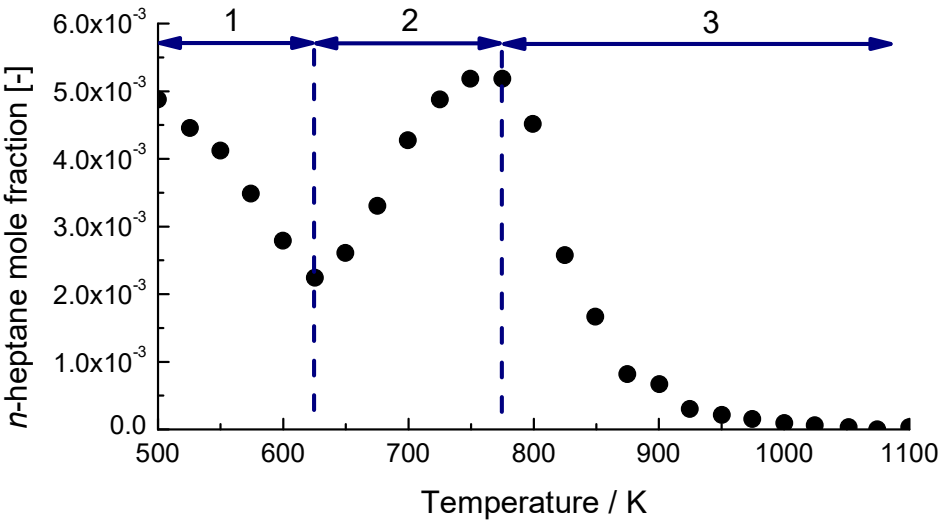

Figure I.7. *n*-heptane oxidation in a jet-stirred reactor, experimental data reproduced from [56].

This phenomenon illustrating the non-Arrhenius behaviour of the oxidation of a fuel is called Negative Temperature Coefficient (NTC). The particular chemical kinetics behind this phenomenon are complex and will be discussed in detail in the next section. The expression 'negative temperature coefficient' was originally introduced in 1929 by Pease in its study on *n*-butane oxidation [12]. It is interesting to understand the close link between the formation and stabilization of cool flames and this phenomenon. When a cool flame is initiated in an open system, the fuel undergoes partial oxidation inside the flame, which causes an increase of the temperature as the heat release is not constrained. When the temperature of the flame reaches the so-called Negative Temperature Coefficient, the reactivity decreases and prevents the flame from turning into a conventional hot flame. If the cool flame takes place into a closed vessel, the chemical heat released by the flame could, in this case, creates a sufficient increase in temperature to turn the cool flame into a hot flame, hence two-stage ignition, as stated by Perkin in 1882 [4].

It is now of interest to introduce the detailed chemical kinetics governing the low-temperature combustion, and by further extent the cool flames, and their difference with the high-temperature combustion mechanisms.

I.2.2. Fuel oxidation: emphasis on the low-temperature domain

The fuel molecule that will be used as an example to describe the low-temperature mechanisms will be noted as RH, with an exclusive focus on 'C-O-H' containing species. The global mechanism proposed below is generally accepted by the combustion community [57], and proceeds through the different steps presented above: initiation, chain-propagation, chain-branching and termination. Many documents report a detailed description of the low- to high-temperature combustion kinetics, which is out of the scope of this manuscript. The following paragraphs aim to highlight the important reactions in the low-temperature domain, the fuel being here an ether molecule.

The first step of the chain reaction mechanism is the initiation. In the low-temperature regime, the H-atom abstraction reaction on the fuel molecule (R1) is the most favoured reaction as its reaction rate is much faster at these temperatures than the unimolecular decomposition reactions, for which the activation energy is higher. In this case, X can either be a molecule (generally O_2), a radical (ȮH, HOȮ, etc) or an atom (Ö, Ḣ).

$$RH + X \Leftrightarrow \dot{R} + XH \qquad (R1)$$

The formed alkyl radical can then add to molecular oxygen to form a ROȮ radical (R2). Another possible fate of the alkyl radical is to undergo a β-scission. The alkyl radical unimolecular decomposition is the favoured reaction above 800 K, however at lower temperatures the Ṙ addition to O_2 is the major reaction pathway. The reaction leading to the formation of the alkylperoxy radical (R2)

is barrier-less, i.e., the activation energy is close to zero, but the reverse reaction is not. As this equilibrium is exothermic, its equilibrium constant decreases as the temperature increases, inhibiting ROȮ formation at elevated temperatures. At low temperatures, the reaction proceeds in the forward direction, producing very efficiently ROȮ radicals. At higher temperatures, the reverse reaction is dominating, thus ROȮ radicals dissociate rapidly.

$$\dot{R} + O_2 \Leftrightarrow RO\dot{O} \quad \text{(R2)}$$

Once ROȮ radicals are formed, several reaction pathways are possible, the most frequent one at low temperatures being the formation of ȮOOH radicals via H-atom internal migration (R3). Other pathways are possible, such as the formation of hydroperoxides (ROOH), which can yield RȮ radicals.

$$RO\dot{O} \Leftrightarrow \dot{Q}OOH \quad \text{(R3)}$$

The subsequent hydroperoxyalkyl radicals, ȮOOH, can then either decompose into alkenes, cyclic ethers or carbonyl species, or react with molecular oxygen to form peroxyalkylhydroperoxide radicals, ȮOQOOH (R4). Considering the energy barriers of each reaction that ȮOOH can undergo, the lower typically being the one of (R4), the formation of ȮOQOOH will be favoured at low temperatures.

$$\dot{Q}OOH + O_2 \Leftrightarrow \dot{O}OQOOH \quad \text{(R4)}$$

Peroxyalkylhydroperoxide radicals, ȮOQOOH, can then react through a two-step mechanism, the first one being the H-atom migration of ȮOQOOH into a hydroxyl radical and a ketohydroperoxide (R5), the latter decomposing into a second hydroxyl radical and a carbonyl radical (R6). As one can observe, from one peroxyalkylhydroperoxide radical two ȮH radicals and a carbonyl radical are formed. It provides chain-branching as this increase in the number of radicals in the system will cause an important rise of the reactivity in this temperature domain. The formed ȮH radicals can then react with the fuel molecules, creating an auto-catalytic system. However, when the temperature increases, the ȮOOH decomposition reactions become faster, leading to a lower reactivity of the system towards the formation of ketohydroperoxides. This phenomenon, caused by the competition between chain-branching and chain-propagating reactions, is known as the Negative Temperature Coefficient (NTC) regime.

$$\dot{O}OQOOH \Rightarrow HOOQ{=}O + \dot{O}H \quad \text{(R5)}$$

$$HOOQ{=}O \Rightarrow \dot{O}Q{=}O + \dot{O}H \quad \text{(R6)}$$

Following recent work from Wang and Sarathy [58], it was shown that for linear alkanes with six or more carbons, a third fuel radical addition to O_2 should be considered. Extensive work from Belhadj and co-workers [59] in characterizing low-temperature oxidation products of different fuels by means of high-resolution mass spectrometry analysis reported the formation of highly oxygenated molecules (HOMs) in the low-temperature regime, resulting in up to five O_2-additions on the fuel radicals.

In Figure I.8. a schematic of the accepted low-temperature oxidation pathway is pictured, in which RH can either be a linear alkane or a linear ether. Black arrows represent the cyclic low-temperature domain, where the fuel oxidation leads to the formation of two hydroxyl radicals. Blue and red arrows respectively represent the pathways leading to the intermediate-temperature combustion and high-temperature combustion domains.

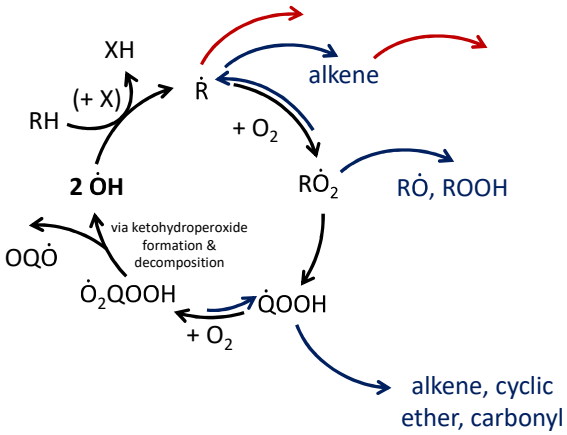

Figure I.8. Schematic of the low-temperature oxidation pathway, re-adapted from [60].

I.2.3. Plasma- and ozone-assisted combustion

I.2.3.1. Fundamentals on plasma-assisted combustion

Plasma discharges possess interesting properties with regards to the initiation of combustion which will be reviewed in this section. Firstly, two different kinds of plasma should be distinguished, respectively equilibrium plasma and non-equilibrium plasma. While both can be applied to combustion systems [61], non-equilibrium plasma recently drew attention as they offer new opportunities in ignition control and flame stabilization. This section will therefore focus on non-equilibrium plasma, which are commonly called 'low-temperature plasma'. Non-equilibrium plasma can be described by their electronic, rotational and vibrational temperatures, which are different, and by the neutral gas temperature and the electron number density, which are very low when compared to equilibrium plasma. The impact of plasma on combustion can be divided in the three following categories, which are summarized in Figure I.9, adapted from the work of Ju and Sun [62]:

- Thermal enhancement: Whatever the kind of plasma, it is generally accompanied by an increase of the temperature in the system. Following the Arrhenius law, the chemical reactions will therefore be accelerated, including the fuel consumption.

- Transport enhancement: Breakdown of large fuel molecules into smaller fragments during the plasma discharge modifies the transport properties, e.g., the mixture diffusivity, which can then alter the combustion process. Additionally, the formation of an 'ionic wind' enhances the flow.

- Kinetic enhancement: High energy electrons and ions produced during the plasma discharge will further produce reactive radicals (e.g., Ö, ȮH or Ḣ) via direct electron impact dissociation, ion impact and recombination dissociation, and collisional dissociation of reactants with electronically (e.g., $O_2(^1\Delta g)$ or N_2*) or vibrationally ($N_2(v)$) excited molecules. Moreover, longer-life species such as ozone, O_3, or nitric oxide, NO, which are especially known to modify the NTC behaviour of fuels [63,64], are also produced during the plasma discharge.

While much research was led these last years in order to better understand the fundamentals of the kinetics behind plasma discharge, and how to model them, important uncertainties remain. Furthermore, it can be observed in Figure I.9. that the thermal, transport and kinetic enhancement effects of plasma on combustion are interconnected, emphasizing the difficulty in accurately understanding the influence of non-equilibrium plasma on combustion processes.

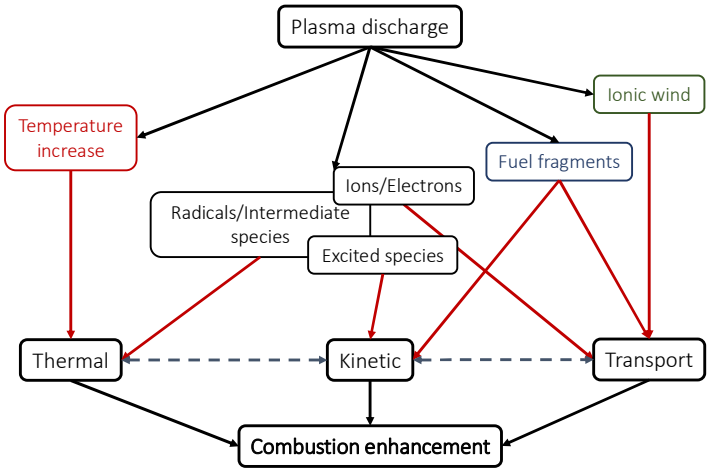

Figure I.9. Plasma influence on combustion, reproduced from [62].

From a macroscopic point of view, plasma discharges affect the combustion process through different aspects. Firstly, the use of a plasma discharge can decrease the lean flammability of a fuel [65], allowing the fuel to burn inside engines at lower equivalence ratios, which is one of the key towards a reduction of soot and NO_x emissions during the combustion process. Plasma discharges can also be used to correct combustion instabilities in engines working in lean conditions [66]. It was also reported that the coupling of a plasma discharge with a rapid compression machine allowed to shorten the first-stage ignition delay time without modifying the combustion end-products distribution [67]. Considering these different aspects, plasma discharges are a main asset for HCCI and alternative combustion modes, as they offer a solution to one of the problems met with compression-ignition engines: precise ignition timing control.

From these three aspects described in Figure I.9, the kinetic enhancement is the most complex, and its study is made even more complex as thermal and transport aspects also affect the plasma kinetics. In order to simplify these studies and improve the understanding of plasma assisted combustion, the effect of nanosecond discharges is sometimes described as an input term of O-atoms and fast heating in combustion simulations [68]. Experimentally, O-atoms can also be provided using the thermal decomposition of ozone.

Ozone is a relatively stable species at room conditions: its half-life time is estimated to ~ 3 days [69] but quickly decreases as the temperature increases or in the presence of surfaces. Its dissociation usually forms one oxygen molecule and one oxygen atom, a very reactive species, as follows (the M stands for the third-body or colliding partner):

$$O_3 (+ M) \Leftrightarrow O_2 + \ddot{O} (+ M) \quad \text{(R7)}$$

In a combustion system, the so-formed oxygen atom can then proceed to H-atom abstraction on the fuel molecule, which will initiate the chain-reaction mechanism (R8).

$$\ddot{O} + RH \Leftrightarrow \dot{R} + \dot{O}H \quad \text{(R8)}$$

It is important to note that the decomposition of ozone (R7) is not the only existing pathway, as it can also react with different species to form different radicals, which will have the same effect: increasing the reactivity by favouring the formation of species that allow H-atom abstraction from the fuel molecules (R9 – 12).

$$O_3 + \dot{H} \Leftrightarrow O_2 + \dot{O}H \quad \text{(R9)}$$

$$O_3 + \dot{H} \Leftrightarrow \ddot{O} + H\dot{O}O \quad \text{(R10)}$$

$$O_3 + \dot{O}H \Leftrightarrow O_2 + H\dot{O}O \quad \text{(R11)}$$

$$O_3 + H\dot{O}O \Leftrightarrow \dot{O}H + O_2 + O_2 \quad \text{(R12)}$$

In the case of molecules possessing unsaturated bonds, ozone can add to the double bond and form an ozonide, which will further decompose in a carbonyl compound and a carbonyl oxide, so-called Criegee intermediate [70], among other pathways [71]. Such reactions are however negligible for saturated molecules. For instance, Morrisey and Schubert [72] reported the reaction rate of ethane + O_3 at 298 K, equal to $k_{alkane} = 2.8 \cdot 10^{-23}$ cm^3·molecule^{-1}·s^{-1}. Becker and co-workers [73] measured the reaction rate of ethene + O_3 at 298 ± 2 K, equal to $k_{alkene} = 2.8 \cdot 10^{-17}$ cm^3·molecule^{-1}·s^{-1} leading to a ratio $k_{alkane}/k_{alkene} \sim 10^{-6}$.

I.2.3.2. Influence of ozone on low-temperature combustion

As previously stated, one of the main goals of ozone-assisted combustion is to facilitate a homogeneous ignition in conditions in which it is either erratic or impossible. This aspect is of primordial importance in the HCCI combustion mode, as ignition takes place in lean conditions, and is governed by low-temperature oxidation chemistry. Nishida and Tachibana [74] studied the combustion

behaviour of natural gas in a HCCI engine, adding ozone up to 1200 ppm. It was experimentally shown that the ignition timing could be controlled by modifying the ozone concentration in the engine. Moreover, from numerical analysis it was emphasized that ozone-seeding acts similarly as atomic oxygen-seeding, which is however an order of magnitude more efficient than ȮH addition. Similarly, Foucher and co-workers [75] studied the influence of ozone-addition on *n*-heptane combustion in a HCCI engine, with concentrations ranging from 0 to ~ 50 ppm. Results from this study are plotted in Figure I.10, in which the evolution of the cool flame phasing, i.e., the timing of the cool flame ignition measured as a Crank-Angle Degree (CAD), and of the heat released by the cool flame (represented as the ratio between the cool flame heat release and the total heat release) are plotted as a function of the ozone concentration. As the ozone concentration in the mixture increases, the cool flame phasing decreases, meaning that the cool flame ignition takes place earlier. Meanwhile, an increase of the ozone concentration in the mixture also increases the heat release from the cool flame. This work supports previous observations by Yamada and co-workers [76] which studied the influence of ozone-addition on dimethyl ether (DME) combustion in an HCCI engine. Similar work was conducted by Masurier and co-workers [77] using *iso*-octane, C_8H_{18}, as the fuel, and by Seignour and co-workers [78], which compared the combustion behaviour of *iso*-octane and hydrogen, H_2, with and without ozone. The main conclusions remained unchanged, ozone acts as an excellent ignition enhancer in HCCI engine, and enables a better control of the auto-ignition timing. Still, these studies only provide limited insight into the influence of ozone on the low-temperature oxidation kinetics.

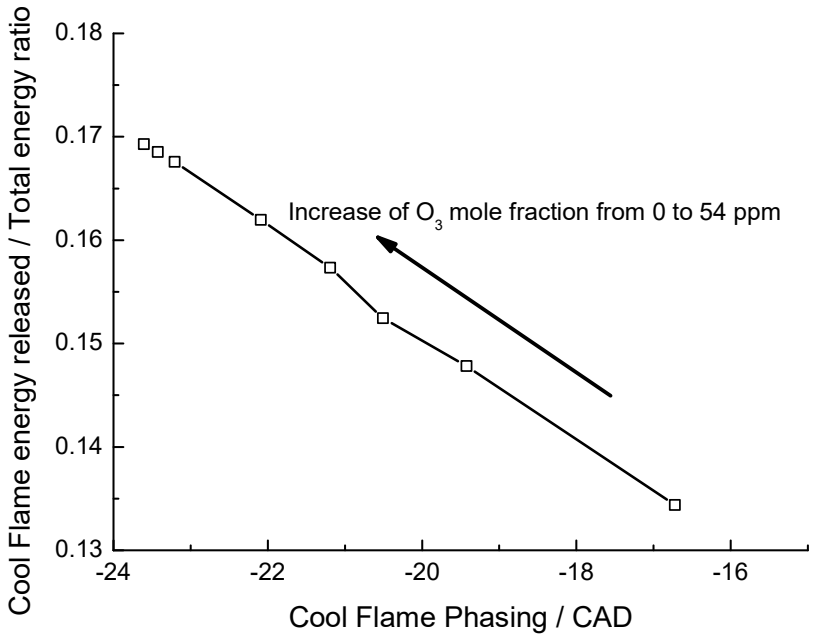

Figure I.10. Cool flame heat release as function of the cool flame phasing and ozone intake, reproduced from [75].

Several studies were led in JSRs or PFRs in order to study the impact of ozone-addition on the oxidation kinetics of fuels. Firstly, Zhao and co-workers [63] studied the low-temperature oxidation of dimethyl ether in a plug flow reactor at atmospheric pressure and for temperatures ranging from 400 to 750 K, in lean conditions (ϕ = 0.33), using different ozone concentrations: 0, 720 and 1460 ppm. Reactant and products were sampled at different temperatures and analysed by employing molecular beam mass spectrometry (MBMS). When adding ozone to the reactive mixture, it was observed that the onset temperature at which the low-temperature reactivity starts was dramatically reduced, and the fuel conversion was increased. CO and CH_3OCHO mole fractions were also seen to increase as the ozone concentration increased, which is consistent with a higher fuel conversion. Similarly, Liao and co-workers [79] studied the low-temperature oxidation kinetics of dimethyl ether in a jet-stirred reactor working at a pressure of 700 Torr, for temperatures ranging from 400 to 825 K, seeding the lean DME/O_2 mixture (ϕ = 0.35) with different ozone concentrations: 0, 1000 and 2000 ppm. Detailed speciation information was obtained using synchrotron vacuum ultraviolet photoionization (SVUV) mass spectrometry, allowing the detection of highly reactive intermediates, such as hydroperoxymethyl formate (HPMF, $HOOCH_2OCHO$), the unique aldohydroperoxide formed during the low-temperature oxidation of dimethyl ether. Consistently with the previous work from Zhao and co-workers, the addition of ozone did not change the distribution of the low-temperature oxidation products, i.e., no new species was detected under ozone-seeded conditions. However, increasing the ozone concentration in the mixture affected the branching ratio between the internal H-atom migration of the $CH_3OCH_2O\dot{O}$ radical and its self-reaction forming two $CH_3OCH_2\dot{O}$ radicals and one molecule of oxygen. This can be explained by the fact that the low-temperature oxidation process is highly dependent on chain-branching reactions, the most important being the decomposition of the $\dot{O}OQOOH$ radical ($\dot{O}OCH_2OCH_2O_2H$ in the case of dimethyl ether), providing $\dot{O}H$ radicals which are crucial in enhancing the reactivity in such conditions. As the formation of oxygen atoms from the decomposition of ozone promotes the radical pool, especially $\dot{O}H$, the low-temperature oxidation of the fuel becomes less dependent on the ketohydroperoxide formation, and shifts towards the formation of $CH_3OCH_2\dot{O}$ radicals. Furthermore, as ozone lowers the onset low-temperature oxidation temperature, $RO\dot{O}$ bimolecular reactions are favoured against H-atom internal migration reactions forming $\dot{Q}OOH$ radicals. This behaviour is pictured in Figure I.11, which is extracted from the presented study.

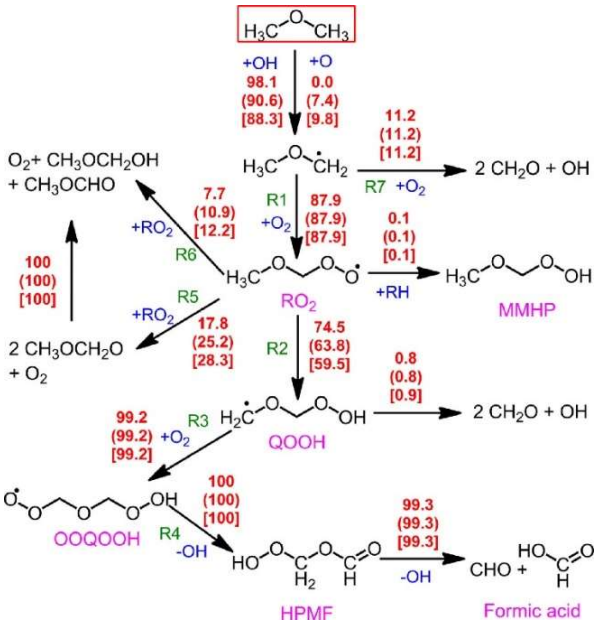

Figure I.11. Reaction pathway analysis of the DME low-temperature oxidation in a Jet-Stirred Reactor, at T = 510 K. The numbers indicate the percent contribution of the species consumption, at different ozone concentrations: 0 ppm, (1000 ppm) and [2000 ppm], from [79].

Finally, ozone was widely used in recent cool flames stabilization studies. While cool flames were successfully established decades ago [16,80], it was frequently under the presence of a trailing hot flame, i.e., a two-stage flame was stabilized above the burner, and experiments were realized using a very rich mixture, condition at which the cool flame was observed. However, considering cool flames in the scope of recent research on advanced combustion strategies, it is important to be able to perform studies in lean conditions, closer to future combustion applications. The use of ozone as a radical input to stabilize cool flames was detailed in Section I.1.4.2.

I.3. Generalities on laminar flame speed measurement

I.3.1. Fundamentals on laminar premixed combustion

Flames can be divided in two categories, which are defined by how the fuel and the oxidizer are brought to react. In a first hand, both fuel and oxidizer are brought separately before reacting in the flame front. The combustion processes are therefore governed by the species diffusivity in the flame front, giving its name to the diffusion flame. On the other hand, the fuel and the oxidizer are homogeneously mixed before the ignition, giving birth to a premixed flame. In diesel engines, the combustion is based on a diffusion flame, which explains the formation of soot particles, while premixed combustion is typical of gasoline engines. The combustion process in HCCI engines and derived technologies, which proceeds via the autoignition of a homogeneous fuel/oxidizer mixture, relies on the physicochemical properties of premixed flames. Thus, only the properties of laminar premixed flames will be addressed.

A fundamental parameter of premixed flames is the equivalence ratio. It characterizes the quantity of fuel and oxidizer relative to the stoichiometry. Its general formula is given below:

$$\phi = \frac{\left(\frac{n_{fuel}}{n_{oxidizer}}\right)_{exp}}{\left(\frac{n_{fuel}}{n_{oxidizer}}\right)_{stoech}}$$

where n designates the mole fraction of each reactant.

Three different regimes can be distinguished as a function of the equivalence ratio, namely the lean domain ($\phi < 1$) in which the fuel is in default, the stoichiometry ($\phi = 1$) in which fuel and oxidizer are present in stoichiometric conditions, and the rich domain ($\phi > 1$) in which the fuel is in excess compared to the oxidizer.

As previously stated, a laminar premixed flame is the site of reactions between the fuel and the oxidizer, already mixed before entering the reaction zone. The heat released by the combustion reactions, along with radicals formed in the flame front, diffuse upstream the flame, in the direction of the unburnt gases, therefore progressively bringing the unburnt mixture to its condition of autoignition. Following the Mallard and Le Chatelier theory, the flame structure can be decomposed in four parts, that are pictured in Figure I.12, which represents the general structure of a freely-propagating, laminar, premixed flame. The premixed reactants enter in the system at the temperature T_{inlet} in the so-called 'fresh gases' or 'unburnt gases' area (**1**). The 'unburnt gases' then enter the second area called 'preheating area' (**2**) in which they are exposed to an important temperature gradient and radical pool due to the presence of the flame. Once the reactants are brought to a sufficient temperature to react, they enter the 'reaction zone' (**3**). In the reaction zone the maximum of the heat release takes place, as well as the formation of numerous reactive intermediates responsible for the reactivity. Finally, products enter the 'burnt gases area' (**4**) in which they are at the equilibrium, and do not react anymore. The temperature T_{outlet} is generally constant in this area, and the heat release is therefore equal to 0. This is not totally true in the case of a freely propagating, laminar, premixed cool flame, but this point will be addressed later in the manuscript.

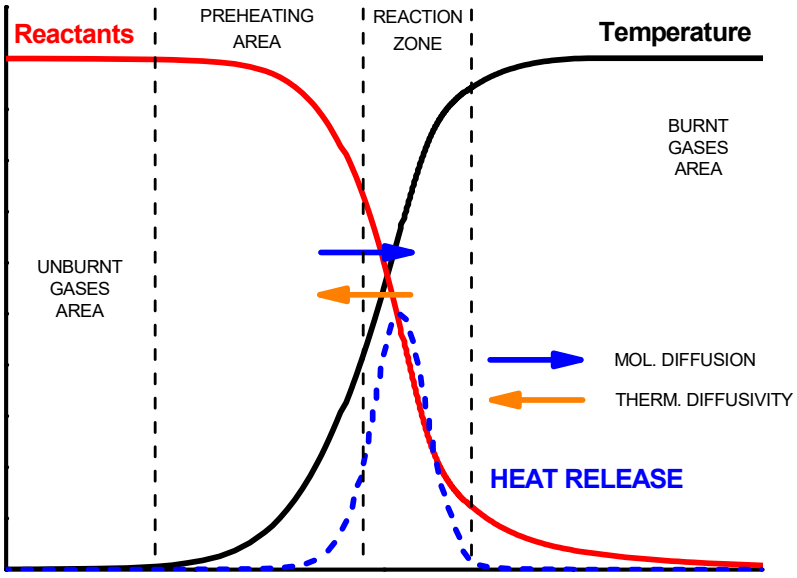

Figure I.12. Typical structure of a premixed laminar flame, reproduced from [81].

I.3.2. Flame propagation speed determination

I.3.2.1. Laminar flame speed and strain definition

The laminar flame speed, also found under the terms 'laminar burning velocity' or 'laminar flame velocity', is a valuable data as its value is intrinsic to the studied fuel at a given temperature, pressure and equivalence ratio. Many efforts were therefore dedicated these last decades to theoretically characterize it, as well as experimentally determine it. Firstly, it is necessary to introduce different definitions of the laminar burning velocity, depending on the considered referential [82,83]:

- Absolute: Flame front speed relative to a fixed reference frame
- Displacement: Flame front speed relative to the flow of unburnt gases
- Consumption: Speed at which the reactants are consumed into the flame front

Although these three definitions seem to be equivalent, a few differences exist on the mathematical treatment. In the following paragraph, only the flame front displacement with respect to the unburnt gases will be considered. Following the work from Poinsot et Veynante [84] the flame front, and the associated gas displacement, are represented in Figure I.13, where $\vec{n}$ represents the normal flame front vector oriented towards the unburnt mixture, $\vec{v}$ the local flow velocity vector, $\vec{u}$ the local flame velocity vector, and S_u the laminar flame velocity. Continuous lines represent isolevels of the flame (temperature isolevels are generally considered).

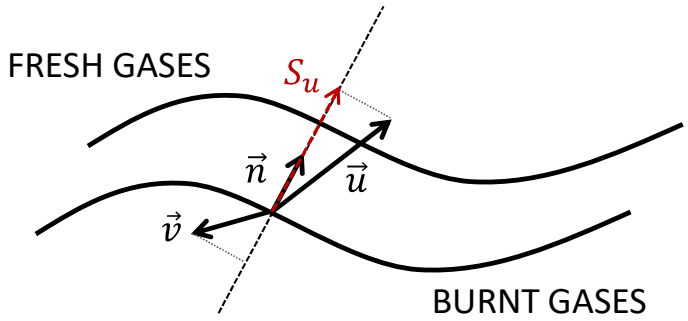

Figure I.13. Illustration of the flame speed determination, reproduced from [85].

The laminar flame velocity, S_u, is determined as follow:

$$S_u = (\vec{u} - \vec{v}) \cdot \vec{n}$$

Theoretically, the laminar flame velocity only depends on the fuel characteristics, and on the temperature and pressure conditions. However, flames are subject to strain, i.e., local deformation of the flame front caused by either aerodynamic or cooling effects, which are known to greatly affect the measured value of S_u. In order to get rid of this strain effect, a reference laminar flame velocity, commonly known as the laminar unstrained velocity, was introduced. Generally denoted S_u^0, it corresponds to the propagation speed of a theoretical one-dimensional, planar, adiabatic, unstrained freely-propagating flame.

The flame strain factor, usually denoted K, can be defined as the relative rate of change of the flame surface area A, and can be expressed as follows [86]:

$$K = \frac{1}{A} \cdot \frac{dA}{dt}$$

Early work from Tien and Matalon [87] showed that, for weakly strained flames, the relation between the laminar burning velocity of the flame and the strain could be considered as linear:

$$S_u = S_u^0 \cdot \left(1 + \frac{\mu K}{S_u^0}\right)$$

where S_u^0 represents the unstrained laminar flame speed, S_u the laminar flame speed (under the effect of strain), K the flame stretch and μ the Markstein length, of the order of the flame thickness. The Markstein length is then defined as follows:

$$\mu = -\left(\frac{D_T}{S_u^0}\right) \cdot \alpha \text{ and } D_T = \frac{k}{\rho \cdot C_p}$$

where D_T is the thermal diffusivity, k the thermal conductivity, ρ the density, C_p the heat capacity (per mass unit) of the unburnt mixture and α a coefficient related to the thermal expansion of the flow. Tien

and Matalon however showed that in some cases, when the strain effects were important enough, the linear relation between S_u and K was not valid anymore. A non-linear relation was therefore introduced, and considered as valid for fuel-lean mixtures of non-heavy hydrocarbons [88]:

$$S_u = S_u^0 \cdot \left\{1 - (\mu - 1) \cdot K_a + K_a \cdot \ln\left(\frac{\theta - 1}{K_a}\right)\right\}$$

where θ represents the density ratio between the unburnt and burnt mixtures, and K_a the Karlovitz number, which can be determined as a function of the fresh mixture diffusivity:

$$K_a = D_T \cdot K \cdot \frac{1}{(S_u^0)^2}$$

The linear and non-linear extrapolation techniques used to determine the unstrained laminar burning velocity of a mixture were compared in numerous studies [89–91]. Depending on the studied conditions, and especially the equivalence ratio of the mixture, the chosen extrapolation method of the laminar burning velocity from strained experiments can lead to an important discrepancy. While the determination of the unstrained laminar flame speed of a given mixture is important in characterizing the reactivity of a fuel or a blend, it was suggested that, for kinetics investigation and model development, the direct comparison of simulated and experimental flame speed S_u should be considered [92,93]. The use of strained and unstrained flame speeds will be discussed later in this manuscript in the Chapter V.

The next section is dedicated to a short, non-exhaustive, list of the different apparatuses used to measure laminar burning velocities, including their advantages and limits.

I.3.2.2. Experimental measurement of laminar flame speed

In order to determine laminar burning velocities of different fuels, different techniques were developed through the years. Each technique possesses advantages and drawbacks, mainly depending on the studied fuel characteristics and the diagnostic used for the laminar burning velocity measurement. The presented techniques were applied solely to hot flame laminar velocity measurements, while the attempts to measure cool flame speeds are presented in the next section.

- Heat flux method: The objective of this method is to stabilize an adiabatic flat flame at the surface of a porous burner, and to suppress the flame deformation induced by the strain. This method was originally proposed by Botha and Padling [94], which stabilized propane/air flames downstream a water-cooled porous plate, the flame being stabilized by losing heat which is transferred to the water-circuit. The temperature of the cooling-water is measured at different flow rates. Then, by extrapolating the flow rate corresponding to a case where no heat from the flame needs to be extracted from the flame (i.e., an adiabatic flame, the burner temperature is not influenced by heat losses from the flame), the laminar burning velocity of the flame can be

deduced. This technique was later modified in order to improve the precision on the flame speed determination [95]. Laser Doppler Velocimetry (LDV) measurements performed in flat flames [96] confirmed that the experimental flame structure was in good agreement with 1-D simulations, reinforcing the validity of this method in determining laminar burning velocities.

- Stagnation plane method: This technique is widely used in two different configurations: the stagnation plate burner, and the opposed-flow burner method. In both cases quasi-adiabatic flames are stabilized near a stagnation plane, either by the presence of a plate or by a counter-flow. Hydrodynamics of stabilized premixed flames in stagnation flows were studied in the past decades [97–99]. In this configuration, flames can be treated as gas discontinuities subject to an important rise in temperature, causing a drop of the gas density and a sharp increase of the axial velocity, and are obviously subject to strain, as introduced above. The unburnt gases decelerate before entering the reaction zone, therefore reaching a minimum velocity, which is known as the reference velocity, $S_{u,ref}$. The associated strain rate, K, is defined as the axial velocity gradient just upstream the minimum velocity. From the plot of $S_{u,ref} = f(K)$, it is possible to extrapolate the reference velocity to zero strain, and to determine the unstrained laminar burning velocity, $S_{u,0}$, as presented below in Figure I.14, extracted from the work of Chong and Hochgreb [90]. It also permits to illustrate the use of linear and non-linear extrapolation methods to determine the unstrained laminar burning velocity at K = 0.

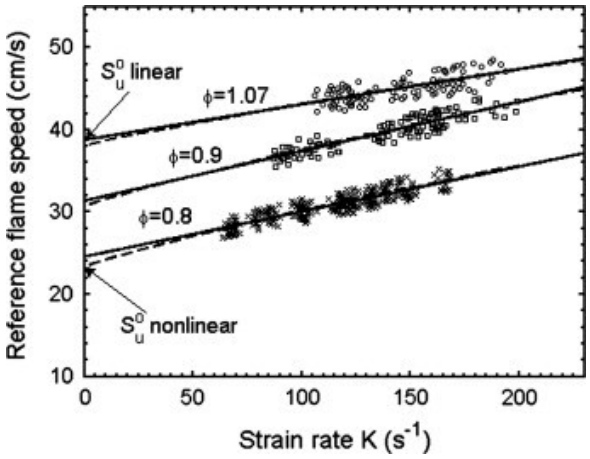

Figure I.14. Unstrained laminar flame speed determination from strained flame experiments in a stagnation flow, extracted from [90].

This method was extensively used in the literature, its main limitations being the uncertainties derived from the unstrained laminar flame speed extrapolation. This method was successfully applied to the determination of laminar cool flame burning velocities in the present work, and will therefore be detailed later in this manuscript in Chapter V.

- Spherical bomb method: This method relies on the ignition, at the centre of a spherical chamber, of a combustible mixture at rest. The flame then propagates in every direction, from the centre of the chamber towards the extremities. Using different visualisation methods permitting to follow the evolution of the flame radius as a function of time, the laminar burning velocity of the considered mixture can be determined after strain effects correction [100]. While this method is not new [101] it was considerably improved through the years, including very recently [102], especially to extend the measurement of the laminar burning velocity at high pressures, which are commonly affected by structural instabilities. An example of a flame propagating in a spherical bomb chamber is represented in Figure I.15, in which the evolution of the flame radius as a function of time can be observed.

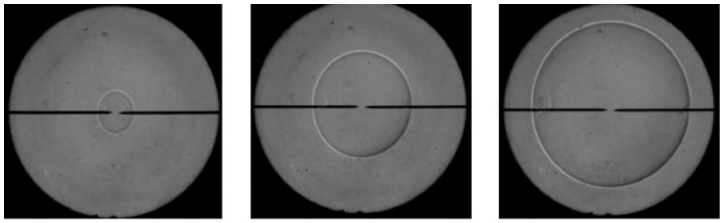

Figure I.15. Evolution of the flame radius as a function of the time in a spherical bomb chamber, extracted from [103].

- The 'Bunsen' cone method: The Bunsen flame rig can also be used to determine laminar premixed flame burning velocities. Using different visualisation techniques, the cone boundaries and the flame area can be determined, and the flame speed deduced from it. This technique is however known to be highly dependent on the determination of the flame area, which can vary depending on the visualization technique used, and leading to an accuracy on the laminar burning velocity measurement of the order of ± 20% [86].

I.3.3. Particularities and specificities of cool flames

Defining the 'cool flame speed' is a challenging task, as it is not as well defined compared to the hot flame speed. This problem was approached and discussed in the 1-D planar configuration by Zhao and co-workers [47], and is tightly linked to the cool flame chemistry. It is well known that the fuel conversion in the cool flame is only partial [104]. The gases downstream a cool flame are therefore in a quasi-chemical equilibrium, and one can imagine that with a sufficiently long time they would transition in a final equilibrium state, characterized by the adiabatic flame temperature of the mixture. In other terms, if a reactive flow was to form a cool flame in a 1-D adiabatic configuration with a sufficiently large domain, it would anyhow yield a conventional hot flame. The literature is very scarce on cool flames laminar flame speeds, but the main outcomes, either experimental or numerical, are presented below.

I.3.3.1. Spherically-propagating cool flames under reduced gravity

A series of studies were performed by Pearlman and co-workers twenty years ago, trying to gain some insight into the propagation speeds of premixed cool flames under normal and reduced gravity using the NASA KC-135 aircraft [105–108]. The cool flame propagation experiments were performed in a heated fused-silica vessel equipped with intensified cameras measuring both visible and ultraviolet chemiluminescence. Figure I.16. shows a comparison between the cool flame propagation in the vessel both at normal gravity and under micro-gravity, the initial conditions being fixed at P_{ini} = 0.3 bar and T_{ini} = 310°C. It can be observed that the cool flame propagation is highly influenced by buoyancy effects under normal gravity, while it propagates spherically under reduced gravity.

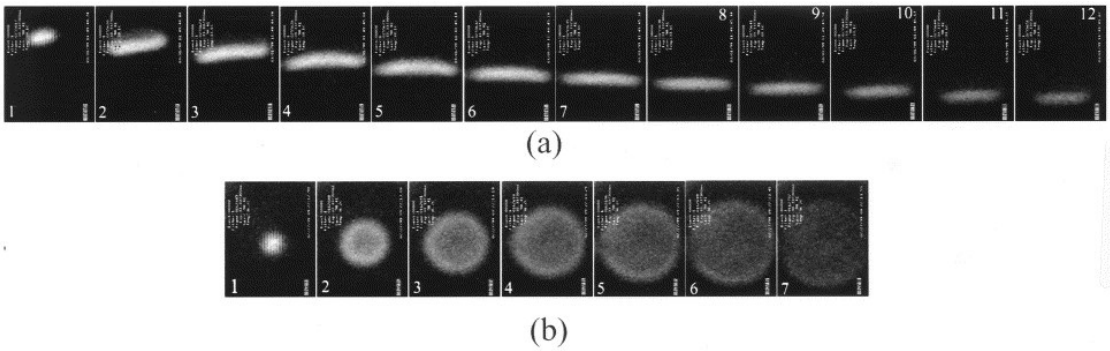

Figure I.16. Cool flame propagation under normal gravity (a) and reduced gravity (b) conditions, extracted from [105]. The acquisition frequency is 10 s^{-1}.

Moreover, in the same study, the author reported that pre-ignition happened prior to the formation of the cool flame. The propagation of the cool flame is therefore governed by autoignition-assisted flame propagation, which differs from the conventional flame propagation. It was thus difficult to extract from these data trustworthy values of unstrained, laminar cool flame speeds.

Later numerical work performed by Ju and co-workers [109] on the ignition characteristics of *n*-heptane/air mixtures in a Spark-Assisted Homogeneous Charge Compression Ignition (SAHCCI), at conditions ϕ = 0.4, T_{ini} = 700 K and P_{ini} = 20 atm, showed that multiple flames regimes existed during the flame propagation. It was notably observed that, after the hot flame ignition, the latter splits into a cool flame and a trailing hot flame, resulting in a considerable increase of the cool flame velocity, before undergoing a low-temperature ignition forming a single propagating hot flame until hot ignition occurred.

These works, although very useful in understanding how cool flames propagate under normal and reduced gravity, did not permit to experimentally measure cool flame speeds.

I.3.3.2. Freely-propagating cool flames

Considerable work was achieved by two groups [41,43,110,111] on the numerical simulation of freely-propagating cool flames, both in 0- and 1-dimensional configurations, at atmospheric or high

pressure. It was shown that a freely-propagating cool flame could be initiated by a hot spot, at the restraining condition that the hot spot temperature was not sufficient to trigger a conventional hot flame [111]. While the cool flame outwardly propagates, high-temperature chemistry ignition occurs at the hot spot, inducing a hot flame propagating behind the cool flame, similarly to the observation of Ju and co-workers in the SAHCCI engine presented previously. As the hot flame propagates faster than the cool flame, it finally merges with the cool flame. It was highlighted that, using three different kinetic models from the literature, describing the low-temperature oxidation of dimethyl ether (the chosen fuel in their study), the cool flame propagation speed was much more sensitive to the selected mechanism than the hot flame propagation speed. This finding reinforced the need in accurate experimental determination of cool flame speeds for LTC kinetic model development. Further work showed that the pressure was of great influence on the transition between the cool flame and the hot flame. At ambient (and slightly higher) pressure, the cool flame -if existing- increases the flammability domain of the combustible mixture [43], as pictured in Figure I.17. for a DME/O_2 mixture. It is interesting to note that the transition from the cool to the hot flame, and vice-versa, is very different depending on the equivalence ratio of the mixture. In rich conditions, the transition is smooth, without any extinction process, while in lean conditions the hot flame extinguishes before turning into a cool flame.

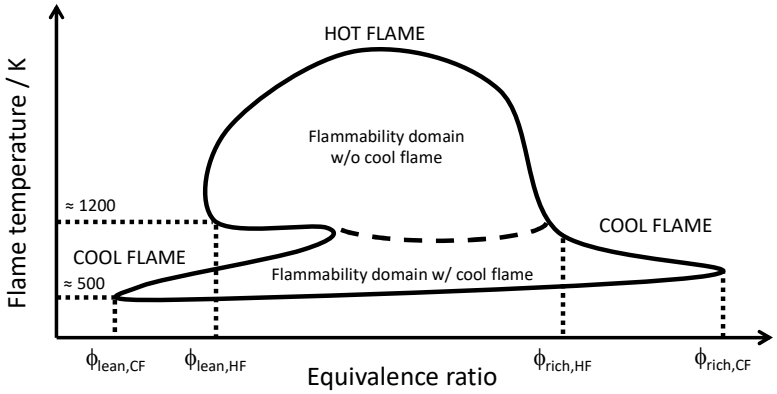

Figure I.17. Flammability domains of a combustible with and without low-temperature chemistry, reproduced from [43]. The lean and rich limits of the cool and hot flames are represented (axis are not set to scale for clarity).

It was shown that when the pressure increases [110], the transition of a lean mixture from a cool to a hot flame happened without any ignition/extinction process, but via the formation of a warm flame, which is of particular importance in engine-like conditions. The influence of EGR (Exhaust Gas Recirculation) dilution on the cool flame dynamics was also addressed in [110]. The addition of nitrogen to the mixture drastically diminished the hot and cool flames temperatures, therefore narrowing the hot flame flammable region, but broadening the cool flame flammable region towards the fuel rich side. Both cool flames and hot flames speeds were seen to be reduced by the addition of N_2 to the mixture.

By restraining the hot flame flammable domain, the N_2 dilution was therefore suggested as a good way to promote cool flame ignition.

The laminar propagation speeds of cool flames were experimentally measured by Belmont and co-workers in the low-pressure Hencken burner previously presented [49–53]. Ozone-seeded fuel/O_2 cool flames are stabilized at the surface of the cool flame burner, at different equivalence ratios and different flow velocities. Using this burner configuration, the estimation of the propagation speed of hot flames could be fairly well predicted at sufficiently high flow rates, allowing the flame to be considered as nearly-adiabatic [48,112]. This procedure, assessed for ethylene and methane hot flames, was transposed to the cool flame propagation speed determination. At a given equivalence ratio, the reactant flow is progressively increased, and the flame position measured at each condition, allowing to distinguish two different regimes: the first one, so-called 'burner stabilized regime', in which the flame position (or lift-off height) does not vary as the flow rate increases, and remains anchored to the surface of the burner. The second regime, so-called 'freely-propagating', defines the regime during which the flame position increases linearly as the flow rate increases. The transition between these two regimes is used for the propagation cool flames speeds determination, as pictured in Figure I.18, reproduced from [49], for a DME/O_2/O_3 cool flame.

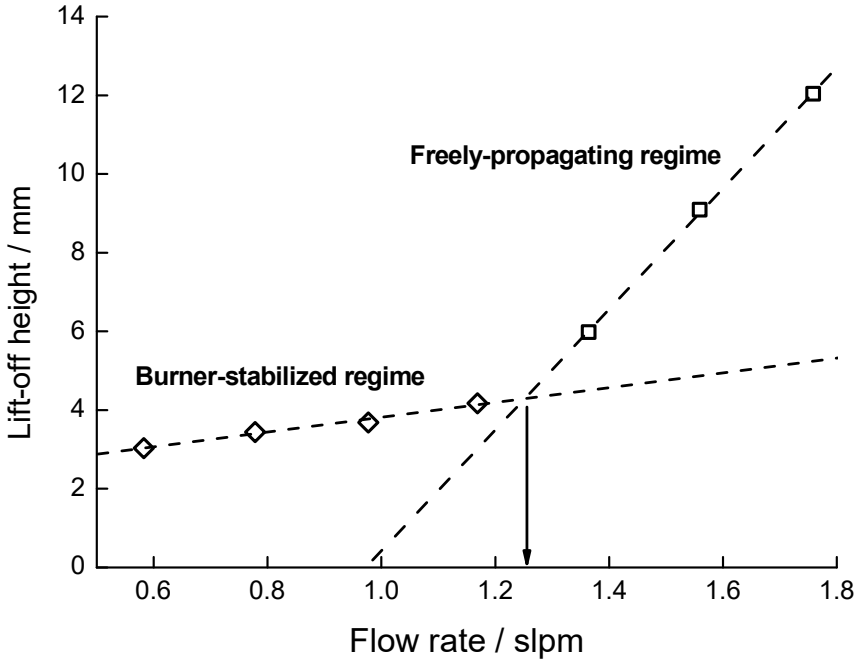

Figure I.18. Determination of the flow rate from which the laminar flame speed of a DME/O_2/O_3 cool flame is inferred at $\phi = 0.6$ and $P = 7.3$ kPa, reproduced from [49].

This procedure was successfully applied to different fuels, allowing to provide useful data, and permitted to highlight, in some cases, high discrepancies between the experimental and predicted cool flame speed. However, this method raises few limits and problematics. Firstly, this method was validated

for hot flames with help from PIV measurements, but not in the case of cool flames. Secondly, operating at low-pressure is essential to avoid flame instabilities in this experimental configuration, therefore limiting the experimental range of conditions in which cool flame speeds can be effectively measured.

I.3.3.3. Strained-stabilized cool flames

This experimental configuration, either in counterflow or stagnation plate setups, was extensively used to study cool flames ignition and extinction processes [46]. However, it was never applied to the measurement of cool flame burning velocities, even if it was suggested by Zhao and co-workers [47] on the basis of numerical work. It was demonstrated in the latter study that, as for a hot flame, the cool flame systematically responds to a strain variation, which allows to apply the methodology described above for hot flames. However, as the heat release of the cool flame is considerably lower than for a conventional hot flame, the accurate definition of a minimum velocity reference value can be challenging. At elevated strain rates, the cool flame does not possess a local minimum in its axial velocity profile but only an inflection point [47]. Moreover, the narrow stability domain of cool flames limits the strain rate range of possible measurements, which can lead to important uncertainties in the unstrained laminar burning velocity of the cool flame. Still, this limitation can be avoided as the evolution of the reference cool flame speed is considered as linear under sufficiently low strain rate variations [47].

I.4. Low-temperature combustion kinetics of ethers: a review

I.4.1. Dimethyl ether (CH_3OCH_3)

In addition to its physicochemical properties, which have made dimethyl ether an excellent candidate as biofuel substitute, dimethyl ether possesses a number of properties that are particularly suited for kinetic studies. Firstly, it is the shortest symmetric ether, which is a great advantage for kinetic studies as the number of intermediates and formed species will be limited. For example, the low-temperature combustion of dimethyl ether forms a single aldohydroperoxide, while the low-temperature oxidation of diethyl ether (the second shortest symmetric ether) can theoretically form 6 different keto- and aldohydroperoxides. Moreover, dimethyl ether is a very reactive species in the low-temperature domain, which makes it a fuel of choice. This justifies the numerous studies that were led on this species, although important uncertainties and blind-spots remain. Table I.1, which is inspired from the work of Rodriguez [113], sums up the dimethyl ether kinetic oxidation and pyrolysis studies that are discussed in the following paragraphs. The table is divided in two distinct sections, differentiating the studies with and without plasma- or ozone-assistance.

Curran and co-workers [114] studied the low-temperature combustion kinetics of dimethyl ether in a plug flow reactor between 550 and 850 K, coupling FTIR (Fourier Transform InfraRed) and NDIR (NonDispersive InfraRed) spectroscopies, allowing to characterize the different low-temperature reaction products. It was found out that dimethyl ether exhibits a negative temperature coefficient. It is

consistent with the previous studies of Pfahl and co-workers [115] in a shock tube and Dagaut and co-workers [116] in a jet-stirred reactor. Formic acid, HOCHO, was measured as one of the major intermediates in the studied conditions. Two different formation pathways were proposed, either by the $\dot{O}CH_2OCHO$ radical decomposition or by hydroxyl radical addition to formaldehyde. The latter pathway is controversial as it was found that at ambient temperature the abstraction reaction between $\dot{O}H$ and CH_2O is favoured against the addition [117]. The role and influence of H_2O_2 on the low-temperature kinetics of dimethyl ether were studied by Guo and co-workers [118] in an atmospheric-pressure flow reactor at temperatures from 490 K to 750 K, samples being analysed using molecular beam electron-ionization mass spectrometry (MBMS). The important formation of H_2O_2 in the reactor peaked at around 530 K before decreasing when the temperature was increased. From kinetic modelling, it was proposed by the authors that H_2O_2 was mainly formed (at 680 K) by the reaction $2\ HO\dot{O} = H_2O_2 + O_2$. Later on, Kurimoto and co-workers [119] simultaneously measured $HO\dot{O}$ and H_2O_2 concentrations during the low-temperature oxidation of dimethyl ether in a flow reactor. $HO\dot{O}$ was measured using Dual-Modulation Faraday Rotation Spectroscopy (DM-FRS) while the MBMS technique was used to measure the H_2O_2 and low-temperature products concentration. The acquired experimental data were compared with models from the literature, and showed that the fuel conversion was highly overestimated by the models, which consequently led to an overestimation of the formation of products, especially for $HO\dot{O}$ and H_2O_2. Overprediction of the fuel conversion by models from the literature was also reported by Rodriguez and co-workers [120], which notably led to an important overprediction of methyl formate (CH_3OCHO) formation.

Table I.1. Synthesis of the studies on DME oxidation from low- to high-temperature.

Experimental configuration	Operating conditions (P, T, x_i)	Fuel – oxidizer – inert	Reference
Studies without plasma and/or ozone			
JSR[4]	$800 < T < 1300$ K, $1 < P < 10$ atm, $0.2 < \phi < 2$	DME/O_2, dil.[7] N_2	[121]
JSR ST[2]	$550 < T < 1100$ K, $P = 10$ atm, $0.2 < \phi < 1$ $1200 < T < 1600$ K, $P = 3.5$ atm, $0.5 < \phi < 2$	DME/O_2, dil. N_2	[116]
PFR[1]	$550 < T < 850$ K, $12 < P < 18$ atm, $0.7 < \phi < 4.2$	DME/O_2, dil. N_2	[114]
PFR	$490 < T < 750$ K, $P = 1$ atm, $\phi = 0.6$	DME/O_2, dil. He, CO_2	[118]
PFR	$400 < T < 1200$, $P = 1$ atm, $0.8 < \phi < 1.2$	DME/O_2, dil. Ar	[122,123]
PFR	$400 < T < 1150$ K, $P = 1$ atm, $\phi = 0.2, 1.06$	DME/O_2, dil. Ar, He	[119]
PFR	$400 < T < 1160$ K, $P = 1$ atm, $\phi = 1$	DME/O_2, dil. Ar	[124]
JSR	$540 < T < 850$ K, $P = 1$ atm, $0.5 < \phi < 2$	DME/O_2, dil. N_2	[125]
JSR	$500 < T < 1100$ K, $P = 1$ atm, $\phi = 0.5, 1, 2$	DME/O_2, dil. He	[120]
JSR	$T = 540$ K, $P = 976$ mbar, $\phi = 0.35$	DME/O_2, dil. Ar	[126]
JSR	$450 < T < 1000$ K, $P = 933$ mbar, $\phi = 0.35$	DME/O_2, dil. Ar	[127]
PFR	$530 < T < 575$ K, $P = 1$ atm, $1 < \phi < 4.1$	DME/air	[128]
ST	$600 < T < 1300$ K, $P = 13, 40$ bar, $\phi = 1$	DME/air	[115]
RCM[3]	$615 < T < 735$, $10 < P < 20$ bar, $0.43 < \phi < 1.5$	DME/O_2, dil. N_2	[129]
Flat flame	$P = 1$ atm, $\phi = 0.67, 1.49$, $T_0 = 298$ K	DME/air	[130]
Flat flame	$P = 1$ atm, $0.7 < \phi < 1.5$, $T_0 = 298$ K	DME/air	[131]
Flat flame	(speciation) $P = 50$ mbar, $\phi = 1.63$, $T_0 = 300$ K (LBV[8]) $1 < P < 20$ bar, $\phi = 0.8, 1.63$, $T_0 = 300$ K	DME/O_2, dil. CO_2	[132]
CFF[5]	$P = 1$ atm, $0.6 < \phi < 1.7$, $T_0 = 295$ K*	DME/air	[133]
SB[6]	$P = 1$ bar, $0.7 < \phi < 1.7$, $T_0 = 295$ K	DME/air	[134]
SB	$1 < P < 10$ atm, $0.7 < \phi < 1.4$, $T_0 = 298$ K	DME/air	[135]
SB	$0.8 < P < 1.5$ bar, $0.7 < \phi < 1.8$, $T_0 = 285$ K	DME/air	[136]
SB	$P = 0.97$ bar, $0.7 < \phi < 1.8$, $T_0 = 293$ K	DME/air, dil. N_2, CO_2	[137]
SB	$1 < P < 10$ atm, $0.7 < \phi < 1.6$, $T_0 = 296$ K	DME/air	[138]
Studies with plasma and/or ozone			
sPFR	$400 < T < 750$ K, $P = 1$ atm, $\phi \sim 0.3$, $0 < x_{O3} < 1460$ ppm	DME/O_2/O_3, dil. He, Ar	[63]
PFR	$T = 300$ K, $P = 30$ Torr, $x_{DME} = 3000$ ppm	DME/O_2, dil. Ar	[139]
JSR	$400 < T < 900$ K, $P = 700$ Torr, $\phi = 0.35$, $0 < x_{O3} < 2000$ ppm	DME/O_2/O_3, dil. Ar	[79]
Flat flame[i]	$P = 17.3$ kPa, $0.17 < \phi < 1$, $x_{O3} = 6.2\%$	DME/O_2/O_3	[49]
CFF	$P = 1$ atm, $0.06 < \phi < 0.24$, $x_{O3} = 3\%$	DME/O_2/O_3	[42]
CFF	$P = 1$ atm, $0.08 < \phi < 0.114$, $x_{O3} \sim 3\%$	DME/O_2/O_3	[44]
CFF	$P = 1$ atm, $0 < \phi < 0.15$, $x_{O3} = 3.5\%$	DME/O_2/O_3	[45]
CFF	$P = 1$ atm, $0.025 < x_{DME} < 0.55$, $0 < x_{O3} < 3.7\%$	DME/CH_4/O_2/O_3/N_2	[46]

[1]Plug Flow reactor, [2]Shock tube, [3]Rapid Compression Machine, [4]Jet-Stirred Reactor, [5]CounterFlow Flame, [6]Spherical Bomb, [7]diluted, [8]Laminar Burning Velocity, [i]Hencken burner, *indicated as 'room temperature'

As stated before, one of the particularities of dimethyl ether is that only one aldohydroperoxide is formed during its low-temperature oxidation process. While the role of these species in low-temperature oxidation reaction mechanisms was postulated for a few decades now, their existence was

only experimentally proven recently, twelve years ago [37], using advanced spectroscopic techniques coupled with molecular beam sampling methods. Coupled studies of Moshammer and co-workers were dedicated to the detection and identification [126] and quantification [127] of intermediates and products formed during the low-temperature oxidation of dimethyl ether in a JSR. The first study focussed on the identification of reactive intermediates at a fixed temperature, 540 K, the oxidation products being analysed by means of a high-resolution time-of-flight molecular beam mass spectrometer coupled to synchrotron-generated vacuum-ultraviolet radiation for photoionization. The hydroperoxymethyl formate (HPMF, the aldohydroperoxide formed during the low-temperature oxidation of DME), was experimentally observed in these conditions, as well as other products as 1,3-dioxetane, *cycl*-CH_2OCH_2O or performic acid, HC(O)OOH. In the second study, the measurement of these species was performed at variable temperatures between 450 and 1000 K in the same jet-stirred reactor. Using available or calculated photoionization cross-sections, it was possible to draw the mole fraction profiles of short-life species, such as HPMF, providing valuable validation data for kinetic mechanisms. However, uncertainties on the calculation of the photoionization cross-sections lead to a relatively high uncertainty on the mole fraction determination of HPMF. A detailed reaction pathway analysis of dimethyl ether at low-temperatures, extracted from the study of Moshammer and co-workers [127], is shown in Figure I.19, illustrating the formation of the different low-temperature oxidation products.

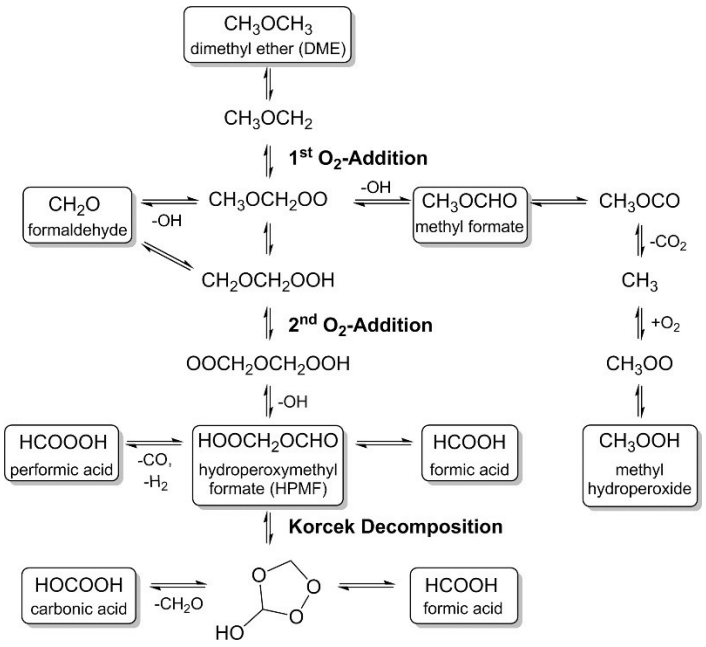

Figure I.19. Low-temperature oxidation mechanism of dimethyl ether, extracted from [127].

Among the numerous studies led on dimethyl ether low-temperature kinetics, many resulted in the development of detailed kinetic mechanisms, allowing to precisely describe the oxidation kinetics of this molecule. The very first published mechanism, covering the high-temperature range, was published in 1996 by Dagaut and co-workers [121], and includes 43 different species for 256 elementary

reactions. A second model, developed by Curran and co-workers in 1998 [140], covers the low- to high-temperature oxidation range. It is composed of 78 different species for 336 reactions, and validated against JSR data from Dagaut and co-workers as well as ST data from Pfahl and co-workers, cited above. The model was developed following the 'reaction class' classification, introduced by Curran and co-workers [141] during the same year. Two years later, Fischer and co-workers [114,142] proposed an updated version of the 1998's dimethyl ether mechanism, resulting in a 82 species and 351 reactions model. Improvements were proposed on the prediction of acidic species, which were absent from the previously published kinetic mechanism. A new model was published in 2008 by Zhao and co-workers [143]. The unimolecular decomposition rate constant of dimethyl ether at different pressures and temperatures was recalculated using the RRKM theory and master equation calculations, while the low-temperature oxidation mechanism was adopted from the one of Fischer and co-workers, with a few modifications made on the initial model. The model was then validated against data from flow reactor, jet-stirred reactor, shock tube, laminar flame speciation and laminar flame speed measurements, leading to an overall good agreement between predicted and measured values. In 2015 two different kinetic models were published, the first of them by Burke and co-workers [144], validated on newly measured RCM and ST ignition delay times, and focussed on the co-oxidation of DME/CH_4 mixtures, and the second by Wang and co-workers [124], which is a modified version of the Zhao and co-workers model, and was validated against speciation data in a laminar flow reactor coupled with MBMS measurements. Both these models allowed an improvement of the current state-of-the-art of dimethyl ether oxidation kinetics. Dames and co-workers [145] published a new model in 2016, dedicated to the co-oxidation of dimethyl ether with propane at elevated pressures, covering the low- and the high-temperature oxidation of both fuels. More recently, the HP-Mech v3.3 [46] was developed using recently measured ozone-seeded and non-ozone-seeded DME/CH_4/O_2 cool flames ignition and extinction strain rates. These data are particularly valuable as they couple low-temperature chemistry, heat release and transport. The ozone submechanism used in this model, which strongly affects the low-temperature kinetics, was developed at Princeton [63]. Finally, Rodriguez and co-workers [120] developed a model for dimethyl ether oxidation, coupled with newly acquired speciation data in a jet-stirred reactor, mainly trying to correct the overestimated intensity of the cool flame as well as the overprediction of methyl formate production in the low-temperature domain. These models, covering the low-temperature oxidation of dimethyl ether, are summarized in Table I.2, along with the publication year as well as the number of species and reactions present in the models.

Table I.2. Existing models dedicated to the LTC kinetics of dimethyl ether.

Model	Publication year	Number of species	Number of reactions	Reference
Curran *et al.*	1998	78	336	[140]
Fischer *et al.*	2000	82	351	[114,142]
Zhao *et al.*	2008	55	290	[143]
Burke *et al.*	2015	119	710	[144]
Wang *et al.*	2015	59	301	[124]
Rodriguez *et al.*	2015	90	576	[120]
Dames *et al.*	2016	120	711	[145]
Reuter *et al.*	2018	130	893	[46]

It is worth noting that while some models are developed exclusively in the aim to describe the oxidation mechanisms of dimethyl ether, or dimethyl ether in a blend with one or more fuels, others describe the oxidation of a variety of molecules, and include a submechanism for the oxidation of dimethyl ether. This is especially the case of the models developed by the National University of Ireland, Galway: AramcoMech 1.3 [146], AramcoMech 2.0 [147], AramcoMech 3.0 [148] or NUIG1.1 [149].

I.4.2. Diethyl ether ($C_2H_5OC_2H_5$)

While dimethyl ether has been thoroughly studied in the last decades (and especially its low-temperature oxidation kinetics), studies on diethyl ether are less common in recent years. Even though diethyl ether has proven to be an excellent additive in diesel [150] as well as useful ignition improver in HCCI engine [151,152], the presence of two C-C bonds in its molecular structure induces a higher production of soot precursors than DME [153]. The kinetic studies presented below are summarized in Table I.3.

The majority of studies performed on the oxidation and pyrolysis kinetics of diethyl ether were done at high temperatures, through ignition delay times measurements in shock tubes [154,155], hot flame speed measurements [156,157], and speciation in reactors [158], shock tubes [155] and hot flames [156,159]. Until recently, only a very few studies were available on the low-temperature oxidation of diethyl ether. The oxidation of rich DEE/air mixtures in a quartz reactor between 450 and 750K was studied by Salooja [160], reporting the first data on the autoignition of this ether in the low-temperature domain. The oxidation of diethyl ether in a jet-stirred reactor was studied by Griffiths and Inomata [161]. Working at 300 mmHg, roughly equal to 0.4 bar, it was observed that diethyl ether started to react at 430 K. An oscillatory phenomenon was observed, its amplitude and intensity varying with the imposed reactor temperature. A detailed kinetic model developed in the cited study, containing 92 elementary reactions, allowed to reproduce this interesting phenomenon, which was proposed to be highly dependent on the decomposition of the $C_2H_5O\dot{C}HCH_3$ radical in acetaldehyde, CH_3CHO. The autoignition of diethyl ether at relatively low temperatures, below 400 K, was studied numerically by means of an extensive density functional theory by Di Tommaso and co-workers [162] and experimentally by Naito and co-workers [163], mainly under the scope of risks associated to its storage.

Ignition delay times were obtained by Inomata and co-workers in 1991 [164]. Later on, Werler and co-workers [155] studied the autoignition of diethyl ether in a rapid compression machine at various equivalence ratios ($0.5 < \phi < 2$), the temperatures ranging from 500 to 1060 K and pressures between 2.5 and 13 bar. The undiluted oxidation of stoichiometric DEE/O_2 mixtures in a shock tube was explored by Uygun [165] at temperatures between 646 and 1100 K and pressures between 18 and 40 bar. Finally, the oxidation of diethyl ether was studied in plug flow and continuously stirred reactors, allowing to measure the products distribution at different steps of the low-temperature combustion of this ether. Serinyel and co-workers [166] studied the low- to high-temperature oxidation of diethyl ether in a jet-stirred reactor at various equivalence ratios, respectively $\phi = 0.5$, 1 and 2, temperatures between 450 and 1250 K and at two pressures, 1 and 10 bar. The main measured low-temperature oxidation products were formaldehyde, acetic acid and acetaldehyde. Tran and co-workers [167] also studied the stoichiometric diethyl ether low-temperature oxidation in atmospheric jet-stirred and plug flow reactors, from 400 to 1100 K. The adequate residence time chosen for this study allowed to assess that diethyl ether exhibits two different negative temperature coefficient domains, as already observed for di-*n*-butyl ether $(C_4H_9)_2O$ [168,169]. This 'double NTC' phenomenon, shown in Figure I.20, is due to competing reactions as the temperature in the reactor increases. As one can see, at the lowest temperatures, the branching ratio between (A) and (B) pathways changes as the temperature increases, and causes the 1st NTC as the decomposition of the $\dot{Q}OOH$ radical causes a decrease of the reactivity. The second observed NTC is due to the competition between the unimolecular decomposition of the fuel radical (C) and its addition to molecular oxygen (D), which tends to become less competitive when the temperature is sufficient. This phenomenon was not observed in the JSR in Orleans. Finally, Belhadj and co-workers [170] studied the products distribution during the oxidation of diethyl ether between 480 and 570 K by means of liquid chromatography-Orbitrap mass spectrometry, allowing to observe highly reactive intermediates such as the ketohydroperoxides formed after two O_2 addition to the fuel molecule. Interestingly, molecules containing a much higher number of carbons ($C_nH_{2n}O_3$ with n varying between 2 and 10) were also observed in stoichiometric conditions, the formation of oligomers being suspected by the authors, but further experimental evidence is needed to support this assumption.

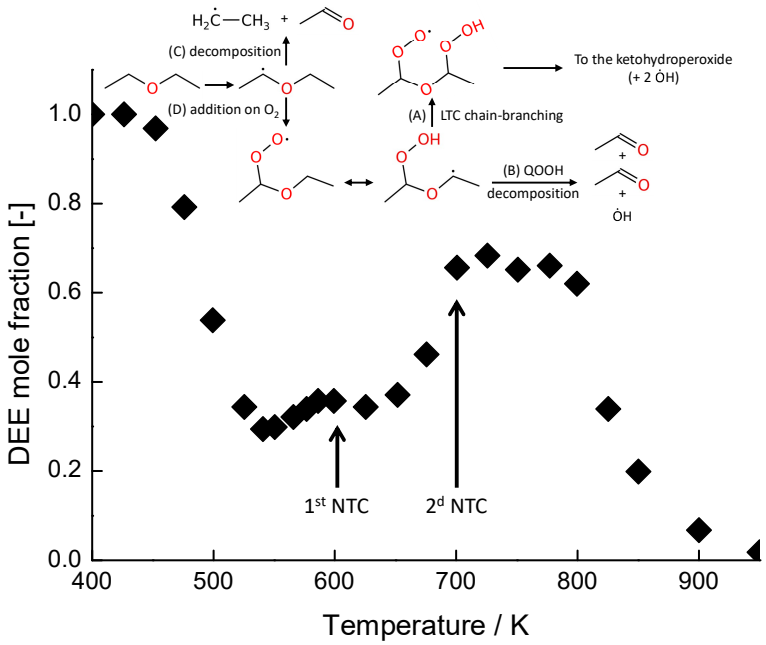

Figure I.20. 'Double NTC' phenomenon during the low-temperature oxidation of diethyl ether, data reproduced from [167].

A few models describe the low- to high-temperature oxidation of diethyl ether. Griffiths and Inomata published the first detailed kinetic mechanism in 1992 [161], in order to explain the observed oscillatory phenomenon in their reactor during diethyl ether oxidation. A second model was proposed by Yasunaga and co-workers in 2010 [154], and is composed of 148 different species and 751 elementary reactions. The model however only covers the high-temperature combustion of diethyl ether, as it is validated against high-temperature shock tube and pyrolysis experiments. Several models were published in 2017, respectively by Eble and co-workers [171], covering a wide range of temperatures and pressures and validated against ignition delay times available in the literature; by Tang and co-workers [172], which developed a reduced model composed of 80 species and 339 reactions, and validated against ignition delay times at low- and high-temperatures; by Sakai and co-workers [173,174], in which reactions rate constants relative to low-temperature intermediates (ROȮ, ȮOOH, etc.) were calculated by ab initio using high-level of theory; by Hu and co-workers [175], who used ab initio and RRKM master equation calculations to build a skeletal mechanism, including 49 species and 192 reactions, and is validated against ignition delay times relevant to engine conditions. Two models were published in 2018 and 2019, respectively by Serinyel and co-workers [166] and Tran and co-workers [167], based on their work detailed above. Finally, a recent model was proposed by Danilack and co-workers [176,177], in which the decomposition rates of some of the ketohydroperoxides and ȮQ=O radical were recalculated and incorporated in the initial model from Tran and co-workers [167].

Table I.3. Synthesis of the studies on DEE oxidation and pyrolysis from low- to high-temperature.

Experimental configuration	Operating conditions (P, T, x_i)	Fuel – oxidizer – inert	Reference
ST	$900 < T < 1900$ K, $1 < P < 4$ atm, $\phi = 0.5, 1, 2, \infty$[3]	DEE/O_2/H_2, dil. Ar	[154]
ST	$622 < T < 1100$ K, $P = 18, 40$ bar, $\phi = 1$	DEE/air	[165]
ST RCM	$900 < T < 1300$ K, $P = 10, 20, 40$ bar, $\phi = 1$ $500 < T < 1060$ K, $2.5 < P < 13$ bar, $\phi = 0.5, 1, 2$	DEE/O_2, dil. Ar DEE/O_2, dil. N_2, CO_2, Ar	[155]
Flat Flame	$P = 1$ atm, $298 < T_0 < 398$ K, $0.5 < \phi < 1.6$	DEE/O_2, dil. N_2	[157]
Flat Flame	(LBS[3]) $100 < P < 507$ kPa, $\phi = 1.4$, $T_0 = 298$ K (speciation) $P = 4$ kPa, $\phi = 1.8$, $T_0 = 333$ K	DEE/O_2, dil. N_2 DEE/O_2, dil. Ar	[156]
CFDF[1]	$P = 0.1$ MPa, $T_{0,fuel} = 333$ K, $T_{0,O2} = 298$ K $0.089 < x_{fuel} < 0.273$, $0.233 < x_{O2} < 0.728$	DEE/O_2, dil. N_2	[159]
CSTR[2]	$450 < T < 750$ K, $P = 1$ atm, $\phi = 2$	DEE/O_2, dil. N_2	[160]
JSR	$400 < T < 650$ K, $P = 300$ mmHg, $\phi = 6$	DEE/O_2, dil. N_2	[161]
JSR	$600 < T < 1100$ K, $26.7 < P < 107.7$ kPa, $\phi = \infty$	DEE, dil. He	[158]
JSR	$450 < T < 1250$ K, $P = 1, 10$ atm, $\phi = 0.5, 1, 2$	DEE/O_2, dil. N_2	[166]
JSR/PFR	$400 < T < 900$ K, $P \sim 100$ kPa, $\phi = 1$	DEE/O_2, dil. He	[167]
JSR	$440 < T < 740$ K, $P = 10$ atm, $\phi = 1$	DEE/O_2, dil. N_2	[170]

[1]CounterFlow Diffusion Flame, [2]Continuously-Stirred Tank Reactor, [3]Pyrolysis

I.4.3. Oxymethylene ether-2 (OME-2, $CH_3OCH_2OCH_2OCH_3$)

The last part of this section reviews the past studies done on the combustion behaviour of oxymethylene ether-2, abbreviated OME-2 hereafter, which was also studied within this work. OMEs, of general formula $CH_3O(CH_2O)_nCH_3$, form a high-potential class of sustainable synthetic fuels when produced via carbon capture and utilization, using CO, CO_2 and hydrogen produced from renewable energies. Thus, OMEs can be considered as e-fuels. The results presented in the next paragraph are also summed up in Table I.4.

Cai and co-workers [178] studied the autoignition of OMEs (OME-*n*, $2 < n < 4$) in a shock tube at 10 and 20 bar, in lean, stoichiometric and rich conditions, and at temperatures between 663 and 1137 K. A new mechanism, based on extrapolation of reaction classes relevant to OME-1, (dimethoxymethane) was developed, and showed a good agreement with their experimental data. Autoignition of OME-2 and OME-3 stoichiometric mixtures was investigated by Drost and co-workers [179] in a rapid compression machine, at pressure ranging from 3 to 10 bar and temperatures between 570 and 690 K. It was observed that both fuels show a negative temperature coefficient. Interestingly, OME-2 and OME-3 have almost similar IDTs at high pressure (10 bar), and are seen to be more reactive in this condition than *n*-heptane and DME (which can be considered as OME-0). A systematic study of the oxidation of OME-*n* ($0 < n < 5$) in a flow reactor coupled with EI-MBMS measurement was done very recently by Gaiser and co-workers [180]. The products formation issued from the oxidation of nearly stoichiometric and rich mixtures of OMEs/O_2 (ϕ = 0.8, 1, 2) between 700 and 1300 K was extensively studied. It was observed that the oxidation temperature onset, i.e., the temperature at which the oxidation of the fuel starts, significantly decreased when the chain-length of OME-*n* was increased

($0 < n < 3$) but remained nearly constant for larger OMEs, whatever the equivalence ratio. Similarly, for larger OMEs the intermediates and products formation were nearly identical, CH_2O and CH_3OCHO being observed as the main oxidation products in the studied conditions. The authors did not observe any soot precursors, even in fuel-rich conditions ($\phi = 2$), reinforcing the interest in these e-fuels. Interestingly, the production of ethanol, C_2H_5OH, was detected in this study for every investigated condition, and in a greater proportion than for DME, which is highly atypical and stresses for further theoretical studies on its formation pathways. The fundamental combustion properties of OME-2 were investigated by Ngugi and co-workers [181] via ignition delay times measurement of stoichiometric mixtures in a shock tube at pressures ranging from 1 to 16 bar and temperatures from 850 to 1700 K. Furthermore, laminar burning velocities of OME-2/air mixtures were measured using the Bunsen cone methodology, for various equivalence ratios ($0.6 < \phi < 2$) at atmospheric and elevated pressures ($1 < P < 6$ bar). Main results showed that, when compared to previous work on OME-1 [182], the oxidation pathways of these two fuels were very similar. De Ras and co-workers [183] studied the low- to high-temperature oxidation and pyrolysis of OME-2, coupling pyrolysis measurements in a pyrolysis reactor and ignition delay times in the University of Lille RCM between 600 and 720 K and pressures equal to 5 and 10 bar. A detailed kinetic model was built from this experimental study, in the aim to be extended to higher OMEs. Further details on the state-of-the-art of OME-2 (and larger OMEs) oxidation kinetics can be found in the mini-review of Fenard and Vanhove [184].

Table I.4. Synthesis of the studies on OME-2 oxidation from low- to high-temperature.

Experimental configuration	Operating conditions (P, T, x_i)	Fuel – oxidizer – inert	Reference
ST	$660 < T < 1140$ K, P = 10, 20 bar, $\phi = 0.5, 1, 2$	$OME_{2\text{-}4}$/'air'	[178]
ST	$570 < T < 690$ K, $3 < P < 10$ bar, $\phi = 1$	$OME_{2\text{-}3}$/'air'	[179]
PFR	$750 < T < 1250$ K, P = 1 atm, $\phi = 0.8, 1, 2$	$OME_{0\text{-}5}/O_2$	[180]
ST BC[1]	$850 < T < 1700$ K, $1 < P < 16$ bar, $\phi = 1$ $T_0 = 473$ K, $1 < P < 5$ bar, $0.6 < \phi < 2$	OME_2/'air'	[181]
PFR RCM	$373 < T < 1150$ K, P = 0.34 MPa, $\phi = \infty$ $600 < T < 720$ K, P = 5, 10 bar, $\phi = 0.5$	OME_2, dil. He OME_2/O_2, dil. Ar, N_2, CO_2	[183]

[1]Bunsen Cone

I.5. General remarks

This first chapter was dedicated to a bibliographic overview of the work operated in the past on cool flames and low-temperature combustion kinetics of some ethers of interest. It was notably highlighted that, while the low-temperature kinetics of fuels are generally studied in JSRs or RCMs, studies concerning this specific temperature domain were needed in flame conditions, coupling kinetics, heat release and transport properties. Few is known about cool flames and much is to be discovered, both on kinetic and physical aspects.

This assessment motivated the development of a stagnation plate burner dedicated to the study of low-temperature combustion through the analysis of stabilized cool flames. The second chapter presents the stagnation plate burner characteristics as well as the different diagnostics that were coupled to it. The third chapter is dedicated to the numerical simulation of cool flames using a one-dimensional solver, along with experimental verifications allowing to use such code. Finally, chapter IV and V present the experimental results, respectively on the low-temperature combustion kinetics of different ethers inside cool flames, and measurement of cool flames propagation speed, illustrating the strength of this new configuration for low-temperature combustion kinetics studies.

Chapter II. Experimental setup: The stagnation plate burner and associated diagnostics

II. Experimental setup

II.1. The stagnation plate burner

II.1.1. Burner description

In order to study the low-temperature combustion kinetics of different fuels in an innovative configuration, a dedicated burner was built at the PC2A laboratory. A scheme of the burner is presented in Figure II.1, and detailed below.

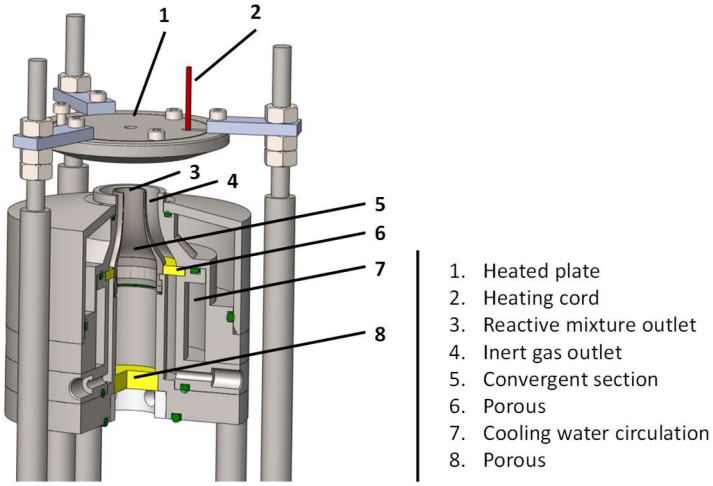

Figure II.1. Scheme of the cool flame burner.

The burner consists of a stainless-steel body with a coaxial nozzle of an inner diameter of 10 mm for the fuel/oxidizer mixture (**3**). The mixture is injected through four orthogonal inlets and flows through a steel porous disc (thickness: 3 mm; porosity: class 40, blocks 98% of particles with $d_p > 8$ µm) (**8**) before entering the convergent section in the centre of the burner (**5**). This geometry was established following the work of Rolon [185], ensuring a laminar and uniform gas flow at the burner exit. A neat N_2 co-flow is injected through the co-axial nozzle (**4**) of 20 mm internal diameter, also equipped with a stainless-steel porous section (**6**), to isolate the flame from external perturbations. The burner body is kept at a constant temperature of 300 K by temperature-controlled water circulation (**7**). A heated plate (**1**), with a diameter of 65 mm and a thickness of 8 mm, is placed above the burner nozzle with a strictly parallel geometry regarding the burner exit. A spiral heating element is inserted into the plate (**2**). The plate temperature has been varied between 600 and 800 ± 0.1 K, and is controlled using a PID controller Eurotherm 3216 coupled with a 1 mm type-K thermocouple inserted in the heated plate. The distribution of temperature along the plate surface was measured and is homogeneous within ± 5 K on the entire diameter. The height above the burner of the heated plate can be varied. It has however been kept at a constant value of 13 mm for all the presented experiments.

The whole burner is kept in an assembly connected to the gas extraction system and is protected from the external light. The assembly is equipped of different optical access that will be presented later in this chapter. A general scheme of the burner is shown in Figure II.2.

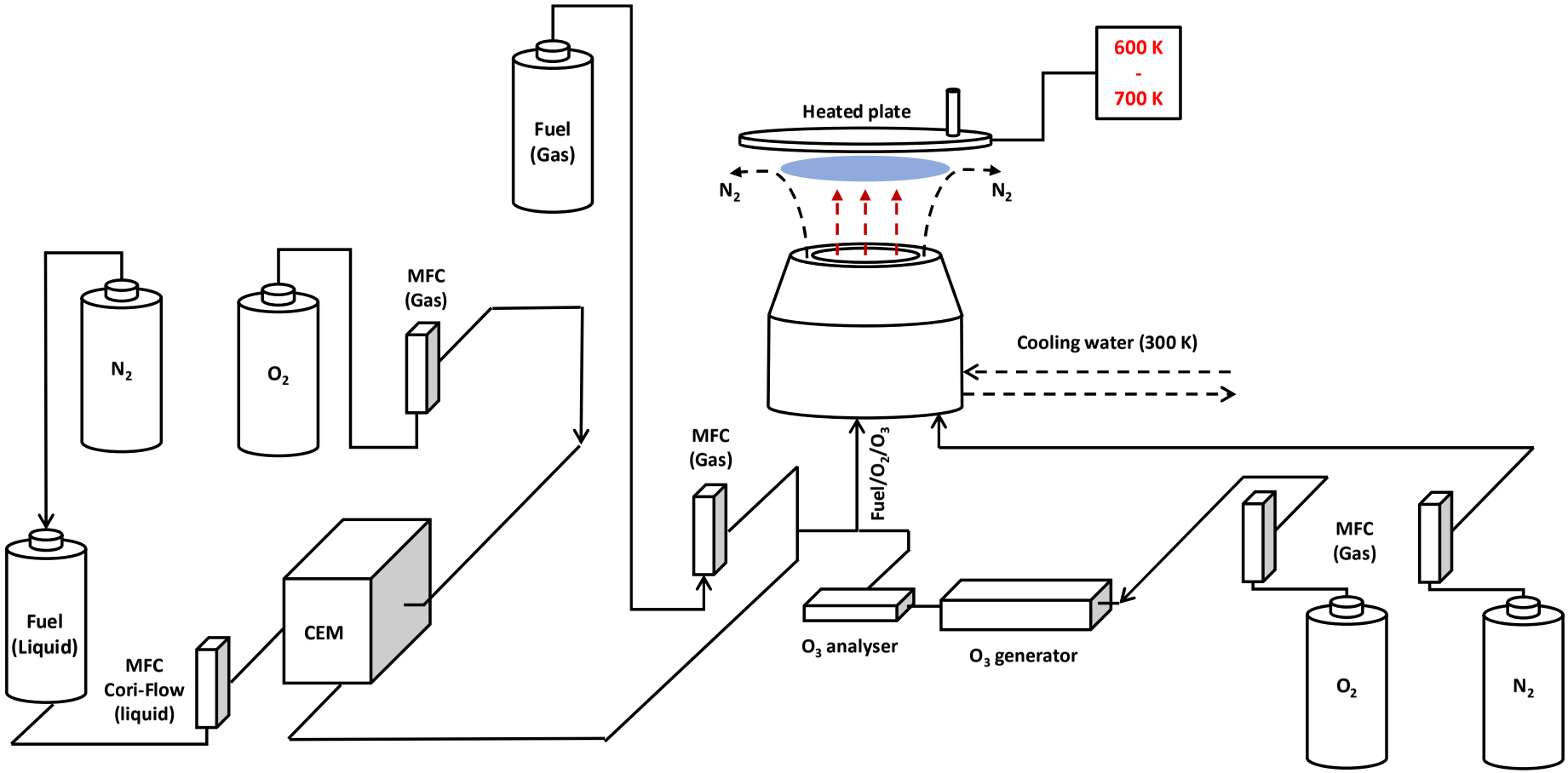

Figure II.2. Schematic of the stagnation plate burner along with gas supply.

II.1.2. Gas supply

The gas flow rates, namely dimethyl ether, nitrogen and oxygen flows, are imposed by Bronkhorst mass flow controllers (MFCs). Although the MFCs are originally calibrated by Bronkhorst, they were periodically re-calibrated using a DryCal DC-Lite flow meter. Calibrations of the MFCs are operated using nitrogen, the response factors between the setpoint and the measurement being then corrected using the gas correction factors provided by Bronkhorst. The calibration factors of oxygen (0.98) and dimethyl ether (0.39) provided by Bronkhorst were verified using a bubble flow meter and showed an overall good agreement with the experimentally measured calibration factors. Calibration factors provided by Bronkhorst were therefore used. Every calibrated gas flow controller showed an excellent linearity within the whole operating range, the determination coefficient (R^2) being systematically superior to 0.999.

In order to vaporize liquid fuels, namely diethyl ether and OME-2 in this work, a Controlled Evaporator Mixer (CEM) provided by Bronkhorst was installed. The liquid is stored in a dedicated tank, pressurized up to 5 bar using N_2. The fuel's flow is controlled by a liquid mass flow meter, which measurement is based on the Coriolis effect. The main advantage of this technique is its universality, as it can be applied to every liquid fuel without fuel-specific calibration. The liquid is then mixed with a gas flow of oxygen in the mixing section, that can be heated to avoid any risks of condensation. In our case, the lines and the mixing section were only slightly heated at a temperature up to 40°C, ensuring that the system is systematically above the ambient temperature. The liquid flow range using this setup can be varied between 2 and 360 $g \cdot h^{-1}$. A simplified scheme of the Controlled Evaporator Mixer is shown in Figure II.3.

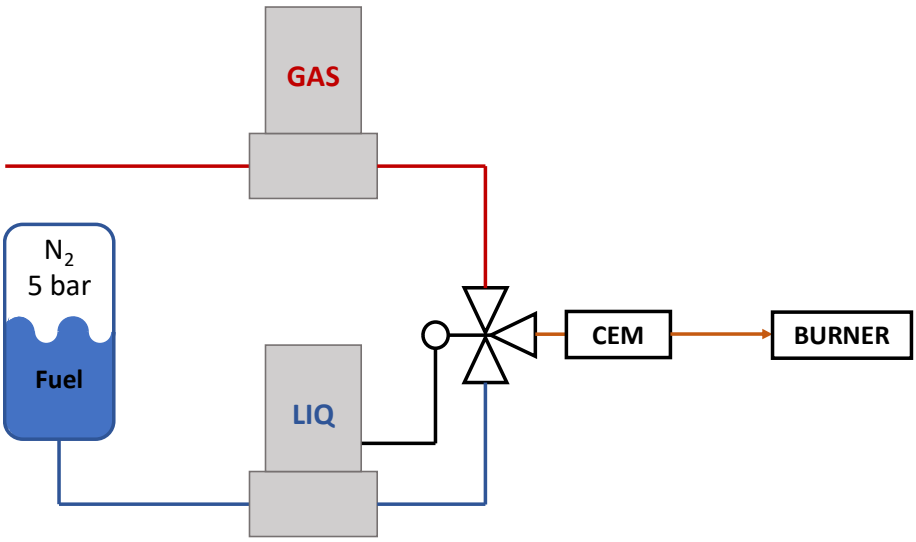

Figure II.3. Schematic diagram of the evaporator.

The major constraint of this system lies in the maximum quantity of liquid fuel that can be vaporized in the gas flow. The factors limiting the fuel vaporization in the gas flow are detailed below:

- Vapor pressure of the fuel: The fuel volatility drastically varies as a function of its molecular structure and its physicochemical properties. At atmospheric pressure some fuels are in a gaseous state at ambient temperature (CH_3OCH_3, T_{vap}^{atm} = - 24°C), some are easily vaporizable ($C_2H_5OC_2H_5$, T_{vap}^{atm} = 34.6°C) and others are hardly vaporizable (OME-2, T_{vap}^{atm} = 174.1°C). The vapor pressure of a fuel therefore limits the operational range in our conditions as the burner is operated at ambient temperature.

- Lower flammability limit of the fuel in pure oxygen: In this work, the cool flames are stabilized in pure oxygen. As a direct consequence, the fuel must be vaporized in the oxygen flow. For safety reasons, the mole fraction of the fuel vaporized in the gas flow is constantly kept below the lower flammability limit of the mixture at ambient temperature.

- Burner temperature: As previously stated, the burner temperature is fixed at 300 K. Thus, even if the CEM and the lines can be heated, one must ensure that there is no risk of condensation of the vaporized fuel in the burner body. The absence of fuel condensation in the burner was verified by measuring the fuel mole fraction at the exit of the burner.

- Ozone production: The last constraint on the fuel vaporization in the oxygen flow is the necessary production of ozone from pure oxygen, which will be presented in the next paragraph. As a consequence, the total oxygen flow had to be divided in two parts, the first one flowing through the ozone generator, and the second part through the CEM module.

Those different factors therefore limit the use of liquid fuels, with the exception of volatile compounds, such as diethyl ether. OME-2, on the other hand, was incorporated in small quantities in a dimethyl ether cool flame.

Gases used in the different studies, along with their purity, are provided in Appendix II.A1.

II.1.3. Ozone production and measurement

Prior to its mixing with the fuel, the oxygen flow (or a part of it when using liquid fuels or performing PIV measurements) flows through an ozone generator. Two different ozone generators were used within this work, respectively a 803N and a 802N model from BMT Messtechnik GMBH, depending on the total ozone concentration needed in the experiments. Both of them operate using a corona discharge. The corona discharge is produced from tungsten electrodes and propagates through a ceramic tube in order to maximise the contact surface with the circulating gas. Ozone dissociates and recombines through the reactions R13 and R14. A simplified scheme of the ozone formation in the generator is pictured in Figure II.4.

$$O_2 + h\nu \rightarrow 2\,\ddot{O} \qquad \text{(R13)}$$

$$\ddot{O} + O_2\,(+M) \rightarrow O_3\,(+M) \qquad \text{(R14)}$$

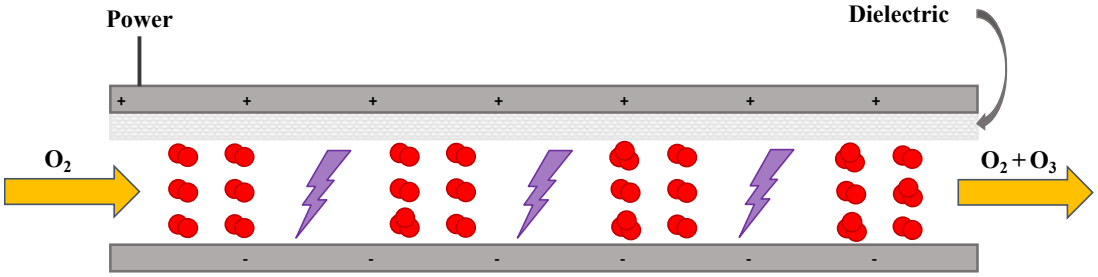

Figure II.4. Simplified scheme of the ozone generator.

The ozone production in the oxygen stream at constant input voltage is dependent on the oxygen flow, and thus on the residence time of the gas in the generator. Appendix II.A2 presents the evolution of the O_3 mole fraction measured in the exit flow of each generator as a function of the oxygen flow. The ozone mole fraction in the exit flow is measured using a Teledyne API 452 analyser, where the ozone mole fraction in the oxygen is determined using an absorption cell operated with a UV light at $\lambda = 254$ nm, near the maximum absorption cross-section of ozone [186]. The relative uncertainty on the reported ozone mole fractions is ± 0.02%.

The absence of significant ozone decomposition through the burner body was verified by sampling O_2/O_3-mixtures at the burner exit, as detailed in Section II.6 of this chapter.

II.1.4. Cool flames parameters

Different parameters are used to define cool flames within this work, and are listed below:

- Equivalence ratio (ϕ): As previously mentioned, the equivalence ratio defines the ratio between the fuel and the oxidant in the mixture relative to the stoichiometry. In our case, the oxidizer flow is composed of a mixture of O_2 and O_3 (which is produced from a fraction of the O_2 stream). The calculation of the equivalence ratio and of the O_3 mole fraction in the mixture is presented in Appendix II.A3.

- Ozone concentration (x_{O3}): The ozone mole fractions indicated within this manuscript will systematically be expressed in the fuel/O_2/O_3 mixture. The ozone mole fraction used to stabilize cool flames is quite high, and varies between 1 and 2% (mol.).

- Geometric strain rate (α): For each flame in this manuscript, a geometric strain rate is reported. It is calculated as the ratio between the exit gas velocity and the distance between the burner and the plate. The geometric strain rate, expressed in s^{-1}, is therefore inversely proportional to the residence time of the gases in the burner.

The two following sections are dedicated to the presentation of the optical diagnostics that were used along with the cool flame burner. Both of them are based on the production of formaldehyde, CH_2O, in the cool flame. On the opposite of the high-temperature domain, CH_2O is a final product of the low-temperature oxidation of a fuel.

II.2. CH_2O*-chemiluminescence

II.2.1. Singularities of cool flames light emission

In hot flames, the relaxation of species such as CH* is responsible for the strong visible light of the flame. In cool flames, such species are formed in lower quantities and merely contribute to the cool flame luminosity. The observation of cool flames is impossible for the naked eye without dark adaptation. Figure II.5 shows a direct photography of a DME/O_2/O_3 cool flame stabilized in the stagnation plate burner, obtained using a Reflex camera with an exposure time of 30 seconds.

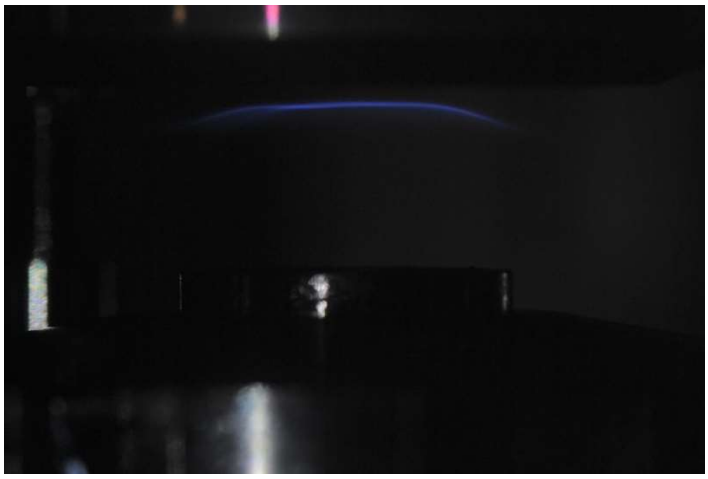

Figure II.5. Direct photography of a DME/O_2/O_3 cool flame, $\phi = 0.3$, $\alpha = 50\ s^{-1}$, $x_{O3} = 2.0\%$.

The light emission of cool flames is mainly due to the formation of excited formaldehyde, CH_2O*, in the flame front. Few studies are available on the formation mechanism of such species in the flame front. Sheinson & Williams [187] proposed that the formation of excited formaldehyde in cool flames was caused by the reactions R16 & R17, the temperature of the flames being too low to permit a thermal transition of formaldehyde from its ground state to the first excited state $^1A_1 \rightarrow {}^1A_2$. The relaxation of CH_2O* (R18) produces photons between 350 and 500 nm in the ultraviolet/visible region, responsible for the pale blue colour of the cool flames.

$$CH_3\dot{O} + \dot{O}H \rightarrow CH_2O^* + H_2O \quad \text{(R16)}$$

$$CH_3\dot{O} + CH_3\dot{O} \rightarrow CH_2O^* + CH_3OH \quad \text{(R17)}$$

$$CH_2O^* \rightarrow CH_2O + h\nu \quad \text{(R18)}$$

In the present work, CH_2O*-chemiluminescence of the cool flame was measured using an intensified camera, following two main objectives: i) CH_2O*-chemiluminescence measurement allowed to ensure the presence of the flame during the experiments; ii) it also allowed measuring the flame front position in the burner. The experimental procedure and signal processing for this measurement are presented hereafter.

II.2.2. Cool flames chemiluminescence acquisition

The CH_2O^* emission from the cool flame is captured using an ICCD (Intensified Charge Coupled Device) camera PIMAX 3 (Princeton Instruments). The latter is equipped with a band-pass filter between 396 and 450 nm and a Sodern Cerco 2085 UV objective (f = 94 mm, f# = 4.1). The filter allows to suppress stray light emission from other species in the cool flame (CO^*, CO_2^*...) or coming from the exterior. A 2 mm thick quartz window separates the camera lens from the burner.

The acquisition of cool flames images is done using the LightField software, which allows to optimize the camera parameters:

- Camera gain: This parameter allows to amplify the sensitivity of the detectors with regards to the light source. Note that increasing the camera gain increases the cool flame luminosity, but also increases the background noise. Giving the very low light emission of the studied cool flames, the camera gain was fixed at 90% of its full range.
- Acquisition time: Sets the duration of the acquisition of a single image. This parameter can also be used to increase the signal to noise ratio of the cool flame, but requires a stable flame. The acquisition time was fixed at 1 second.
- Number of images: One can record several independent images in a row. It is generally done to avoid the recording of a single image on a long duration, which could result in the saturation of the detectors. If the cool flame is stable, images can be either averaged or summed. 20 images were recorded for each condition, and averaged.
- Camera background: Allows to subtract the intrinsic background signal of the camera, allowing to increase the signal-to-noise ratio.

An image of the CH_2O^*-chemiluminescence of a $DME/O_2/O_3$ cool flame is shown in Figure II.6.

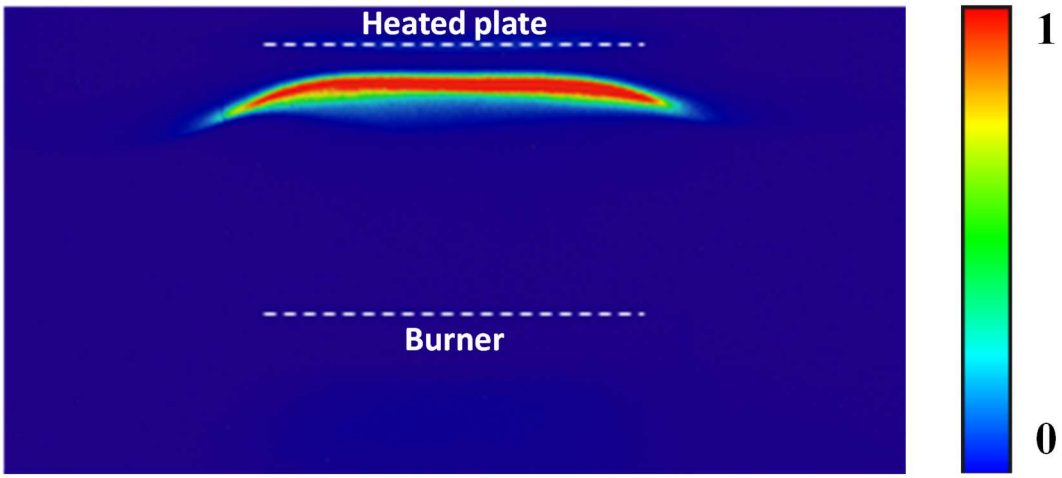

Figure II.6. Raw-CH_2O^* image of a $DME/O_2/O_3$ cool flame, $\phi = 0.3$, $\alpha = 50\ s^{-1}$, $x_{O3} = 2.0\%$. The relative intensity of the signal is indicated on the right side of the image.

II.2.3. Images post-processing: Abel Inversion

From Figure II.6. it can be observed that the flame is flat in the centre of the burner, and mostly axisymmetric. Because of the influence of the converging nozzle on the velocity field, and the recirculation of burnt gases under the plate, the flame is not flat on its extremities. Moreover, the recorded images of chemiluminescence are integrated on the depth of the burner, making it difficult to precisely extract the position of the flame front in the centre of the burner from the raw images. Abel inversion was therefore used. It allows to reconstruct a slice of a cylindrically symmetric 3-dimensional object from its 2-dimensional projection. Semi-automatic image post-treatment was realized using the PyAbel module.

A 2-D slice plane image representing the CH_2O^*-chemiluminescence signal above the burner is then obtained. The 1-D profile of the CH_2O^*-chemiluminescence signal as a function of the Height Above the Burner (abbr. HAB) is extracted from the image by averaging the signal on 40 pixels around the burner axis. A comparison between the raw- and treated-signal is shown in Figure II.7. The influence of the extremities of the flame is visible between HAB 8 and 11 mm. The flame front position determined with and without Abel inversion is similar in both conditions, the slight discrepancy being attributed to the spatial resolution of the camera.

The uncertainty on the front flame position determination after the Abel inversion operation was estimated at ± 250 µm, representing an uncertainty of ± 5 pixels on the raw-image, as 1 pixel ≈ 0.045 mm.

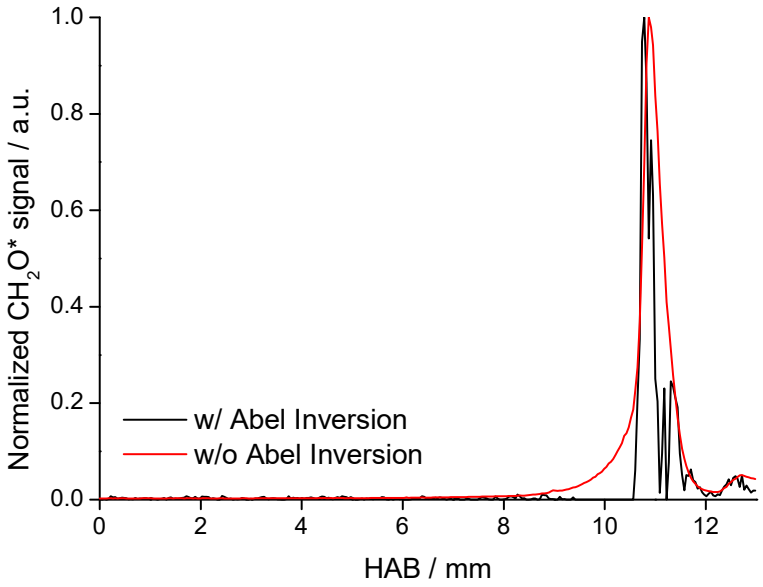

Figure II.7. Comparison of the CH_2O^*-chemiluminescence signal of a DME/O_2/O_3 cool flame as a function of the HAB, with and without Abel inversion. $\phi = 0.3$, $\alpha = 50\ s^{-1}$, $x_{O3} = 2.0\%$.

II.3. Planar Laser Induced Fluorescence of formaldehyde

Laser-based techniques are frequently used in the combustion field, as they allow the characterization of reactive systems without intrusive techniques. Moreover, they are species selective, as a wisely chosen wavelength allows to detect a single species. In our case, formaldehyde was measured using Laser Induced Fluorescence.

II.3.1. CH_2O-PLIF generalities

Fluorescence is the light emission induced by the absorption of a photon by a substance, immediately followed by a spontaneous emission. A simplified scheme of the absorption/emission phenomena leading to fluorescence is shown in Figure II.8. A laser is employed to excite molecules from their ground state, E_0, into an electronically excited state, E_1. The molecules then relax back to their ground state, emitting light via different processes. Fluorescence is characterized by the spontaneous emission of a photon, but competes with other phenomena: i) 'Stimulated emission', a consequence of the interaction between an incident photon and an excited species which creates a new photon with identical frequency, polarization and direction than the incident one; ii) 'Quenching' caused by collisions with other species. This technique can be operated using a focussed beam, named 'Laser Induced Fluorescence' (LIF), or using a laser sheet, named 'Planar Laser Induced Fluorescence' (PLIF).

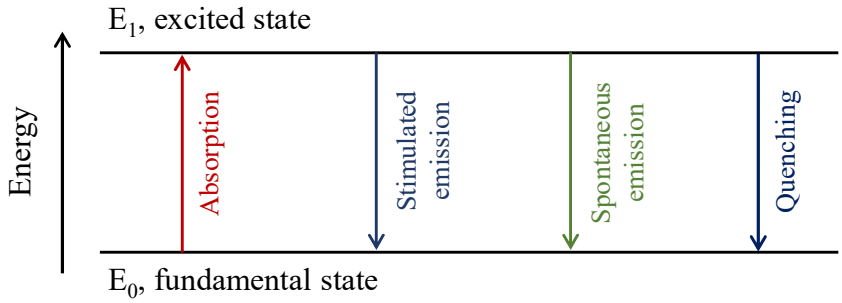

Figure II.8. Simplified scheme of Laser Induced Fluorescence (FIL) principle.

In the case of formaldehyde fluorescence, few absorption bands can be used, thus determining the operating wavelength of the laser. As an example, Shin and co-workers [188] conducted LIF experiments in an atmospheric CH_4/air flame. The authors selected the $2^1_0 4^1_0$ vibronic band of the $\tilde{A}^1A_2$-$\tilde{X}^1A_1$ system at 339 nm, using a tunable dye laser. The fluorescence signal was collected between 380 and 500 nm behind a stray-light-rejecting long-pass filter. On the other hand, Bäuerle and co-workers [189,190] selected the 4^1_0 transition of the $\tilde{A}^1A_2$-$\tilde{X}^1A_1$ system at 353.2 nm, also using a tunable dye laser, to detect hot spots in the end-gas of internal combustion engines. The signal was collected between 400 and 450 nm using a band-pass filter. Using the $2^1_0 4^1_0$ band requires to use a tunable dye laser, while an incident wavelength of λ = 355 nm can be simply obtained with a Nd:YAG laser in conjunction with a second and a third harmonic generators, which justifies why the 4^1_0 transition at λ = 355 nm was preferred in this work.

The formaldehyde Planar Laser Induced Fluorescence was also used to characterize the structure of stabilized cool flames in past-works. Reuter and co-workers [44] used CH_2O-PLIF to properly distinguish a cool flame from a hot flame, the CH_2O signal being stronger in the cool flame as it is produced but not consumed in the cool flame. A tripled Nd:YAG laser was used for the excitation of CH_2O at $\lambda = 355$ nm, and the signal was collected between 400 and 450 nm. Brown and co-workers [53] used a similar experimental setup to characterize the structure of *n*-decane cool flames stabilized at low-pressure in a Hencken burner. Finally, Lee and co-workers [54] used CH_2O-PLIF to study the ignition characteristics of lean DME/O_2 mixtures at the surface of a heated plate. The authors calibrated the fluorescence signal using CH_2O/O_2 gas mixtures obtained by bubbling carrier gas through formalin. The CH_2O concentration in the gas phase was estimated using semi-empirical relation between the mole fraction of CH_2O in formalin and its partial pressure [191]. When calibrating the signal of CH_2O in the gas phase, the authors found out that the signal intensity was not proportional to the concentration of CH_2O in O_2, while a linear response was obtained when the calibration was performed in N_2. The authors attributed this behaviour to the quenching of the fluorescence signal by O_2 molecules. This phenomenon can therefore not be neglected in flame environments where the O_2 concentration represents 85 to 90% of the gas-phase composition, and will be discussed further in Section II.3.2.4.

In this work, CH_2O-PLIF was used to precisely measure the flame front position. It is particularly suited for parametric studies as it allows to quickly record CH_2O fluorescence profiles. It also helped to ensure that no significant reactivity took place upstream the flame front, which would have resulted in important CH_2O signal. The experimental setup and further signal-processing methodology are described in the following sections.

II.3.2. CH_2O-PLIF experimental setup

II.3.2.1. Laser & optics

Formaldehyde excitation is operated at $\lambda = 355$ nm, using the third harmonic of a Nd:YAG laser (Q-Switched Quantel Brilliant B, f = 20 Hz). The laser beam, $\lambda_i = 1064$ nm, passes through a second harmonic generator, resulting in a $\lambda = 532$ nm, and a third harmonic generator, yielding a final wavelength $\lambda_F = 355$ nm. Residual harmonics, respectively at $\lambda = 1064$ and $\lambda = 532$ nm, are separated from the $\lambda_F = 355$ nm laser beam using a Pellin-Broca prism placed at the laser output. A first correction of the shape of the incident laser beam is operated using a circular pinhole. The laser beam then passes through a series of lenses, aiming to transform the laser beam into a laser sheet. The laser beam first passes through a convergent lens (f# 500) which focusses the laser beam, then through two cylindrical lenses (f# -50 mm, f# 300 mm), forming the laser sheet. A correction slit allows to correct the height and the thickness of the laser sheet. The fluorescence signal is collected at an angle of 90° using the same ICCD camera and bandpass filter (396 – 450 nm) than for chemiluminescence. The estimated laser sheet dimensions are ~ 300 µm thick and ~ 11.5 mm height. The power of the laser beam, measured

before the first convergent lens, is $P_{\lambda=355\ nm} \approx 1.40$ W, corresponding to an energy per pulse of $E_{pulse} \approx$ 70 mJ. A descriptive scheme of the apparatus is shown in Figure II.9.

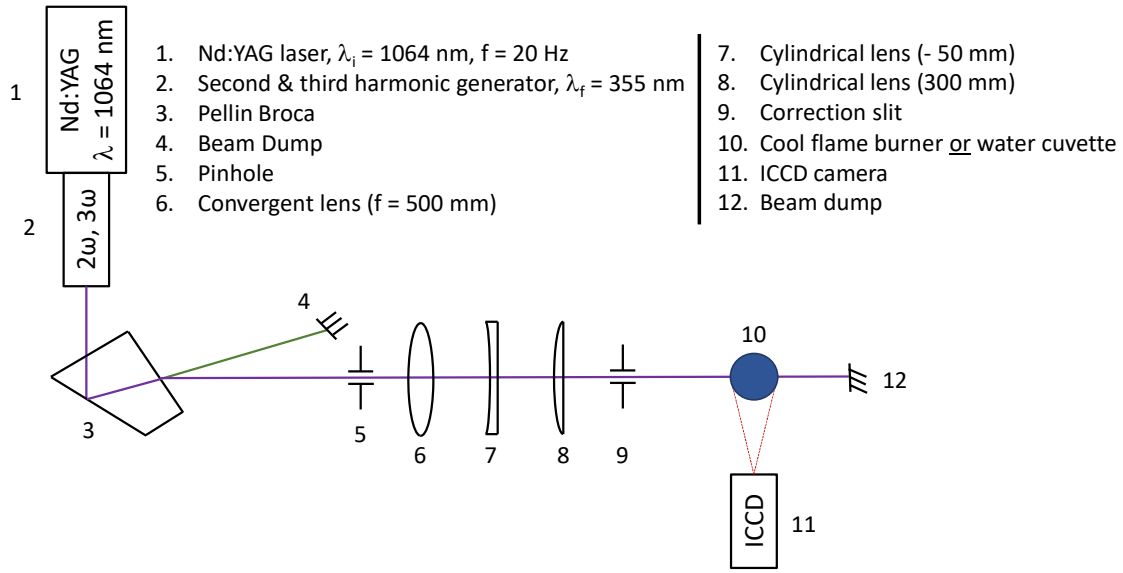

Figure II.9. Simplified scheme of the CH_2O-PLIF apparatus.

The Nd:YAG laser produces a pulsed laser beam with a duration of 4.6 ns at λ = 1064 nm , it is thus necessary to synchronize the opening gate of the ICCD camera with the laser pulse. A photodiode triggers the camera. The gate opening is fixed at 50 ns, as seen in Figure II.10. The acquisition settings were kept constant between the measurements to allow comparison of the CH_2O-fluorescence profiles.

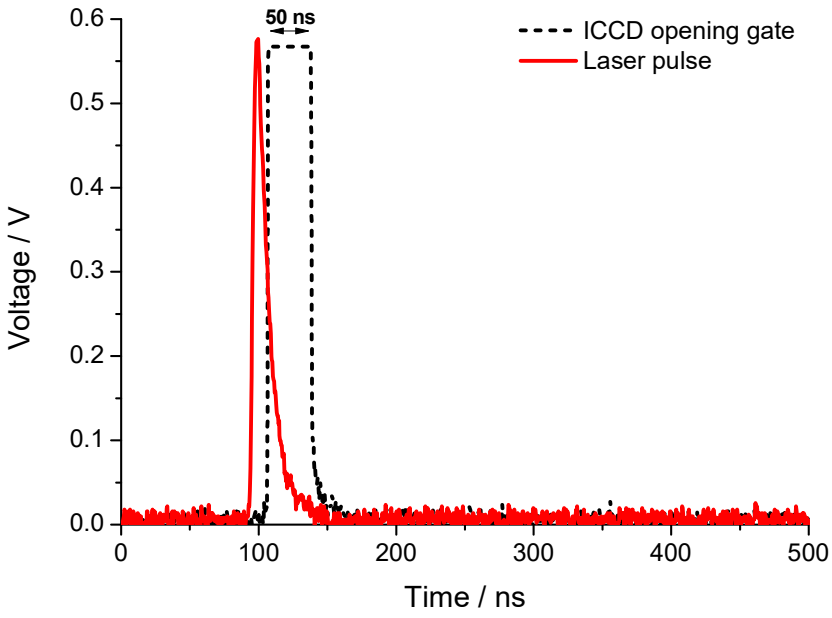

Figure II.10. ICCD camera opening gate triggered by the laser pulse.

II.3.2.2. Energy distribution measurement and correction

The produced laser sheet is not homogeneous in energy, as the energy of the laser sheet is generally higher in the middle of the sheet and then decreases at the extremities. It is thus necessary to correct the obtained fluorescence signal of the flame by this laser energy inhomogeneity along the vertical axis. This correction is operated by using a quartz cuvette with pure water, using the Raman diffusion of water at $\lambda = 355$ nm.

Two configurations were used within this work. Initially, the burner had to be removed to place the quartz cuvette. Then, a movable apparatus for the camera was designed, allowing to place the cuvette besides the burner. Demineralized water circulates in the cuvette, and the camera settings are strictly the same than for CH_2O-PLIF measurements. An image of the illuminated quartz cuvette filled with water is shown in Figure II.11, along with the resulting axial intensity profile averaged along the centreline of the burner, smoothed using a Savitzky-Golay algorithm. The Raman diffusion (cuvette) or CH_2O-PLIF (flame) signal is averaged on 40 pixels around the centre of the burner.

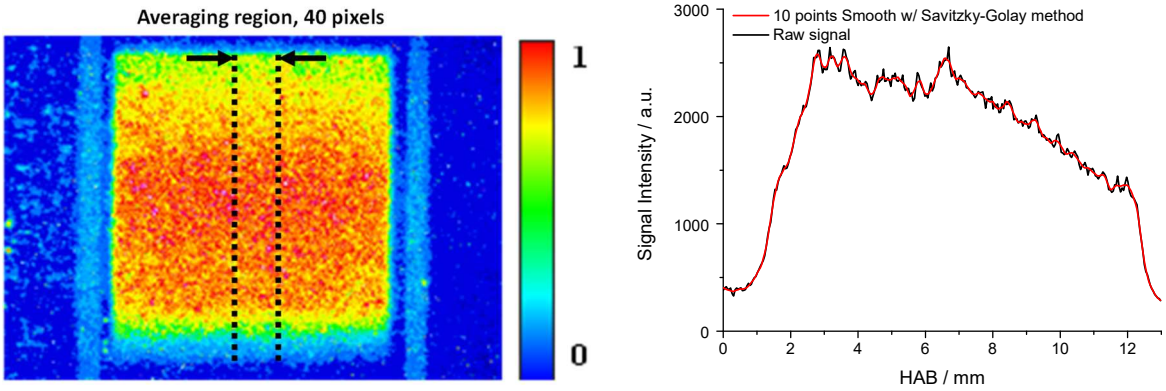

Figure II.11. Illuminated water by the laser sheet (left-hand side) and laser sheet axial energy distribution (right-hand side).

The second objective in measuring the laser sheet energy distribution is to ensure that it is constant throughout the day. Measurements were conducted at different times of a day, the first one being done just after the laser was switched on. As one can observe in Figure II.12, after a certain duration necessary for the laser stabilization, the signal variations are negligible. Note that the laser sheet energy distribution was also measured at different days of a week, and is also plotted in Figure II.12. It was observed that the energy distribution could vary significantly from one day to another, justifying the need to measure the laser sheet energy distribution daily.

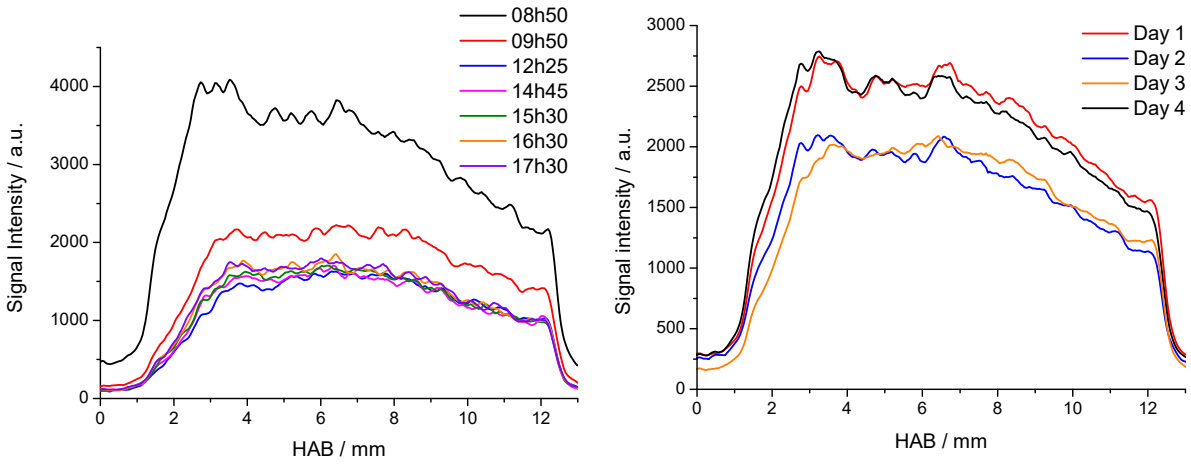

Figure II.12. Measured variations of the laser sheet energy distribution at λ = 355 nm during a day (left-hand side) and at several days of a week (right-hand side).

II.3.2.3. CH_2O profile & flame front position measurement

The 2-Dimensional repartition of formaldehyde, formed in the flame front, is then obtained from CH_2O-PLIF measurement after correction. The fluorescence signal is averaged on 40 pixels around the axis of the burner. Profiles of the formaldehyde fluorescence signal with the HAB are then obtained. The measurement parameters of the ICCD camera are listed below:

- Camera gain: Alike chemiluminescence measurements, the camera gain was fixed at 90% of its full range.
- Acquisition duration: The gate opening was fixed at 50 ns.
- Number of images: 3 images were recorded for each condition. Each single image results of 1000 on-CCD accumulations. Finally, images were averaged.
- Camera background: Allows to subtract the intrinsic background signal of the camera, allowing to increase the signal-to-noise ratio. Background images were verified without flame and without laser, yielding similar corrections

A 2-D image of the CH_2O-fluorescence signal is presented in Figure II.13, along with the extracted CH_2O-intensity signal at the centre of the burner, with and without correction of the laser sheet energy distribution. The CH_2O signal increases in the flame front, and is present all the way to the heating plate, as observed in both graphs in Figure II.13. The maximum of CH_2O-signal is observed on the sides of the burner, which is due to the burnt gases recirculation caused by the presence of the heated plate.

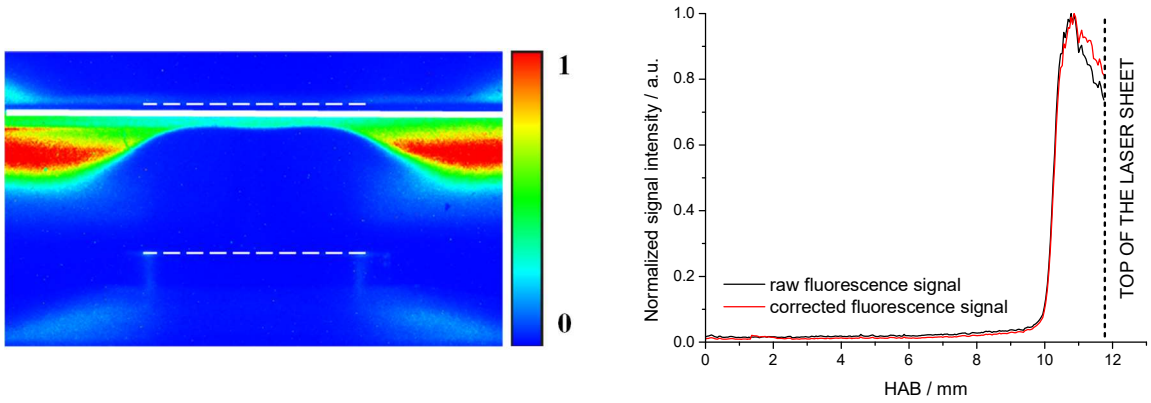

Figure II.13. Raw CH_2O-PLIF image (left-hand side) and extracted profile along the burner axis (right-hand side). $\phi = 0.3$, $\alpha = 50\ s^{-1}$, $x_{O3} = 2.0\%$. The white dashed lines represent the burner and heated plate positions, and the continuous white line represents the top of the laser sheet.

Finally, the flame front position is inferred from the CH_2O profile. The flame front position is defined as the maximum of the derivative of the CH_2O signal, as pictured in Figure II.14. The uncertainty on CH_2O-PLIF measurement of the flame front is estimated to ± 150 µm, i.e., ± 3 pixels.

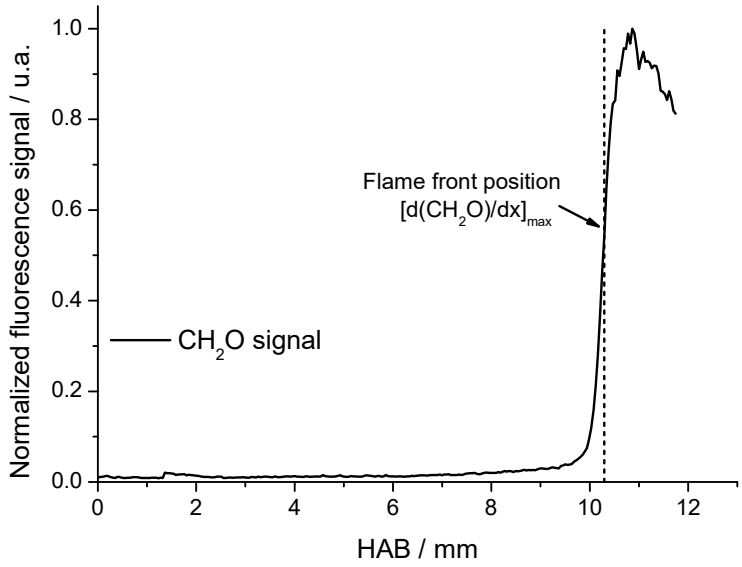

Figure II.14. CH_2O-PLIF signal as a function of HAB, and front flame position determination.

II.3.2.4. Quenching of the CH_2O-fluorescence signal

As stated before, in an oxygen-rich environment, quenching can have an important impact on the measured CH_2O-PLIF profiles. This is especially important in the present conditions, as cool flames are stabilized without inert gas dilution. It results in a high oxygen mole fraction in the mixture, generally between 85 and 90% of the reactive mixture. The objective of this section is to provide an estimation of the quenching of CH_2O fluorescence by O_2 using simulated temperature and CH_2O profiles.

However, no cross-section data of CH_2O fluorescence quenching by O_2 has been reported in the literature, which renders quantitative measurement of CH_2O in cool flames difficult using Laser Induced Fluorescence. For a given CH_2O concentration, the temperature dependence of the fluorescence signal mainly originates from collisional quenching and Boltzmann population fraction. The absorption coefficient B_{12} and the incident laser irradiance are thus considered as non-temperature dependent. Following Eckbreth [192], the LIF signal intensity S_f can be written as (Eq. 1):

$$S_f \propto N_1 \cdot f_{B,1} \cdot B_{12} \cdot \frac{A_{21}}{A_{21} + Q_{21}} \cdot I_v \qquad \text{(Eq. 1)}$$

where N_1 is the total number density of formaldehyde in its fundamental state, $f_{B,1}$ the Boltzmann population fraction of the lower electronic (pumped) state, B_{12} the absorption coefficient, A_{21} the spontaneous emission coefficient, Q_{21} the collisional quenching rate, and I_v the incident laser irradiance.

It was suggested by Mulla and co-workers [193] that for some species, including CH_2O, the spontaneous emission A_{21} can be neglected with regards to the collisional quenching rate Q_{21}. Thus, it comes (Eq. 2):

$$S_f \propto N_1 \cdot f_{B,1} \cdot B_{12} \cdot \frac{A_{21}}{Q_{21}} \cdot I_v \qquad \text{(Eq. 2)}$$

The quenching rate, Q_{21}, can be expressed as the sum of the contributions of all quenching species (Eq. 3):

$$Q_{21} = \sum_i N_i \cdot \sigma_i \cdot \nu_i = \sum_i N_i \cdot \hat{k}_i \qquad \text{(Eq. 3)}$$

where N_i is the number density of the collision species i, σ_i the quenching cross-section of the species i and ν_i the relative velocity of the excited CH_2O and the collision partner i. $\hat{k}_i$ is the quenching rate coefficient calculated as the product $\sigma_i \cdot \nu_i$.

The temperature dependence of the number density, N_i, scales as $N_i \propto T^{-1}$, whereas $\nu_i \propto T^{0.5}$. It thus comes that $N_i\nu_i \propto T^{-0.5}$. Moreover, the quenching cross-section scales as $\sigma_i \propto T^{\beta}$. From the work of Ayoola and co-workers [194], it is assumed that $-0.5 \leq \beta \leq 0$. Mulla et co-workers [193] used the value $\beta = -0.25$ in their work, leading to a quenching rate $Q_{21} \propto T^{-0.75}$. This value is used in the present work.

The Boltzmann population fraction of the lower electronic state, $f_{B,1}$, is determined following the recommendations of Kyritsis and co-workers [195]. Assuming decoupled energy modes, it comes (Eq. 4):

$$f_{B,1} = f_{ele} \cdot f_{vib} \cdot f_{rot} \qquad \text{(Eq. 4)}$$

where f is the population fraction given by the Boltzmann statistics for each mode, respectively the electronically excited states contribution (f_{ele}), the vibrational contribution (f_{vib}) and the rotational contribution (f_{rot}). In this case, f_{ele} is neglected and is considered equal to 1.

Following the work from Clouthier and Ramsay [196], the temperature dependence of the vibrational contribution can be calculated using the following empirical correlation (Eq. 5):

$$f_{vib} = \left(1 - e^{-\frac{1680.5}{T}}\right) \quad \text{(Eq. 5)}$$

Similarly, following the work of Clouthier and Ramsay, the rotational contribution, f_{rot}, can be expressed (Eq. 6):

$$f_{rot} = \frac{40.1969 \cdot e^{-\frac{740}{T}}}{\left(1 + \frac{0.134}{T} + \frac{0.037}{T^2}\right) \cdot T^{\frac{3}{2}}} \quad \text{(Eq. 6)}$$

Using these empirical correlations, it is thus possible to calculate the temperature dependence of Q_{21} and $f_{B,1}$, and then to determine the evolution of S_f as a function of the temperature using (Eq. 2). The results are plotted in Figure II.15. The red continuous line represents the simulated temperature profile as a function of the height above the burner, the continuous black line the simulated CH_2O mole fraction profile and the dashed black line the simulated CH_2O mole fraction profile corrected from quenching. Further details on the simulation of such profiles will be given in Section III.2. of this manuscript. As observed in Figure II.15, the shape of the CH_2O mole fraction profile is only slightly modified when quenching is considered. As long as CH_2O-PLIF was not used in this work to extract quantitative mole fraction profiles of cool flames, CH_2O-fluorescence profiles can then be used without further corrections from quenching. Step-by-step quenching corrections calculations are provided in Appendix II.A4.

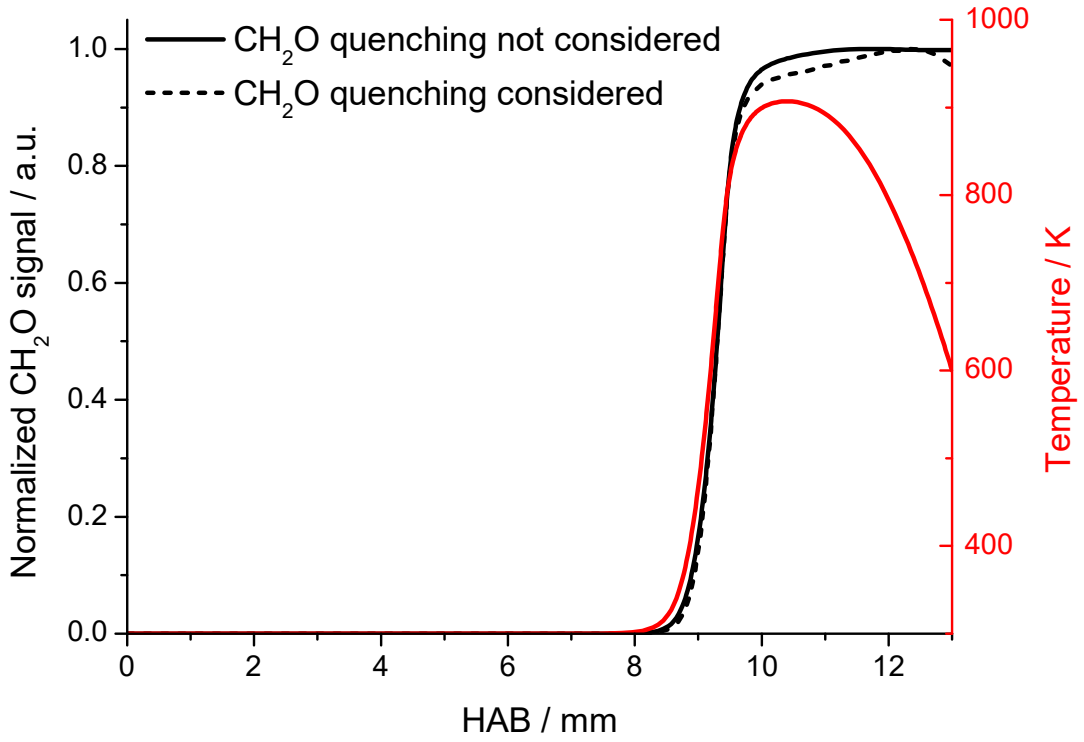

Figure II.15. Simulated temperature (red continuous) and normalized CH_2O mole fraction profiles, without (black continuous line) and with (black dashed line) quenching correction.

II.3.3. Comparison of CH_2O*-chemiluminescence and CH_2O-PLIF

A comparison of the excited and ground-state CH_2O profiles as a function of the height above the burner, acquired using both techniques, is presented in Figure II.16. The determination of the flame front position, described earlier for both techniques, yields similar results within the uncertainty in the cool flame front position determination.

Both techniques come along with their advantages and drawbacks. While chemiluminescence is easier to set up as it only requires the ICCD camera, lens and filter, it leads to slightly more important uncertainties in the flame front measurement (± 250 µm for the CH_2O*-chemiluminescence, ± 150 µm for the CH_2O-PLIF). The first reason is the need to use Abel inversion to infer the flame front position from the raw-chemiluminescence image. The second reason lies in the low light emission from the cool flame, which leads to an important signal/noise ratio. On the other hand, CH_2O-PLIF allows to reduce the uncertainty on the cool flame front position but needs a more complicated set-up. In the example presented in Figure II.16, the flame front position inferred from the PLIF measurement is 11.00 mm, and 10.98 mm using the chemiluminescence profile.

While both techniques yield similar results, CH_2O-PLIF was preferred for the parametric studies, e.g., following the flame front position evolution as the ozone concentration is varied. CH_2O*-chemiluminescence was however preferred for temperature and speciation measurements, especially because an intrusive thermocouple or probe is inserted inside the flame, which would interfere with the laser sheet.

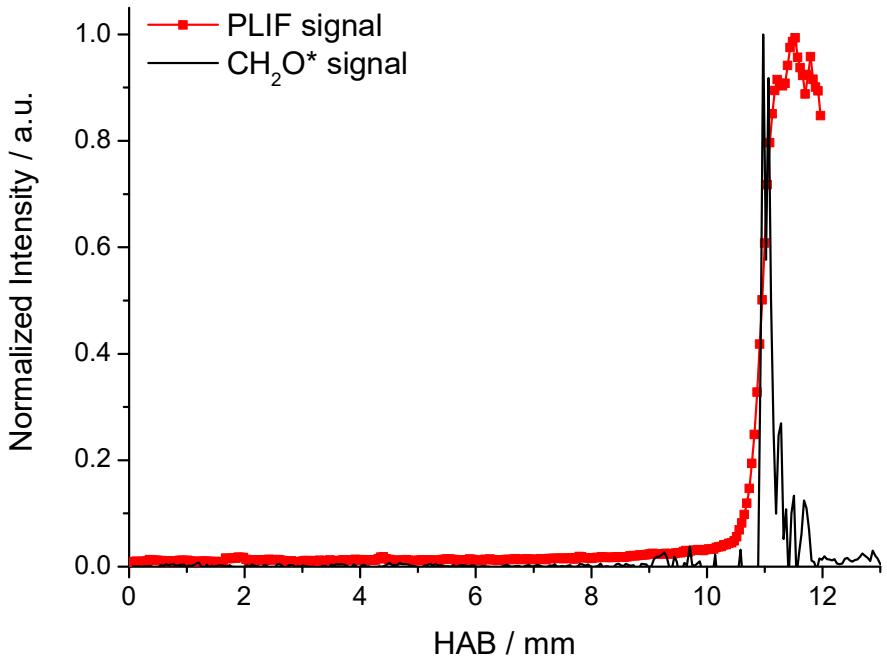

Figure II.16. Comparison of the CH_2O-PLIF signal (red dotted-line) and CH_2O*-chemiluminescence (black continuous line). $\phi = 0.4$, $\alpha = 50\ s^{-1}$, $x_{O3} = 1.6\%$.

Combustion being a complex process, many different intermediates and products are formed in flames, which limits the use of laser-based techniques to measure most of them. On the other side, intrusive techniques such as thermocouple for temperature measurement or GC/MS for speciation are generally less time consuming. Moreover, and especially in the case of species measurement, techniques such as gas chromatography or mass spectrometry allow to measure simultaneously different species, which is of great advantage in the present case. Within this work, intrusive techniques were used to measure temperature and species mole fraction profiles inside cool flames, and are described in the following sections.

II.4. Temperature measurement in cool flames

Temperature measurements have always been a critical issue within the combustion field. Given the large range of operating conditions in terms of pressure and temperature, many different techniques were developed to meet the specificity of each combustion system. Thermocouple measurement is the most used technique due to its simplicity of use and its low cost [197]. However, this intrusive technique quickly becomes inefficient in high-pressure, high-temperature, or corrosive environments. Laser based techniques are generally preferred in extreme conditions, as they are non-intrusive and are believed to be more reliable in such cases. Techniques such as NO-LIF [198,199] or Coherent Anti-stokes Raman Scattering, CARS [200], have been developed and are widely used in systems where thermocouple measurements are inefficient. In this work, temperature measurements were however realized using thermocouples. The aim of this section is to demonstrate that thermocouple measurements can be applied to cool flames temperature profiles without further corrections.

II.4.1. Thermocouple position

Two different thermocouple configurations were tested within this work. In the first case, temperature measurements are performed from the side of the burner, the tip of the thermocouple lying along the axis of the burner. In the second case, temperature measurements are performed from the top of the burner, the body of the thermocouple passing through the centre of the heated plate. Such a configuration requires the use of a plate equipped with an orifice. In both cases, the measurements are performed using a type-K (Chromel/Alumel) thermocouple which external diameter is equal to 250 µm. The 0-position of the thermocouple is measured using a precision scope, and the thermocouple is moved using a 1-D motored translation with a minimum step of 20 µm. Temperature measurements are performed every 240 and 260 µm.

The resulting temperature profiles are plotted in Figure II.17. The measurements start from the burner exit (HAB = 0 mm) and ends up near the heated plate (HAB = 13 mm). In the first case, in which the thermocouple goes through the heated plate, the measured temperature rises monotonically from HAB = 0 mm until HAB ~ 11 mm, position at which the maximum temperature is reached (~ 700 K),

then decreases until the thermocouple reaches the plate, at which the measured temperature is slightly above 600 K. In the second case, the temperature gradient at the burner exit is equal to 0 $K \cdot mm^{-1}$ until HAB ~ 6 mm, then starts to slightly increase until HAB ~ 8 mm as the thermocouple approaches the flame front. The temperature increases drastically from HAB ~ 8 mm to HAB ~ 11 mm, reaching a maximum temperature around 780 K, and then decreases monotonically until the thermocouple reaches the heated plate. While these two temperature profiles were measured using the same thermocouple and the same flame condition, the results are significantly different.

From the CH_2O-PLIF measurement, it was clearly observed that no significant reactivity takes place before the mixture reaches the flame front. No temperature rise is thus expected at such low HAB as the one observed in the left-hand side of Figure II.17. This early increase in the temperature profile is explained by the fact that the thermocouple crosses the flame and the heated plate when measuring the temperature upstream the flame. In the second case, as the thermocouple is placed horizontally, it does not cross the flame zone when measuring the temperature in the fresh gases.

The measurement configuration with the thermocouple lying on the side of the burner was therefore used.

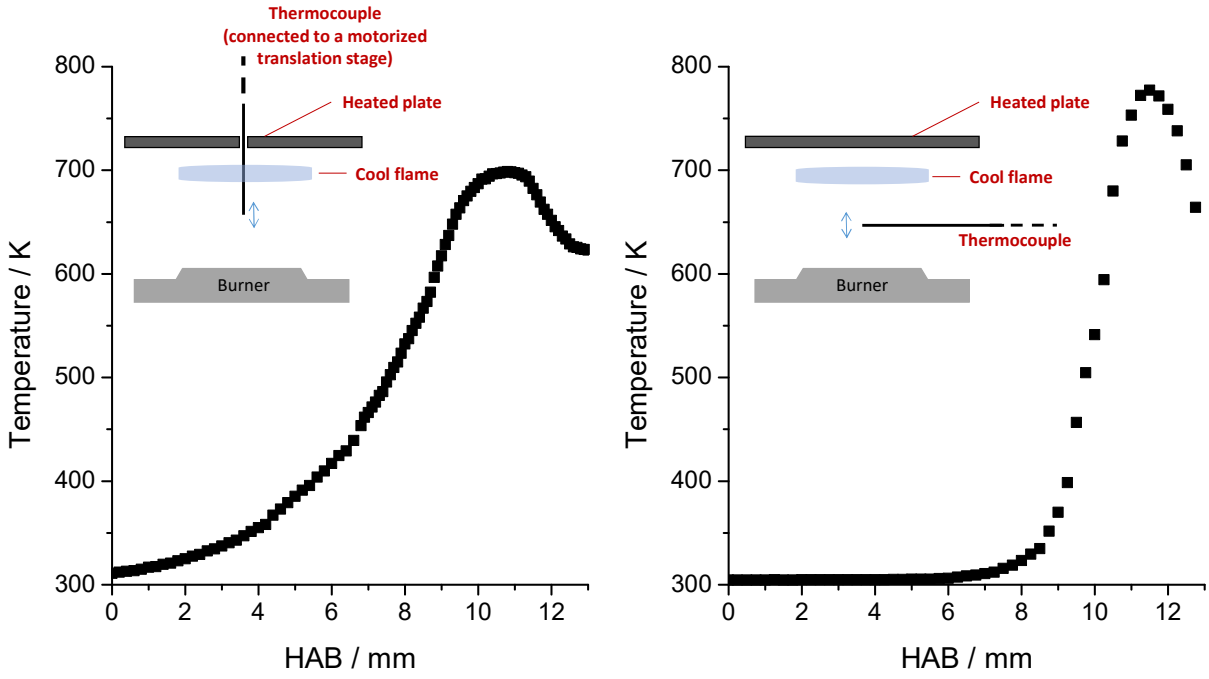

Figure II.17. Measured temperature profiles using the thermocouple positioned vertically (left-hand side) and horizontally (right-hand side). Schemes of the two configurations are inserted. DME/O_2/O_3 cool flame, ϕ = 0.3, α = 20 s^{-1}, x_{O3} = 1.1%.

II.4.2. Heat losses along the thermocouple

Inserting a thermocouple in a flame can perturb the velocity field, and yield other interactions with the flame. Thermocouple are known to undergo radiative and conductive heat losses along the thermocouple. Catalytic effects at the surface of the thermocouple can also take place. These losses are partially or totally compensated by the convection heat transfer by the hot gases around the thermocouple. The power balance on the thermocouple bed can be written as follow [201]:

$$\dot{Q}_{cat} + \dot{Q}_{conv} + \dot{Q}_{rad} + \dot{Q}_{cond} = 0$$

where $\dot{Q}_{cat}$ represents the heat loss by catalytic effect, $\dot{Q}_{conv}$ the heat gain by convection, $\dot{Q}_{rad}$ the heat loss by radiation and $\dot{Q}_{cond}$ the conductive heat losses. It is important to ensure that these different parameters can, or not, be neglected while measuring the temperature profiles of cool flames.

II.4.2.1. Catalytic effects

One of the common limits to the use of thermocouples is the significant influence of catalytic effects at the surface of the thermocouple when the latter is placed under reducing atmosphere. This kind of atmosphere is generally encountered downstream hot flames, where the concentrations of species such as carbon monoxide, water vapour or hydrogen is important. The metals composing the thermocouple tend to react with these chemically active species, thus modifying the composition downstream the flame and its temperature. Because of the important oxygen concentration upstream the cool flames, such effect is not expected to be significant, but was still verified.

In our case, the type-K thermocouple is non-coated. Following the recommendations from Heitor & Moreira [197], the absence of catalytic effects at the surface of the thermocouple was verified by measuring the temperature profiles of each flame in two directions: the first one from the bottom of the burner to the heated plate, and then in the inverse direction. If catalytic effects were to take place at the surface of the thermocouple, a hysteresis would be observed between the two measured temperature profiles, since catalytic activity would result in higher measured temperatures for the temperature profiles initiated at the high-temperature area of the flame, i.e., at the plate.

A comparison of these two operating procedures is shown in Figure II.18. No significant modification of the temperature profile can be observed in both cases, ensuring that catalytic effects can be neglected. The absence of catalytic effect in the case of cool flames can be explained by two reasons: Firstly, the end-products of the low-temperature combustion are different from the ones met in hot flames. Secondly, the maximal temperatures of cool flames are generally lower than those measured in hot flames, reducing the catalytic activity at the surface of the thermocouple as the temperature of the gas-phase is lower. Every other reported temperature profile was measured in both directions, ensuring that such catalytic effects never significantly interfered in the measured temperature of cool flames.

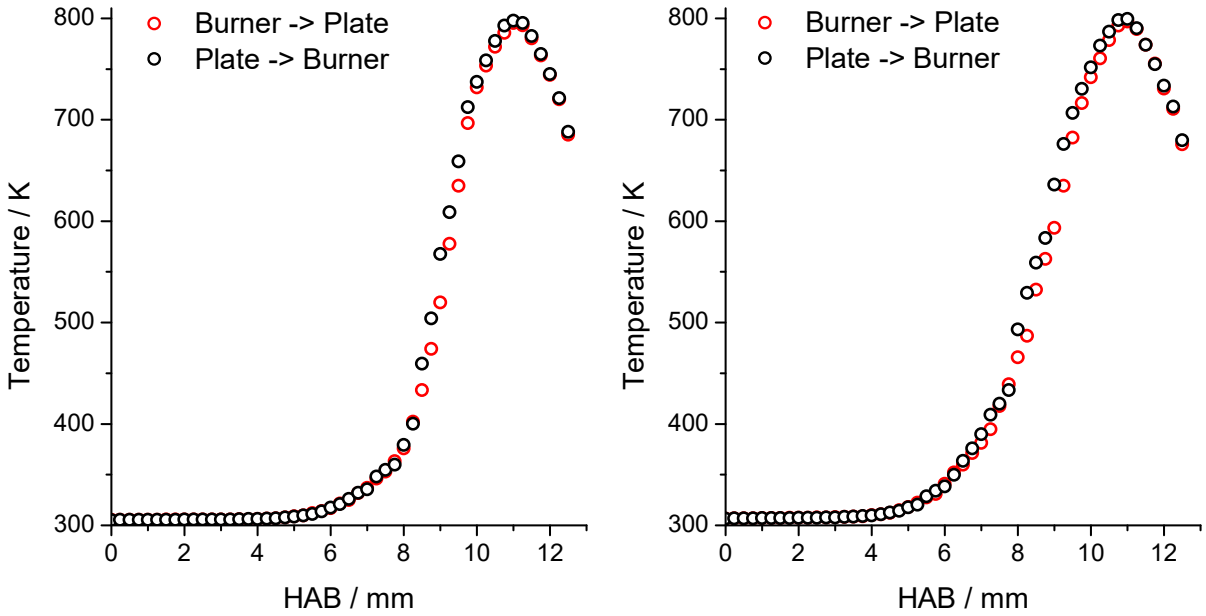

Figure II.18. Temperature profiles of cool flames measured from the cold reactants to the high-temperature area (red circles) and in the opposite direction (blue circles). $\phi = 0.3$, $\alpha = 20\ s^{-1}$, $x_{O3} = 1.1\%$ (left hand-side), $\phi = 0.5$, $\alpha = 20\ s^{-1}$, $x_{O3} = 0.8\%$ (right-hand side).

II.4.2.2. Conductive heat losses

Following the recommendations from Cafiero and co-workers [201], the conductive heat losses along the thermocouple surface were neglected for the following arguments:

i. As explained in Section II.4.1, the thermocouple was placed parallel to the burner surface, leading to more accurate measurements of the cool flame temperature profile. The cool flames being considered as flat flames, the temperature is fairly uniform near the measurement section of the thermocouple, which tends to limit heat losses near the measurement point.

ii. As proposed by Bradley & Matthews [202] and Heitor & Moreira [197], conductive heat losses are considered as negligible for thermocouples with a length-to-diameter ratio superior to 200. In our case, the thermocouple dimensions are Ø = 250 µm and l = 60 mm, yielding a ratio of 240, i.e., slightly above the proposed limit. This assumption was recently verified by Cafiero and co-workers [201] which observed only a small deviation when comparing measurements with and without conductive heat losses corrections using a thermocouple, verifying this assumption.

II.4.2.3. Radiative heat losses

The last effect that could affect the temperature measurement with a thermocouple in these conditions is the possible radiative losses at the surface of the thermocouple. The absence of such perturbation was verified in two different ways:

i. Visually, the thermocouple did not exhibit any red colour when immersed inside the cool flames. As for catalytic heat losses, this was verified for each studied cool flame condition.

ii. As radiative heat losses from the thermocouple to the environment are dependent on the thermocouple diameter [203], a cool flame temperature profile was measured using thermocouples with different diameters, respectively equal to 250, 500 and 1000 µm. The measured temperature profiles are presented in Figure II.19. As the diameter of the thermocouple increases, higher perturbation of the flow field above the burner is evidenced. However, the maximal temperature of the cool flame does not significantly vary using different thermocouples and remains within the experimental uncertainty, suggesting that radiative heat losses can be neglected.

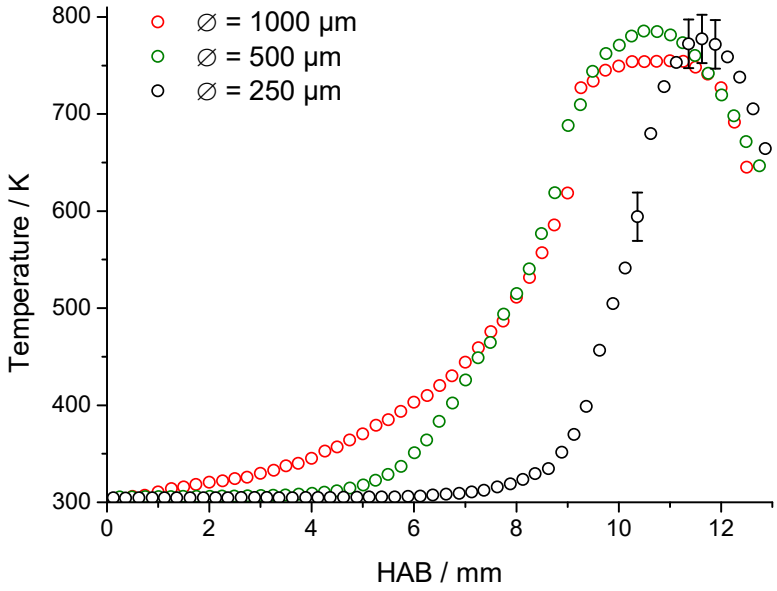

Figure II.19. Cool flame temperature profile measured with different thermocouples, respectively Ø = 1000 µm (red circles), Ø = 500 µm (green circles) and Ø = 250 µm (black circles). $\phi = 0.3$, $\alpha = 20\ s^{-1}$, $x_{O3} = 1.1\%$.

II.4.2.4. Uncertainties on temperature measurement

Two sources of uncertainty were considered:

- Uncertainty on the thermocouple position: The 'zero', i.e., the closest position of the thermocouple from the burner exit, is verified using a precision scope before each set of experiment. The uncertainty on the thermocouple position is estimated to be ± 250 µm, i.e., its diameter.

- Uncertainty on the flame temperature: The uncertainty on the flame temperature is estimated as a mean deviation when comparing the temperature profiles of several cool flames measured in the two directions (from the burner to the heated plate and in the inverse direction). It led to a mean temperature uncertainty of ± 25 K.

II.5. Species distribution measurement inside cool flames

Developing a sampling and analysis method of the gases in the cool flame allows to follow the progress of the reactant conversion and products formation as a function of the height above the burner. This technique is widely used within the combustion community as it provides valuable data regarding pollutant formation, or kinetic modelling.

The aim of this section is to describe the different equipment and techniques that were used in order to measure the species mole fraction profiles along the cool flames. Three different techniques were used to analyse the chemical structure of cool flames. These data are particularly valuable as recent literature data are scarce on the product distribution inside cool flames. Sampling inside a DME/O_2/O_3 cool diffusion flame, established in a counter-flow burner, was reported by Reuter and co-workers [46], but the data are presented in the supplementary material and are not discussed in the article. Comparison between their experimental data and their developed kinetic model (HP-Mech v3.3) showed an important discrepancy on the mole fraction prediction of species in the cool flame, respectively H_2O, CO, H_2, CH_3OCHO, CH_2O and CO_2. Sampling data were reported by the Belmont group for quasi-freely propagating cool flames of dimethyl ether [49], propane [50] and *n*-heptane [51]. They reported the mole fraction profiles of O_2, CO, H_2, CO_2, CH_2O and the fuel. However, the authors did not resolve the entire profile of the cool flame, and only considered the upstream area of the cool flame for the gas-phase analysis. From this work it was evidenced that fully resolved mole fraction profiles of the different species formed in cool flames could be of interest either for our understanding of cool flames chemistry as well as for the kinetic modelling of low-temperature combustion.

First, the gas chromatography (GC) method, coupled with different detectors, respectively a Flame Ionization Detector (FID), a Thermal Conductivity Detector (TCD) and a Mass Spectrometer (MS), are described. Then, the analyses using a micro-gas chromatograph (μGC) coupled with a micro-Thermal Conductivity Detector (μTCD) are addressed. The use of an online quadrupole mass spectrometer (QMS) for the detection of ozone is then described.

II.5.1. Generalities on gas chromatography

II.5.1.1. Gas-phase separation

Gas chromatography is a well-known method that allows separation of different constituents from a mixture. To do so, a gaseous mixture is injected into a column, which can be filled or coated using different materials (chosen depending on the initial mixture characteristics). The compound placed at the surface of the column, or the column packing, is called the stationary phase. The mixture is carried in the column using an inert carrier gas. Common carrier gases are Argon, Helium, Nitrogen or Hydrogen. Each compound present in the initial mixture (named the vapor phase) is pushed inside the column. The separation of the different constituents of the gas mixture operates as each component of

the gas mixture possesses its own affinity with the stationary phase. At the end of the column are the detectors, which help identifying and/or quantifying the compounds separated in the column. A typical chromatogram shows a series of peaks as a function of time, each peak indicating that one compound (or several, if not separated) is ejected from the column. Each species is identified by its retention time (τ), also called eluting time.

Using detectors such as FIDs or TCDs, the mole fraction of a species *i* is proportional to its signal acquired by the detector, and can be determined by calculating the area under the curve for each separated species, which can be expressed as follow:

$$F_i = \frac{A_i}{x_i \cdot P_{inj}}$$

where F_i is the response factor of the species *i*, A_i the area under the curve and above the baseline of the species *i*, x_i the mole fraction of the species *i* and P_{inj} the injection pressure of the mixture in the GC. The determination of the response factor of the species *i* can be performed using an internal standard or by performing external calibrations, as detailed in Section II.5.4.

II.5.1.2. Detectors associated with gas chromatography

Different kinds of detectors were used in order to analyse different families of species with GC and are detailed hereafter.

- **Flame Ionization Detector (FID)**: The flame ionization detector is based on the detection and count of ions, mainly HCO^+ [204], formed when a carbon containing compound is burned inside a hydrogen flame. The currently accepted two-step FID mechanism is detailed below. The chemi-ionization step is considered as the primary reaction, which creates HCO^+, which then rapidly reacts to produce H_3O^+ and other secondary hydrocarbon ions [205]:

$$CH + O \rightarrow HCO^+ + e^- \quad \text{(R18)}$$

$$HCO^+ + H_2O \rightarrow H_3O^+ + CO \quad \text{(R19)}$$

  The generation of ions is proportional to the concentration of the species in the initial mixture, which allows this technique to be quantitative. As ions are formed inside the detector, they are impelled by an electric potential towards an electrode, producing a current that can be converted into a voltage. FIDs present many advantages, as they are relatively inexpensive to operate, require only little maintenance over the time, have a very large linear response range and are very sensitive. However, the main limitation of FIDs is their absence of response to some species, especially CO, CO_2 and CH_2O which are important combustion intermediates. Moreover, FID is a destructive technique, i.e., the gas sample is deteriorated in the detector. It therefore has to be placed at the end of the analytic section of the gas chromatograph.

- **Thermal Conductivity Detector (TCD)**: The thermal conductivity detector, also known as katharometer, senses the change in the thermal conductivity of the eluent compared to a reference carrier gas flow. Helium or Hydrogen are generally employed as carrier gas flow due to their high thermal conductivity. If the eluting gas possesses a lower thermal conductivity than the carrier gas, a change in the reference thermal conductivity is detected and a detectable signal is reported. The main advantage of using a TCD is its quasi-universality, as the only required condition is that the analysed species possesses a different thermal conductivity from the reference carrier gas. As for FIDs, TCDs exhibit a very large linear response range, ensuring reliable measurements. They are however usually less sensitive. CO, H_2O and CO_2 can be measured using TCDs detectors.

While TCDs and FIDs allow the quantification of separated species in a gas chromatograph, they do not provide information on their identification, except by injecting pure samples of expected species, and identifying them based on their retention time. However, this technique requires that the expected species are known beforehand, and available as a pure product. This result in a time-consuming method, that can be avoided by using a mass spectrometer at the outlet of the GC column.

- **Quadrupole Mass Spectrometer (QMS)**: In a QMS detector, the gas sample exiting the GC column is first ionized through Electron Ionization (EI). The ionization energy (IE) is generally fixed at 70 eV, ensuring that every compound is ionized. The positive ions then pass between four electrically-connected parallel rods, between which an electric field is generated, as shown below in Figure II.20. The ions trajectory inside the quadrupole is altered depending on their mass-to-charge ratio, allowing them to be discriminated when reaching the detector placed at the end of the quadrupole. Each ionized molecule generally gives two pieces of information: The first one is the signal of the molecular ion, and the second is the signals of the different fragments that are formed from the original molecule. By collecting these data, it is possible to identify the majority of the molecules exiting the GC column by comparing their mass spectrum to a spectrum library or analysing their fragmentation pattern.

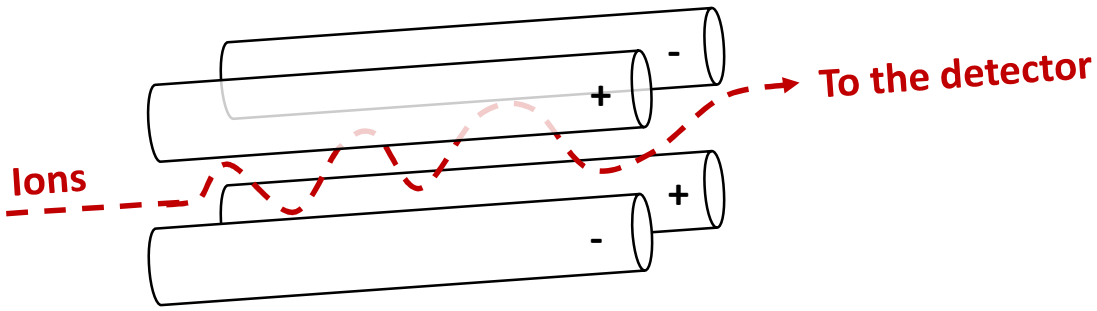

Figure II.20. Schematic of an ion trajectory in a quadrupole.

By coupling thermal conductivity or flame ionization detectors with a quadrupole mass spectrometer, it is possible to simultaneously identify and quantify the different eluting compounds. If the QMS is generally used for identification, it can also be used for quantification, especially for species that do not exhibit any signal on the other detectors. This detector is also destructive.

The next sections present the different gas- and micro gas-chromatographs that were used within this work, along with their specificities.

II.5.2. Specificities of the used gas-chromatographs

II.5.2.1. Gas-chromatographs

Two different GCs were used in this work to identify and quantify the fuel and intermediates:

- **GC-MS Bruker**: The GC-MS Bruker SCION 546-GC couples two different detectors in parallel, a FID for the quantification of organic compounds, and a QMS detector for species identification. Gas-phase mixtures sampled in the flame are injected at low-pressure in the column. It is equipped with a RT Bond Q column (characteristics: 30 m long, 0.25 mm internal diameter, 8 µm stationary phase thickness), composed of a silica surface on which is placed a highly apolar stationary phase. It allows the separation of most hydrocarbons and oxygenated species up to C_6, and is thus particularly suited for flame analysis. The maximum admissible temperature of the column is 280°C. After the species separation, the gas flow is divided in two distinct flows: a first part flows through the FID, while the second part flows through the QMS detector. An example of FID chromatogram obtained downstream a DEE/O_2/O_3 cool flame is shown in Figure II.21. In this work, the QMS was also used to quantify a few products that did not exhibit any signal on the FID detector, namely formaldehyde and acetic acid. Specific calibration methods for these species will be explained later in this manuscript.

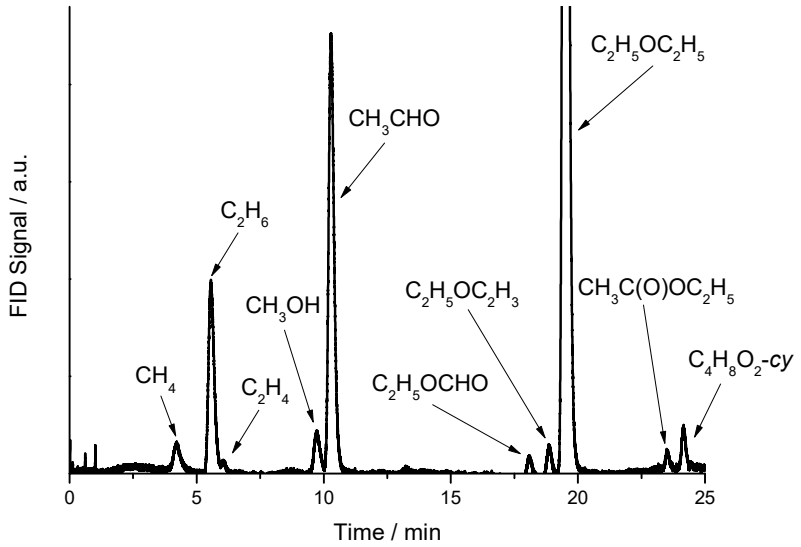

Figure II.21. FID chromatogram obtained in the burnt gases of a DEE/O_2/O_3 cool flame.

- **TCD/FID Agilent**: The second chromatograph used within this work is an Agilent 6890 gas chromatograph. As for the GC-MS Bruker, the injection of the gaseous mixture is realized at low-pressure. A packed ShinCarbon ST column (characteristics: 2 m long, 0.53 mm internal diameter, 80/100 mesh size) was installed, the objective being the quantification of light gases, especially CO, CO_2, CH_4 or O_2. A TCD and FID are installed at the exit of the packed column.

While gas chromatographs are powerful tools for the identification and quantification of the different species composing a mixture, a long eluting time is generally required to separate the different compounds of the gas-phase mixture. A micro-gas chromatograph was also used within this work, and is described in the following section.

II.5.2.2. Micro gas-chromatography

Micro-gas chromatography is the preferred technology for rapid gas analysis. The advantages of µGCs against GCs are the shortened analysis time, the reduced instrument size and a low detection limit. µGCs technology uses narrow bore capillary and micro packed column that allow for compact gas analysis. The reduction of the column diameter increases the separation speed.

The µGC used in this work is the Agilent 490 Micro GC, equipped with a CP-PoraPLOT U (characteristics: 10 m long, 250 µm internal diameter) and a µTCD detector. µTCD detection technique operates as TCDs, yet possesses a much lower detection limit. The identification of the separated species was realized by comparing the retention time of the different species in the gas mixture and the retention time of pure species. Thus, the µGC has only been used to analyse the gas-phase composition of DME/O_2/O_3 after initial analyses using the Bruker GC/MS which allowed to identify the formed intermediates. A chromatogram obtained downstream a DME/O_2/O_3 cool flame is shown in Figure II.22. The different species sampled are separated inside the column in less than 1.5 minutes, while a similar analysis using a GC usually lasts between 20 and 25 minutes to obtain sufficient peak resolution.

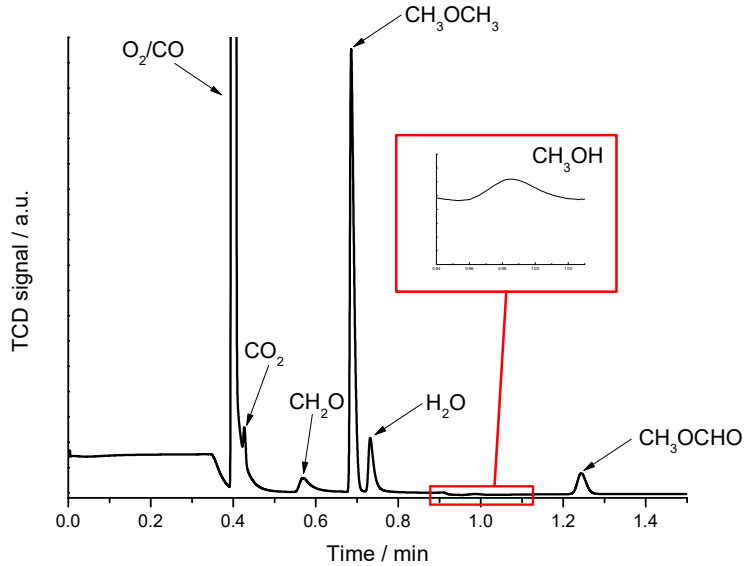

Figure II.22. µTCD chromatogram obtained in the burnt gases of a DME/O_2/O_3 cool flame.

While the chromatographs are generally operated by using a temperature ramp to optimize the separation of the different species, the µGC is operated isothermally. The main characteristics of the µGC and GCs operating conditions are listed in Appendix II.A5. The injector temperature was reduced as much as possible to avoid pre-reactivity of the mixture in the injector, while also avoiding products condensation.

II.5.3. Sampling & injection

II.5.3.1. Sampling procedure

Several probe geometries and sampling procedures were investigated as part of this work.

Concerning the sampling probe geometry, the first probe is a fused silica capillary of 150 µm internal diameter and 220 µm external diameter, while the second one is a quartz probe with a tip opening of around 100 µm and of 4.1 mm external diameter. Both are shown in Figure II.23.

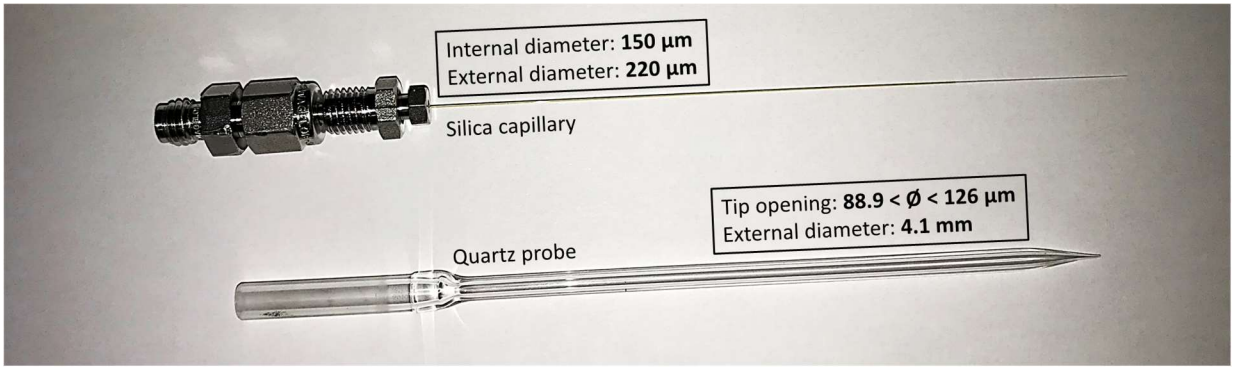

Figure II.23. Fused silica capillary and quartz probe considered for the sampling procedure.

After initial tests, the capillary probe was preferred over the quartz probe, mostly because its thin body minimalizes the perturbation of the velocity field. As for the temperature measurements, two different configurations were tested for the sampling: on one hand, the sampling capillary passes through the holed heated plate, and on the other hand the capillary is placed horizontally to the burner axis (see Section II.4.1). After stabilizing a DME/O_2/O_3 cool flame seeded at x_{O3} = 1.1%, the ozone concentration was measured in both cases as a function of HAB. The results are shown in Figure II.24. and are discussed hereafter.

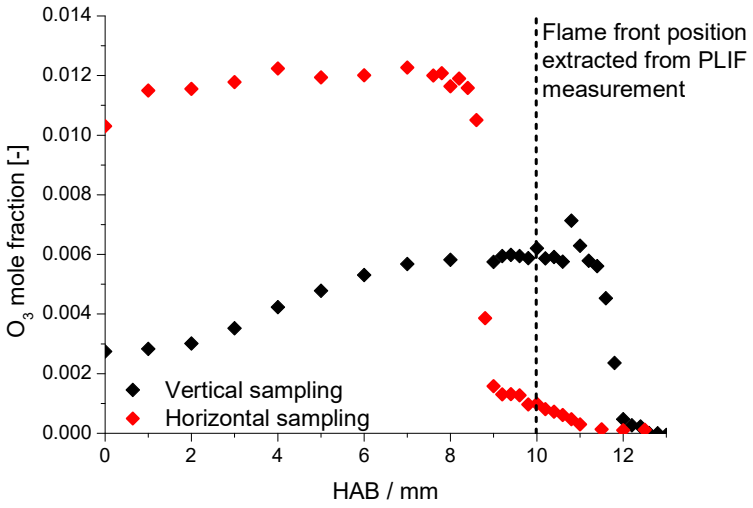

Figure II.24. Ozone mole fraction profile measured with a vertical & horizontal sampling. DME/O_2/O_3 cool flame condition: ϕ = 0.3, a = 20 s^{-1}, x_{O3} = 1.1%.

When the sampling capillary is placed vertically, the measured ozone inlet mole fraction equals 0.3% which is much lower than the expected 1.1%. Its mole fraction then increases progressively until it reaches the value of 0.6% at HAB ~ 8 mm, and remains constant until it reaches the flame front where it is fully consumed. On the other hand, when the sampling capillary is placed horizontally, the measured inlet ozone concentration agrees with the expected 1.1%. The ozone concentration is constant until it reaches the flame front, where it is also fully consumed. This suggests that, when the capillary is placed vertically, a major part of the ozone sampled in the upstream area of the flame is converted inside the sampling capillary, as it is heated by both the flame and the heated plate. In this second configuration the sampling capillary does not cross the flame zone while sampling in the upstream area of the flame, explaining that ozone is not converted in the capillary in this condition.

It has been decided, as for thermocouple measurements, to perform sampling measurements from the side of the burner, the tip of the capillary lying along the axis of the burner. One should finally note that, in this configuration, the ozone decomposition takes place at a lower position than the measured flame front position by CH_2O-PLIF. This discrepancy is discussed and explained in Section III.5.

II.5.3.2. Injection procedure

Two different injection methods were used, depending on the operated chromatograph, and are detailed hereafter.

- **GC-MS Bruker & Agilent 6890**: One important feature of both GCs is their ability of injecting samples at pressures below 1 atm. Samples from the cool flame are accumulated in a vacuumed stainless-steel cylinder, isolated from the sample loop of the GCs until the injection phase. The mean injection pressure lies around 180 – 200 mbar. It is a compromise between a satisfying signal/noise ratio and a relatively quick sampling time.

- **Agilent µGC 490**: To the contrary of GCs, the µGC injection pressure must lie between 1 and 2 bar (abs.). As the mixture is sampled at low-pressure, it needs to be pressurized. To do so, two different approaches were investigated: i) compressing the sample with a piston, or ii) diluting the sample in nitrogen. The main concern was to limit ozone decomposition, and induced reactivity, during the compression phase. This was assessed by following the methyl formate concentration, CH_3OCHO, as a marker of the reactivity of the DME/O_2 mixture with ozone. Its measured mole fraction profile using both techniques is pictured in Figure II.25. While both profiles exhibit an overall similar shape, and yield the same concentration downstream the flame, one can notice that its formation is increased upstream the flame when the piston is used. It indicates that using the piston instead of nitrogen dilution increases the reactivity of the unburnt gas mixture. The nitrogen dilution of samples prior to the injection in the µGC has thus been used further. Scheme, protocol and repeatability tests can be found in Appendix II.A6.

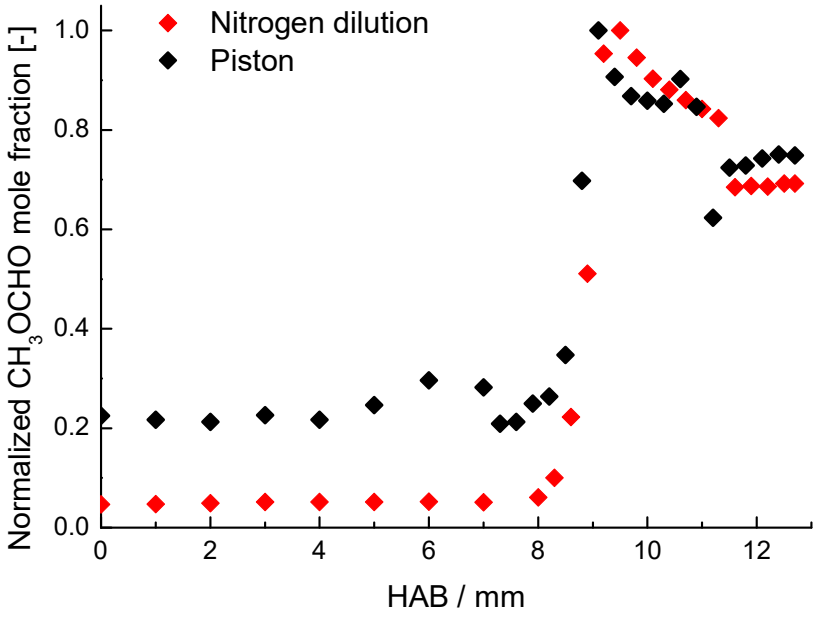

Figure II.25. Comparison of CH_3OCHO normalized mole fraction profiles in a $DME/O_2/O_3$ cool flame using two different techniques to increase the pressure of the sampled mixture. Flame condition: $\phi = 0.3$, $\alpha = 50\ s^{-1}$, $x_{O3} = 2.0\%$.

II.5.4. Species calibration

Different calibration techniques were used in order to extract species concentrations from detectors signals, and are described in the present section. Calibration curves for each species, along with the corresponding calibration technique used, are presented in Appendix II.A7.

II.5.4.1. Direct calibration (FID, TCD, µTCD)

If the species of interest can be either obtained as a pure compound or as a standard reference gas, i.e., contained inside a 'calibration cylinder', it can be directly calibrated by injecting in the GC a known concentration of the species. For standard reference gases, repeatability is ensured by injecting the

mixture several times at constant pressure. For products that are not available as standard reference gases but are available as pure species, in-house mixtures are prepared using a heated mixture preparation vessel and the partial pressures method. In this case, several mixtures with different mole fractions of the species of interest can be prepared.

II.5.4.2. Calibration by sampling in the burner (FID, TCD, µTCD)

This method consists in calibrating some species from direct sampling above the burner. It was used for DME, DEE, OME-2 and O_2 calibrations. Species concentrations are determined from the delivered gas flow rates by the mass flow controllers, which were calibrated beforehand.

II.5.4.3. Calibration by the ECN (FID)

One of the advantages of the FID is its linear response which depends on the amount of analysed sample, regardless of its composition. Moreover, a strong link exists between the chemical composition of the sample, i.e., functional family, and its response factor. This rule, known as the Equivalent Carbon Number (ECN), attributes a relative response signal on the FID depending on the molecule chemical structure, which relies on the type of ions formed in the hydrogen flame. The ECN is calculated from the contribution of each functional group in the considered species [206]. For a reference species *k*, for which the response factor on the FID was determined beforehand, and a species *i*, for which the response factor is unknown, the response factor of *i* can be calculated as follows:

$$Response\ Factor\ (i) = Response\ factor\ (k) * \frac{ECN\ (i)}{ECN\ (k)}$$

This allows to determine the response factor of some molecules that cannot be calibrated using the previous methods. It however induces a higher uncertainty on the calculated mole fraction as the ECN varies significantly depending on the chemical structure of the sample, and this method assumes that peak widths are equivalent whatever the species. Comparison of species calibration using both the ECN and in-house prepared gas mixtures are presented in Appendix II.A8, ensuring the validity of this method.

II.5.4.4. Calibration on the QMS detector

While the QMS detector in a GC setup is generally used for identification purposes, it can be used for species quantification to a certain extent. In this work, the QMS detector was used to calibrate two species that do not exhibit any signal on the FID: formaldehyde (CH_2O) and acetic acid (CH_3COOH). Please note that formaldehyde was quantified in the DME/O_2/O_3 cool flames with the µGC, but this apparatus was not used for DEE/O_2/O_3 and DME/OME-2/O_2/O_3 cool flames. The developed methods to calibrate these species on the QMS detector are explained hereafter.

- **Calibration of formaldehyde (CH_2O) on QMS detector**

Formaldehyde is mainly found in the commerce in aqueous solution (~ 40% formaldehyde in water) called formalin. A formaldehyde calibration method using formalin was proposed by Giaracca [207] by preparing calibration mixtures of CH_2O-CH_3CHO-H_2O. Analysing aqueous solutions with a GC-MS can however be difficult. Another technique was therefore developed within this work, and is based on the use of 1,3,5-trioxane. The thermal decomposition of 1,3,5-trioxane proceeds by the concerted rupture of three C-O bonds in the ring to form CH_2O:

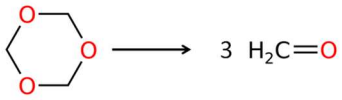

Hochgreb and Dryer [208] studied the unimolecular decomposition rate of 1,3,5-trioxane into formaldehyde between 700 and 800 K and showed that the decomposition of 1,3,5-trioxane is much faster than the decomposition or oxidation of formaldehyde. It confirms the use of 1,3,5-trioxane as a source of monomeric formaldehyde at gaseous state.

1,3,5-trioxane was purchased from Sigma-Aldrich (purity > 99.0%), and is under the form of solid crystals at ambient temperature and pressure. To produce formaldehyde from 1,3,5-trioxane, the solid is placed inside a glass vial and heated using an intense source of heat, here a blowtorch. The glass vial is connected to the heated bench, in which the concentration of formaldehyde is determined by measuring its partial pressure. Formaldehyde is then diluted in nitrogen prior to its injection in the GC. It is important to note that, during 1,3,5-trioxane thermal decomposition, a minor part of this species underwent sublimation, yielding gaseous 1,3,5-trioxane. It means that 1,3,5-trioxane/CH_2O mixtures were obtained. The residual 1,3,5-trioxane concentration in mixtures was calibrated by preparing pure 1,3,5-trioxane/N_2 mixtures, the solid being sublimated under vacuum at bench temperature, 70°C, to avoid formaldehyde formation. 1,3,5-trioxane was then calibrated on the FID while formaldehyde was calibrated on the QMS detector, using the mass-to-charge ratio 30 m/z, corresponding to the molecular ion of formaldehyde.

- **Calibration of acetic acid (CH_3COOH)**

Calibration of acetic acid on the QMS detector was realized by injecting liquid acetaldehyde/acetic acid mixtures dissolved into methanol. Methanol was chosen as solvent as its retention time is very different from the two other species, allowing excellent peak separation. Liquid mixtures were prepared by measuring the mass of each species added to the mixture using a precision balance. For each prepared solution, the ratio of the mole fraction of acetic acid and acetaldehyde is calculated as follow:

$$\frac{x_{acetic\ acid}}{x_{acetaldehyde}} = \frac{\left(\frac{m_{acetic\ acid}}{M_{acetic\ acid}}\right)}{\left(\frac{m_{acetaldehyde}}{M_{acetaldehyde}}\right)}$$

where m is the mass and M the molar mass. This ratio was measured for different solutions by selecting the proper mass-to-charge ratio: 44 m/z for the acetaldehyde and 60 m/z for the acetic acid. The acetaldehyde signal on the QMS was calibrated using its FID signal, previously determined using in-house acetaldehyde/nitrogen mixtures. Finally, the acetic acid mole fraction was deduced from the measurement in flame, using the acetaldehyde signal as internal reference.

In Table II.1. are summarized, for each cool flame study, the species measured inside the flame along with the associated apparatus, detector, calibration method and uncertainty. Details on calibration curves and comparison between the different methods are presented in Appendix II.A7 and II.A8.

Table II.1. Detected species with the different techniques, along with the associated uncertainties.

Species	Apparatus	Detector	Calibration method	Uncertainty
DME cool flame				
CH_3OCH_3	µGC	µTCD	Burner sampling	± 5%
CH_2O	µGC	µTCD	In-house mixture	10%
CH_3OH	µGC	µTCD	In-house mixture	10%
CO_2	µGC	µTCD	In-house mixture	5%
CH_3OCHO	µGC	µTCD	In-house mixture	5%
CO	GC	TCD	In-house mixture	20%
DEE cool flame				
$C_2H_5OC_2H_5$	GC	FID	Burner sampling	5%
CO	GC	TCD	Standard reference gas	10%
CO_2	GC	TCD	Standard reference gas	5%
O_2	GC	TCD	Burner sampling	5%
C_2H_6	GC	FID	Standard reference gas	5%
C_2H_4	GC	FID	Standard reference gas	5%
CH_4	GC	TCD	Standard reference gas	5%
CH_3OH	GC	FID	In-house mixture	5%
CH_3COOH	GC	QMS	In-house mixture	10%
CH_3CHO	GC	FID	In-house mixture	5%
C_2H_5OCHO	GC	FID	Equivalent Carbon Number	15%
$C_2H_5OC_2H_3$	GC	FID	In-house mixture	5%
$CH_3C(O)OC_2H_5$	GC	FID	Equivalent Carbon Number	15%
$C_4H_8O_2$-*cy*	GC	FID	Equivalent Carbon Number	15%
CH_2O	GC	QMS	In-house mixture	10%
OME-2/DME cool flame				
CH_3OCH_3	GC	FID	In-house mixture	5%
CH_3OCHO	GC	FID	In-house mixture	5%
CO_2	GC	TCD	In-house mixture	5%
CH_3OH	GC	FID	In-house mixture	5%
OME-1	GC	FID	Equivalent Carbon Number	10%
OME-2	GC	FID	In-house mixture	10%
CH_3OCH_2OCHO	GC	FID	Equivalent Carbon Number	10%
CO	GC	TCD	Standard reference gas	10%
CH_2O	GC	QMS	In-house mixture	15%

II.6. Ozone concentration measurement

The ozone mole fraction in the oxidizer flow is measured with an ozone analyser before the injection into the burner, as presented in Section II.1. It was however desired to measure the ozone mole fraction profile in cool flames. The used method is described hereafter.

A mass spectrometer Omnistar GSD 301 O2 Pfeiffer Vacuum was used for ozone measurements. It is an electronic impact quadrupole analyser mass spectrometer with a constant IE = 70 eV, which is the same type of detector than the one presented before (Section II.5.1.2). In the present apparatus, molecules are not separated and enter the QMS as a bulk. As a consequence, this QMS cannot be used to identify and quantify molecules that possess a peak shared with other species. An example of obtained mass spectra in the unburnt and burnt gases of a DEE/O_2/O_3 cool flame is pictured in Figure II.26. The important number of peaks illustrates the difficulty of obtaining selective information on a species. However, the molecular ion peak of ozone is located at 48 m/z, and is expected to be the only species at this mass-to-charge ratio, justifying the use of this apparatus for ozone measurements.

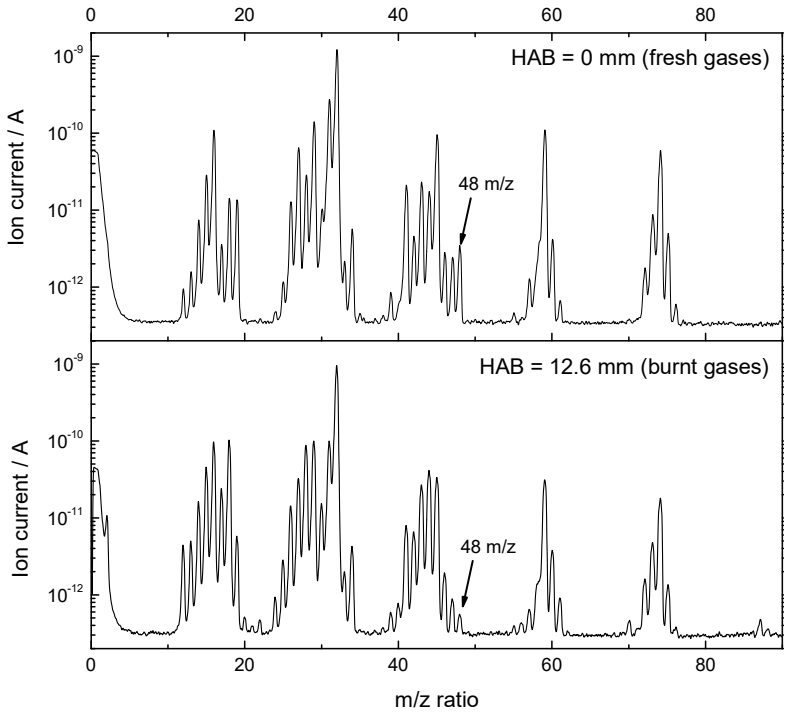

Figure II.26. Obtained mass spectra at IE = 70 eV in unburnt (upper graph) and burnt gases (lower graph) of a DEE/O_2/O_3 cool flame. ϕ = 0.5, α = 50 s^{-1}, x_{O3} = 1.4%.

Ozone was expected to be the only species at molecular mass-to-charge ratio 48 m/z. After different tests it was found out that a small contribution came from oxygen, as a peak at the same mass-to-charge ratio was detected when sampling pure O_2 from the burner exit, as seen in Figure II.27. The most reliable suggested explanation is the oxygen molecules or ions recombination in the detector after ionization. This contribution from oxygen was corrected by measuring the oxygen concentration along the burner axis with the Agilent 6890 chromatograph, which was then used to correct the extra-signal

on the mass spectra obtained with the QMS detector. For each flame condition, measurements of Fuel/O_2 and Fuel/O_2/O_3 mixtures in non-reactive conditions, i.e., in the absence of cool flame, were realized in order to get a reference signal with and without ozone, ensuring a reliable correction of O_2 contribution to the ozone signal.

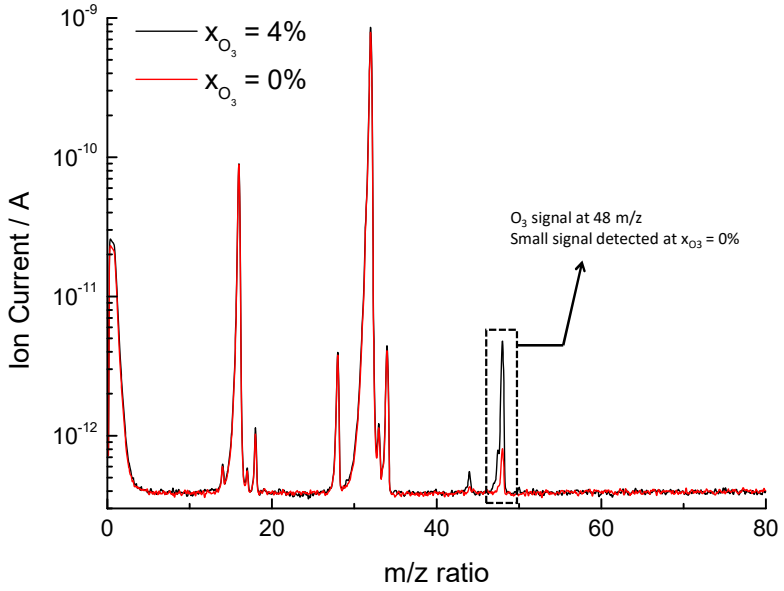

Figure II.27. Mass spectra at EI = 70 eV of pure oxygen (red line) and of oxygen/ozone mixture (black line) at the exit of the burner.

From repeatability measurements, and considering the correction of oxygen contribution, the uncertainty on the ozone concentration measurement was estimated to be ± 10%. The ozone calibration curves are provided in Appendix II.A9.

Ozone measurements notably allowed to ensure that no significant ozone loss took place in the burner. In the present configuration, ozone losses at burner walls surface are expected to be non-significant as the ozone concentration used for cool flame stabilization is high (generally 1 to 2% of the reactive mixture). Absence of ozone decomposition on the walls was verified by measuring the ozone concentration both at the entrance and exit of the burner using the Teledyne API 452 Analyser, yielding similar concentrations. These results are provided in Appendix II.A10.

II.7. Particle Image Velocimetry (PIV) in a stagnation flow

Particle Image Velocimetry is an experimental technique that allows, by following particles displacement within a liquid or gaseous flow, to measure its velocity field or its streamlines. It is also used to infer laminar flame speed of fuels from strained flames experiments, as briefly presented (Section I.3.2.2). In the scope of this work, PIV was used following two main purposes: the first one was to measure axial and radial velocity profiles in the burner, allowing to reconstruct the velocity field in reactive and non-reactive conditions. The second objective was to experimentally determine the laminar burning velocity of cool flames. This is the first time, to the best of our knowledge, that this technique is applied to cool flames.

II.7.1. Principle of PIV

The PIV technique is based on the tracking of particles within a flow. To do so, the flow is seeded with small solid or liquid particles, their diameter being generally around the micrometre. The particles are then illuminated using a pulsed laser sheet, and the diffused light at the surface of the particles is collected by a rapid camera. If the delay between two pulses is short enough, the particles displacement can be extracted from two successive images, which is then used to reconstruct the global flow field. A synthetic scheme of a PIV setup is shown in Figure II.28, taken from the thesis manuscript of Nicolas Bouvet [85]. From a twin-pulse laser, a laser sheet that cuts the field of interest is produced, and the camera is placed with an angle of 90° (similarly as CH_2O-PLIF measurement). Images recorded by the camera are divided into individual 'Interrogation Spot (or Window)', in which the displacement of each particle is tracked by an algorithm. The 2-D velocity field can be reconstructed by assembling the displacement of every particle in every interrogation window.

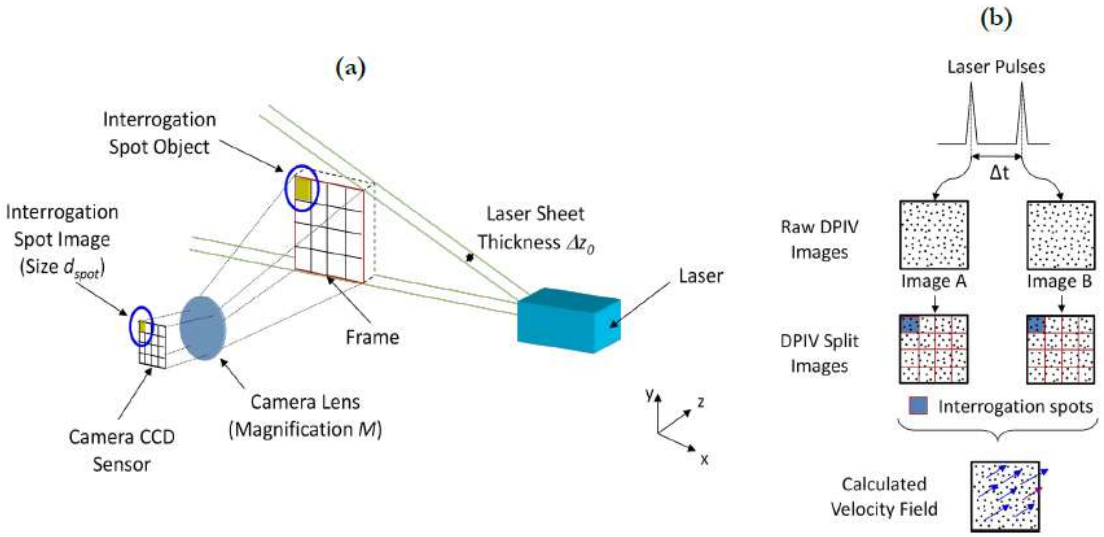

Figure II.28. Principle of the PIV measurement, from Nicolas Bouvet [85].

The quality of the obtained velocity field depends on many parameters related to the PIV setup, flow and particle characteristics. The most critical aspect of PIV is the particle-seeding. It is assumed

that every particle follows the mean flow displacement. However, if the particles size is too important, forces such as gravity or buoyancy can interfere and modify the velocity or trajectory of the particles. On the other side, smaller particles tend to agglomerate, which can then alter the measurement by forming bigger agglomerates that, in turn, may be affected by external forces. Details on the choice of the particle seeding were addressed by Melling [209]. Seeded particles can either be solid or liquid, depending on the experimental conditions. Along with the particle size, the density of particles in the field is of primary importance. Operating PIV measurements with a too low, or too high density of particles, may result in errors coming from the algorithm analysing the experimental data. As examples, if the particle density is too low, the velocity field cannot be sufficiently resolved, and if it is too high, the algorithm can fail in finding correlations between two images. The laser sheet thickness is also an important point, as well as the energy distribution within the sheet. These problematics, along with more complex ones, such as the effect of thermophoresis or electrostatic forces on the particles displacement, were extensively addressed within the scientific literature [210–212].

The next sections are dedicated to the experimental PIV apparatus and image post-processing methodology. This work was performed as a collaboration with the Laboratoire de Mécanique des Fluides de Lille – Kampé de Fériet (LMFL) and the CORIA (COmplexe de Recherche Interprofessionnel en Aérothermochimie).

II.7.2. Experimental PIV setup

II.7.2.1. Laser sheet formation

The particles are illuminated at the wavelength λ = 532 nm. The pulsed laser beam is provided by a dual cavity Nd:YAG Splitlight Compact laser from Innolas (delivering two 50 mJ pulses at 532 nm, at a frequency of 10 Hz). The initial pulsed laser beam is delivered at λ = 1064 nm, and passes through a second harmonic generator to provide the λ = 532 nm laser beam. The laser beam first passes through a dichroic filter to eliminate the remaining stray light at the λ = 1064 nm wavelength. The laser sheet is then generated using spherical (f# 550 mm) and cylindrical (f# - 80 mm) lenses. As for the CH_2O-PLIF measurement the laser sheet is centred on the burner axis. A simplified scheme of the laser sheet generation is shown in Figure II.29. The laser height is approximately 12 mm, and the thickness estimated to 600 µm, both being measured at the centre of the burner.

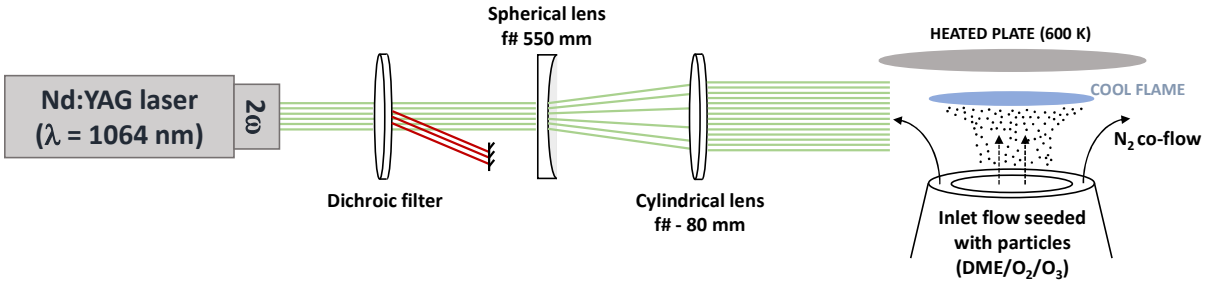

Figure II.29. Simplified scheme of the PIV setup used in this work.

The particles displacement between two laser pulses is captured using a LaVision Scmos camera of 2560 by 2160 pixels, equipped with a 105 mm Nikkor lens at an aperture of f#8. The resulting magnification is equal to 20 µm per pixel. The time between two pulses (Δt) was fixed at 220 µs in order to record a mean 10 pixels displacement of the particles between the pulses at the lowest flow rate. A total of 1000 images were recorded for each condition, yielding a measurement duration for each condition of 100 seconds.

II.7.2.2. Particles generation

Solid particles are widely used in the combustion field, as they possess a high decomposition and sublimation temperature, which is suited for flame studies. In our case, the lower temperature of cool flames is an advantage as liquid particles with a sufficiently high vaporization temperature can be used. Silicon oil, provided by Chem-Lab, is chosen for its well-defined characteristics in terms of viscosity, surface tension, etc. It also possesses a particularly high vaporization temperature, around 600 K.

The seeding of particles in the inlet flow was realized using an in-house atomizer, which is presented in Figure II.30. The inlet flow, composed of pure oxygen, passes through a needle (Needle 1). The section restriction at a constant flow rate increases the gas velocity and its dynamic pressure at the needle exit. Increase of dynamic pressure at the exit induces a drastic diminution of the static pressure via the Venturi effect in a second needle (Needle 2) lying vertically next to the extremity of the first needle. The other extremity of the second needle is immersed into a silicon oil reservoir. The low pressure in this needle allows the oil to be pumped, and then atomized in the carrier flow. The density of the particles in the gas flow is controlled by the arrangement of the two needles, and by the inlet oxygen flow. At the lowest flow rates ($\dot{Q}_{O2} \leq 1.6$ L·min^{-1}) the overpressure inside the first needle is not high enough to permit particles dragging in the oxygen flow. At higher flow rates, particles can be detected in the oxygen flow, the density of which increasing as the inlet flow rate increases. The particle diameter was estimated to be in the range 1 – 5 µm, as usually met for this kind of atomizer [213].

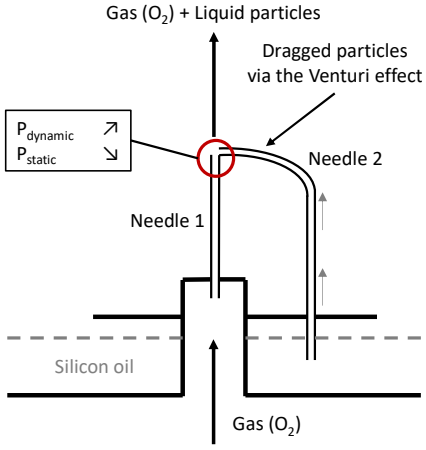

Figure II.30. Experimental atomizer setup.

In this configuration, the total inlet oxygen flow has to be divided into two parts. The first part flows through the ozone generators, and the second part flows through the atomizer. It avoids liquid particles fouling inside the ozone generators, and the presence of ozone inside the atomizer, in order to limit ozone decomposition before the burner exit. As the oxygen flow rate of the studied flames is generally quite low, around 2-3 $L \cdot min^{-1}$, this division of the flow limits the production of particles. At the highest oxygen flow rates in reactive conditions, the particle density in the vicinity of the flame was estimated to 0.005 particles per pixel (ppp). An image of the particles illuminated by the laser sheet is presented below, in Figure II.31. The reactive mixture, seeded with particles, can be visualized. The presence of the heated plate and the burner exit are visible thanks to the laser sheet reflections. The position of the flame front can be deduced from the disappearance of the particles due to their vaporization downstream the flame front.

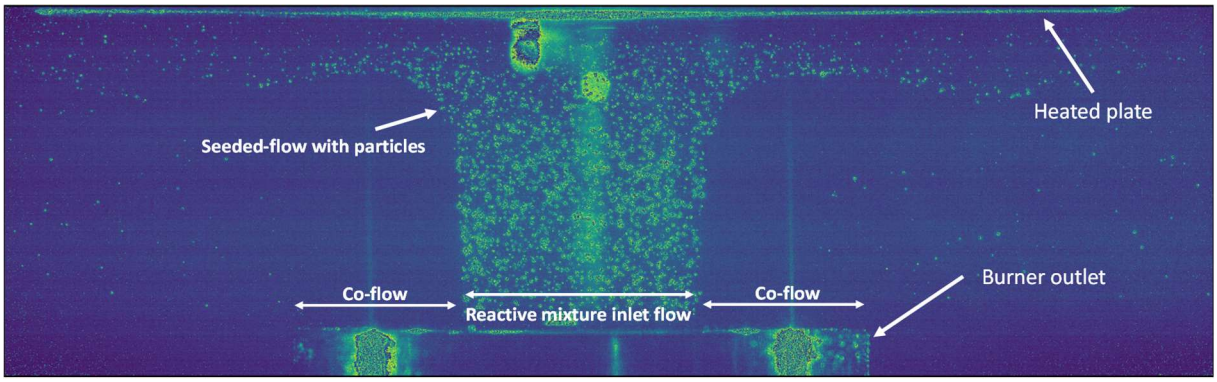

Figure II.31. Image of the seeded-particles flow in a $DME/O_2/O_3$ cool flame. $\phi = 0.45$, $\alpha = 60\ s^{-1}$, $x_{O3} = 1.7\%$.

The last step of the PIV measurement is to extract the particles displacement in the flow from the acquired images. To do so, two different approaches were tested to obtain as precise and reliable measurements as possible.

II.7.2.3. Image processing

The presented image processing procedures were respectively performed by Pierre Bragança from the LMFL laboratory and Bertrand Lecordier from the CORIA laboratory. As a consequence, only a brief explanation of each treatment is given in this section.

The first approach, realized by the LMFL laboratory, is motivated by the very low particle density in our experimental conditions. As explained before, each acquired image is divided into small 'interrogation windows' in which each particle displacement is tracked. The interrogation window size, IWS, varies accordingly to the particle density, expressed as a number of particles per pixel. As the density decreases, the IWS must generally be increased so that the algorithm used for particles displacement tracking is able to precisely locate every particle within an interrogation window. However, increasing the IWS yields a lower spatial resolution, and can affect the final result. In this first image processing, the low particles concentration (0.005 ppp) in our experimental conditions required a

minimum IWS of 32 x 32 pixels (0.64 x 0.64 mm^2), resulting in 64 points axial velocity profiles (along the HAB). In order to obtain a better spatial resolution, a more advanced and adapted PIV approach was specifically developed at the CORIA laboratory and is detailed below.

Before applying the PIV image processing, an advanced background correction is performed from conditioned averaged images, one at t and one at $t + \Delta t$. A standard background correction is not adapted in the case of low-density condition due to the difficulty to remove the individual particle signal on averaged images, even when 1000 images are considered. In our approach, the conditioned background images are then obtained by averaging all the instantaneous images but without integrating the signal of particles in the process using a Kuwahara filter. This specific image processing improves the estimation of background images in particular in low density regions. Next to the background correction, only the particle signal remains on the corrected images. Then, the spatial calibration is done with a well-defined target (0.977 x 0.977 mm), and is used to estimate a polynomial camera model of 3^{rd} order used to dewarp each image, ensuring a perfect alignment of both wall and burner axes within the (x, y) frame. This step also corrects any image distortion induced by the camera lens. From this step, PIV processing starts by an extraction of the particles position in the images using a 2D correlation pattern recognizing technique. Between 1500 and 3500 particles are detected on each image, depending on the experimental conditions. The vector calculation is then initiated at the particle location, and not on a regular mesh as it is usually performed when the particles density is higher. This calculation is based on an iterative continuous window shift technique [214], starting with an interrogation window size (IWS) of 64 x 64, and reaching an IWS of 8 x 8 pixels (0.16 x 0.16 mm^2) in the final pass. This results in a series of non-regular velocity fields which are validated with a rate higher than 85%. The scaling in the real coordinated system is realized with the burner plate as reference, with an accuracy of ± 20 µm. The final step consists in computing a mean velocity field on a regular mesh by averaging every instantaneous vector in small cells at each mesh node, the cell size being compatible with the PIV resolution of 8 x 8 pixels. This processing method allows a significant improvement in the particle detection in the area close to the flame front. A comparison of the axial velocity profiles in non-reactive conditions determined using a conventional image processing method, i.e., with an IWS of 32 x 32 pixels, and the present one is presented in Figure II.32. While the conventional PIV processing method with IWS size of 32 x 32 pixels resulted in 64 points on the axial profiles, the second PIV processing with IWS size of 8 x 8 pixels yields 241 points. This considerable increase in the spatial resolution results in significant improvement of the quality of the extracted information from these profiles. Thus, the second method was kept and used for every experimental condition. A comparison of both image-processing methods is also presented in Appendix II.A11. in reactive conditions, i.e., in the presence of a cool flame.

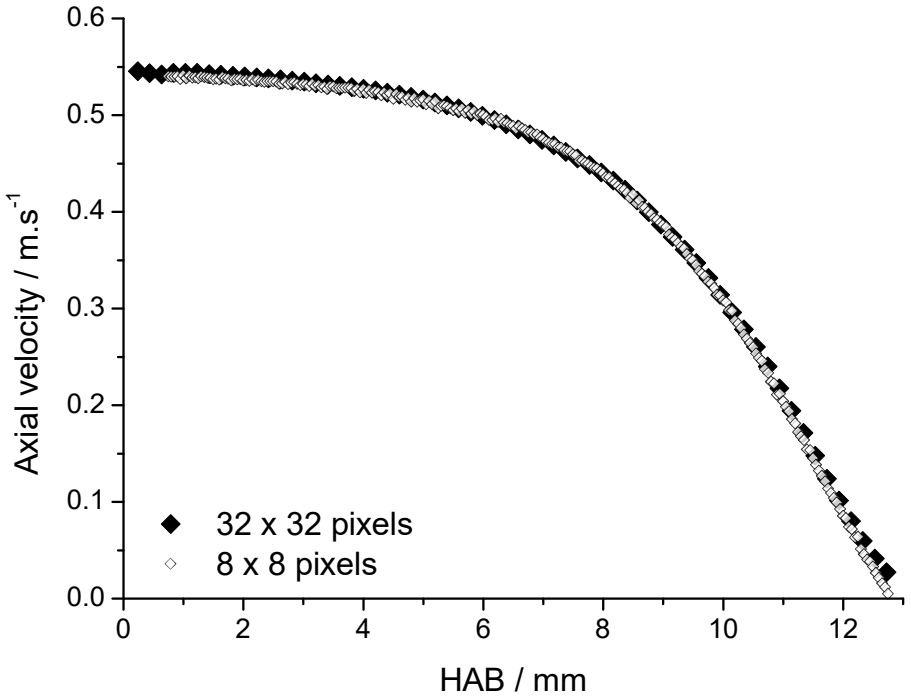

Figure II.32. Comparison of the two image-processing methods, respectively with 64 (black lozenges) and 241 (empty white lozenges) points per axial profile.

II.7.3. Flow velocity field in the burner

One of the objectives behind the use of PIV in the stagnation plate burner was to measure the axial and radial velocity profiles above the burner. In this work, the burner is equipped with a convergent nozzle, which theoretically ensures a laminar flow and a homogeneous velocity field at the exit of the burner. From the cool flame images acquired by CH_2O-PLIF or CH_2O*-chemiluminescence, the visible flat and axisymmetric flame front seems to confirm this assumption. Further confirmation was however required, and was obtained via PIV measurements in reactive and non-reactive conditions.

In Figure II.33. the axial velocity is plotted as a function of the burner radius at different HABs, both in non-reactive (left-hand side) and reactive conditions (right-hand side). The inlet flow rates were respectively equal to 0.54 $m \cdot s^{-1}$ at HAB = 1 mm in the non-reactive case, and 0.68 $m \cdot s^{-1}$ at HAB = 1 mm in the reactive case. As observed in Figure II.33, the velocity profiles form a plateau at the exit of the burner, and remain almost constant at higher HABs, confirming the strength of the nozzle geometry in establishing an axisymmetric, homogeneous flow field at the exit of the burner. In the reactive case one can note that the flow undergoes some non-uniformities at these higher flow rates, which may be due to local overpressure behind the porous discs. These uniformities however do not significantly impact the cool flame aerodynamics, as assessed by the flat flame front observed by CH_2O*-chemiluminescence. In order to solve this problem when working at higher flow rates, glass beads were placed between the gas entry in the burner body and the porous section, ensuring a better homogenization of the mixture and avoiding this local overpressure effect.

Moreover, as both reactive and non-reactive conditions exhibit a roughly constant velocity over few millimetres in the centre of the burner, it was chosen to average the axial velocity on ± 1 mm in the centre of the burner. A comparison of a non-averaged and an averaged axial velocity profile is presented in Appendix II.A12, showing no significant difference on the overall profile, while random vector attribution errors are discarded. A comparison of axial velocity profiles resulting from 200 images and 1000 images average is also shown in Appendix II.A13. It justifies the choice of selecting 1000 images for the averaging process.

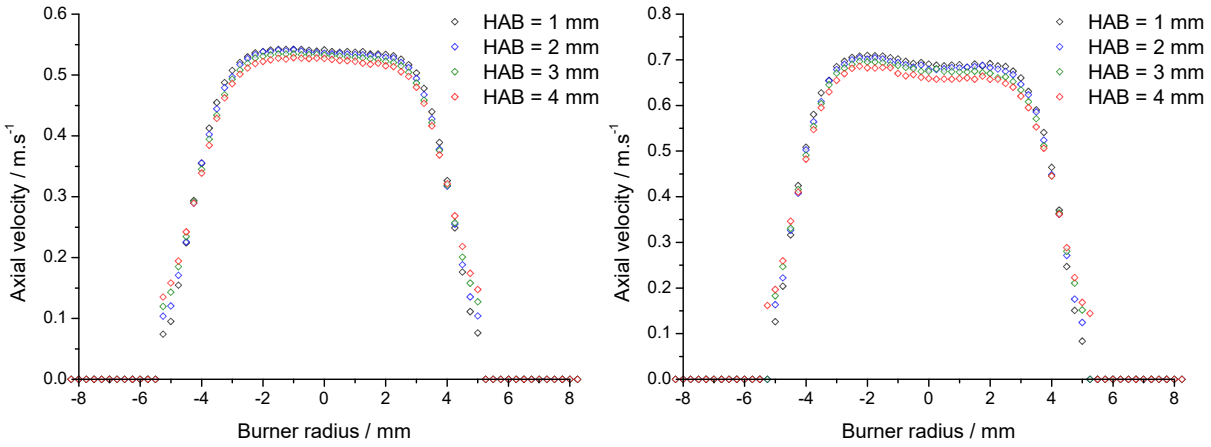

Figure II.33. Axial velocity profiles as a function of the burner radius for different HABs at the bottom of the burner: HAB = 1 mm (◊), 2 mm (◊), 3 mm (◊) and 4 mm (◊). The graph on the left-hand side is a non-reactive condition (O_2/O_3 flowing in the centre of the burner, $\alpha = 25\ s^{-1}$). The graph on the right-hand side is a reactive condition (DME/O_2/O_3, $\phi = 0.3$, $\alpha = 36\ s^{-1}$, $x_{O3} = 2.0\%$).

From PIV measurements two-dimensional velocity fields are also extracted, and an example in a reactive condition is shown in Figure II.34. It also demonstrates that the radial (u_r) distribution of the velocities is axisymmetric, and that the axial velocity (u_a) profile at the burner exit is almost uniform over the burner diameter. The cool flame front, stabilized two millimetres under the heated plate, can be distinguished on the axial velocity profile (u_a). In addition to the previous PIV results, it confirms the efficiency of the converging nozzle geometry, and constitutes further justification of the averaging process over a region of ± 1 mm used for image post-processing, as the axial velocity can be considered constant over a significant portion of the burner diameter (10 mm).

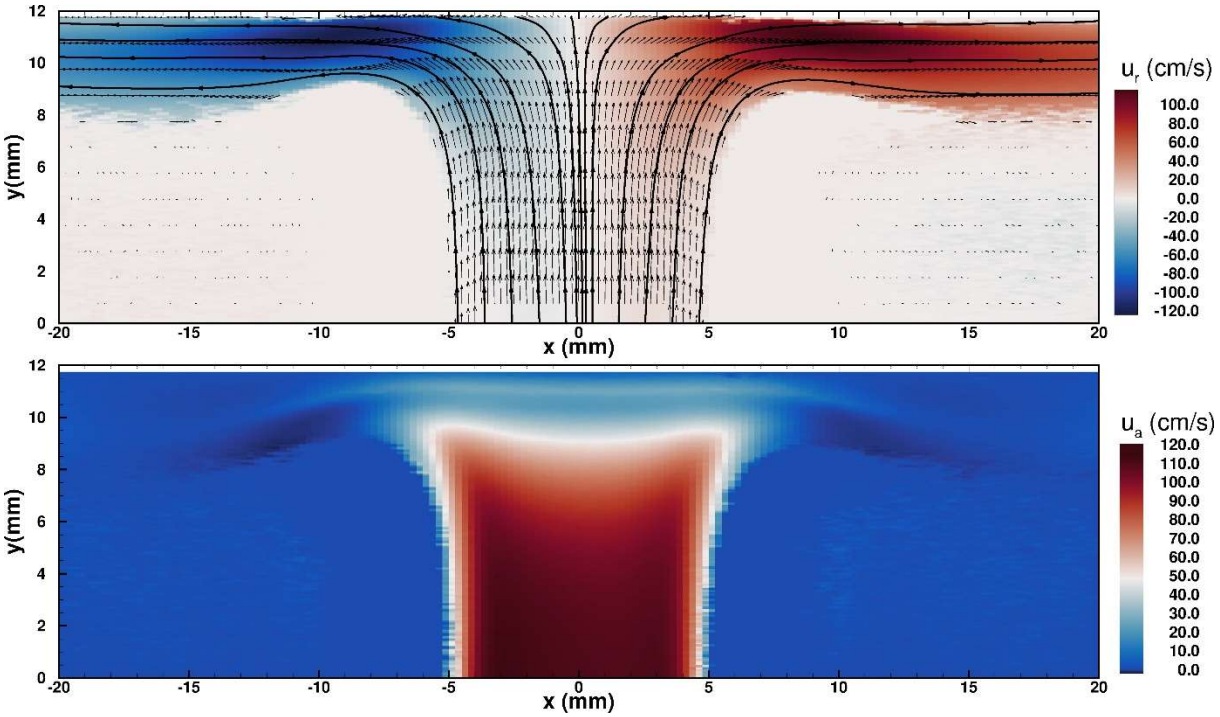

Figure II.34. Radial velocity streamlines (top) and axial velocity profile (bottom) of a DME/O_2/O_3 cool flame at ϕ = 0.4 and x_{O3} = 1.9%. u_r represents the radial velocity, u_a the axial velocity, y the Height Above the Burner (HAB) and x the burner radius.

Finally, the uncertainty on the determination of the axial velocity profile with the PIV technique was calculated using Root Mean Square (RMS) analysis, and was estimated to be ± 5%. The uncertainty is mainly due to difficulties in sufficiently seeding the flow in our experimental configuration.

II.8. General conclusions

The aim of this second chapter was to present an overview of the different techniques that were developed in the present work and coupled to the stagnation plate burner. While these techniques were already used in the past, their application to cool flame analyses is scarce or inexistent. It is especially true for PIV, as well as detailed species measurement in cool flames. Each of these techniques therefore required a careful implementation, ensuring that measurements done within this work are reliable.

Both intrusive and non-intrusive techniques were developed. On the first hand, CH_2O*-chemiluminescence and CH_2O-PLIF were used to measure the flame front position and the formaldehyde distribution in a wide range of experimental conditions. Then, thermocouple measurements were employed to measure the temperature profiles of the cool flames. Species distribution inside cool flames were measured by coupling a variety of different analytical techniques, allowing the detection and quantification of many intermediates resulting from the low temperature combustion of different fuels. PIV measurements were also operated, enabling the establishment of the

velocity field above the burner which will be used for the first determination of laminar burning velocity of cool flames at atmospheric pressure (Chapter V).

The next chapter of this manuscript presents the simulation of cool flames with a one-dimensional code, using either Cantera or Chemkin-Pro. Different aspects of cool flames stability will be addressed, notably regarding their simulation using a one-dimensional code, which assumes some hypotheses that need to be verified. It serves as a base for the next chapters, which are focussed on the kinetics of cool flames using different fuels.

Chapter III. Cool flames stabilization & numerical simulation

III. Cool flames stabilization & numerical simulation

This third chapter introduces the experimental procedure associated with cool flames stabilization in the stagnation plate burner. Igniting and stabilizing a cool flame instead of a hot flame requires some adaptations that will be addressed. Secondly, the numerical simulation of cool flames is presented. Moreover, before selecting few experimental conditions in which cool flames will be extensively studied in Chapters IV and V, parametric studies were necessary in order to find the best suited experimental conditions. The aspects relevant to the experimental conditions such as the inlet flow velocity, the N_2 co-flow rate, etc. will be discussed in the following sections. These investigations focus on the reduction of the impact of aerodynamic forces on cool flames to serve the purpose of their simulation using a one-dimensional code. DME/O_2/O_3 mixtures were used for these studies.

III.1. Cool flames stabilization domains

Burner stabilized flames are generally ignited using a lighter, a stove igniter or an electric filament. If such procedure is reproduced in our experimental conditions, a hot flame is ignited instead of a cool flame. In order to avoid the formation of a hot flame, the following procedures were chosen. The first procedure is followed when no stable cool flame condition was previously determined. Firstly, the plate temperature is fixed at its setpoint (600 or 700 K, depending on the experimental conditions). The N_2 co-flow is brought to its setpoint. Then, a DME/O_2 mixture without ozone is injected in the burner, each flow rate being progressively brought to its setpoint, which depends on the equivalence ratio and strain rate. In most of our usual work conditions, i.e., lean conditions, no flame can be stabilized without ozone adjunction. The O_3 concentration is then progressively increased until a stabilized cool flame is obtained. As the O_3 concentration increases, a flame will first ignite at the surface of the plate. When a sufficient O_3 concentration in the mixture is reached, the flame will come off the heated plate and stabilize between the burner exit and the heated plate. The different steps of the cool flame ignition and extinction are presented in Figure III.1 and described hereafter.

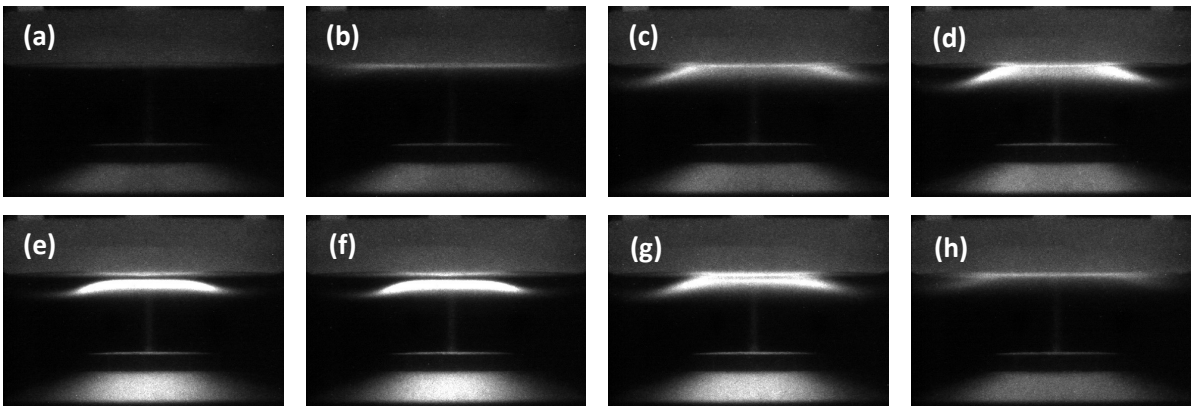

Figure III.1. Ignition, stabilization and extinction of a DME/O_2/O_3 cool flame (ϕ = 0.3, α = 50 s^{-1}) in the stagnation plate burner. The ozone concentration is progressively increased from (a) to (e) and decreased from (f) to (h).

The images are acquired with the ICCD camera without the band-pass filter, meaning that a large spectrum (300 – 900 nm) is recorded. In this example, a DME/O_2 mixture at $\phi = 0.3$ is flowing through the burner. Without ozone-addition, no flame is seen in (a). From (b) to (e), the O_3 concentration in the mixture is progressively increased until a cool flame is stabilized (e, f). Finally, the O_3 concentration is decreased, causing the flame to progressively extinguish at the surface of the heated plate (g, h). It demonstrates the importance of ozone-addition, permitting the stabilization of the cool flame in such lean conditions

In the second case, where a stable condition was already determined, the plate temperature, the N_2 and O_2/O_3 flow rates are brought to their respective setpoints. The fuel flow rate is then progressively increased until it also reaches its setpoint, resulting in a stabilized cool flame under the heated plate.

Ozone was used to draw stabilization domains for the DME/O_2/O_3 cool flames. At fixed strain rate and equivalence ratio (α ; ϕ) the ozone concentration can be progressively increased from 0 until a cool flame is stabilized. This is the lower stability limit of the cool flame for the fixed condition. The ozone concentration is then gradually increased, generally 0.1% by 0.1%, causing the flame to move towards the burner as the mixture becomes more reactive. When a certain ozone concentration is reached a hot flame is initiated, illustrating the higher stability limit. The hot flame propagation speed in the presence of ozone is however too important to be stabilized in our configuration, and thus results in a flashback, i.e., the flame enters inside the burner and is quenched on the porous plate. On the contrary, if the ozone concentration decreases, the flame tends to extinguish on the heated plate surface. This is the blow-off limit. Figure III.2. shows the stability maps of cool flames at fixed strain rates, respectively $\alpha = 10$ s^{-1} and $\alpha = 50$ s^{-1}, respectively the lowest and highest strain rates presented in this work. The position of the flame front, measured by CH_2O-PLIF, is plotted at each equivalence ratio condition ($0.1 \leq \phi \leq 0.55$) as a function of the ozone concentration in the mixture. At a constant equivalence ratio, the flame tends to get closer to the burner exit as the ozone concentration increases, indicating that the ozone acts positively on the cool flame propagation speed. As the strain rate, i.e., the inlet flow rate, increases, the cool flames are stabilized closer to the heated plate, and their positions tend to become far less sensitive to variations of the ozone concentration. The overall trend of the flame front position variation as a function of ozone concentration is the same whatever the studied strain rate. At 50 s^{-1}, cool flames below $\phi = 0.3$ could not be stabilized due to the insufficient ozone production of the ozone generator. One should also notice that the ozone concentration necessary to ignite cool flames increases as the strain rate increases. It is directly linked to the residence time scale, which is lower at higher strain rates. Stability maps for intermediate strain rates (α = 15, 20, 25 & 40 s^{-1}), for which the conclusions are similar, are provided in Appendix III.A1. Flame conditions (flow rate of DME, O_2, N_2) are also provided in Appendix III.A2, along with the corresponding CH_2O-PLIF profiles in Appendix III.A3. Establishing first these stability maps was necessary in order to i) explore the behaviour of cool flames regarding different experimental parameters, and ii) selecting experimental conditions for further detailed analysis.

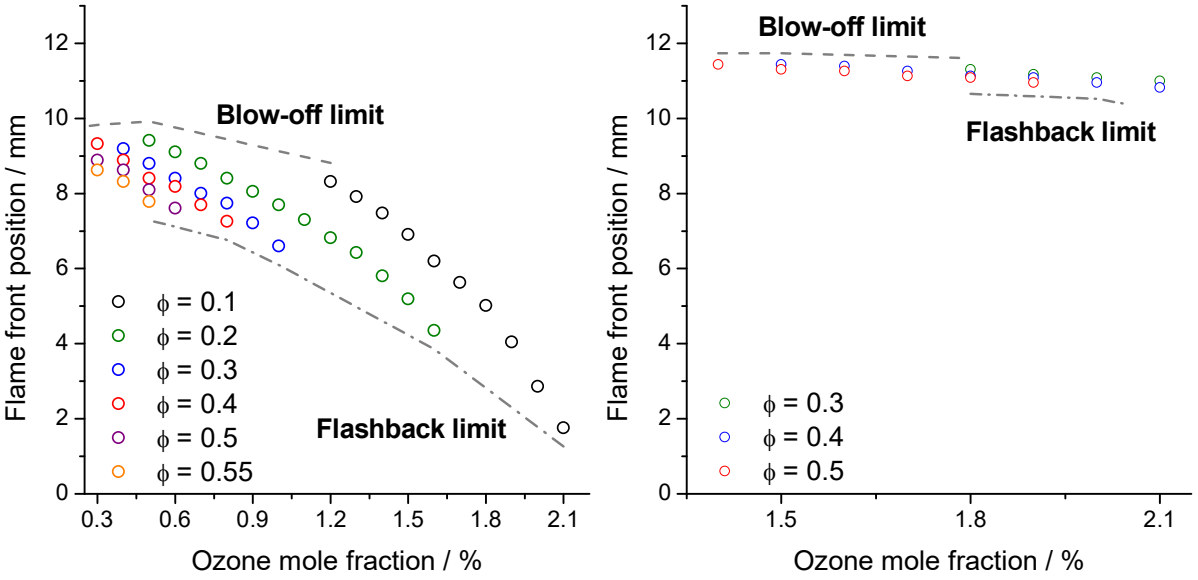

Figure III.2. Impact of ozone on the flame front position at different equivalence ratios for two strain rates, α = 10 s^{-1} (left-hand side) and 50 s^{-1} (right-hand side).

III.2. Numerical simulation of premixed cool flames

Kinetic modelling performed within this work was realized using either Cantera [215] or Ansys Chemkin-Pro [216] solvers. It is important to distinguish two different aspects of the kinetic modelling. On one hand, the so-called detailed kinetic mechanism, that includes kinetic, thermodynamic and transport data for each species of interest, and on the other hand the solver, which includes the governing differential equations adapted to the system of interest. Equations related to the solver are discussed in the next section. Generalities on kinetic modelling, respectively concerning definition of kinetic and thermodynamic data, are provided in Appendix III.A4.

III.2.1. Stagnation flame burner solver

III.2.1.1. Governing equations

The simulation of axisymmetric flames in a stagnation flow, in which the solution is computed along the stagnation streamline, is realized by solving the following governing equations [217] that are summarized in Table III.1.

Table III.1. Governing equations in a stagnation flow.

Continuity	$\frac{\partial \rho u}{\partial z} + 2\rho V = 0$
Radial momentum	$\rho u \frac{\partial V}{\partial z} + \rho V^2 = -\Lambda + \frac{\partial}{\partial z}\left(\mu \frac{\partial V}{\partial z}\right)$
Energy	$\rho c_p u \frac{\partial T}{\partial z} = \frac{\partial}{\partial z}\left(\lambda \frac{\partial T}{\partial z}\right) - \sum_k j_k c_{p,k} \frac{\partial T}{\partial z} - \sum_k h_k W_k \dot{\omega}_k$
Species	$\rho u \frac{\partial Y_k}{\partial z} = -\frac{\partial j_k}{\partial z} + W_k \dot{\omega}_k$

where ρ is the density, u the axial velocity, v the radial velocity, V = v/r the scaled radial velocity, Λ the pressure eigenvalue, μ the dynamic viscosity, c_p the heat capacity, T the temperature, λ the thermal conductivity, Y_k the mass fraction of the species *k*, j_k the diffusive mass flux of *k*, $c_{p,k}$ the specific heat capacity of *k*, h_k the enthalpy of *k*, W_k the molecular weight of *k* and $\dot{\omega}_k$ the molar production rate of *k*. Concerning the diffusive mass flux j_k, as the multicomponent transport data is enabled in our case, the mass fluxes are computed as follows:

$$j_k = \frac{\rho W_k}{\bar{W}^2} \sum_i W_i D_{ki} \frac{\partial x_k}{\partial z}$$

where $\bar{W}$ is the mean molar mass of the mixture, D_{ki} is the multicomponent diffusion coefficient and x_k the mole fraction of *k*. Thermophoresis, also known as Soret effect, is not considered in our calculations as it was verified that it did not significantly influence the simulated cool flames, while considerably lengthening the computational time. A comparison of simulated cool flames with and without the thermophoresis enabled is shown in Appendix III.A5. If the problem is solved using a mixture averaged formulation, j_k is calculated based on the following formula:

$$j_k^* = -\rho \frac{W_k}{\bar{W}} D'_{km} \frac{\partial x_k}{\partial z}$$

$$j_k = j_k^* - Y_k \sum_i j_i^*$$

III.2.1.2. Boundary conditions & initial guess

Boundary conditions are imposed at $z = z_0$, i.e., at the position of the inlet flow, and at $z = z_P$, i.e., the position of the plate. The imposed conditions for the stagnation flame simulations are listed below.

- **Boundary conditions at $z = z_0$**

T_0 / K	Temperature of the inlet flow
$\dot{m}_0$ / kg·m^{-2}·s^{-1}	Inlet mass flow rate expressed as a function of the section area
$x_{i,0}$	Composition of the mixture
V_0 / s^{-1}	Inlet radial strain rate

- **Boundary conditions at $z = z_P$**

T_P / K	Temperature of the heated plate
$x_{i,P}$	Composition of the mixture

In this work, the size of the domain is set at 13 mm, which is the position of the plate regarding the burner exit in every presented experimental condition. The inlet temperature (T_0) is kept at 300 K for every experiment, and the V_0 parameter, the radial strain rate, is fixed at 0 s^{-1} (See Chapter V for

more details on the relative importance of this parameter). On the other side, the imposed boundary conditions at the plate are its temperature T_P and the mixture composition. The definition of the composition at the plate $z = z_P$ will be discussed below.

The main difficulty met in the simulation of cool flames in a stagnation flow configuration is the occurrence of convergence of the simulation towards a cool flame instead of a hot flame, or no flame at all. As an example, the mixture composition by default at $z = z_P$ in Cantera and Chemkin-Pro is computed from equilibrium conditions. As a result, the solver will frequently yield into a hot flame. It is thus necessary to constrain the solver in order to avoid this specific case. Two strategies were coupled in order to maximize the probability that both solvers converge into a cool flame in the studied conditions. Firstly, the composition of the mixture at $z = z_P$ was fixed equal to the composition of the mixture in the inlet flow, such as $x_{i,0} = x_{i,P}$. By imposing a non-reacting composition at the position of the heated plate, the convergence into a hot flame can be avoided. Secondly, the maximal temperature of the flame can be restrained. Very often, trying to simulate a cool flame starting with a $T_P = 600$ K and a non-reacted composition at the outlet results in the absence of a flame. To avoid this problem, the simulation is initiated at a higher plate temperature -generally 700 K when the experimental plate temperature is 600 K and 800 K when it is experimentally fixed at 700 K. If the first guessed flame reaches a temperature superior to a fixed limit (here 920 K) it is considered as a hot flame, and the temperature of the heated plate T_P is slightly decreased. This process is repeated until the flame temperature does not exceed the limit temperature. When a cool flame ($T_{max} < T_{limit}$) is found on the initial grid, the plate temperature is then lowered to its initial value and the grid is refined. An example of this method is illustrated in Figure III.3, for a DME/O_2/O_3 cool flame modelled with the Cantera solver.

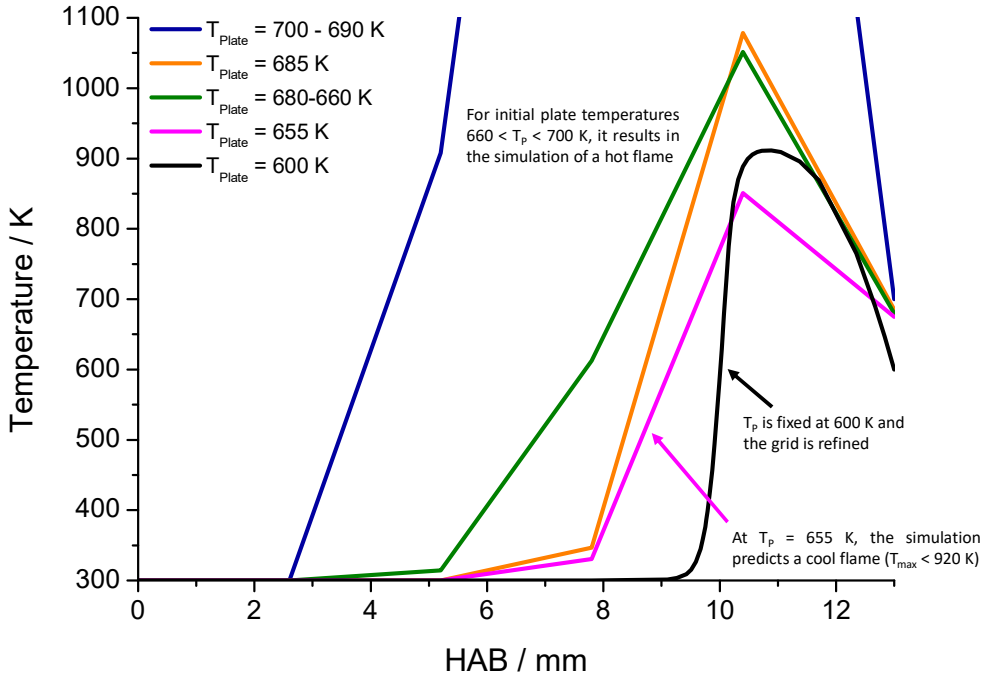

Figure III.3. Example of the convergence method into a cool flame using the Cantera stagnation flow solver, for a DME/O_2/O_3 reactive mixture. Condition: $\phi = 0.3$, $\alpha = 40$ s^{-1}, $x_{O3} = 2.2\%$.

It was verified that the simulated profile did not exhibit any change depending on the initial plate temperature. Moreover, the experimental investigation of the effect of the plate temperature on the cool flame is provided in Appendix III.A6, showing no significant impact on the cool flame at high strain rates.

Considering a stagnation flow configuration as a 1-D configuration involves some hypotheses that need to be experimentally verified. First of all, the cool flames stabilized in the stagnation plate burner are surrounded by a nitrogen co-flow, which is not considered in the 1-D simulation. It is therefore necessary to ensure that there is no effect of this co-flow on the cool flame. Secondly, in our experimental configuration, relatively low flow rates are necessary to stabilize cool flames. This is essentially due to the limited ozone production and the narrow stability domain of cool flames (compared to conventional hot flames). In this precise case, external forces such as buoyancy could affect the flame, and are not considered in the simulation.

III.2.2. Inlet velocity & inlet radial strain rate

Among the required user inputs for modelling stabilized flames in a stagnation flow, important data are the inlet velocity, or inlet mass flow rate, and the radial strain rate at $z_0 = 0$ mm. Velocity field measurements using PIV are necessary to ensure that these data are known, as they are dependent on the nozzle geometry and the burner exit – plate distance. In this study, the boundary conditions at the burner exit were verified by means of PIV measurements in non-reactive and reactive conditions.

The inlet axial velocity field is not constant along the burner radius because of the converging nozzle (see Chapter II, Figure II.33). Considering the velocity field completely homogenous, the inlet velocity can be calculated as the ratio of the volumetric flow rate on the inlet section, which will be referred as the ‘calculated velocity’. On the other hand, inlet velocity deduced from PIV measurements will be referred as the ‘measured velocity’.

The inlet velocity was thus measured in various conditions that are summed up in Figure III.4. and detailed in Appendix III.A7. The measurements were operated 0.8 mm above the burner in reactive conditions with DME/O_2/O_3 mixtures, and the reported uncertainty is ± 5% for each measured value. As expected, the measured velocity in the centre of the burner is constantly superior to the calculated velocity. The measured velocity evolves quasi-linearly against the calculated velocity, and was thus fitted as a linear function. The correlation factor R^2 is superior to 0.999. It comes out that both values are correlated by a factor equal to 1.46.

This factor can then be used to determine the actual velocity at the centre of the burner for conditions that were unexplored with PIV measurements. It is expected that this factor is valid for different fuels and mixtures, and not only for DME/O_2/O_3 mixtures, which were used for those measurements. This relation is however not expected to be valid at low inlet velocities, as the velocity

distribution at the exit of the burner may be significantly affected by buoyancy. The effect of the inlet velocity and potential buoyancy effect will be discussed hereafter.

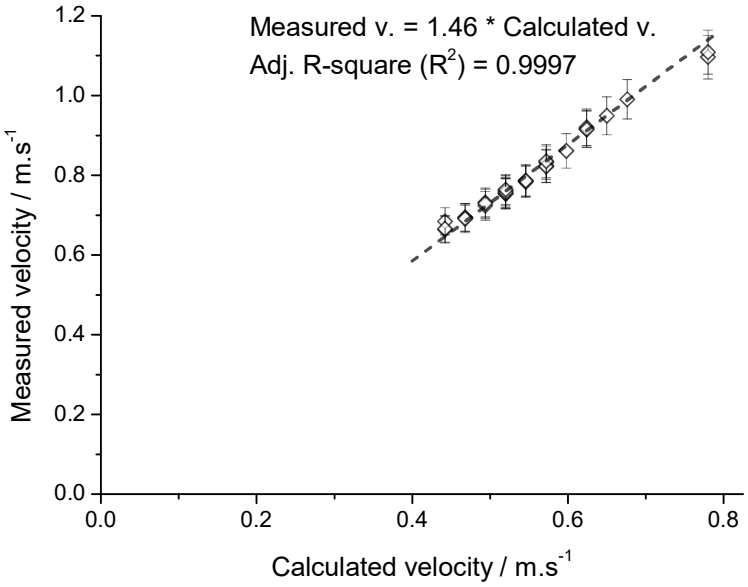

Figure III.4. Measured velocity as a function of calculated velocity at the centre of the burner (see Appendix III.A7 for details).

The second inlet parameter that needs to be experimentally measured is the radial strain rate at the exit of the burner. When using a convergent nozzle in a stagnation flow configuration, two different inlet behaviour can be expected: either a 'plug-flow' or a 'potential flow' [218]. The plug-flow boundary condition is characterized by a zero-radial velocity gradient at the exit of the burner, while this gradient is inferior to 0 in the potential-flow condition, meaning that the flow is radially expanding at the outlet. These two configurations are schematically represented in Figure III.5.

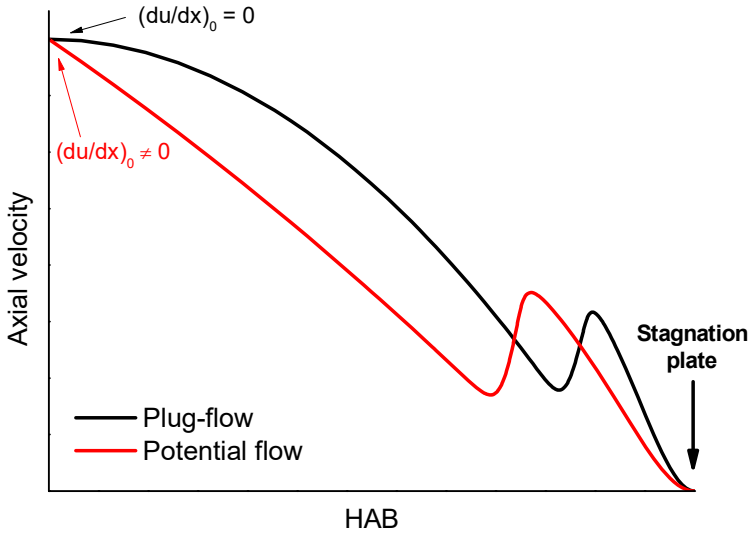

Figure III.5. Comparison between a plug-flow and a potential flow inlet behaviour in a stagnation flow burner.

As for the inlet velocity, the inlet radial strain rate is a parameter that can be easily inferred from axial velocity profiles using PIV measurements. The axial velocity profiles of different flames at different inlet velocities are plotted in Figure III.6. Every studied condition clearly exhibits a plug-flow behaviour at the inlet. The inlet radial strain rate was thus fixed to 0 when simulating temperature and species mole fraction profiles on the entire burner length (see Chapter IV). A different procedure was applied for flame speed simulations, and is detailed in Chapter V.

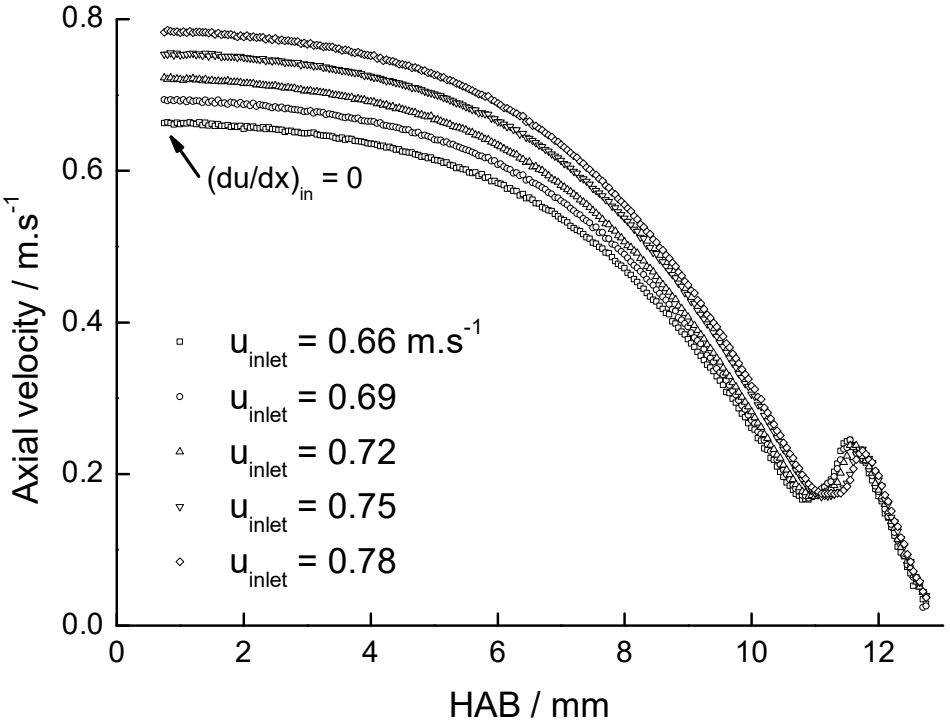

Figure III.6. Axial velocity profiles of a DME/O_2/O_3 cool flame at different inlet velocities, ϕ = 0.5, x_{O3} = 1.5%.

III.3. Buoyancy influence on stabilized cool flames

The potential influence of buoyancy effects on cool flames is addressed in this section. As mentioned, this effect is not considered in 1-D simulations. It is therefore necessary that the operating conditions are not influenced by this effect. In their experimental and numerical work on DME cool flames, Reuter and co-workers [46] found an important discrepancy between their experimental and simulated temperature profile when a plug-flow regime at the inlet was fixed. In order to set a correct inlet boundary condition, they varied the radial strain rate at z_0 = 0 mm until their simulated temperature profile matched the experimental one. A different approach is addressed in this work, and is illustrated in Figure III.7. The temperature profiles of two different cool flames were measured, respectively at the condition ϕ = 0.3, α = 20 s^{-1}, x_{O3} = 1.1%, considered as a 'low strain rate' condition, and at the condition ϕ = 0.3, α = 50 s^{-1}, x_{O3} = 2.0%, considered as a 'high strain rate' condition. Both temperature profiles were simulated using the AramcoMech 1.3 model [146] coupled with an ozone sub-mechanism from Halter and co-workers [219]. The choice and relevance of the kinetic models will be discussed later in

chapters IV and V. The flame front positions, measured in both conditions without the presence of the thermocouple, were measured using CH_2O-PLIF. When α = 20 s^{-1}, the predicted maximal flame temperature is overpredicted by roughly 90 K, far beyond the experimental uncertainty. Moreover, the flame front position is measured ~ 1.5 mm below the position at which the maximal cool flame temperature is reached. On the other hand, when α = 50 s^{-1}, the simulated flame temperature is fairly well predicted by the kinetic model, as well as the position at which the maximal flame temperature is reached. Finally, the simulated flame front position measured by PLIF agrees also well with the experimental measurement. It was recently highlighted by Pejpichestakul and co-workers [220] that, for laminar premixed ethylene/air sooting flames, buoyancy effect could greatly affect the flame at low strain rates. These effects are particularly important at low inlet velocities and/or important plate height – burner diameter, L/D, ratio. It was hypothesized that buoyancy effect could intervene in the 'low strain rate' cases, causing this shift of the cool flame towards the heated plate. This assumption is also supported by the lower maximum temperature reached after the flame front in the 'low strain rate' case when compared to the 'high strain rate' cool flame, as buoyancy effect tends to accelerate the burnt gases velocity. Buoyancy effect was further assessed by calculating Froude numbers of 'high strain rate' flames.

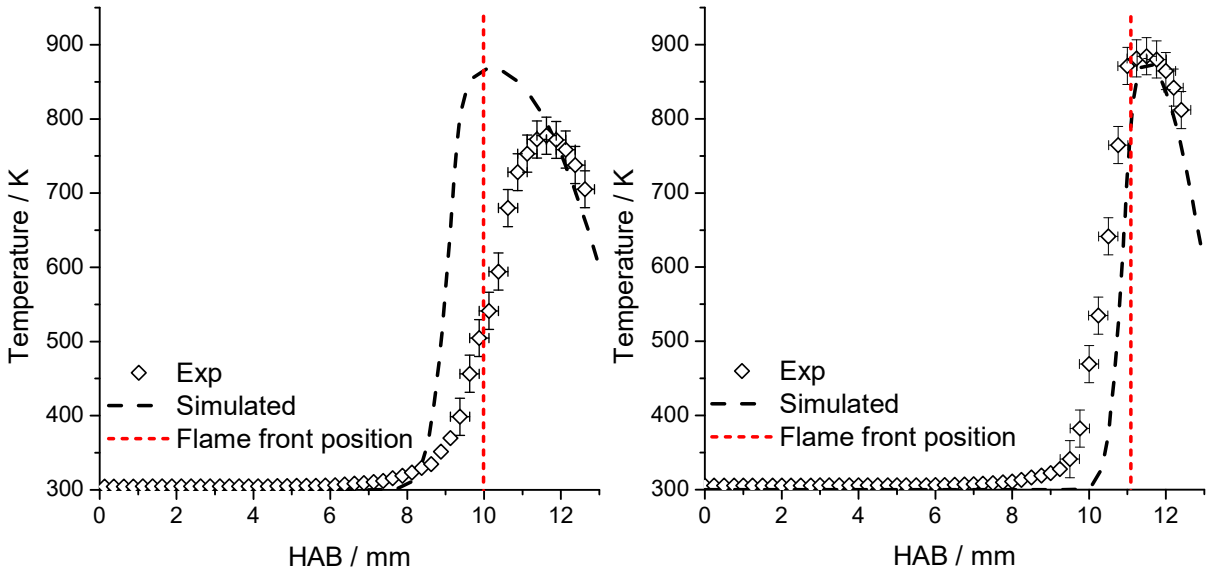

Figure III.7. Experimental and simulated temperature profiles at ϕ = 0.3, α = 20 s^{-1}, x_{O3} = 1.1% (left-hand side) and ϕ = 0.3, α = 50 s^{-1}, x_{O3} = 2.0% (right-hand side).

The dimensionless Froude number, Fr, which is defined as the ratio of the flow inertia to the external field, was calculated:

$$Fr = \frac{u^2}{g \cdot L}$$

where u is the flow velocity, g the gravitational acceleration (9.8 $m \cdot s^{-2}$) and L a characteristic length of the studied system. If the Froude number is consistently inferior to unity (Fr < 1) then the flow is considered as subcritical and external forces (generally gravity) dominate. In the other sense, if Fr > 1, the flow is said to be supercritical and inertia dominates the flow behaviour.

In the case of stabilized laminar cool flames in a stagnation flow, two different flow velocities were considered: i) the minimum velocity reached before the flame front, and ii) the inlet flow rate (HAB = 0 mm). The characteristic length L is the flame front thickness. While the minimum and inlet velocities could be measured using the PIV technique, the flame front thickness was determined using the CH_2O-PLIF profile. The axial velocity of 'low strain rate' flames could not be measured, the Froude number are therefore only calculated for two conditions at $\alpha = 40\ s^{-1}$ and $\alpha = 50\ s^{-1}$, at $\phi = 0.5$ and x_{O3} = 1.5% for both conditions. The results are summed up in Table III.2, including the estimated flame thickness, the cool flame velocity and the associated Froude number. Considering both velocities, the calculated Froude numbers are seen to be consistently greater than 1, which also supports the assumption that buoyancy effects are less influent at high strain rates.

Table III.2. Experimental conditions for Froude number determination at high strain rates.

Cool flame condition	Flame thickness / µm	Flow velocity / $cm \cdot s^{-1}$		Froude number	
		Minimum	Inlet	Minimum	Inlet
$\phi = 0.5$, x_{O3} = 1.5%, **$\alpha = 40\ s^{-1}$**	600	17.0	74.4	4.9	141
$\phi = 0.5$, x_{O3} = 1.5%, **$\alpha = 50\ s^{-1}$**	400	15.7	95.4	6.3	154

Regarding the effect of strain rate on the cool flame stabilization, and potential influence of buoyancy, only cool flames with strain rates $\alpha > 40\ s^{-1}$ were considered for kinetic studies (Chapter IV) and flame speed measurements (Chapter V). Cool flames with lower strain rates were discarded for these studies, but were however used for parametric studies that are presented hereafter.

In addition to buoyancy effects that affect the cool flame stabilization, it is expected that the co-flow rate of nitrogen may impact the flame. In the previous cited study from Pejpichestakul and co-workers [220], the reactive mixture velocity in the centre of the burner is consistently inferior to the co-flow velocity, respectively $u_{mixture}$ = 5.87 $cm \cdot s^{-1}$ and $u_{co\text{-}flow}$ = 21 $cm \cdot s^{-1}$. In such case the nitrogen co-flow could constrain the inlet velocity field of the reactive mixture in the centre of the burner, resulting in a deviation when compared to 1-D modelling in which the effect of the nitrogen co-flow is not considered. Thus, even if in our conditions the inlet flow rates are not as low as those used by Pejpichestakul and co-workers, the influence of the nitrogen co-flow was also investigated.

III.4. Influence of the nitrogen co-flow

The influence of the nitrogen co-flow was investigated through two different aspects, i) its influence on the flame position in the burner and ii) its influence on the flame axial velocity profile. As a starting point, it was chosen to set the velocity of the nitrogen co-flow equal to the velocity of the mixture in the centre of the burner such as:

$$u_{Fuel/O_2/O_3} = u_{N_2} \Leftrightarrow \frac{\dot{Q}_{Fuel/O_2/O_3}}{\frac{\pi d_{in}^2}{4}} = \frac{\dot{Q}_{N_2}}{\frac{\pi\left(d_{out}^2 - d_{in}^2\right)}{4}}$$

where d_{in} is the internal diameter of the burner and $d_{in,co\text{-}flow}$ the internal diameter of the co-flow nozzle. The condition at which the velocity of the nitrogen co-flow is equal to the velocity of the reactive mixture will be noted as '100% N_2'.

III.4.1. Influence on the flame front position

Co-flow impact on the cool flame position was investigated. Cool flames conditions were selected for different strain rates ranging from 10 to 50 s^{-1}. Then, the nitrogen co-flow was set at its initial value ('100% N_2') and progressively decreased until reaching 5% of its initial value. The cool flame position was measured at each step using CH_2O-PLIF, and the obtained results are presented below in Figure III.8, while the flow rates corresponding to each experimental condition are given in Appendix III.A8. The corresponding CH_2O-PLIF profiles, for each condition, are provided in Appendix III.A9. In the left-hand side graph the evolution of the flame front position is plotted at α = 20 s^{-1}, equivalence ratios varying between 0.25 and 0.55, and ozone concentrations varying between 1.2 and 1.7%. In every studied case, the flame front position decreases for N_2 flow rates between 50% and 100% of its initial value. At 40% and lower values, the flame front position does not vary significantly. The same trend can be observed in the right-hand side graph, which represents the evolution of the flame front position as a function of the N_2 flow rate for different cool flames conditions, the strain rate varying between 10 s^{-1} and 50 s^{-1}. High-strain rate cool flames, at α = 40 s^{-1} and α = 50 s^{-1}, could not be stabilized at N_2 flow rates superior to 40% of its initial value. The flame front position at α = 40 s^{-1} is fairly insensitive to the co-flow rate variations while it slightly varies at α = 50 s^{-1} between 20% and 40% of its initial value. It is suggested that confinement induced by the co-flow on the flame increases as its flow rate increases, resulting in a lowered position of the flame front in the burner. It is however expected that at low N_2 flow rates this phenomenon does not influence anymore the cool flame, explaining that the position remains constant. It was thus decided to set the co-flow rate at 20% of its initial value, ensuring both the stability of cool flames as well as a negligible effect on its position in the burner.

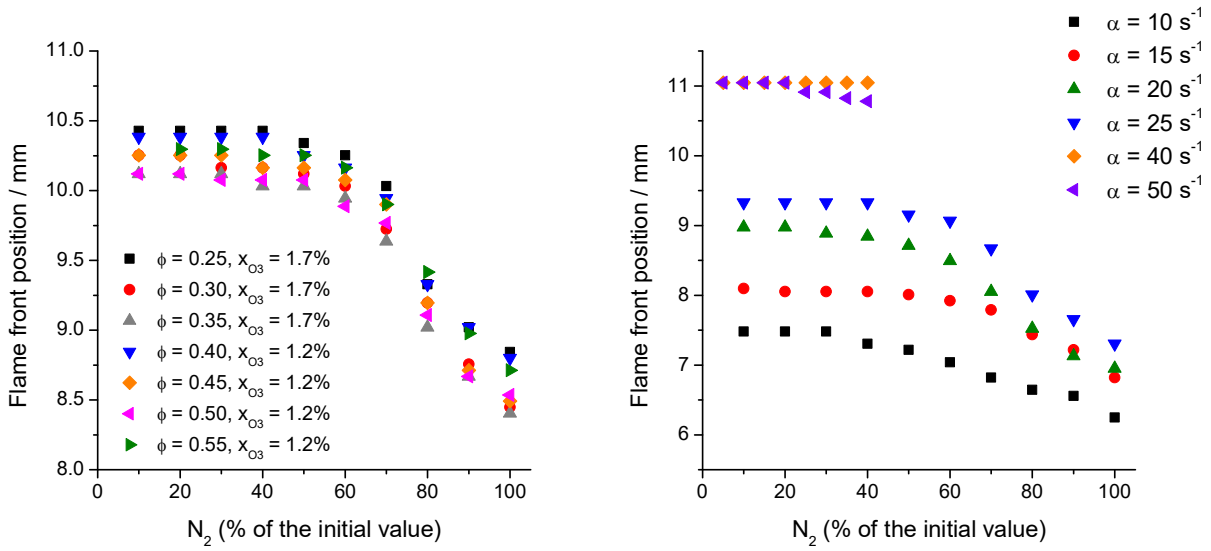

Figure III.8. Evolution of the flame front position at a fixed strain rate, $\alpha = 20\ s^{-1}$, for different equivalence ratios and ozone concentrations (left-hand side), and at different strain rates (■ $\alpha = 10\ s^{-1}$, $\phi = 0.07$, $x_{O3} = 3\%$; ● $\alpha = 15\ s^{-1}$, $\phi = 0.1$, $x_{O3} = 3\%$; ▲ $\alpha = 20\ s^{-1}$, $\phi = 0.14$, $x_{O3} = 3\%$; ▼ $\alpha = 25\ s^{-1}$, $\phi = 0.19$, $x_{O3} = 3\%$; ♦ $\alpha = 40\ s^{-1}$, $\phi = 0.5$, $x_{O3} = 1.6\%$ and ◄ $\alpha = 50\ s^{-1}$, $\phi = 0.5$, $x_{O3} = 1.8\%$) (right-hand side).

III.4.2. Influence on the axial velocity profile

The influence of the N_2 co-flow was also investigated by means of PIV measurements. Only one condition was selected for this measurement, at $\alpha = 50\ s^{-1}$, which was also presented in Figure III.8. The axial velocity profiles were measured for N_2 co-flows ranging from 40 to 5% of its initial value, and the results are presented in Figure III.9. Varying the N_2 flow rate slightly influences the axial velocity profile. As the flow rate increases from 5 to 40%, the axial velocity profiles seem to tend towards a potential flow, characterized by a non-zero velocity gradient at the inlet of the burner. Such a variation of the flow behaviour is of importance regarding the simulation of the burner, as it can greatly affect the cool flame characteristics (temperature, propagation speed, etc.). The insert in Figure III.9. represents the evolution of the reference velocity of the cool flame, i.e., the minimal velocity upstream the flame front (see Chapter V for further details), as a function of the nitrogen flow rate. For N_2 flow rates varying from 40 to 20% of its initial value the reference velocity significantly decreases, while it remains roughly constant at lower N_2 flow rates. This result is consistent with the flame front position variations observed previously, as a lower flame velocity results in a higher flame position.

Considering both results from PIV and CH_2O-PLIF measurements, the nitrogen flow rate was fixed at 40% of its initial value for the 'low strain rate' conditions, i.e., $10 \leq \alpha \leq 25\ s^{-1}$, and 20% for the 'high strain rate' conditions, i.e., $\alpha = 40$ and $\alpha = 50\ s^{-1}$.

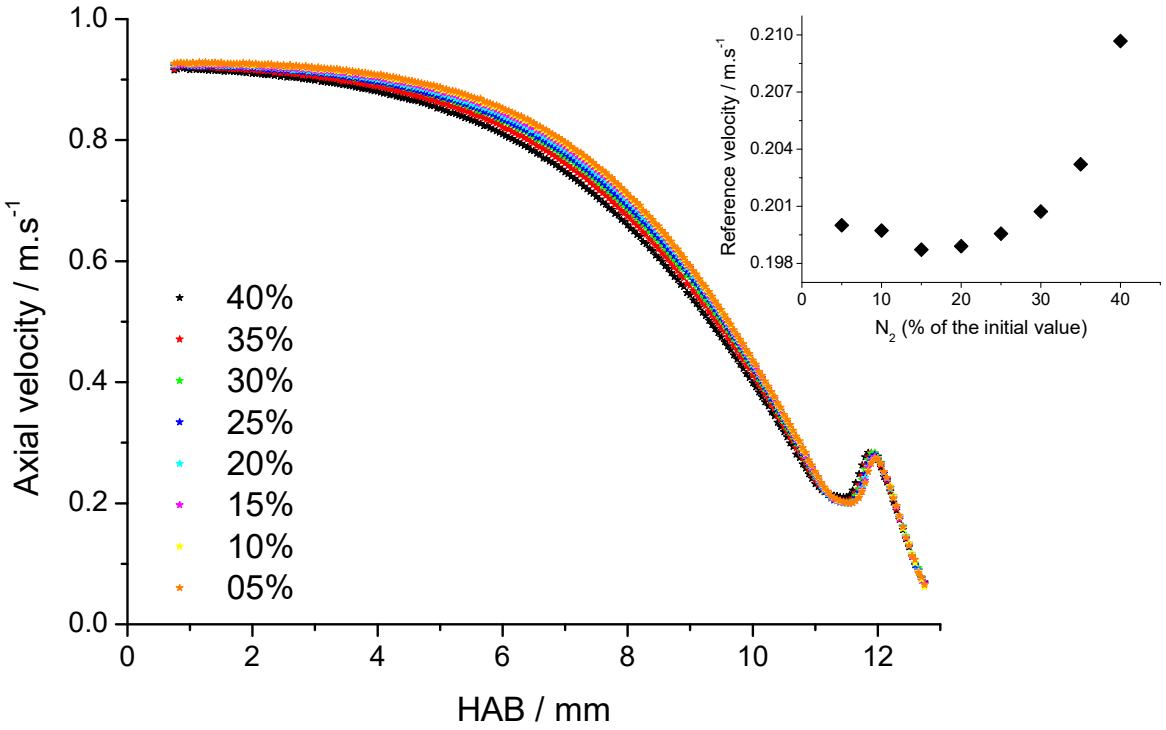

Figure III.9. Axial velocity profiles of a cool flame at different N_2 flow rates. Insert: Variation of the cool flame reference velocity at different N_2 flow rates.

III.5. Species mole fraction modelling

III.5.1. Description of the problematic

As presented in Section II.5, sampling along the cool flame is realized by placing the capillary horizontally, perpendicular to the burner exit, the tip of the capillary lying along the burner axis. In this case the capillary does not cross the flame when sampling gases in the upstream area of the flame, avoiding reactivity in the capillary at low HABs. As previously presented in Figure II.24 (Section II.5.3.1), when the capillary is placed at the horizontal the ozone conversion starts roughly 1.5 mm before the flame front position that was measured using CH_2O-PLIF. While it is expected that ozone decomposes slightly before the flame front, such an important difference on the position was not expected. Moreover, when measuring the fuel mole fraction profile in ozone-seeded cool flames, it was observed that the fuel conversion happened in a two-step process along the HAB. As an example, DME and ozone conversion through a DME/O_2/O_3 cool flame at $\phi = 0.3$, $\alpha = 50$ s^{-1}, $x_{O3} = 2.0\%$ is shown in Figure III.10, along with the CH_2O^* signal (treated with the Abel inversion method) indicating the position of the flame front. In this condition, the DME and O_3 concentrations are constant upstream the cool flame, until they first decrease at HAB ~ 8 mm. While the ozone is entirely consumed between HAB = 8 and 9 mm, DME is partially converted, and its mole fraction profile forms a plateau until approximately HAB = 11 mm. After 11 mm a second conversion step happens, before reaching a second plateau in which the DME concentration remains constant until the plate is reached. It should be noted that the position at which the ozone decomposition takes place corresponds to the first conversion step

of the fuel, around HAB = 8 mm, which is located 3 mm before the flame front position indicated by the CH_2O*-chemiluminescence signal. This is not consistent with the measured temperature profile that indicates a temperature nearly equal to 300 K at this HAB. It was thus hypothesized that this phenomenon was not related to the fuel conversion in the cool flame, but was relative to the conversion of reactants inside the sampling capillary. In the stagnation plate configuration, the flame is represented as a flat axisymmetric flame. As the capillary is placed horizontally, its body is placed inside a zone where the burnt gases recirculate, which will heat it and cause premature ozone conversion.

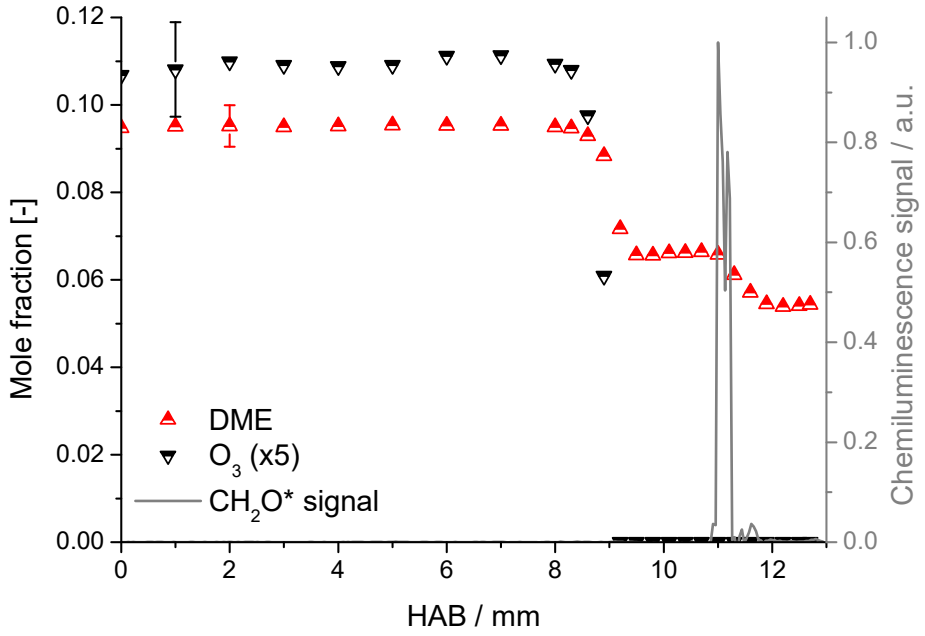

Figure III.10. Experimental DME (black points) and ozone (red points) mole fraction profile, and chemiluminescence signal (red line) of a DME/O_2/O_3 cool flame. ϕ = 0.3, α = 50 s^{-1}, x_{O3} = 2.0%.

A numerical solution to account for such a phenomenon in the simulation of the burner has been proposed and is presented in the following sections.

III.5.2. 2-D temperature map

In order to draw a 2-D temperature map in the burner, temperature profiles (as a function of the HAB) were measured at different radial positions from the burner centre, using the same thermocouple as the one used for the centreline temperature measurements. The selected flame is the same as the one shown in Figure III.10, i.e., ϕ = 0.3, α = 50 s^{-1}, x_{O3} = 2.0%, and its two-dimensional temperature map is pictured in Figure III.11. The radial position x = 0 indicates the centre of the burner, and the arrows indicate the radial positions at which the temperature profiles were measured. As the flame is flat, the temperature is constant until 5 mm away from the axis of the burner, the scattering being attributed to the measurement uncertainties using the 250 µm type-K thermocouple. However, at greater distances from the burner, the presence of the plate causes the burnt gases to recirculate on the side of the burner and leads to the formation of a 'warm area' at a lower HAB than the flame front position. In this area,

the temperature varies from ~ 360 to 540 K, depending on the height above the burner. As ozone quickly decomposes at temperatures above 450 K, it is thus highly probable that it decomposes in the sampling capillary at such HAB. Following Figure III.10, the ozone decomposition starts at a HAB ~ 8 mm, which is the position at which the temperature on the side of the burner exceeds 450 K. This observation supports the assumption that ozone decomposition in the capillary is triggered by recirculating gases heating the sampling capillary.

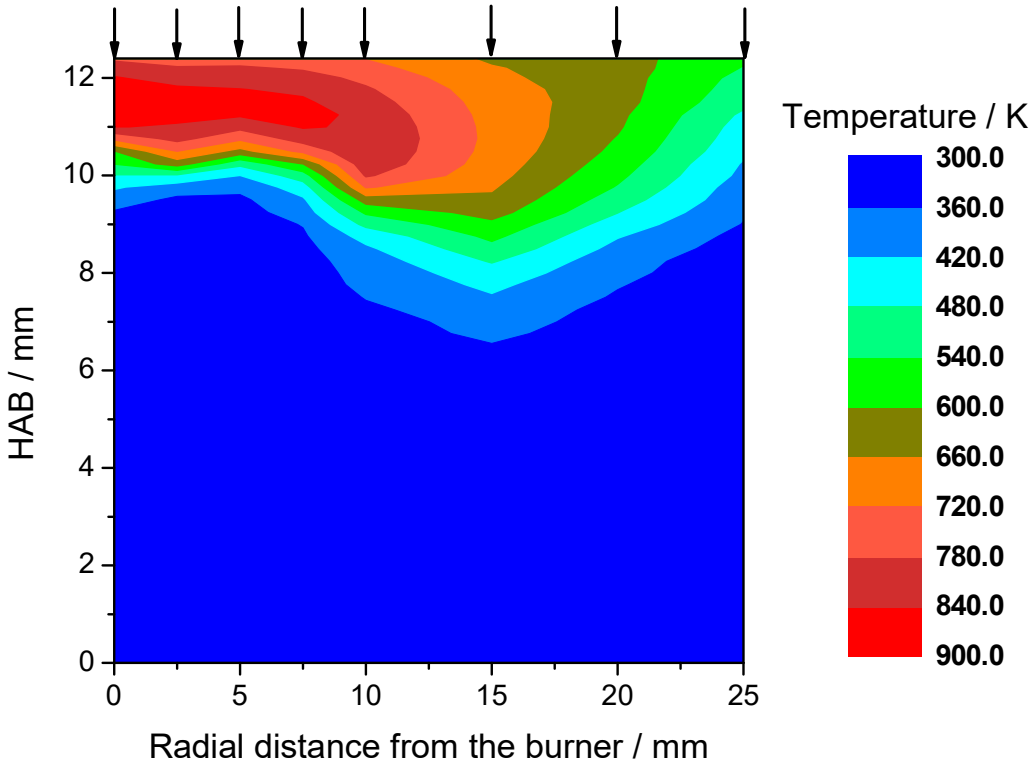

Figure III.11. 2-dimensional temperature map of a cool flame at $\phi = 0.3$, $\alpha = 50\ s^{-1}$, $x_{O3} = 2.0\%$.

This assumption was confirmed through kinetic modelling of the reactivity inside the capillary, as demonstrated in the next section.

III.5.3. Capillary modelling

The sampling capillary was simulated as a plug-flow reactor (PFR). The flow conditions were fixed by following the work from Wißdorf and co-workers [221]. The flow in the capillary was considered turbulent, and its flow rate was estimated as follow [222]:

$$Q_{turbulent} = d\left(0.39\pi^2 \cdot \frac{d^3(p_0^2 - p_1^2)}{2l}\right)^{\frac{4}{7}} \cdot \left(\frac{R}{M \cdot T_0}\right)^{\frac{3}{7}} \cdot \left(\frac{4}{\pi \cdot \eta}\right)^{\frac{1}{7}} \cdot \frac{1}{p_0}$$

where d is the internal diameter of the capillary, l its length, p_0 and p_1 are respectively the pressure at the capillary entrance and outlet, M is the molar mass of the mixture, T_0 is the temperature at the capillary entrance and η the dynamic viscosity of the fluid.

First, the cool flame is simulated along the burner centreline using the conventional 1-D solver. Then, temperature & gas composition are extracted at axial positions corresponding to the spatial resolution of the axial temperature profile and used as an input for the PFR calculations. The radial temperature profiles, which were only measured every 240 and 260 µm, are interpolated linearly so that each simulated point on the axial axis of the burner corresponds to a radial temperature profile. The results of such a simulation are plotted in Figure III.12. for the reactants, respectively DME and O_3. Considering the reactivity inside the capillary allows to fairly reproduce the position above the burner at which both reactants are consumed. The PFR simulation does however not consider surface reactions of ozone, which can be an important process inside the capillary. Therefore, it is expected that the reactivity inside the capillary is highly overestimated, leading to a 'worst-case' scenario. It can be witnessed by the significant overestimation of the DME conversion in the region 8 < HAB < 11 mm, in which the agreement on the species mole fraction cannot be expected to be quantitative. From these simulations it can also be seen that sampling DME/O_2/O_3 mixtures at ambient temperature (condition met at HAB < 8 mm) does not induce any pre-reactivity in the capillary. Considering the reactivity inside the capillary however allows us to demonstrate:

- that the reactivity observed upstream the flame front is due to the presence of ozone-rich mixtures inside the capillary. Such phenomenon was previously reported by Hajilou and co-workers for DME/O_2/O_3 mixtures [49] and C_3H_8/O_2/O_3 mixtures [50]. They attributed the early conversion of the fuel at low HABs as some auto-reactivity of the mixture, but it seems that the authors met a similar phenomenon as the one presently explained.

- that since both simulation approaches lead to comparable results downstream the flame front, that is, within the experimental uncertainty limits, the post-flame species mole fractions can be trusted to build useful kinetic analysis.

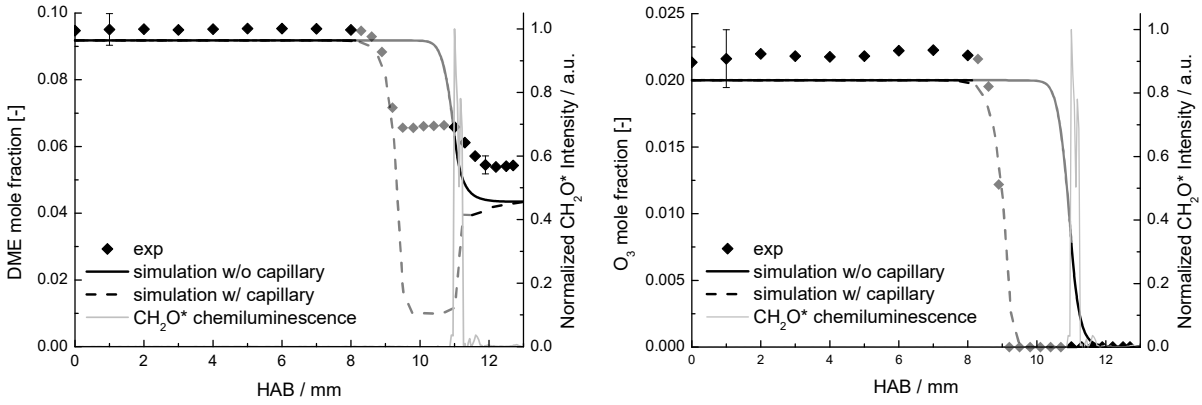

Figure III.12. DME (left-hand side) and O_3 (right-hand side) mole fraction profiles simulated with and without the sampling effect. Experimental conditions are the same than in Figure III.10 and III.11, i.e., $\phi = 0.3$, $\alpha = 50\ s^{-1}$, $x_{O3} = 2.0\%$.

III.6. General conclusions

The aim of this third chapter was first to introduce the cool flame stabilization procedure in the stagnation plate burner. Stable cool flames were successfully obtained in a wide range of experimental conditions (strain rate, ozone concentration, equivalence ratio, etc.) showing the convenience of such experimental configuration to study cool flames. The simulation of the stagnation plate burner was then addressed. The feasibility of simulating cool flames in a stagnation plate burner using a one-dimensional code was discussed regarding the different effects that could intervene in the experiments, while not being considered in the simulation. Finally, the simulation of the species mole fraction profiles regarding the ozone decomposition in the sampling capillary was discussed, showing that perturbations in the measurement caused by the sampling capillary could be explained.

All of these verifications were necessary in order to proceed to kinetic studies of different ethers. The first one that was studied is dimethyl ether, and is presented in the next section.

Chapter IV. Low-temperature oxidation of ethers in cool flames

IV. Low-temperature oxidation of ethers in cool flames

The hereby chapter discusses the low-temperature oxidation of three ethers, namely dimethyl ether (DME), diethyl ether (DEE) and oxymethylene ether-2 (OME-2), in cool flames.

IV.1. Study of dimethyl ether LTC

The low-temperature combustion kinetics of dimethyl ether in the stagnation plate burner was studied by coupling CH_2O*-chemiluminescence, CH_2O-PLIF, temperature and species mole fraction measurements. The experimental results were compared to simulations obtained using two different models that are presented hereafter. These experimental results were published in the Journal of Physical Chemistry A in July, 2021 [223]. The simulations are however slightly different from those shown in the published article as a different ozone-submechanism was used in the present case.

IV.1.1. Kinetic modelling

IV.1.1.1. Dimethyl ether submechanism

Many different kinetic mechanisms describing the low-temperature oxidation of dimethyl ether were developed in the past two decades, and were summed up in Section I.4.1. It is not the objective, within this work, to develop a new model from a fresh start. Thus, an existing mechanism was chosen in order to simulate the newly acquired experimental data. Among the available kinetic mechanisms, AramcoMech 1.3 [146] was selected as it showed the best capacity in predicting the occurrence of cool flames in our conditions. In the tested conditions this model is the only one being able to systematically predict a cool flame, while the other tested models mainly converge towards hot flames, or do not predict sufficient reactivity to form a cool flame. This is illustrated in Appendix IV.A1. in which the cool flame occurrence is presented in different conditions using different models from the literature. In order to give some insight into such disparity, the first-stage and ignition delay times of DME/O_2/O_3 mixtures were simulated with a constant volume reactor code using different kinetic models. The simulated condition was chosen to be the closest from our cool flame experimental conditions, and is $\phi = 0.3$, $x_{O3} = 2.0\%$. The used models were respectively AramcoMech 1.3 [146], AramcoMech 3.0 [148], Burke and co-workers [144], Dames and co-workers [145], HP-mech v3.3 [46], NUIG 1.1 [149] and Wang and co-workers [124]. An ozone-submechanism from Halter and co-workers [219] was added to each of these models (except the HP-mech v3.3, which already contains an ozone submechanism). The simulated results are plotted in Figure IV.1. Above 550 K every tested model yields roughly similar ignition delay times, AramcoMech 1.3 being the slowest at 700 K while the model of Wang and co-workers predicts the fastest ignition delay times. A greater disparity however emerges below 550 K, the AramcoMech 1.3 predicting the shortest first-stage ignition delay times in this temperature domain while every other model predicts significantly higher first-stage ignition delay times. The model from Burke and co-workers also predicts shorter first-stage ignition delay times, which are however more or less one order of magnitude higher than the ones predicted by the AramcoMech 1.3 model.

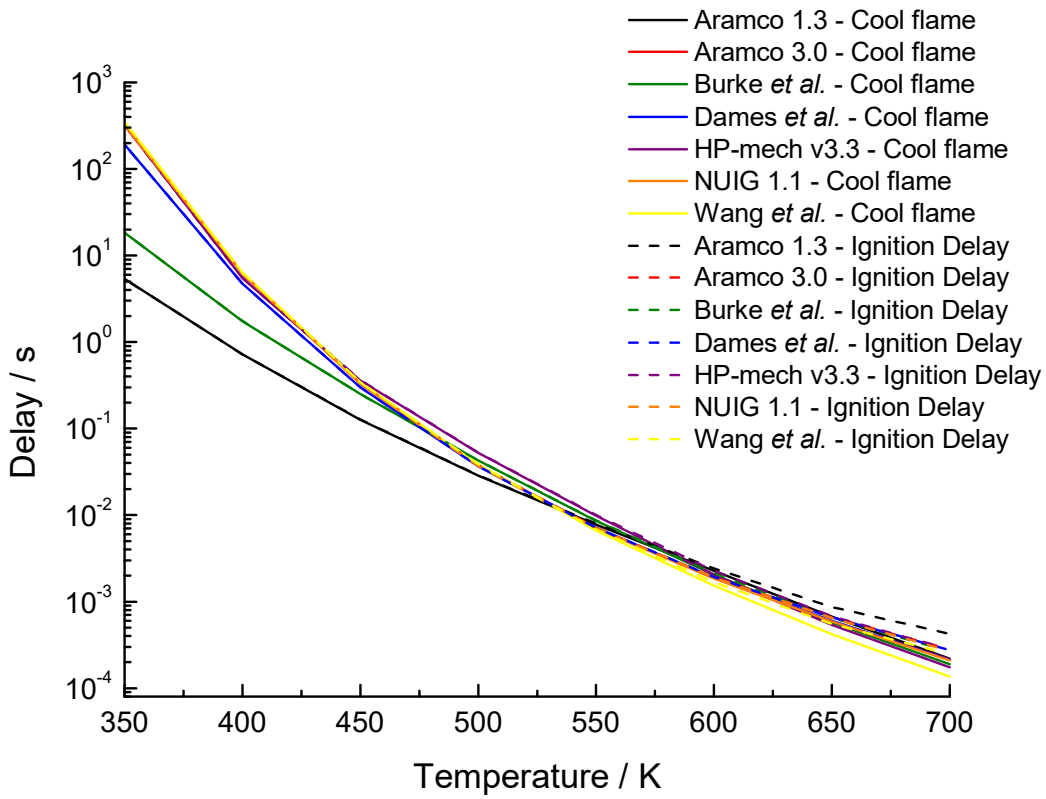

Figure IV.1. Cool flame and ignition delay time of a DME/O_2/O_3 mixture (ϕ = 0.3, x_{O3} = 2.0%) using various kinetic models from the literature.

While simulating ignition delays and cool flames are two very different things, it is believed that the graph plotted in Figure IV.1. gives us important information on ozone-assisted reactivity. As shown in jet-stirred reactors [63,79] the ozone addition shifts the onset temperature at which the fuel conversion starts to lower temperatures. It is also expected that at a constant temperature the ignition delay time of a reactive DME/O_2 mixture is shortened when ozone is added. This shift to lower temperatures induces that the chemistry governing the combustion phenomenon is also modified, i.e., some reactions that are generally not influent without ozone will become influent. This is notably the case for some biradical reactions that are usually encountered in atmospheric kinetic studies, as discussed later in this chapter. Nevertheless, it is assumed that the reason behind the excellent cool flame occurrence predictions by the AramcoMech 1.3 model (allowing to simulate a cool flame corresponding to every experimental condition) is somehow linked to this secondary chemistry which is generally overlooked in combustion studies.

The AramcoMech 1.3 model is mostly suited for oxygenated and non-oxygenated hydrocarbons with up to two carbons in their molecular structure. It is composed of 257 different species, yielding 1557 reactions. The base-model was slightly modified, and the modifications are summed up in Table IV.1. Such motivations were necessary as AramcoMech 1.3 failed in accurately describing the gas-phase

composition downstream the cool flame, which is detailed in Section IV.1.4. Modified or added reactions rate constants parameters were taken from past-work from the literature.

Concerning first the added reactions to the kinetic model, the Ö-atom addition to methyl radical and methoxymethyl radical, $CH_3O\dot{C}H_2$, rate constants were respectively taken from Hardin and co-workers [224] and Song and co-workers [225], and were added as the formation of O-atoms from ozone decomposition plays an important role in ozone-seeded cool flames. Dimethyl ether roaming reactions forming either methanol and a carbene or methane and formaldehyde rate constants were respectively taken from Döngten and co-workers [226] and Yasunaga and co-workers [227]. Reaction rate constants of methoxymethyl radical with $HO\dot{O}$ forming a methoxymethoxy radical and a hydroxyl radical were taken from the work of Wang and co-workers [124], and the rate constant of the reaction between methoxymethyl radical and methoxymethylperoxy radical, $CH_3OCH_2\dot{O}_2$, forming two methoxymethoxy radicals $CH_3OCH_2\dot{O}$ was taken from Keiffer and co-workers [228]. Both reaction rates of methoxymethoxy radical β-scissions leading to the formation of methyl formate, and the reaction of DME with the methoxy radical forming a methoxymethyl radical and methanol, were taken as analogies to the dimethoxymethane mechanism from Vermeire and co-workers [229].

Concerning now the modified rate constants, the rate constants of $CH_3OCH_2\dot{O}_2$ and $\dot{O}_2CH_2OCH_2O_2H$ radicals H-atom internal migrations, and DME β-scission forming both methyl and methoxymethyl radicals, were modified following recent work from Konnov and co-workers [230]. The submechanism of methyl formate was modified using the work from Minwegen and co-workers [231]. The rate constant of the self-reaction of methoxymethylperoxy radical yielding two methoxymethoxy radicals and molecular oxygen was taken from Rosado-Reyes and co-workers [232]. Finally, the decomposition of methoxymethoxy radical in methyl formate and H-atom was modified following the work from Wang and co-workers [124].

Table IV.1. Modified or added rate constants to the AramcoMech 1.3 model.

Reaction		A	n	Ea	k[d]	Reference
Added						
$\dot{C}H_3 + \ddot{O} = CH_3\dot{O}$		$5.54 \cdot 10^{13}$	0.05	-32		[224]
CH_3OCH_3 (+M) = $CH_3OH + \ddot{C}H_2$ (+M)		$9.03 \cdot 10^{13}$	0.00	84083		[226]
CH_3OCH_3 (+M) = $CH_4 + CH_2O$ (+M)		$1.00 \cdot 10^{14}$	0.00	65200		[227][a]
$CH_3O\dot{C}H_2 + HO\dot{O} = CH_3OCH_2\dot{O} + \dot{O}H$		$9.00 \cdot 10^{12}$	0.00	0		[124]
$CH_3O\dot{C}H_2 + CH_3OCH_2O\dot{O} = 2\ CH_3OCH_2\dot{O}$		$5.08 \cdot 10^{12}$	0.00	-1411		[228]
$CH_3OCH_2O\dot{O} = CH_3OCHO + \dot{O}H$		$2.82 \cdot 10^{6}$	1.97	34895		[229][b]
$CH_3OCH_3 + CH_3\dot{O} = CH_3O\dot{C}H_2 + CH_3OH$		$2.24 \cdot 10^{12}$	0.00	19646		[229][b]
$CH_3O\dot{C}H_2 + \ddot{O} = CH_3OCH_2\dot{O}$		$1.00 \cdot 10^{14}$	-0.56	22		[225]
Modified						
$CH_3OCH_2O\dot{O} = \dot{C}H_2OCH_2O_2H$	**p.w.**	$\mathbf{2.73 \cdot 10^{2}}$	**2.332**	**14168**	$\mathbf{5.67 \cdot 10^{3}}$	[230][a]
	AM1.3	$6.00 \cdot 10^{10}$	0.00	21580	$8.26 \cdot 10^{2}$	
$\dot{O}OCH_2OCH_2O_2H = HO_2CH_2OCHO + \dot{O}H$	**p.w.**	$\mathbf{3.86 \cdot 10^{7}}$	**0.98**	**17467**	$\mathbf{8.84 \cdot 10^{3}}$	[230][a]
	AM1.3	$4.00 \cdot 10^{10}$	0.00	18580	$6.82 \cdot 10^{2}$	
CH_3OCH_3 (+M) = $\dot{C}H_3 + CH_3\dot{O}$ (+M)	**p.w.**	$\mathbf{2.33 \cdot 10^{19}}$	**-0.661**	**84139**	$\mathbf{7.60 \cdot 10^{-14}}$	[230][a]
	AM1.3	$4.38 \cdot 10^{21}$	-1.57	83890	$5.25 \cdot 10^{-14}$	
$2\ CH_3OCH_2O\dot{O} = O_2 + 2\ CH_3OCH_2\dot{O}$	**p.w.**	$\mathbf{1.80 \cdot 10^{11}}$	**0.00**	**-1390**	$\mathbf{5.78 \cdot 10^{11}}$	[232]
	AM1.3	$1.55 \cdot 10^{23}$	-4.5	0.00	$4.88 \cdot 10^{10}$	
$CH_3OCH_2\dot{O} = CH_3OCHO + \dot{H}$	**p.w.**	$\mathbf{1.75 \cdot 10^{16}}$	**-0.66**	**11720**	$\mathbf{1.38 \cdot 10^{10}}$	[124]
	AM1.3	$1.00 \cdot 10^{13}$	0.00	7838	$1.40 \cdot 10^{10}$	
CH_3OCHO *submechanism*	**p.w.**	-	-	-		[231][c]

[a]High-pressure limit, [b]Analogy from dimethoxymethane, [c]Full sub-mechanism added, [d]Calculated at 600 K for comparison between the old and new Arrhenius parameters. A and E_a units are: cm^3, mol, s, $cal \cdot mol^{-1}$. AM1.3 means AramcoMech 1.3, p.w. stands for « present work »

IV.1.1.2. Ozone submechanism

Few ozone submechanisms exist within the literature, namely published by Halter and co-workers [219], Zhao and co-workers [63] and more recently by Jian and co-workers [233]. These models include the reaction rates of the ozone decomposition and recombination. The choice of the ozone submechanism was done following two aspects, respectively the prediction of the cool flame temperature and the cool flame propagation speed. These aspects will be discussed in detail in Chapter V, dedicated to cool flame propagation speed measurements. For the following simulations in this chapter the ozone submechanism of Jian and co-workers is systematically used.

IV.1.2. Cool flame temperature

IV.1.2.1. Temperature profiles

Since one of the purposes of studying low-temperature combustion kinetics of ethers inside cool flames is the quantification of the heat release, temperature profiles were measured and simulated in different conditions. The experimental procedure was presented in Section II.4. Since temperature profiles are not used as an input in cool flame simulations, it is important that models are able to accurately predict the cool flame heat release, as it will also affect the simulated species mole fraction profiles. A typical temperature profile is shown in Figure IV.2. and was measured in a $\phi = 0.3$, $\alpha = 40$ s^{-1}, $x_{O3} = 1.8\%$, cool flame. The chemiluminescence signal, post-processed using the Abel inversion

method, is also plotted in red, and indicates the flame front position. The simulated profiles using both AramcoMech 1.3 and its modified version, named 'current model' hereafter, are also plotted.

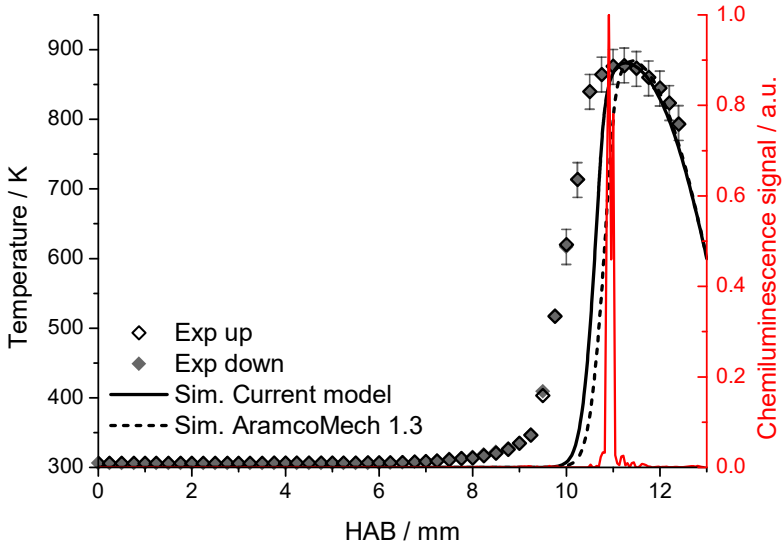

Figure IV.2. Experimental and simulated temperature profiles of a cool flame, $\phi = 0.3$, $\alpha = 40\ s^{-1}$, $x_{O3} = 1.8\%$.

Comparison between simulated and experimental temperature profiles shows a close agreement on the maximal temperature of the cool flame, which does not exceed 900 K in this case. The position at which this maximal temperature is reached is also closely reproduced by both models. Downstream the flame front, the temperature decrease under the plate is captured within the experimental uncertainty. No significant change in the temperature profile can be observed between the AramcoMech 1.3 model and the current model, except that the flame front position, indicated by the position of the temperature rise, is predicted at a slightly lower position with the current model. The largest discrepancy between the experimental and simulated profiles can be observed upstream the flame front, where perturbation of the flame by the thermocouple is evidenced by comparing the experimental temperature profile and the chemiluminescence signal. It results in a steeper temperature gradient in the simulation in comparison with the experiment.

The cool flame temperature profiles were measured at different equivalence ratios and ozone concentrations at $\alpha = 40\ s^{-1}$ and $\alpha = 50\ s^{-1}$, and are plotted in Figure IV.3 along with the simulated profiles using both AramcoMech 1.3 and the current model. One can observe that the six temperature profiles lead to similar results, the maximal temperature reached after the cool flame being systematically between 875 and 890 K. In non-isothermal experiments the increase of the temperature induces a loss of competitivity of the low-temperature branching against propagation or termination reactions. As a consequence, the reactivity decreases. This phenomenon is known as the NTC, Negative Temperature Coefficient, and was introduced earlier in this manuscript. In the current configuration, the same cause results in an interruption of the low-temperature reactivity downstream the cool flame, where

the temperature reaches a maximum between the flame front and the stagnation plate. This prevents the cool flame from triggering high-temperature ignition and forming a hot flame. The simulated cool flame temperature profile of each condition gives an excellent agreement, well within the experimental uncertainty, whatever the used model.

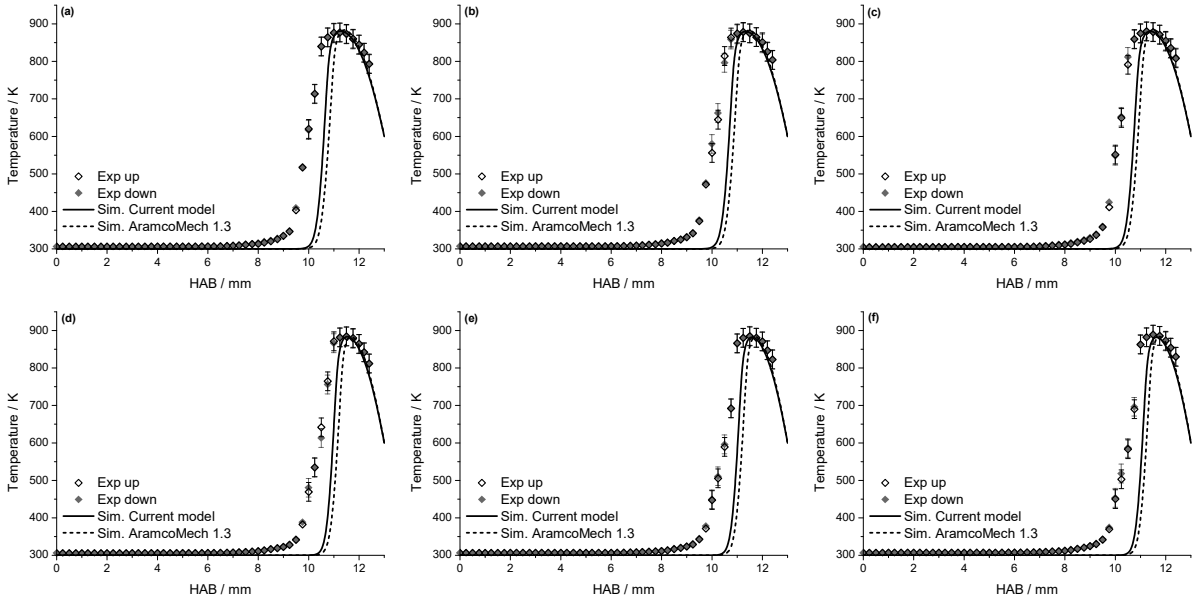

Figure IV.3. Experimental & numerical temperature profiles at 40 s^{-1} (ϕ = 0.3, x_{O3} = 1.8% (a), ϕ = 0.4, x_{O3} = 1.6% (b), ϕ = 0.5, x_{O3} = 1.5% (c)) and 50 s^{-1} (ϕ = 0.3, x_{O3} = 2.0% (d), ϕ = 0.4, x_{O3} = 1.8% (e), ϕ = 0.5, x_{O3} = 1.7% (f)).

IV.1.2.2. Ozone influence on cool flame temperature

The ozone influence on the cool flame was investigated using temperature measurements. It is known that ozone highly influences the NTC behaviour of the fuel, as demonstrated in JSR by Liao and co-workers [79], or in HCCI engine by Foucher and co-workers [75]. It is thus interesting to study how ozone-addition can modify the cool flame heat release.

Firstly, the entire temperature profile of 'low strain rate' cool flames with different ozone concentrations were measured, and are plotted on the left-hand side in Figure IV.4. The strain rate and the equivalence ratio were kept constant in order to solely investigate the effect of ozone. Its influence is illustrated by two major effects. One can see that the cool flame temperature increases while the ozone concentration increases from 1.0% to 1.3%, signifying an increase of the heat released. Moreover, the cool flame position tends to move towards the burner as the ozone concentration increases. This suggests that the cool flame propagation speed is also increased by the addition of ozone, supporting the simulations of Ju and co-workers [43]. These results were not modelled, accordingly to buoyancy issues that were addressed in Section III.3. Secondly, the maximal temperature after the cool flame front was measured at higher strain rates, α = 40 s^{-1} and α = 50 s^{-1}, and compared with the simulated results using both models in the right-side in Figure IV.4. In accordance with the previous observations, an increase

of the ozone concentration in the cool flame results in an increase of its temperature. This increase is here almost linear, and is roughly equal to 15 K per 0.1% of ozone added in the mixture, in both cases. Both models are able to capture this trend, even if at low ozone concentrations the cool flame temperature is systematically overpredicted. The current model gives slightly better results, especially at the highest ozone concentrations. It suggests that the current model better captures the cool flame chemistry in the presence of an important concentration of ozone in the reactive mixture, possibly linked to the modification of chain propagation reactions rate constant parameters which are more influent in ozone-seeded conditions.

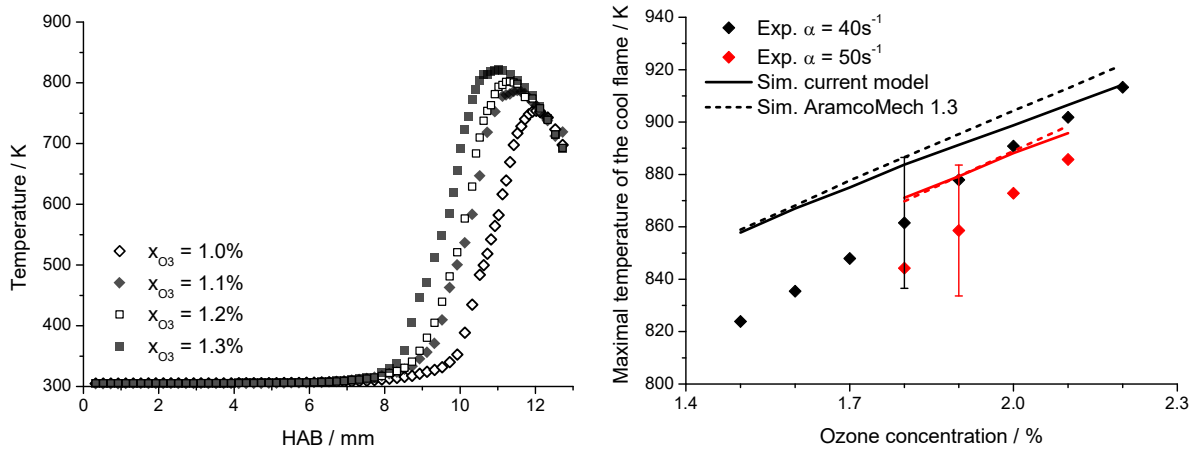

Figure IV.4. Temperature profiles of cool flames seeded with different ozone concentrations at $\alpha = 20\ s^{-1}$, $\phi = 0.3$ (left-hand side) and influence of the ozone concentration on the maximum flame temperature at $\phi = 0.3$ and two different strain rates, $\alpha = 40\ s^{-1}$ and $\alpha = 50\ s^{-1}$ (right-hand side).

IV.1.3. Cool flame position in the burner

IV.1.3.1. Influence of the ozone concentration

The influence of the ozone concentration on the cool flame position in the burner was studied using CH_2O-PLIF. The results for two strain rates, namely $\alpha = 40\ s^{-1}$ and $\alpha = 50\ s^{-1}$, at equivalence ratios varying between 0.2 and 0.5, are pictured in Figure IV.5, along with the experimental flashback limits. Ozone-addition induces a decrease of the flame front position towards the burner exit in every studied case. This behaviour is well captured by both models, and the agreement between experimental and simulated flame front positions is overall good, with a maximum discrepancy of about 500 µm at the lowest ozone concentrations. Interestingly, the global discrepancy between the experimental and simulated results is lower at low ozone concentration with the AramcoMech 1.3 model, while the current model predictions are more accurate at important ozone concentrations. Still, both models predict the flame front position within the uncertainty limits in most of the cases. The better predictions of the current model at high ozone concentration are consistent with the previous comparison of the experimental and simulated flame temperatures. As the equivalence ratio decreases, the required ozone mole fraction for flame stabilization and flashback increases, which is also very well predicted by both

kinetic models. The current model constantly predicts lower flame front positions compared to the AramcoMech 1.3 model. This behaviour can be explained by the modification of the rate constants for both internal H-atom migration of ROȮ ($CH_3OCH_2O\dot{O}$) and ȮOQOOH ($\dot{O}OCH_2OCH_2O_2H$) radicals which causes a rise of reactivity in the low-temperature range. It is also interesting to note that the influence of the ozone concentration on the cool flame position is more important at 40 s^{-1} than at 50 s^{-1}, the stabilization domain being narrower as the strain rate increases.

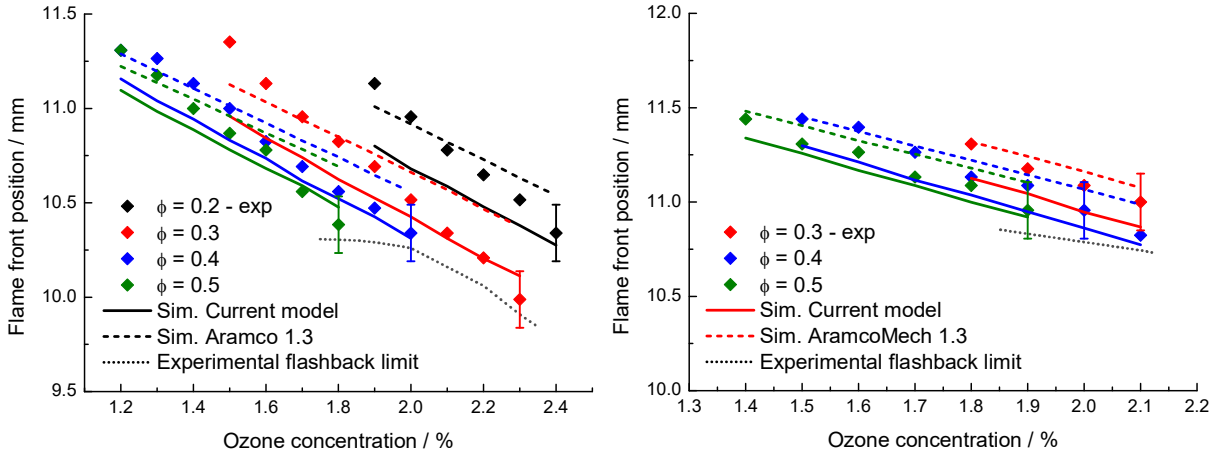

Figure IV.5. Experimental and simulated flame positions at $\alpha = 40\ s^{-1}$ (left-hand side) and $\alpha = 50\ s^{-1}$ (right-hand side) at various equivalence ratios and ozone mole fractions.

IV.1.3.2. Influence of the equivalence ratio

At two fixed strain rates, $\alpha = 40\ s^{-1}$ and $\alpha = 50\ s^{-1}$, and a fixed ozone concentration, $x_{O3} = 1.9\%$, the equivalence ratio was varied between 0.2 and 0.5. The results are pictured in Figure IV.6. The flame front tends to get closer to the burner exit as the equivalence ratio increases for both conditions, indicating an increase of the cool flame propagation speed. It is consistent with previous demonstrations of Ju and co-workers for DME [43] and Brown and Belmont for *n*-decane [53] in ultra-lean conditions. This trend is also well captured in the simulations. The flame front positions are also globally well predicted by the simulations within the uncertainty limit, at the exception of the lowest equivalence ratio $\phi = 0.2$ at $\alpha = 40\ s^{-1}$. As previously discussed, the different flame fronts simulated with the current model are located at a lower HAB than with the AramcoMech 1.3 model, the global agreement on the flame front position however remains fair.

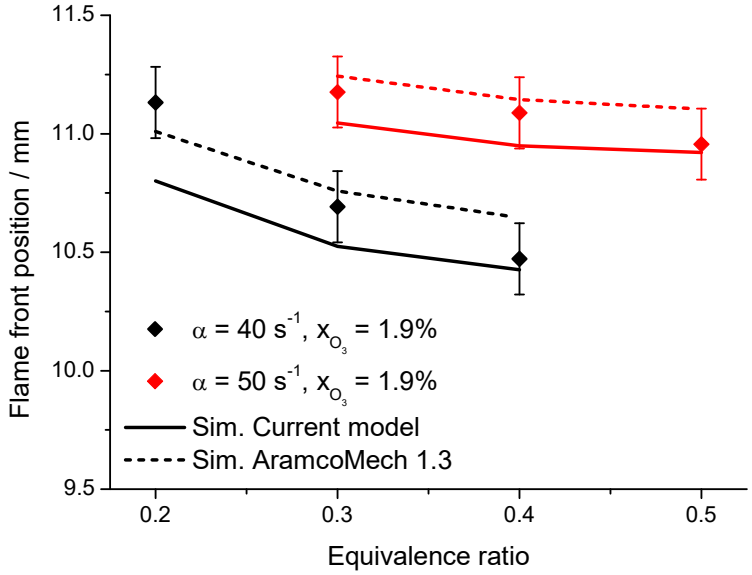

Figure IV.6. Influence of the equivalence ratio on the cool flame position at two different strain rates, $\alpha = 40\ s^{-1}$ and $\alpha = 50\ s^{-1}$, the ozone concentration being kept constant at $x_{O3} = 1.9\%$.

IV.1.4. Chemical structure of the cool flame

In order to shed some light into the mechanisms governing the occurrence and stabilization of cool flames, the mole fraction profiles of the reactants and major stable species formed in the cool flame were established using the procedure described in Chapter II. For DME/O_2/O_3 cool flames, the micro gas chromatograph (Agilent 490), gas chromatograph (Agilent 6890) and mass spectrometer (Omnistar GSD 301 O2) were jointly used. As discussed in Section III.5, early reactivity takes place during the sampling upstream the cool flame. In this context, only the experimental results in the post-flame region are exploited to discuss the kinetics of cool flames.

Two different cool flame conditions were selected at a constant strain rate, $\alpha = 50\ s^{-1}$, the cool flame showing least disturbance by the sampling capillary in these conditions. Two different equivalence ratios were studied, $\phi = 0.3$ and $\phi = 0.5$, with an ozone concentration $x_{O3} = 2.0\%$ and $x_{O3} = 1.7\%$, respectively. The results for the cool flame at $\phi = 0.5$ and $x_{O3} = 1.7\%$ are plotted in Figure IV.7, while the results obtained in the second cool flame ($\phi = 0.3$, $x_{O3} = 2.0\%$) are plotted in Figure IV.8. The Abel-inversed chemiluminescence signal is also plotted as a red continuous line. The simulated results using both AramcoMech 1.3 and the current model are also presented, respectively by a black dashed and black continuous line. In both cases the experimental carbon balance is close to 100%, with a maximum deviation of ± 6% in both flames. Deviation from the carbon balance in each condition is provided in Appendix IV.A2.

Firstly, the discussion focusses on the reactant mole fraction profiles, respectively the fuel, CH_3OCH_3, and ozone, O_3. The fuel is partially consumed through the flame, resulting in a 30-40% conversion of the fuel into low-temperature oxidation products in both flames. This partial conversion

of the fuel is typical of the cool flame process, as the NTC phenomenon limits the fuel conversion downstream the flame. Ozone, on the other side, is totally decomposed inside the flame front, forming atomic oxygen, Ö, and molecular oxygen, O_2. The Ö atom will then further react with the fuel molecule, giving ȮH and radicals, yielding $CH_3\dot{O}$ or $CH_3OCH_2\dot{O}$ by addition reactions, and therefore enabling the initiation of the reactivity in our conditions. ȮH radicals will also participate in the H-atom abstraction reaction through $CH_3OCH_3 + \dot{O}H \Leftrightarrow CH_3O\dot{C}H_2 + H_2O$, reinforcing the impact of ozone-addition on the reactivity as ozone decomposition can thus be considered as chain-branching. The fuel radical will then undergo several oxygen additions, leading to the formation of characteristic products of its low-temperature oxidation. Both models slightly overpredict the DME conversion, yielding roughly the same fuel concentration downstream the cool flame. As expected from the previous comparison of the flame front positions, the fuel conversion simulated with the current model takes place at a slightly lower position in the burner than with the AramcoMech 1.3 model.

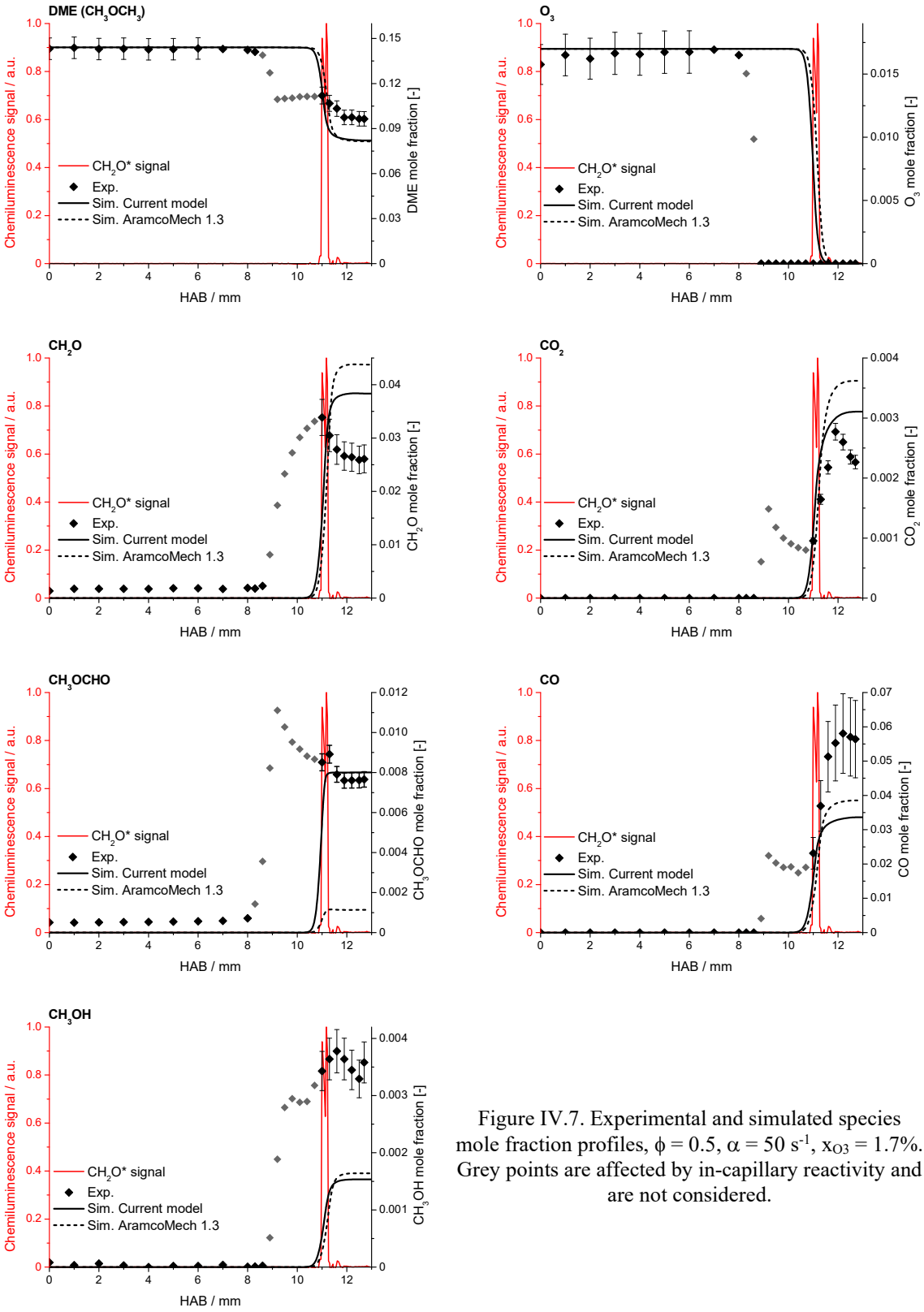

Figure IV.7. Experimental and simulated species mole fraction profiles, $\phi = 0.5$, $\alpha = 50\ s^{-1}$, $x_{O3} = 1.7\%$. Grey points are affected by in-capillary reactivity and are not considered.

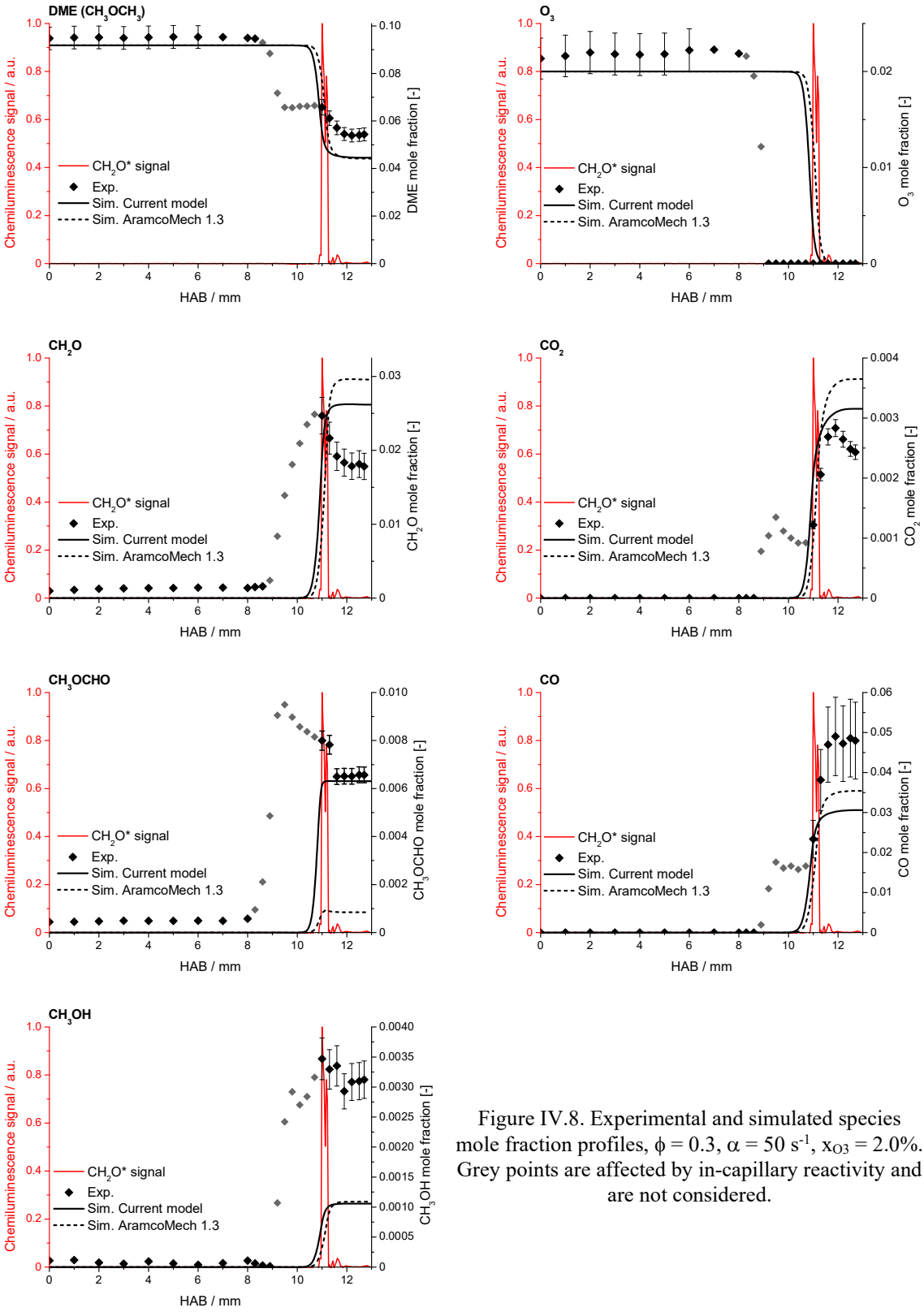

Figure IV.8. Experimental and simulated species mole fraction profiles, $\phi = 0.3$, $\alpha = 50\ s^{-1}$, $x_{O3} = 2.0\%$. Grey points are affected by in-capillary reactivity and are not considered.

On the products side, the CH_2O mole fraction decreases in the post-flame region, which is consistent with the obtained PLIF results, as shown in Figure IV.9. for the $\phi = 0.5$ cool flame. A deviation exists when comparing the intrusive and non-intrusive method in the pre-flame region, which can directly be related to the perturbation of the flame by the sampling capillary. The important production of formaldehyde is typical of cool flames, which can be produced from the fuel radical β-scission and the decomposition of the hydroperoxymethoxymethyl radical, $\dot{C}H_2OCH_2OOH$, formed after fuel radical addition to oxygen and further isomerization. The modifications made to the model allowed us to improve its performance in the prediction of the CH_2O mole fraction in both flames. The update of the kinetic parameters of the formation of $\dot{Q}OOH$ by internal H-atom migration has the effect of decreasing the reaction rate constant of this reaction for temperatures higher than 700 K in comparison to the AramcoMech 1.3 model. Moreover, the consumption of methoxymethoxy radical, $CH_3OCH_2\dot{O}$, takes place by C-C and C-H β-scissions in the AramcoMech 1.3 model, the first one being favoured. A combined experimental and theoretical study of these reactions however showed that more than 95% of the consumption of $CH_3OCH_2\dot{O}$ takes place through β-CH bond cleavage [225]. Finally, the reaction $CH_3O\dot{C}H_2$ + Ö ⇔ $CH_3OCH_2\dot{O}$ was added to the current model [225]. The formation of the methoxymethoxy radical will compete with the addition of the methoxymethyl radical to O_2, partially explaining the improvement of the CH_2O mole fraction prediction by the current model.

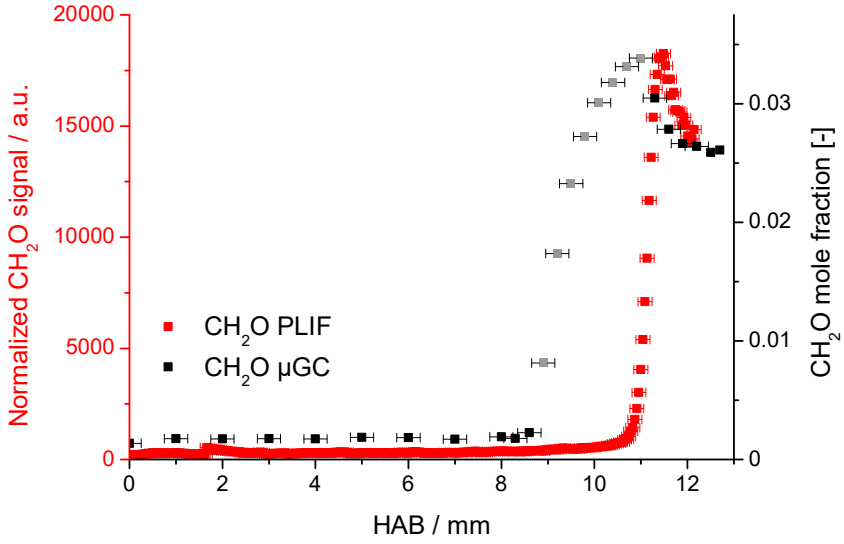

Figure IV.9. Comparison of the CH_2O profiles obtained by PLIF (red points) and µGC (black points), $\phi = 0.5$, $\alpha = 50\ s^{-1}$, $x_{O3} = 1.7\%$. Grey points represent the perturbed zone where in-capillary reactivity takes place.

Another point that was addressed in this work is the mole fraction prediction of methyl formate, CH_3OCHO. As one can see, the AramcoMech 1.3 model highly underpredicts this species mole fraction after the cool flame. Using the work of Song and co-workers [225], combined with the utilization of the methyl formate submechanism from Minwegen and co-workers [231] and the modification of the

biradical reaction 2 $CH_3OCH_2O\dot{O} \Rightarrow 2\ CH_3OCH_2\dot{O} + O_2$ rate constant parameters, taken from Rosado-Reyes and co-workers [232], led to a significant improvement of the prediction of the formation of methyl formate by the current model. A reaction pathway analysis at 10% fuel conversion (T_{flame} = 494 K) indicates that methyl formate nearly exclusively originates from the decomposition of the $CH_3OCH_2\dot{O}$ radical yielding $CH_3OCHO + \dot{H}$. The methoxymethoxy radical itself is mainly formed through the reaction 2 $CH_3OCH_2O\dot{O} \Rightarrow 2\ CH_3OCH_2\dot{O} + O_2$. In the presence of ozone, the onset temperature of the low-temperature oxidation is lowered. It explains that chain-propagation reactions become influent, instead of the conventional low-temperature oxidation chemistry pathway that goes through indirect chain-branching. The role of ozone will be discussed in further details in the diethyl ether oxidation study, in Section IV.2.

The improvement of the current model is also observable for the CO_2 mole fraction profile, where the current model shows better performance in comparison to the AramcoMech 1.3 model. In can be noted that this high CO/CO_2 ratio is also typical of the LTC of the fuel, as the thermal conversion of CO to CO_2 is not effective given the limited maximum temperature of the cool flame [234]. CO formation is however underpredicted by both models by a factor of ~ 2. In the present conditions, both CO and CO_2 are formed from the decomposition of the aldohydroperoxide $HOOCH_2OCHO$.

Finally, methanol was also measured as a minor product of the low-temperature combustion of dimethyl ether. Both models underestimate the formation of this species by about a factor of 3 in both flames, demonstrating the need for further improvement of the submechanism for this species. One should note that the rate constant used in the AramcoMech 1.3 model for the $CH_3OCH_3 + CH_3\dot{O}$ reaction, forming $CH_3O\dot{C}H_2$ and CH_3OH, is taken by analogy with the $CH_3OH + CH_3\dot{O}$ reaction from the work of Tsang [235]. As this reaction is very sensitive to the production of methanol in these low-temperature conditions, further investigation of the $CH_3OCH_3 + CH_3\dot{O}$ reaction is recommended.

IV.1.5. Kinetic analysis

IV.1.5.1. Brute-force sensitivity analysis

Sensitivity analyses were performed on the first-stage ignition delay in a constant volume reactor in order to limit the required computational time that is generally required for such simulation. The detailed procedure is provided in Appendix III.A4. A comparison between the sensitivity analysis performed with Cantera on the first-stage ignition delay time and the sensitivity analysis on the flame speed and flame temperature performed with Chemkin-Pro, using the same initial mixture condition, is shown in Appendix IV.A3. The comparison shows that whatever the targeted parameter, the sensitivity analysis globally emphasizes the same reactions. Thus, it was chosen to perform the sensitivity analysis on the first-stage ignition delay as it allowed to save computational time.

The results of the brute-force analyses performed on the first-stage ignition delay time for the condition ϕ = 0.3, x_{O3} = 2.0% are plotted in Figure IV.10 at two different temperatures, respectively T = 450 K and T = 600 K. A positive sensitivity coefficient, corresponding to a lower ignition delay time when a rate constant is increased, indicates a lowered reactivity. To the contrary, a negative sensitivity coefficient indicates an increased reactivity of the mixture.

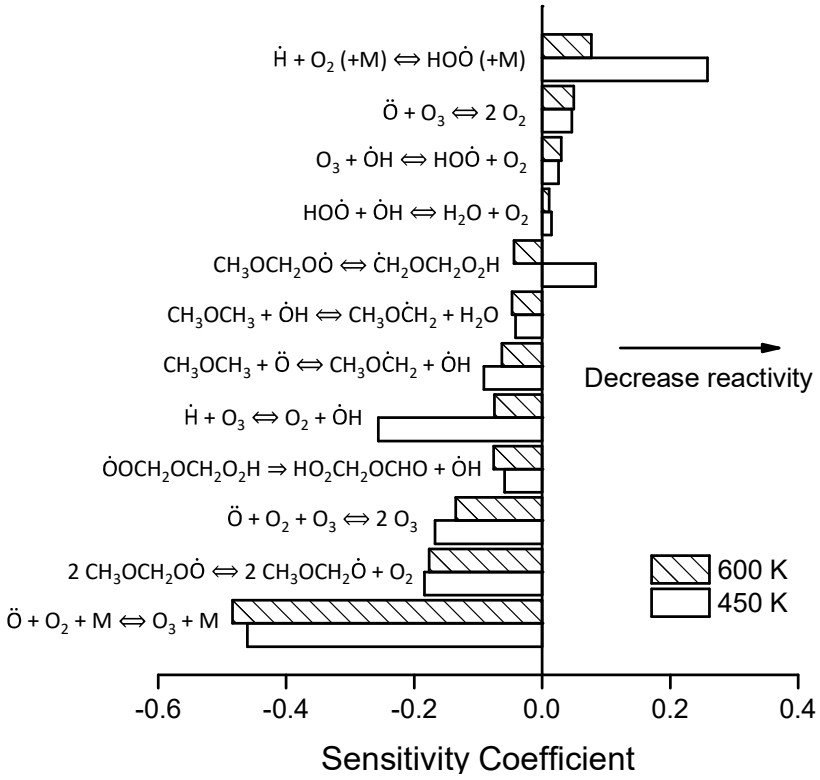

Figure IV.10. Brute-force sensitivity analyses performed on the first stage ignition delay time at ϕ = 0.3, x_{O3} = 2.0% and two different temperatures, T = 450 K (empty bar) and T = 600 K (dashed bar).

As expected, the DME/O_2/O_3 system is particularly sensitive to the O_3 submechanism which contains three of the six most sensitive reactions at both 450 and 600 K, describing the ozone decomposition respectively through $O_3 + M \Leftrightarrow Ö + O_2 + M$, $O_3 + O_3 \Leftrightarrow O_3 + O_2 + Ö$ and $Ḣ + O_3 \Leftrightarrow O_2 + ȮH$. Note that, in the Jian model, the efficiency of Ö as a third-body collider is set to 0 so there is no duplicate reaction rate between O_3 + M and O_3 + O_3. The production of radicals from ozone decomposition increases the reactivity at 450 and 600 K, the sensitivity coefficients being similar in both cases. The ozone decomposition is crucial in this temperature range for the initiation of combustion. The H-atom abstraction by Ö on the fuel molecule is slightly more sensitive at 450 K than at 600 K, and is also slightly more sensitive than the H-atom abstraction by ȮH at both temperatures. Due to the low temperatures reached in cool flames, and especially between 450 and 600 K, the formation of Ö-atoms and ȮH radicals mainly comes from ozone decomposition. Reactions inhibiting the reactivity are mainly O_3 recombination in O_2 or reactions yielding HOȮ, which are less reactive in this temperature domain.

Finally, it is interesting to note that in the present condition the ROȮ H-atom internal migration reaction yielding ȮOOH, $\dot{C}H_2OCH_2O_2H$, has a negative effect on the first-stage ignition delay at 450 K but a positive one at 600 K. It suggests that the most important contribution to the reactivity at the lowest temperatures among fuel-specific reactions comes from the biradical reaction 2 $CH_3OCH_2O\dot{O} \Rightarrow 2\ CH_3OCH_2\dot{O} + O_2$, which was previously highlighted as the main source of methyl formate in our conditions. This assumption is supported by the important negative sensitive coefficient of this reaction at both temperatures. This last point will be highlighted in the next section.

IV.1.5.2. Rate of production analysis

A reaction pathway analysis was performed in the $\phi = 0.3$, $\alpha = 50\ s^{-1}$, $x_{O3} = 2.0\%$ flame case at 5 and 20% fuel conversion, corresponding respectively to HAB = 10.78 mm and HAB = 10.98 mm, and temperatures of 419 K and 612 K, i.e., close to the temperatures used for the sensitivity analyses presented above. The detailed procedure is also provided in Appendix III.A4. The main pathways of dimethyl ether conversion in these two conditions are shown in Figure IV.11. For a comprehensive reading of the figure, fluxes are not indicated for values lower than 0.1%. The observed and quantified species in this study are highlighted by red rectangles.

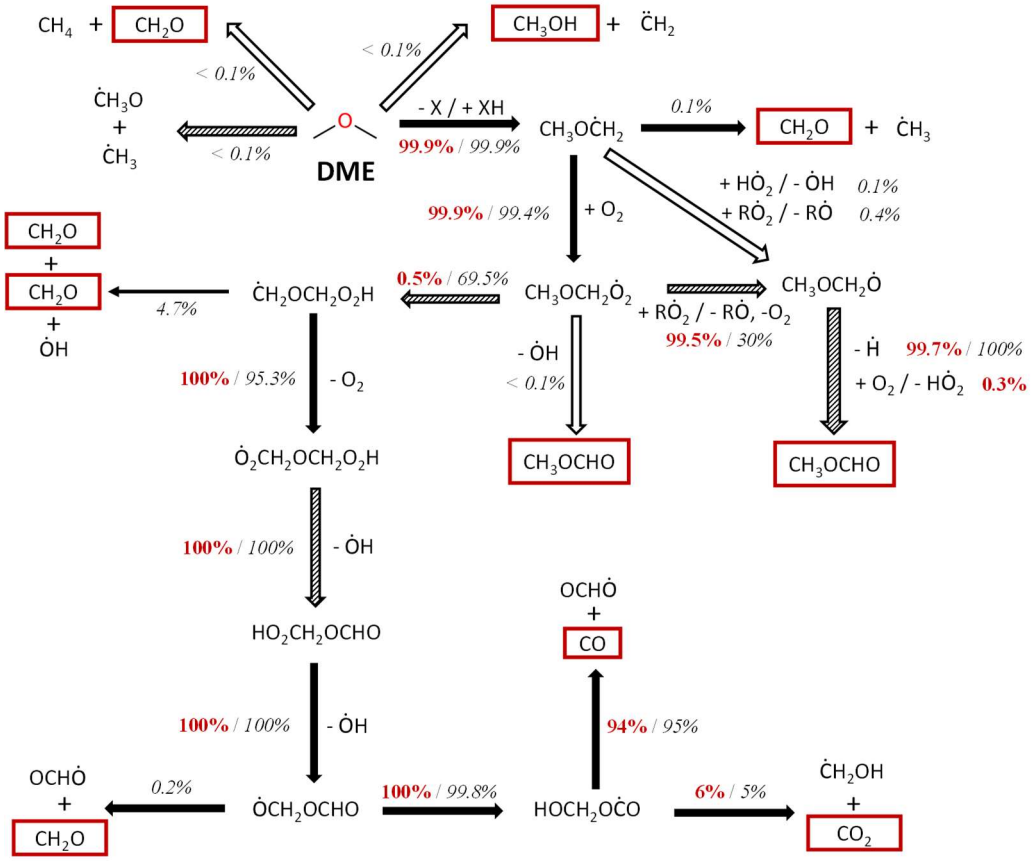

Figure IV.11. Rate of production analysis in the cool flame with the current model at 5%, $T_{flame} = 419$ K (bold, red) and 20%, $T_{flame} = 612$ K (italic, black) fuel conversion, $\phi = 0.3$, $\alpha = 50\ s^{-1}$, $x_{O3} = 2.0\%$. Empty arrows represent added reactions, dashed arrows represent modified reactions in the current model.

As explained above, the initiation of the reactivity takes place through H-atom abstraction on the fuel molecule, assisted by the decomposition of O_3 above the burner and followed by addition to O_2. At 5% fuel conversion, it is noticed that the major reaction of conversion of the ROȮ radical is not the H-atom migration as expected from the low-temperature combustion of dimethyl ether [144] but the biradical reaction 2 $CH_3OCH_2OȮ \Rightarrow$ 2 $CH_3OCH_2Ȯ + O_2$. The decomposition of $CH_3OCH_2Ȯ$ into methyl formate, CH_3OCHO, plays an important role in the improvement of the prediction of this species by the current model. A change in the branching ratio is observed when the temperature increases, at 20% fuel conversion, where ROȮ isomerization into ȮOOH becomes more predominant, as commonly observed in LTC studies [144].

The importance of ROȮ propagation reactions in the presence of ozone was previously highlighted in JSRs studies. Liao and co-workers [79] found out that as the ozone concentration in the mixture increases, the branching ratio between the 2 ROȮ $\Rightarrow$ 2 RȮ + O_2 reaction and the ROȮ isomerisation reaction is progressively shifted to the bimolecular reaction side, i.e., O_3-addition weakened the predominant role of ROȮ isomerisation. As previously addressed in Section I.2.3, the role of ȮOOH formation is vital for the cool flame as it allows the formation of an important ȮH radical pool. However, the significant increase in ȮH concentration provided through the ozone decomposition renders the low-temperature combustion of DME less dependent on ROȮ isomerization. In their work, Zhao and co-workers [63] also came up with the same conclusion, showing that chain propagation at low temperatures was predominant over degenerated chain branching in the presence of ozone. It should also be stressed that the ROȮ mole fraction is very different in a JSR and in our cool flame conditions. As cool flames are stabilized without inert gas dilution, some intermediates mole fractions are considerably higher in this case. In Figure IV.12. is pictured a comparison between the ROȮ mole fraction profile in a JSR following the experimental conditions of Liao and co-workers [79], $\phi = 0.35$, $x_{O3} = 2000$ ppm, diluted in Argon, and in a stabilized cool flame following our experimental conditions, $\phi = 0.3$, $\alpha = 50\ s^{-1}$, $x_{O3} = 2.0\%$. The presented results are simulated using the current model and the Chemkin-Pro PSR (Perfectly Stirred Reactor) & Pre-Mixed Burner Stagnation Flame modules. One can observe that the simulated ROȮ mole fraction in the cool flame is two orders of magnitude higher than in the JSR. Such a difference is expected to favour bi-molecular reactions between ROȮ radicals in the cool flame, also explaining why this reaction is so influent in the studied conditions. Finally, the importance of ROȮ radical chemistry was very recently pointed out in studies of the low- to intermediate-temperature oxidation of methanol [236] and propane [237] in a supercritical-pressure jet-stirred reactor (up to 100 atm), stressing for better insight into the reactivity of these radicals at moderately high temperatures.

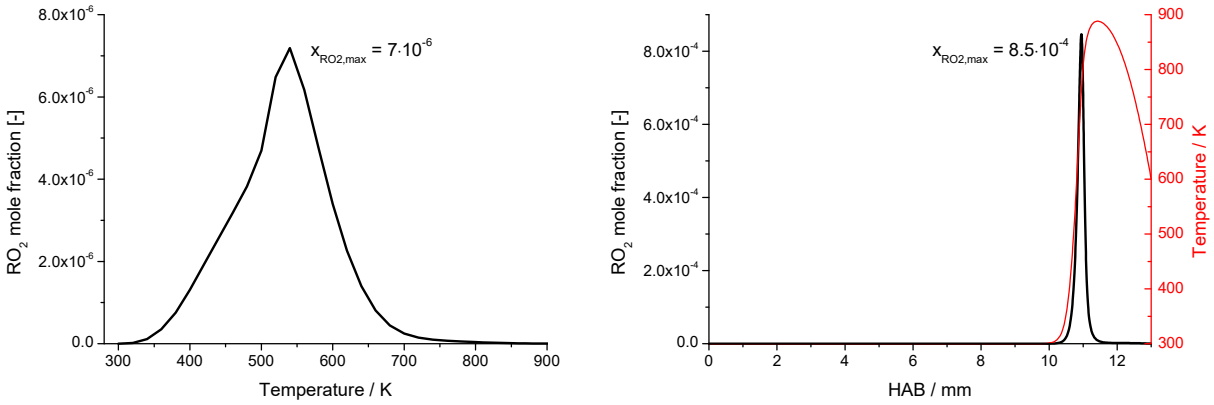

Figure IV.12. Comparison of ROȮ simulated mole fraction profiles as a function of temperature in a JSR (left-hand side) in the experimental conditions of Liao and co-workers (ϕ = 0.35, x_{O3} = 2000 ppm, diluted in Argon) and as a function of HAB in a stabilized cool flame (ϕ = 0.3, α = 50 s^{-1}, x_{O3} = 2.0%, right hand-side).

As an overall conclusion on the performance of the modified model, one can observe that it predicts a slightly higher reactivity at low temperatures, illustrated by a lower position of the flame in the burner compared to the original AramcoMech 1.3 model and by a lower first-stage ignition delay time, as pictured in Appendix IV.A4. where the prediction of the current model was assessed against literature data. However, changes brought to the current model permitted to better predict the composition of the post-flame area, especially for methyl formate, which was highly underpredicted by the original AramcoMech 1.3 model.

IV.1.6. Conclusions on the ozone-assisted low-temperature combustion of dimethyl ether

In this first section on the low-temperature combustion of ethers inside cool flames dedicated to dimethyl ether, the AramcoMech 1.3 mechanism was chosen as a base model and was further modified in order to improve its prediction against the newly obtained experimental results. An ozone submechanism from Jian and co-workers was added to the core mechanism.

The prediction abilities of both models were assessed against a newly, innovative, set of experimental data. DME/O_2/O_3 cool flames were stabilized at two different strain rates, α = 40 s^{-1} and α = 50 s^{-1}, and for a wide range of equivalence ratios varying from 0.2 to 0.5 and ozone mole fractions varying from 1.2 to 2.1%. Firstly, the effect of ozone on both cool flame temperature and position was studied. An increase of the ozone mole fraction in the cool flame led to an increased flame temperature as well as an increased propagation speed, illustrated by a lowered cool flame position above the burner. These results are consistent with the previous studies in which an increase of the heat release of a *n*-heptane cool flame was observed as the ozone concentration was increased in a HCCI engine [75]. Both models gave excellent results on the prediction of these parameters. Secondly, the detailed chemical structure of DME/O_2/O_3 cool flames was obtained by means of gas sampling and further analysis by coupling micro-gas chromatography, gas chromatography and mass spectrometry. Reactants and

products mole fraction were measured as a function of the Height Above the Burner, and compared to the simulation using both models. While the initial model was able to fairly predict the reactants conversion and major low-temperature products formation, the formation of two minor species, namely methyl formate and methanol, was significantly underpredicted. Modifications brought to the AramcoMech 1.3 model in order to predict the methyl formate formation inside cool flames allowed to highlight the importance of chain propagating reactions in the case of ozone-assisted low-temperature combustion, as the typical indirect chain branching pathway characterizing the low-temperature combustion of fuels is rendered less influent in its presence.

In order to gain some further insight into the influence of ozone in the low-temperature combustion of ethers, the second study that is presented hereafter focusses on the comparison between ozone-assisted and spontaneous cool flames stabilized in the same configuration, using diethyl ether as fuel.

IV.2. Study of diethyl ether LTC and influence of ozone-seeding on the cool flame products distribution

IV.2.1. Motivations of the study

The second chosen fuel to be studied inside the stagnation plate burner is diethyl ether, DEE, of detailed structure $CH_3CH_2OCH_2CH_3$. This fuel exhibits a very strong reactivity in the low-temperature range, which makes it a candidate of choice to produce self-sustaining stabilized cool flames. A comparison of the DME and DEE conversion in the Nancy JSR is shown in Figure IV.13 [120,167]. As one can see, the DEE conversion happens 75 K earlier than for DME in the same equivalence and residence time conditions. Its conversion in the cool flame region is also far more important than for DME, reaching 70% conversion at 525 K for 30% at 575 K in the case of DME.

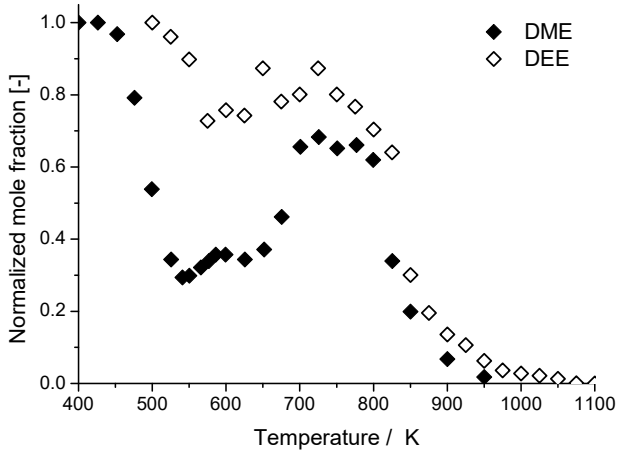

Figure IV.13. DME and DEE conversion as a function of temperature inside the Nancy JSR. The equivalence ratio and residence time are the same in both studies [120,167], $\phi = 1$, $\tau = 2$ s.

The objectives behind this study on diethyl ether stabilized cool flames are i) acquiring a new original set of data on the low-temperature combustion of diethyl ether, and ii) to compare an ozone-assisted and a spontaneous cool flame, to discuss the influence of ozone on the cool flame, especially on its temperature and products distribution. These experimental results were presented during the 39th International Symposium on Combustion, and accepted for publication [238]. Like the dimethyl ether study, the simulations are slightly different from those shown in the published article as a different kinetic model was used in the present case.

IV.2.2. Experimental conditions & kinetic models

Two different experimental conditions were chosen in this study, the objective being to stabilize cool flames with and without ozone, and are summed up hereafter in Table IV.2.

Table IV.2. Experimental conditions of stabilized diethyl ether cool flames.

Condition	ϕ	x_{O3}	x_{DEE}	x_{O2}	α / s^{-1}
With ozone	0.5	0.014	0.078	0.908	50
Without ozone	1	0	0.143	0.857	40

The first condition is a lean cool flame, stabilized in similar conditions than those previously used for dimethyl ether. The equivalence ratio is $\phi = 0.5$, the ozone concentration $x_{O3} = 1.4\%$ and the strain rate $\alpha = 50\ s^{-1}$. The second cool flame was stabilized without ozone-seeding, i.e., $x_{O3} = 0\%$. To promote the flame stability, few parameters were changed. On one hand, the equivalence ratio was increased to the stoichiometry, i.e., $\phi = 1$. It is known that the cool flame propagation speed exhibits only minor dependence to equivalence ratio variation, however shifting from $\phi = 0.5$ to $\phi = 1$ allowed to stabilize the cool flame without ozone. On the other hand, the inlet velocity of the mixture was slightly decreased to favour the flame stabilization, yielding $\alpha = 40\ s^{-1}$. The plate temperature was also increased to 700 K.

Regarding now the simulation of diethyl ether cool flames, two recent kinetic models from the literature were used. The first model was developed by Tran and co-workers [167], abbreviated ‘Tran model’ in the following paragraphs, and includes 749 species and 3570 reactions. The second model was developed by Serinyel and co-workers [166], and is abbreviated ‘Serinyel model’. We however used a reduced version of the latter mechanism, that was published by Murakami and co-workers [239] and reduced using a Path-Flux Analysis (PFA) method [240]. The use of a reduced version of the Serinyel mechanism was motivated by the absence of transport data in the full mechanism. The reduced mechanism finally includes 194 species and 1128 reactions. As for dimethyl ether, the ozone-submechanism from Jian and co-workers [233] was added to the diethyl ether models. In this study, the kinetic models were not modified, but results are discussed regarding the newly acquired experimental measurements.

IV.2.3. Diethyl ether cool flames temperature profiles

Experimental and simulated temperature profiles in both flames are shown in Figure IV.14. The absence of catalytic effect at the surface of the thermocouple was verified by measuring the temperature profiles in both directions. For a comprehensive reading of the figure the experimental temperature profiles measured in both directions are presented in Appendix IV.A5. for the $\phi = 0.5$, $x_{O3} = 1.4\%$ cool flame. The temperature profile of the $\phi = 1$ cool flame could not be measured at a lower thermocouple position than 7.5 mm. It was caused by a too important flame instability which systematically resulted in a flashback.

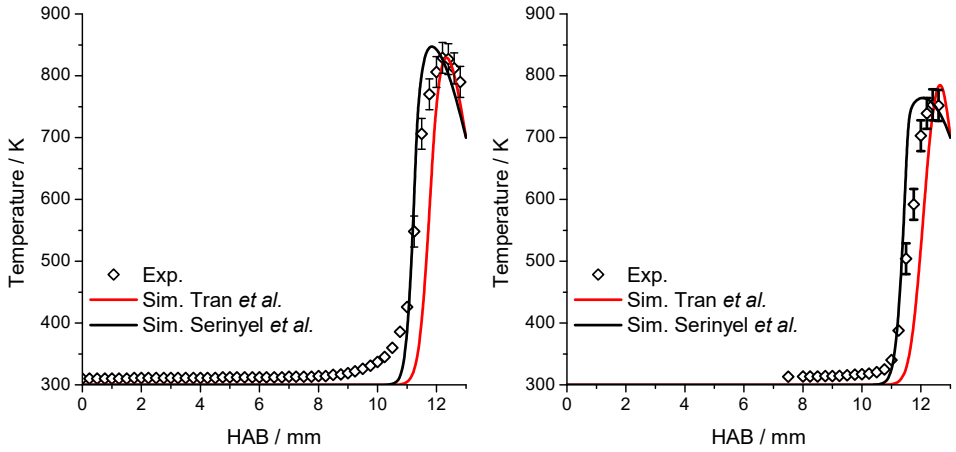

Figure IV. 14. Temperature profiles of the ozone-seeded cool flame, $\phi = 0.5$, $\alpha = 50\ s^{-1}$, $x_{O3} = 1.4\%$ (left-hand side) and spontaneous cool flame, $\phi = 1$, $\alpha = 40\ s^{-1}$, $x_{O3} = 0\%$ (right-hand side).

Maximal experimental temperatures of 829 K and 753 K, respectively for the $\phi = 0.5$ (with ozone) and $\phi = 1$ (without ozone) conditions, were measured after the cool flame front. Achieving a good spatial resolution in the $\phi = 1$ experimental case is complex due to the short distance separating the flame from the heated plate. This lower temperature for the $\phi = 1$ cool flame seems counterintuitive as a more important heat release of a stoichiometric flame is expected compared to a lean flame. It illustrates the important effect of ozone on the cool flame heat release, highlighted in Section IV.1.2.2. (Figure IV.4) for dimethyl ether.

Both models are able to reproduce this trend, the maximum simulated temperature being in both cases inferior for the stoichiometric cool flame compared to the lean cool flame. In the lean condition, the maximum simulated temperature by the Tran model is in excellent agreement with the experimental data ($T_{sim,max} = 829$ K) while the Serinyel model predicts a slightly higher temperature ($T_{sim,max} = 847$ K) which however remains within the measurement uncertainty of ± 25 K. Moreover, the position at which this maximum temperature is reached is also accurately reproduced by the Tran model, while the predicted position by the Serinyel model is closer to the burner exit. In the stoichiometric case, the prediction of the Serinyel model ($T_{sim,max} = 764$ K) is slightly better than the Tran model which is barely out of the uncertainty limit of the experimental measurement ($T_{sim,max} = 785$ K). The maximum cool

flame temperature position is however still more accurately predicted by the Tran model than by the Serinyel model.

IV.2.4. Species distribution in diethyl ether cool flames

A total of 16 stable species were detected, identified and quantified in both cool flames. These species were measured using the GC-MS (Bruker SCION), GC-TCD (Agilent 6890) and mass spectrometer (Omnistar). Deviation from the carbon balance in both flames is* provided in Appendix IV.A6.

IV.2.4.1. Reactants & products distribution inside DEE cool flames

The ozone mole fraction profile of the $\phi = 0.5$, $x_{O3} = 1.4\%$ cool flame is pictured in Figure IV.15. along with the simulated profiles using both Tran and Serinyel models. The Abel-inversed chemiluminescence profile is also plotted in order to locate the position of the flame front. As for dimethyl ether, early reactivity takes place before the flame front in the ozone-seeded cool flame. In the present case, the stabilization of a spontaneous diethyl ether cool flame without ozone allowed to experimentally demonstrate the aforementioned hypothesis, i.e., that ozone decomposition in the capillary was responsible for the early reactivity. In this context, only the experimental results in the post-flame region for the ozone-seeded cool flame are exploited for discussion.

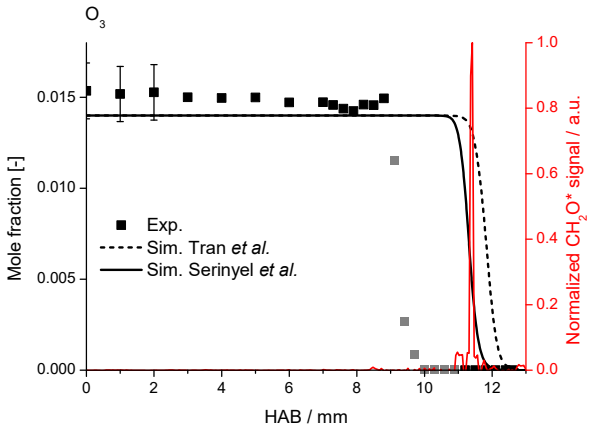

Figure IV.15. Ozone mole fraction profile, $\phi = 0.5$, $x_{O3} = 1.4\%$. Grey symbols represent the area of the flame perturbed by in-capillary reactivity.

In Figure IV.16. is pictured the diethyl ether conversion through the cool flame for both studied conditions, $\phi = 0.5$ and $\phi = 1$. Experimentally, 60% of the diethyl ether is converted in the $\phi = 0.5$ cool flame, and 55% in the $\phi = 1$ flame. A similar result was obtained for dimethyl ether conversion in Section IV.1.4. It should however be noted that, as it was observed in the Nancy JSR and presented in Figure IV.13, the fuel conversion in the cool flame is more important in the case of diethyl ether than for dimethyl ether. This result is also consistent with a previous comparison of Serinyel and co-workers

[166] that compared the DME and DEE oxidation in a JSR. Their experimental conditions were not kept exactly constant, but allowed to highlight the more important fuel conversion in the cool flame regime in the case of DEE compared to DME. Interestingly, despite not being able to predict the correct position at which the fuel is oxidized, especially in the $\phi = 1$ case, the Serinyel model shows an excellent agreement with the experimental fuel mole fraction after the cool flame. On the other hand, the fuel conversion is overpredicted in both cases by the Tran model, predicting roughly 75% fuel conversion in both conditions. The overprediction of the fuel conversion by the Tran model will be discussed in further details in the next paragraph.

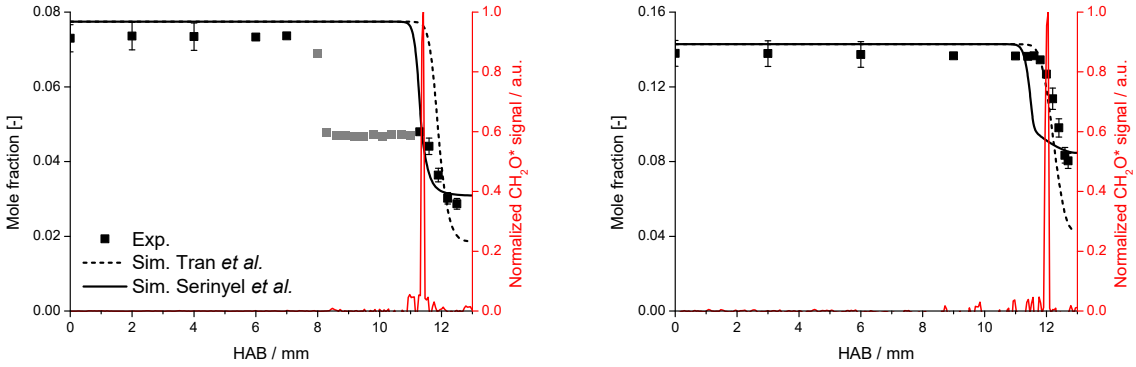

Figure IV.16. Diethyl ether mole fraction profile in the lean, ozone-seeded ($\phi = 0.5$, left-hand side) and stoichiometric, spontaneous ($\phi = 1$, right-hand side) cool flame.

The mole fraction profiles of the reactant (O_2) and different products measured in both cool flames are pictured along with the prediction of the Tran and Serinyel models in Figure IV.17 for the $\phi = 0.5$ case and in Figure IV.18 for the $\phi = 1$ case. The Abel-inversed chemiluminescence profiles are also plotted in both cases.

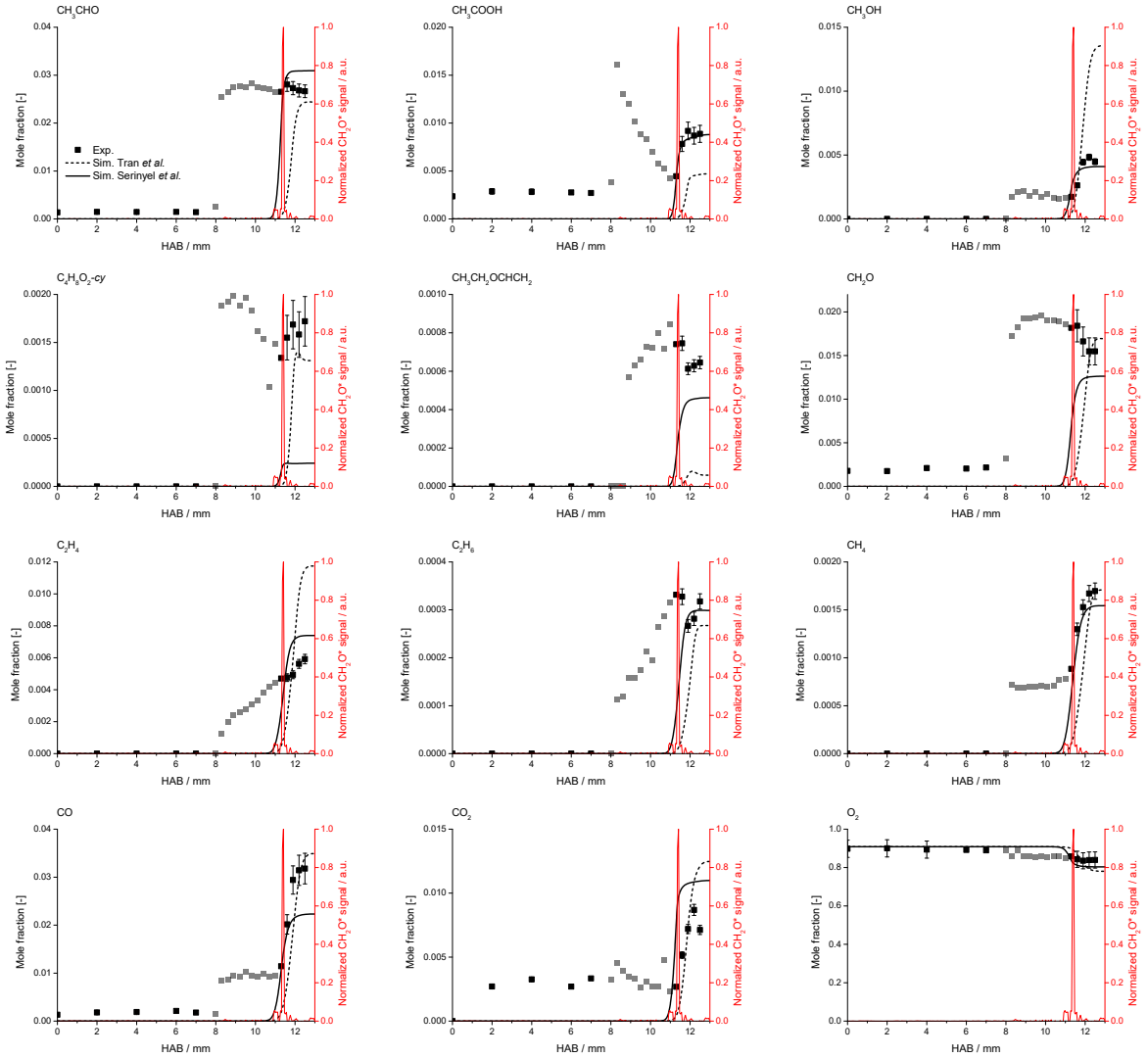

Figure IV.17. Experimental and simulated species mole fraction profiles in the $\phi = 0.5$, $x_{O3} = 1.4\%$ cool flame. Black points are experimental results, continuous line simulated results using the Serinyel model and dashed line simulated results using the Tran model. Grey points are affected by in-capillary reactivity and are not considered.

On the reactant side, complementary to the previously presented ozone and diethyl ether mole fraction profiles, the oxygen mole fraction profile is shown on the bottom right in both figures. As for diethyl ether conversion, the Tran model overpredicts the oxygen conversion through the cool flame, while the Serinyel model agrees well with the experimental results within the experimental uncertainty. The early reactivity in the ozone-rich flame is also visible in Figure IV.17 (grey points) both for the reactant conversion and products formation.

The major product measured in diethyl ether cool flames is acetaldehyde, CH_3CHO, which mainly originates from the decomposition of the ketohydroperoxides $CH_3C(O)OCH(O_2H)CH_3$ and $OCHCH_2OCH(O_2H)CH_3$, as well as the decomposition of the RȮ radical, $CH_3CH_2OCH(\dot{O})CH_3$. Acetaldehyde mole fraction roughly equals 3% downstream the $\phi = 0.5$ cool flame while it exceeds 4% in the stoichiometric flame. The Serinyel model slightly underestimates its formation in both cool flame

conditions, while the Tran model predictions are in fair agreement with the experiments. Major products also observed during the low-temperature combustion of diethyl ether in cool flames are formaldehyde, CH_2O, and acetic acid, CH_3COOH. The formaldehyde formation in the cool flame is also decently predicted by the Tran model. Similarly, as acetaldehyde, formaldehyde can be obtained from ketohydroperoxides decomposition. Acetic acid is accurately predicted by the Serinyel model in the lean cool flame, but significantly underpredicted in both conditions by the Tran model. This product is known to be formed in important quantity in the low-temperature combustion domain [166]. Methanol, CH_3OH, is also measured as one of the main products of diethyl ether low-temperature combustion in the cool flame, its final mole fraction reaching 1% in the stoichiometric case. The Tran model notably overpredicts its formation inside the cool flames, whilst the Serinyel model better reproduces its mole fraction downstream the cool flames, especially in the $\phi = 0.5$ case. As one of the sources of methanol is the H-atom abstraction by $CH_3\dot{O}$ on the fuel molecule, overprediction of the methanol mole fraction by the Tran model partially explains the overprediction of the fuel conversion seen in Figure IV16. The formation of 2-methyl-1,3-dioxolane, $C_4H_8O_2$-*cy*, is underestimated by the Serinyel model. The Tran model however gives better results regarding its formation prediction in both flames. This species is formed in both models by the decomposition of the following $\dot{Q}OOH$ radical, $CH_3\dot{C}HOCH_2CH_2OOH$. The formation of ethyl vinyl ether (EVE), $C_2H_5OC_2H_3$, is also underestimated by both models, the Serinyel model giving better predictions of this species mole fraction. In the tested models, EVE is formed by the decomposition of $C_2H_5OCH_5(O\dot{O})CH_3$ and $C_2H_5OCH(OOH)\dot{C}H_2$ radicals, leading in both cases to the formation of EVE + $HO\dot{O}$. The direct oxidation reaction of the fuel radical forming EVE is not present in both models, which could partially explain the underestimation of this species mole fraction.

Concerning smaller species, the formation of C_2H_4 and C_2H_6 is well reproduced by the Serinyel model, a more important discrepancy being observed with the Tran model. These two species, known as soot precursors, were not detected in lean, ozone-seeded, dimethyl ether cool flames, and are directly linked to the presence of C-C bonds in the diethyl ether molecule. CH_4 and CO production prediction by the Tran model is in overall good agreement compared to the experimental results. The CO_2 mole fraction after the cool flame is consistently underestimated by the Tran model, while the Serinyel model gives more accurate predictions in both cases regarding the experimental results.

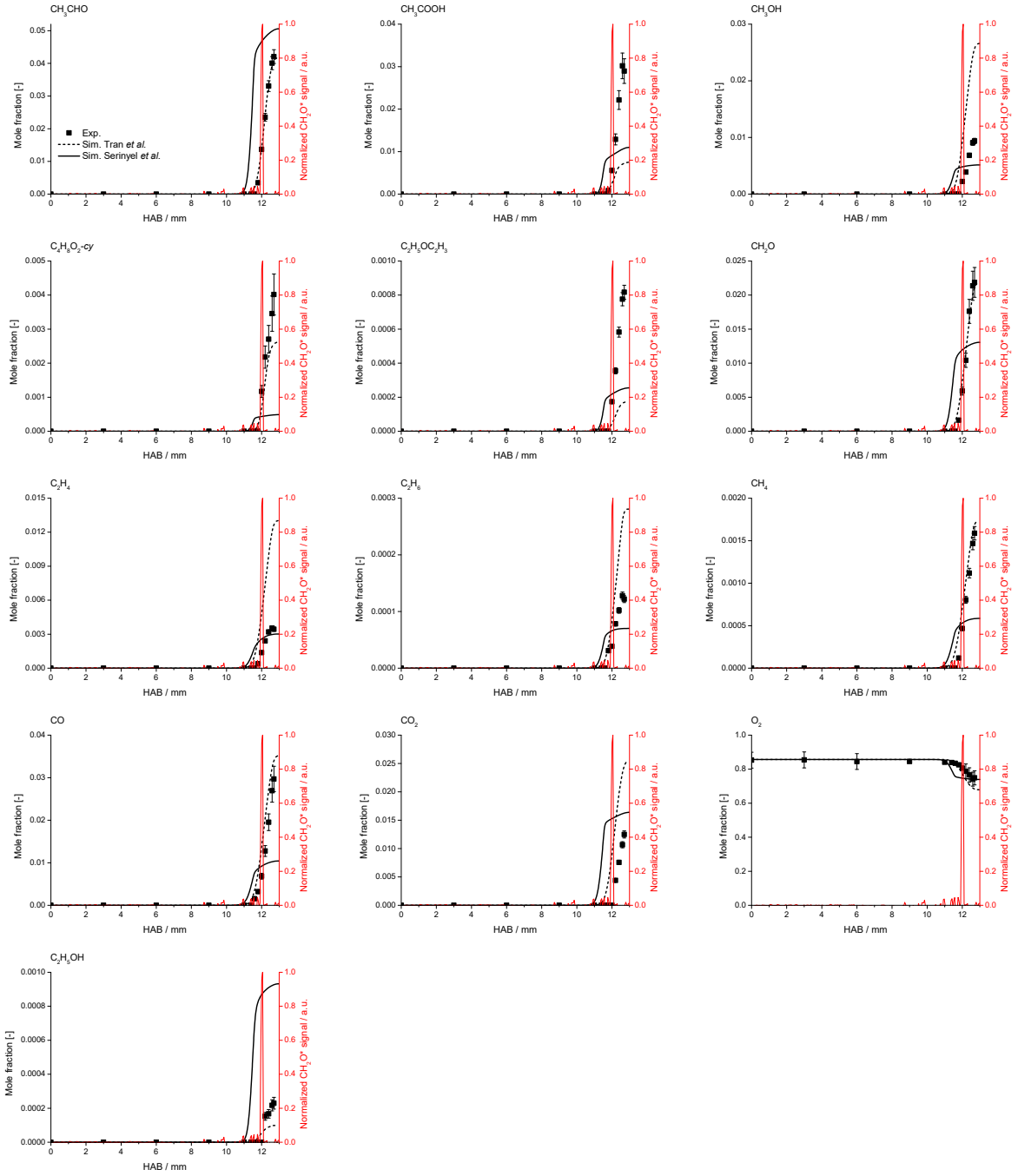

Figure IV.18. Experimental and simulated species mole fraction profiles in the $\phi = 1$, $x_{O3} = 0\%$ cool flame. Black points are experimental results, continuous line simulated results using the Serinyel model and dashed line simulated results using the Tran model. Grey points represent in-capillary reactivity and are not considered.

The presence of ethanol was only detected in the stoichiometric cool flame. Giving its low signal intensity on the chromatogram, it is expected that its detection in the stoichiometric flame is due to the higher fuel mole fraction, leading to a formation of a greater quantity of products. Ethyl formate, C_2H_5OCHO, was detected in both flames. Ethyl formate is not present in the Serinyel model; thus, the simulation of this species is only performed with the Tran model. The experimental and numerical results obtained on the ethyl formate mole fraction profile in both flames are presented in Figure IV.19.

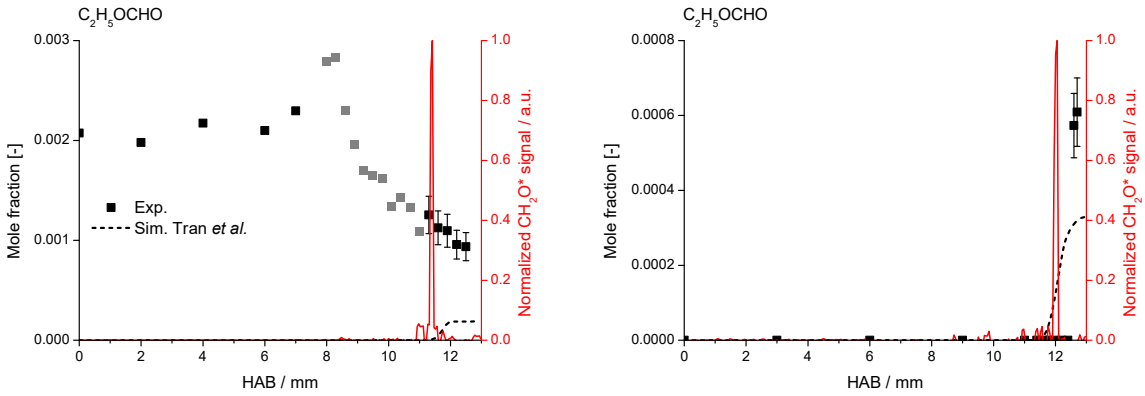

Figure IV.19. Ethyl formate mole fraction profiles in the $\phi = 0.5$ (left-hand side) and $\phi = 1$ cool flames (right-hand side).

As one can see in Figure IV.19, ethyl formate is formed in non-negligible quantity at the burner exit in the ozone-seeded cool flame and presents a mole fraction profile similar to reactants. It was initially assumed that ethyl formate was present as an impurity in the fuel tank, but no ethyl formate is detected upstream the O_3-free stoichiometric flame, which contradicts this assumption. A similar profile is obtained in the $\phi = 0.5$ cool flame for ethyl acetate, $C_2H_5OC(O)CH_3$, which is shown in Figure IV.20. In the case of ethyl acetate, this species was not observed in the $\phi = 1$ cool flame, i.e., without the presence of ozone. The simulated profile of ethyl acetate is also only shown with the Tran model as this species is not included in the Serinyel model. It is highly suspected that, given the important underprediction of these species by the Tran model in the presence of ozone, these species could come from direct interaction between O-atoms, produced by ozone decomposition, and the fuel radical, possibly inside the capillary.

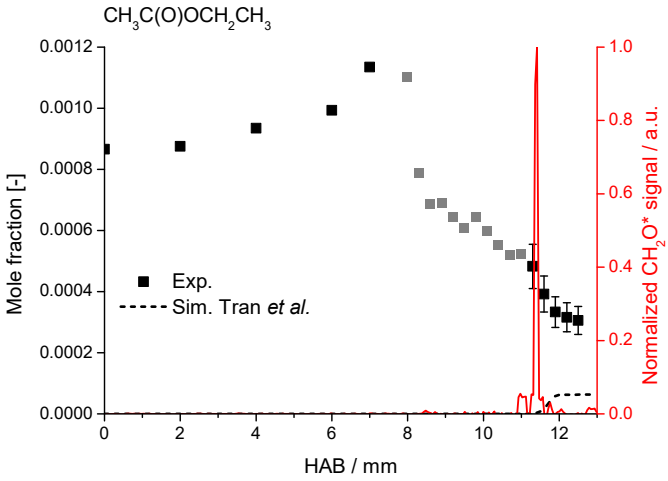

Figure IV.20. Ethyl acetate mole fraction profile in the $\phi = 0.5$, $\alpha = 50\ s^{-1}$, $x_{O3} = 1.4\%$ cool flame.

IV.2.4.2. Ozone influence on the LTC kinetics of diethyl ether

The current experimental conditions, in which the ozone concentration, the equivalence ratio and the strain rate were changed at the same time, make it difficult to precisely assess on the ozone impact on the cool flame, and more especially on the products distribution. To do so, a stoichiometric cool flame at x_{O3} = 1% was simulated in order to compare with the experimental ϕ = 1, x_{O3} = 0% cool flame. The ϕ = 1, x_{O3} = 1% cool flame was not experimentally studied, but is only presented to discuss the ozone influence on the cool flame. Firstly, Figure IV.21. shows the comparison of the temperature profiles of the ϕ = 1 flames both with and without O_3-addition. As expected, ozone addition significantly increases the cool flame temperature, of about 70 K. Its position is also shifted towards the burner exit, as ozone-addition tends to increase the flame speed of the cool flame. These results are consistent with the previous observations on ozone-seeded dimethyl ether cool flames presented in Section IV.1.

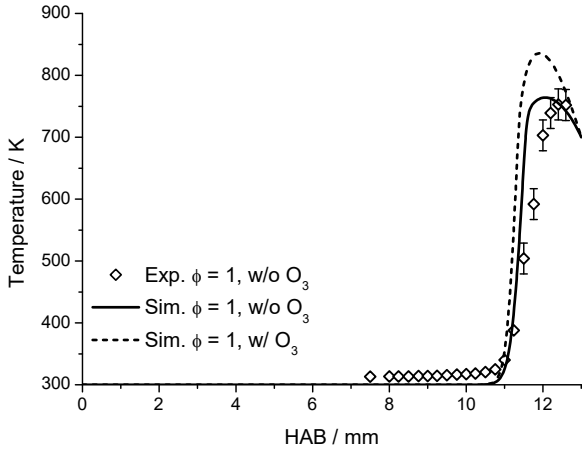

Figure IV.21. ϕ = 1 cool flame temperature profiles in the presence and absence of ozone.

Secondly, a comparison between the experimental and simulated species mole fraction profiles at ϕ = 1, with and without ozone, is plotted in Figure IV.22. These results were simulated using the Serinyel model, this choice being largely motivated by the fair prediction of this model regarding the fuel and oxygen conversion in the cool flame, as well as globally fair agreement on all the cool flame major and minor products, unlike the Tran model.

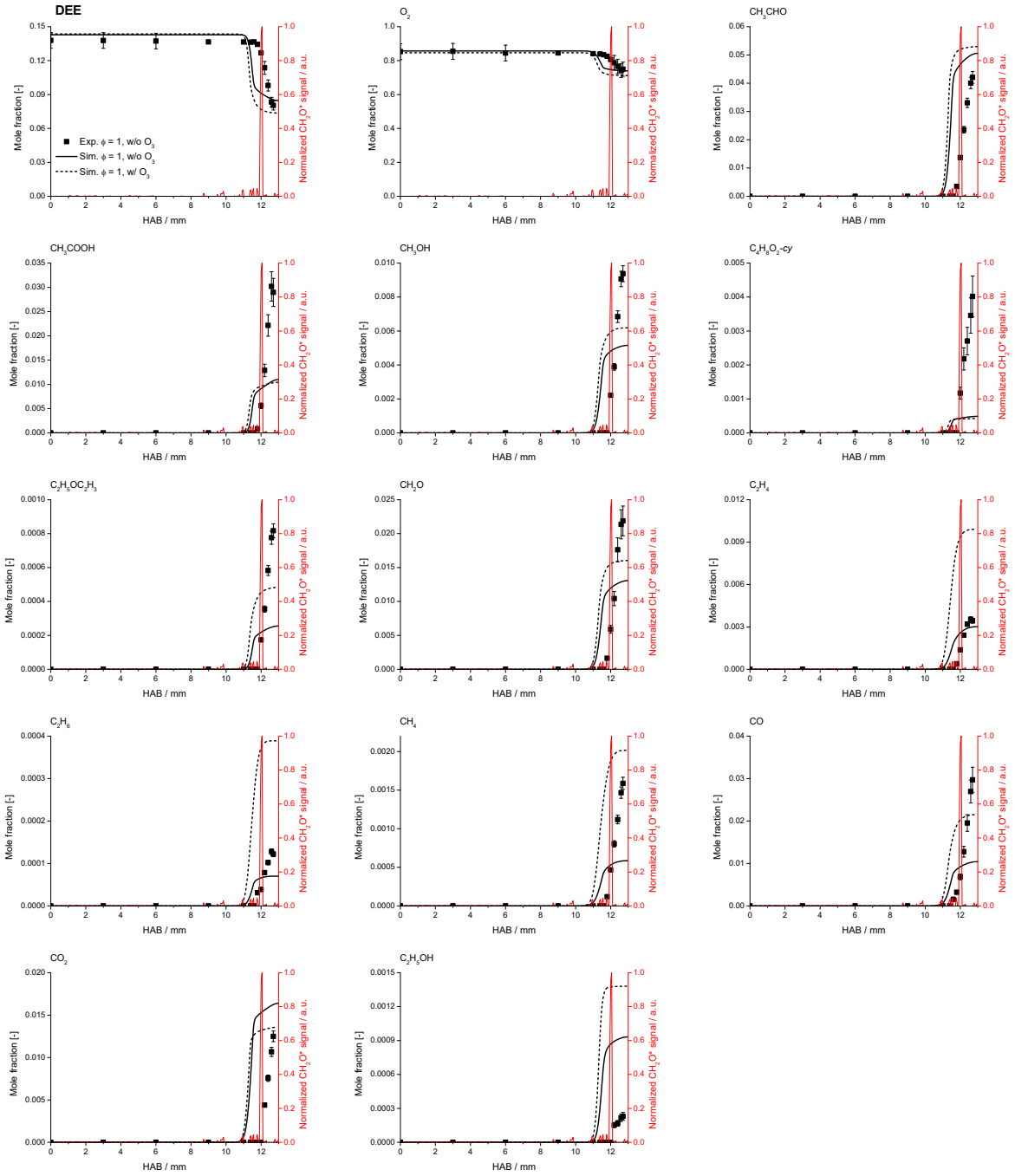

Figure IV.22. Experimental and simulated species mole fraction profiles in the $\phi = 1$, $x_{O3} = 0\%$ cool flame, and simulated results for the $\phi = 1$, $x_{O3} = 1\%$ cool flame. Black symbols are experimental results, continuous line simulated results without ozone and dashed line simulated results with $x_{O3} = 1\%$.

Comparing the simulated $\phi = 1$, $x_{O3} = 0\%$ to the $\phi = 1$, $x_{O3} = 1\%$ case evidences the effect of ozone on the cool flame. Adding O_3 to the reactive mixture increases the fuel consumption in the cool flame as the O-atom production from O_3 favours the H-atom abstraction by Ö or ȮH radicals on the fuel molecule. Consequently, the O_2 consumption is also increased. On the products side, the formation of each species, with the exception of CO_2, is increased in the cool flame, which is expected to be a direct consequence of the increased fuel conversion in the cool flame. Few species, such as acetic acid,

CH_3COOH, or 2-methyl-1,3-dioxolane, $C_4H_8O_2$-*cy*, are almost insensitive to the ozone-addition to the cool flame.

To gain further insight into the formation pathways of the different species observed experimentally, a rate of production analysis was performed in the cool flame at 5% fuel conversion. At this low conversion rate, the kinetic analysis can precisely capture the initial stages of the cool flame. At this stage of conversion, the temperature is equal to 449 K in the $\phi = 0.5$, $x_{O3} = 1.4\%$ cool flame, 454 K in the $\phi = 1$, $x_{O3} = 0\%$ cool flame and 447 K in the $\phi = 1$, $x_{O3} = 1\%$ cool flame. It illustrates the effect of ozone on the onset temperature of the low-temperature combustion that slightly decreases. At 5% fuel conversion in the flame, respectively 15% and 18% of the ozone is converted in the $\phi = 0.5$ and $\phi = 1$ cool flame. The reaction pathway analysis is presented in Figure IV.23. For a comprehensive reading of the figure, fluxes are not indicated for values lower than 0.1%. The observed and quantified species in this study are highlighted by red rectangles. The bold numbers stand for the $\phi = 0.5$, $x_{O3} = 1.4\%$ condition, the italic numbers stand for the $\phi = 1$, $x_{O3} = 0\%$ condition and the underlined numbers stand for the $\phi = 1$, $x_{O3} = 1\%$ condition.

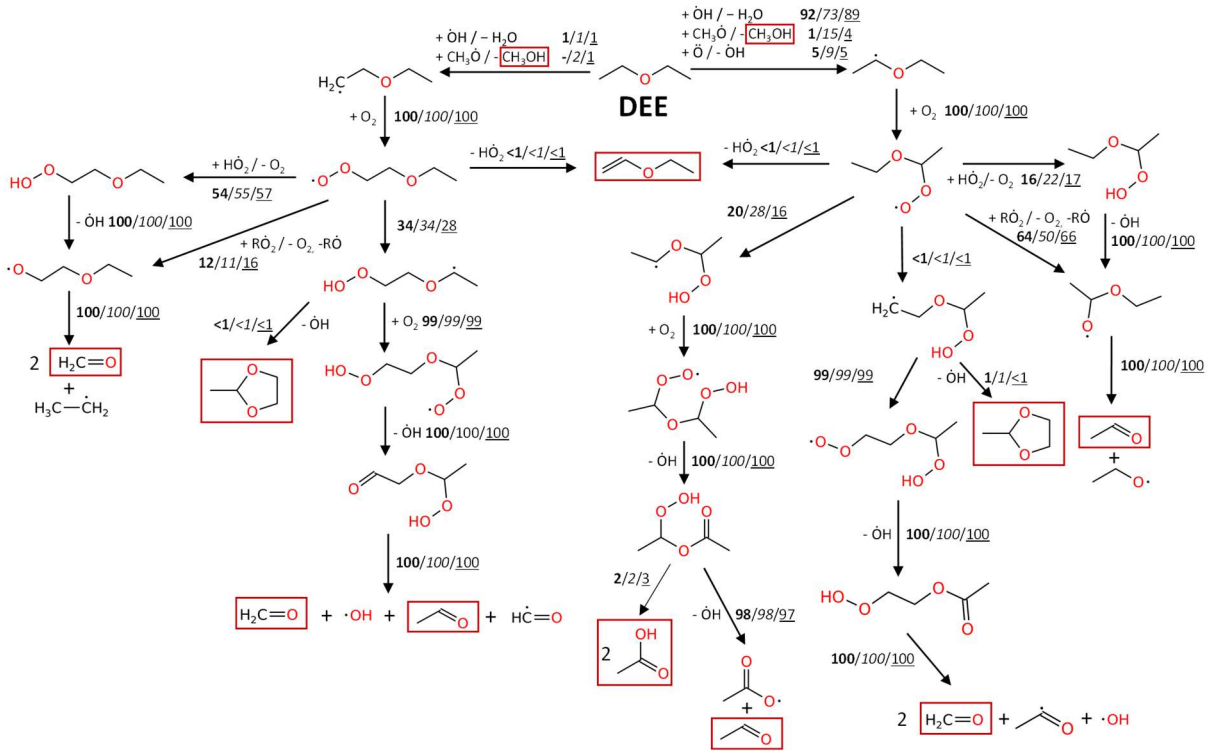

Figure IV.23. Rate of production analysis at 5% fuel conversion in a diethyl ether cool flame (T ~ 460 K) at the following conditions: $\phi = 0.5$, $x_{O3} = 1.4\%$ (**bold**), $\phi = 1$, $x_{O3} = 0\%$ (*italic*) and $\phi = 1$, $x_{O3} = 1\%$ (underlined).

In every condition H-atom abstraction reaction occurs preferentially on the α-position to the ether oxygen, which is consistent with previous studies [166,167]. It is explained by the weakened C-H bond on the α-position compared to the β-position, due to the closest presence of O-atom in the molecule,

inducing a negative inductive effect. In the lean ozone-seeded cool flame, 92% of the H-atom abstraction reaction takes place with ȮH radical, while it only represents 73% in the ϕ = 1 cool flame without ozone. The ozone decomposition upstream the flame front, especially forming O-atoms, which will subsequently yield ȮH radicals, can explain this difference. It is confirmed with the stoichiometric flame with x_{O3} = 1%, where the branching ratio of H-atom abstraction by the hydroxyl radical is increased in comparison with the same case without ozone. It is interesting to note that, from Figures IV.17 and IV.18, the experimentally measured CH_3OH mole fraction is two times higher in the ϕ = 1 case, which is consistent with the fact that H-atom abstraction on the fuel molecule by $CH_3\dot{O}$ is promoted in the absence of ozone. Finally, it should also be pointed out that, looking at Figure IV.22, the ozone addition in the stoichiometric cool flame leads to an increased formation of CH_3OH whereas the branching ratio relative to H-atom abstraction by $CH_3\dot{O}$ is reduced, hinting at another, ozone-dependent, formation pathway for CH_3OH.

The fuel radical can add to molecular oxygen, O_2, to form a RO$\dot{O}$ radical. In low-temperature oxidation conditions, it is expected that this radical undergoes internal H-atom migration reaction to form a $\dot{Q}$OOH radical, the $CH_3\dot{C}HOCH(OOH)CH_3$ radical being favoured in the studied conditions. However, as observed for dimethyl ether, at very low fuel conversion this pathway competes with the formation of R$\dot{O}$ radicals, that can be formed either by reaction with HO$\dot{O}$ and subsequent ȮH subtraction, or by reaction with another RO$\dot{O}$ radical. The branching ratio of RO$\dot{O}$ yielding R$\dot{O}$ radical is almost unchanged in the two ozone-seeded conditions, while it is slightly shifted towards the formation of $\dot{Q}$OOH, $CH_3\dot{C}HOCH(OOH)CH_3$, in the ozone-free flame. It supports the assumption that the presence of ozone, through the production of a consistent ȮH radical pool after its decomposition, weakens the dependence to the formation of the $\dot{Q}$OOH radical and its further decomposition forming hydroxyl radicals.

The Serinyel model describes the R$\dot{O}$ radical decomposition as the formation of CH_3CHO and $CH_3CH_2\dot{O}$. A number of studies, performed under atmospheric conditions, demonstrated that R$\dot{O}$ decomposition could yield different products, such as ethyl formate or ethyl acetate [241–244]. Including other decomposition pathways of R$\dot{O}$ could explain the slight overprediction of the acetaldehyde formation in the cool flame, as products from the R$\dot{O}$ decomposition will not majorly consist of acetaldehyde.

Interestingly, for the RO$\dot{O}$ radicals formed after $\dot{C}H_2CH_2OCH_2CH_3$ addition to O_2, i.e., from H-atom abstraction on the β-position, the branching ratio towards $\dot{Q}$OOH or R$\dot{O}$ radicals seems to be unaffected by both modifications of equivalence ratio and ozone concentration. It is however a minor pathway in the cool flame, which is not expected to largely influence the reactivity.

Finally, a brute-force sensitivity analysis was performed on the first-stage ignition delay time at T = 600 K using the Serinyel model. Three different conditions were also simulated, respectively ϕ = 0.5, x_{O3} = 1.4%, ϕ = 1, x_{O3} = 0% and ϕ = 1, x_{O3} = 1%, so that both the influences of ozone concentration & equivalence ratio can be discussed. The results are plotted in Figure IV.24. A positive sensitive coefficient indicates a decrease of the reactivity, and vice-versa.

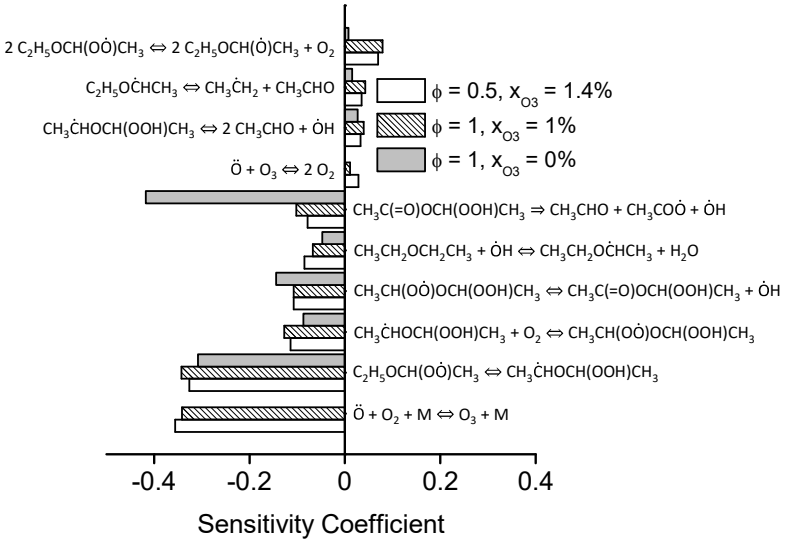

Figure IV.24. Brute-force sensitivity analysis on the first-stage ignition delay at T = 600 K, at ϕ = 1, x_{O3} = 1.4% (empty bar), ϕ = 1, x_{O3} = 0% (grey bar) and ϕ = 1, x_{O3} = 1% (dashed bar).

As expected, in both ozone-seeded conditions the most influent reaction is the O-atom production from ozone decomposition. The second most sensitive reaction is the ROȮ radical, $CH_3CH_2OCH(O\dot{O})CH_3$, H-atom internal migration reaction leading to the formation of ȮOOH, $CH_3\dot{C}HOCH(O_2H)CH_3$. As diethyl ether possesses two carbon-carbon bonds, the initial H-atom abstraction can occur both on the carbon in the α- or β-position, but preferentially occurs here on the α-position due to the presence of the ether functional group in the centre of the molecule. ȮOOH addition to O_2 and its further decomposition are also sensitive reactions in the three studied cases. The decomposition of one of the diethyl ether ketohydroperoxides, $CH_3C(=O)OCH(O_2H)CH_3$, forming acetaldehyde and two different radicals, $CH_3C(=O)\dot{O}$ and ȮH, is significantly more sensitive in the ozone-less condition than in both conditions where ozone is present in the mixture. It is directly linked to the ȮH production from ozone-decomposition, as previously addressed. Finally, it is interesting to note that the bimolecular reaction 2 ROȮ ⇒ 2 RȮ + O_2 is seen to increase the first stage ignition delay time, i.e., decrease the reactivity, whereas the equivalent reaction had the opposite effect in the case of dimethyl ether (see Section IV.1.5.1). This could be directly linked to the reactivity of the RȮ radical that only undergoes β-scission to form acetaldehyde in the present model.

IV.2.5. Conclusions on ozone and non-ozone seeded diethyl ether cool flames studies

This second section on the low-temperature combustion of ethers inside cool flames was dedicated to diethyl ether, $C_2H_5OC_2H_5$. To shed some light on the influence of ozone on LTC kinetics, two cool flame conditions were selected, respectively at $\phi = 0.5$ with $x_{O3} = 1.4\%$ and at $\phi = 1$ without ozone addition. Temperature and species mole fraction profiles were measured in both conditions, yielding useful experimental data. Two models from the literature, respectively from Tran and co-workers [167] and from Serinyel and co-workers [166,239], both coupled to an ozone-submechanism from Jian and co-workers [233], were used to simulate the experimental results.

As expected, ozone plays an important role in the flame stabilization in the lean condition. Temperature measurements showed that the presence of ozone in the flame also influences its heat release. Both tested models are able to accurately reproduce this trend. Ozone also slightly modifies the products distribution after the cool flame, as it increases the fuel conversion and constitutes an important source of hydroxyl radicals. Only one species, ethyl acetate, was detected in the ozone-rich flame while it was absent from the ozone-less cool flame.

Concerning the species mole fractions, the fuel and oxygen conversion is largely overpredicted in both cases by the Tran model while the Serinyel model closely agrees with the experimental results. Giving that methanol is also largely overpredicted by the Tran model in both cases, it is expected that the H-atom abstraction on the fuel molecule by $CH_3\dot{O}$ is responsible for this discrepancy. The comparison of these two experimental conditions with a third simulated cool flame ($\phi = 1$, $x_{O3} = 1\%$) allowed to discuss the effect of ozone on the cool flame more specifically. While ozone addition increases the fuel conversion and therefore products formation in the cool flame, it only plays a minor role on cool flame kinetics. Ozone-addition influences the H-atom abstraction on the fuel molecule, and the $RO\dot{O}$ branching ratio leading either to $\dot{Q}OOH$ or $R\dot{O}$ radicals. As previously shown for dimethyl ether cool flames, the formation of $R\dot{O}$ radicals cannot be neglected in ozone-rich conditions, and its decomposition pathways need to be properly considered in kinetic models.

IV.3. Low-temperature combustion of OME-2 inside cool flames

The last section of this chapter deals with the low-temperature oxidation of OME-2, $CH_3OCH_2OCH_2OCH_3$, inside stabilized cool flames. This work is part of a collaboration between the PC2A and the Laboratory for Chemical Technology (LCT) in Ghent. The main objective of this work is to build trustworthy kinetic models for large OMEs, starting with OME-2, and to further validate them against newly acquired experimental data using different setups: pyrolysis unit, rapid compression machine, cool flame burner, etc. In the scope of this work, the low-temperature oxidation of OME-2 was experimentally studied inside stabilized cool flames.

IV.3.1. Experimental & numerical conditions

Because of its low vapour pressure, OME-2 was added in small quantities inside dimethyl ether cool flames, in conditions close to the one previously studied in Section IV.1.1. The experimental conditions are listed below in Table IV.3. Two different equivalence ratios were selected, respectively $\phi = 0.3$ and $\phi = 0.5$, and the strain rate was fixed at $\alpha = 50\ s^{-1}$. Decreasing the equivalence ratio allowed to incorporate a slightly larger proportion of OME-2 in the mixture. OME-1, $CH_3OCH_2OCH_3$, was detected as an impurity in the fuel reservoir. As it is also an intermediate of the low-temperature oxidation of OME-2, its initial mole fraction was measured and is considered as a reactant in the simulations.

Table IV.3. Experimental conditions for the OME-2/DME cool flames stabilization.

Condition (%mol.)	ϕ	x_{O3}	x_{DME}	x_{OME-2}	x_{OME-1}	x_{O2}	α / s^{-1}
$2.5_{(OME-2)}/97.5_{(DME)}$	0.5	0.016	0.138	0.0035	$5.32 \cdot 10^{-5}$	0.84	50
$5_{(OME-2)}/95_{(DME)}$	0.3	0.02	0.085	0.0044	$6.68 \cdot 10^{-5}$	0.89	50

With regards to the kinetic modelling of those cool flames, a recently developed kinetic model dedicated to the low- and high-temperature oxidation of OME-2, developed at the LCT, was used [183]. An update of the present model was recently presented during the 39th Symposium on Combustion by the same group [245], the changes however mainly concerned the high-temperature combustion kinetics and this version was therefore not used in the present manuscript. The ozone submechanism used previously [233], was also coupled to the core mechanism.

The kinetic model for the combustion of OME-2 was constructed using the Genesys code [246]. The DME low-temperature chemistry inside the model is taken from the AramcoMech 1.3 model [146]. As the current model is still under development in order to precisely capture the low-temperature chemistry of OME-2, some reaction pathways are still not included, e.g., the addition of hydroperoxyl alkyl radical, ȮOOH, to molecular oxygen to form ȮOQOOH. It should finally be stressed out that the only modification brought, in this work, to the model from De Ras and co-workers concerns the H-atom abstraction by Ö on the OME-2 molecule. The original rate constant of this reaction was replaced by the

H-atom abstraction by Ö on dimethyl ether rate constant, following the study of Takahashi and co-workers [247], as the original rate constant was far too important.

IV.3.2. OME-2/DME cool flame temperature profiles

Following the same methodology than for the previous ethers, the temperature profiles of both cool flames, $\phi = 0.3$ (5% OME-2) and $\phi = 0.5$ (2.5% OME-2), were measured. The experimental results, along with simulations, are plotted in Figure IV.25. The Abel-inversed chemiluminescence profile is plotted in both cases. The absence of catalytic activity at the thermocouple surface was ensured by measuring the temperature profiles in both directions.

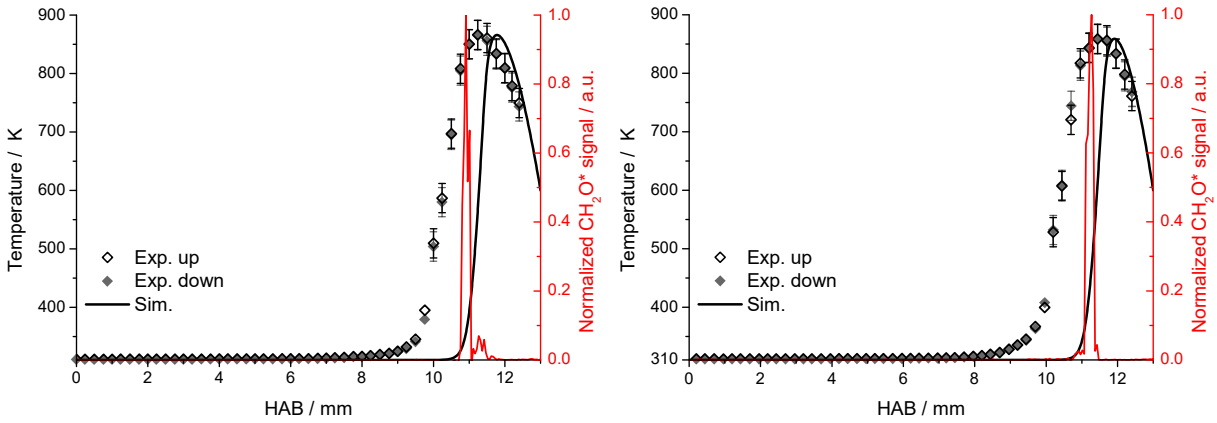

Figure IV.25. OME-2/DME cool flame temperature profiles, respectively at $\phi = 0.3$, $x_{O3} = 2.0\%$, 5% OME-2/95% DME (left-hand side), and $\phi = 0.5$, $x_{O3} = 1.6\%$, 2.5% OME-2/97.5% DME (right-hand side).

Given the very low amount of OME-2 added to the dimethyl ether cool flame in both cases, the temperature profiles are almost identical to those measured for pure dimethyl ether cool flames in Section IV.1.1. The maximum measured temperatures equal T = 866 K in the $\phi = 0.3$ cool flame and T = 859 K in the $\phi = 0.5$ cool flame. Both simulated cool flames predict a maximal cool flame temperature close to the experiments. The position at which this maximum temperature is predicted however deviates by roughly 300 µm from the experimental measurement, which is slightly superior to the experimental uncertainty (± 250 µm). The predicted cool flame position is closer to the plate, meaning that the simulated cool flame is slightly less reactive.

IV.3.3. Species distribution inside OME-2/DME cool flames

IV.3.3.1. Experimental & numerical results

In order to gain deeper insight into LTC kinetic of OME-2, reactants and intermediates were sampled and analysed above the burner. DME and OME-2 share many common oxidation products, and the only exclusive low-temperature intermediate of OME-2 that was detected during the speciation experiments is methoxymethyl formate, CH_3OCH_2OCHO. The fuels, DME and OME-2, along with the methoxymethyl formate and methyl formate, CH_3OCHO, mole fraction profiles are plotted in Figure IV.26 for the $\phi = 0.3$ (5% OME-2/95% DME) case and in Figure IV.27 for the $\phi = 0.5$ (2.5% OME-2/97.5% OME-2) case. The supplementary species mole fraction profiles, namely O_2, CH_3OH, CH_2O, CO, CO_2, OME-1 and O_3, can be found in Appendix IV.A7. The Abel-inversed CH_2O^*-chemiluminescence profile is also plotted. Deviation from the carbon balance, also provided in Appendix IV.A7, was verified in both cases and did not exceed 5% divergence.

Fuels follow the same trend in the cool flames, both of them being partially converted into low-temperature combustion products. The model tends to overpredict the OME-2 conversion in both conditions, the experimentally measured fuel conversion being roughly equal to 60% against 70% predicted by the kinetic model. The DME conversion is fairly predicted in the $\phi = 0.3$ (5% OME-2/95% DME) cool flame but slightly overpredicted in the other case. On the other hand, the methyl formate mole fraction is underpredicted by a factor 2 in both cases. It should however be noted that the modifications previously brought to the AramcoMech 1.3 mechanism (Section IV.1.1.1), which is the base mechanism for this OME-2 model, were not repeated in the present case as this study focusses on OME-2 oxidation. It explains the consistent underprediction of methyl formate formation in the simulated OME-2/DME cool flames. Finally, methoxymethyl formate was measured as the only specific product of OME-2 low-temperature oxidation, and its simulated mole fraction is underpredicted in both cool flames, the agreement at $\phi = 0.5$ being slightly better than in the $\phi = 0.3$ case.

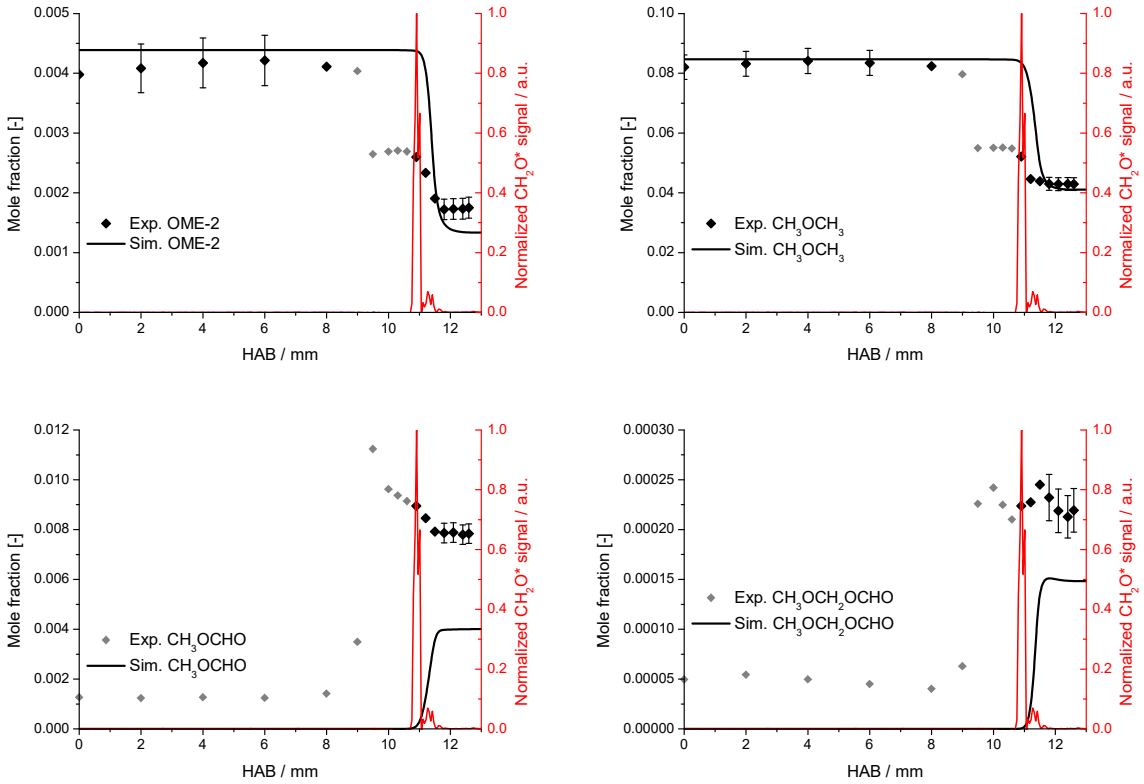

Figure IV.26. Fuels (OME-2 & DME), methoxymethyl formate and methyl formate mole fraction profiles in the $\phi = 0.3$, $x_{O3} = 2.0\%$, 5% OME-2/95% DME cool flame. Grey points represent in-capillary reactivity.

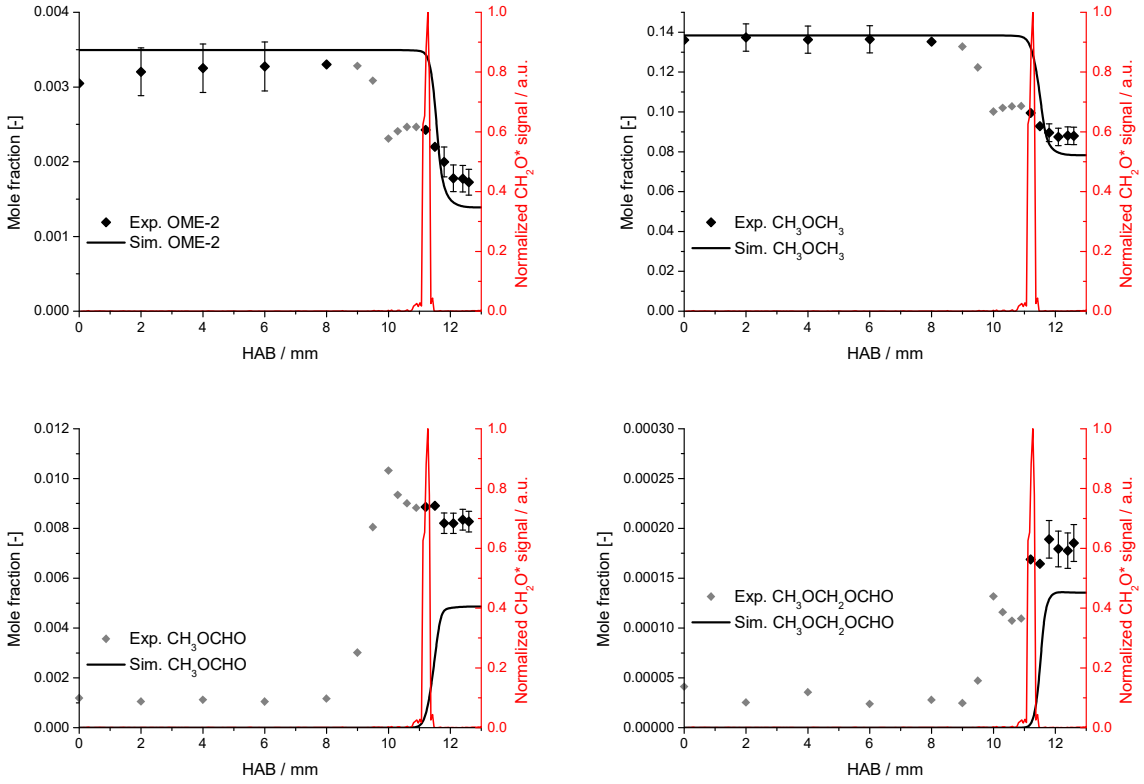

Figure IV.27. Fuels (OME-2 & DME), methoxymethyl formate and methyl formate mole fraction profiles in the $\phi = 0.5$, $x_{O3} = 1.6\%$, 2.5% OME-2/97.5% DME cool flame. Grey points represent in-capillary reactivity.

IV.3.3.2. Kinetic analysis

To support the discussion on the previously presented species mole fraction profiles, both rate of production and sensitivity analyses were performed and are presented hereafter. Firstly, a sensitivity analysis on the first-stage ignition delay time was performed at two different temperatures, respectively T = 450 K and T = 600 K. Results are plotted in Figure IV.28. The experimental condition ϕ = 0.3, x_{O3} = 2.0%, 5% OME-2/95% DME was chosen as the OME-2 mole fraction is the highest. Sensitive reactions belonging to DME or O_3 submechanisms are deliberately ignored, and thus do not appear in the figure.

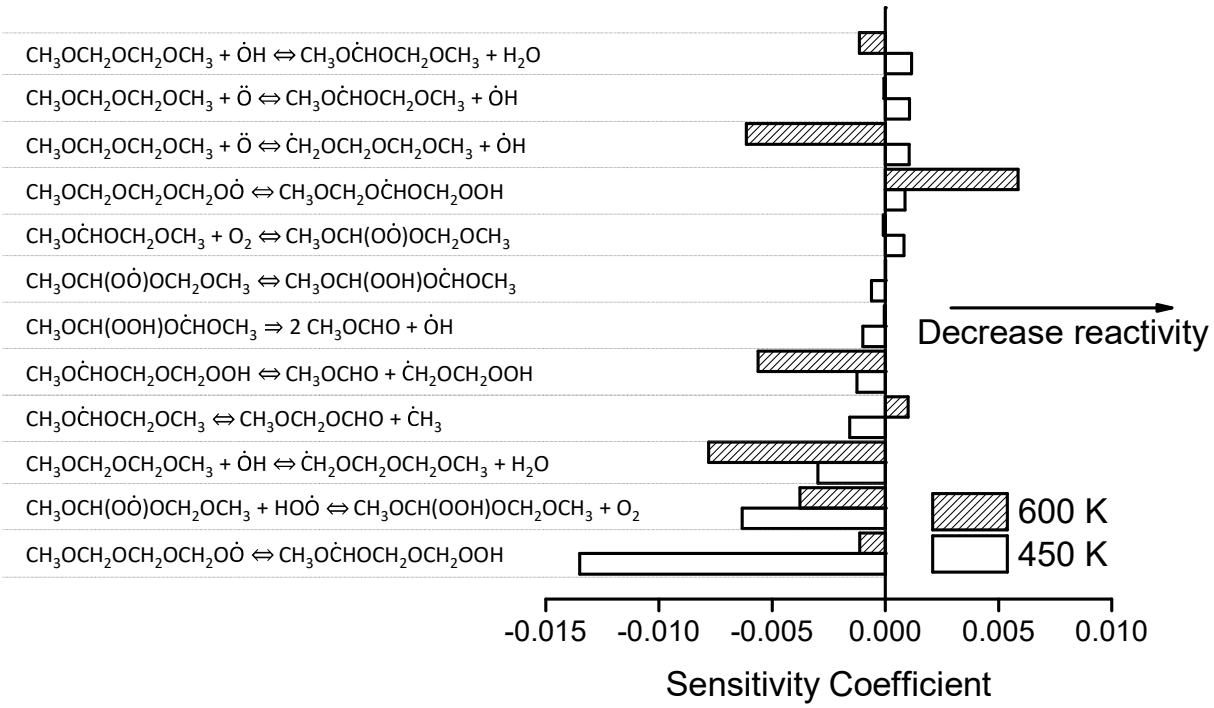

Figure IV.28. Sensitivity analysis performed on the first-stage ignition delay time at T = 450 K (white bar) and T = 600 K (dashed bar), for the condition ϕ = 0.3, x_{O3} = 2.0%, 5% OME-2/95% DME.

At 450 K, the most influent reaction is ROȮ (O_2-addition on primary carbon site) H-atom internal migration reaction, forming ȮOOH, while it is interestingly almost non influent at 600 K. H-atom addition to ROȮ forming ROOH, as well as H-atom abstraction by ȮH on the primary carbon site of the fuel molecule, is seen to increase the reactivity at both temperatures. H-atom abstraction by Ö on the primary carbon site of the fuel molecule inhibits the reactivity at 450 K while it is significantly positively influent at 600 K. The same is also true for H-atom abstraction on the secondary carbon site of the fuel molecule, although the effect is less significant. Reactivity thus seems to be controlled by H-atom abstraction on different fuel sites at 600 K, while it is more dependent on ROȮ radical chemistry at lower temperatures.

Finally, a rate of production analysis was performed in the ϕ = 0.3 (5% OME-2) cool flame at two different conditions, respectively 5% and 20% of OME-2 conversion in the cool flame. The corresponding temperatures are 480 K (5% conversion) and 630 K (20% conversion), which closely correspond to the temperatures used for the sensitivity analysis on the first-stage ignition delay. The main oxidation pathway for OME-2 is plotted in Figure IV.29. The red-squared species were experimentally identified and quantified within this work. As for the sensitivity analysis, only species belonging to the OME-2 submechanism are shown.

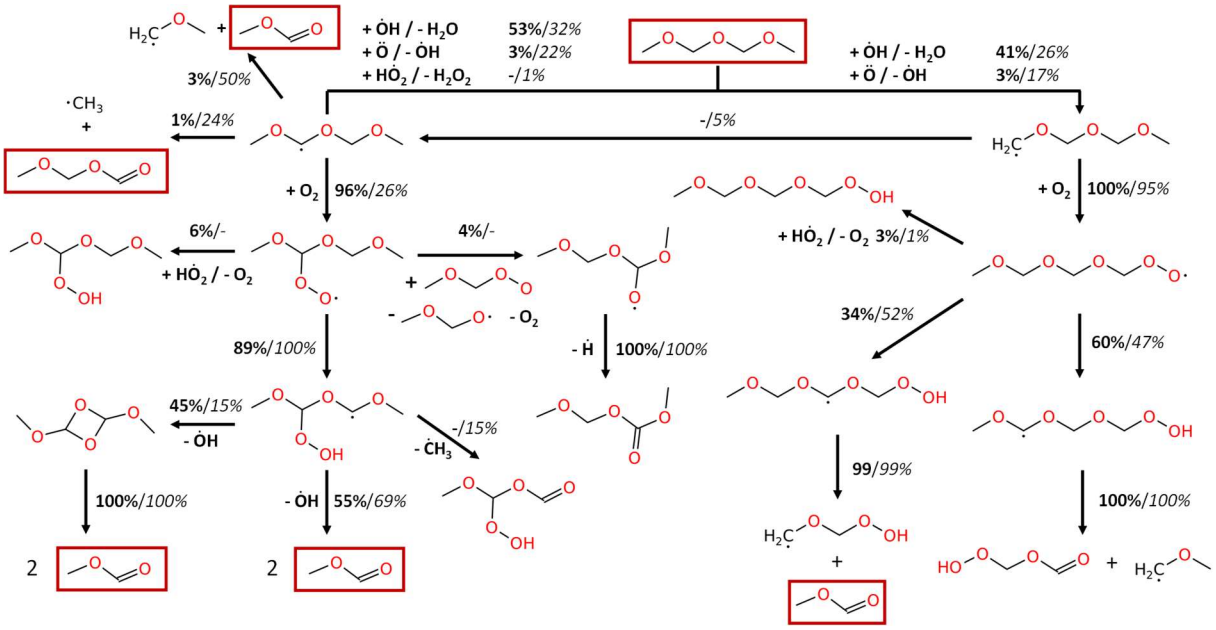

Figure IV.29. Rate of production analysis performed in the cool flame at 5% OME-2 conversion (T = 480 K, **bold**) and 20% OME-2 conversion (T = 630 K, *italic*). Condition ϕ = 0.3, x_{O3} = 2.0%, 5% OME-2/95% DME.

The fuel oxidation starts via H-atom abstraction on OME-2, mainly operated by ȮH and Ö. H-atom abstraction on secondary carbons is only slightly predominant. There is however no strict consensus on the preferential H-atom abstraction site on OME-2. As the temperature increases, abstraction by O-atom is favoured in comparison to ȮH radical. This can be explained by the increasing conversion of ozone between these two conditions, as 25% of ozone is converted at 480 K while 50% of ozone is converted at 630 K, promoting the formation of Ö. It also explains why H-atom abstraction by Ö was seen to be more sensitive at 600 K than 450 K in Figure IV.28. Firstly, on the secondary carbon radical site, Ṙ mainly adds to molecular oxygen to form ROȮ at 430 K. This pathway however becomes minor at 630 K as β-scissions on primary and secondary carbons become predominant, leading to the formation of methyl formate and methoxymethyl formate. The fate of the ROȮ radical is almost similar at both temperatures, as it mainly undergoes H-atom internal migration to form the ȮOOH radical. At 480 K the latter decomposes directly yielding two methyl formate molecules, or via the formation of a cyclic ether which also leads to the formation of two methyl formate molecules. At 680

K the formation of cyclic ethers is hindered by the increasing importance of β-scissions, forming aldehydes. Secondly, on the primary carbon radical site, Ṙ mainly adds to molecular oxygen to form ROȮ. The fate of this ROȮ radical, for which the O-O group is located on the primary carbon site, is slightly different from the other one. ROȮ radical undergoes two different H-atom internal migration, respectively on the first and second closest carbons. Increasing the temperature between 480 and 630 K favours H-atom migration on the first closest carbon, located in the centre of the radical. Both formed radicals then undergo β-scission to form either an aldehyde or methyl formate.

One major difference between the presented oxidation pathway of OME-2 compared to those of DME and DEE is the absence of ROȮ + ROȮ reactions, yielding two RȮ and O_2. In the current condition, as the initial mole fraction of OME-2 is very low compared to DME, the effect of such bimolecular reactions is not expected to be significant. However, as previously discussed, these reactions are partly responsible for the formation of formate species in cool flames. In the current model, such reaction rates are taken as analogy from OME-1, and may need to be precisely addressed in the case of OME-2. Furthermore, the second addition of ȮOOH radicals to O_2 is not included for now in the kinetic model developed by the team working on OME-2 at the LCT. As these reaction pathways are known to be critical for cool flames chemistry, it is expected that simulated results can be improved to better match the experiments. As a closing to this section, the schematic potential energy surfaces for ȮOOH addition to molecular oxygen, calculated at the CBS-QB3 level of theory and shared by courtesy of Kevin De Ras (unpublished results yet), are shown in Figure IV.30. From current calculations, it is seen that ȮOOH addition to O_2 tends to form ketohydroperoxides or cyclic ethers, that are particularly important for OME-2 reactivity by producing hydroxyl radicals when decomposing. Cyclic ethers were however not detected in the present study.

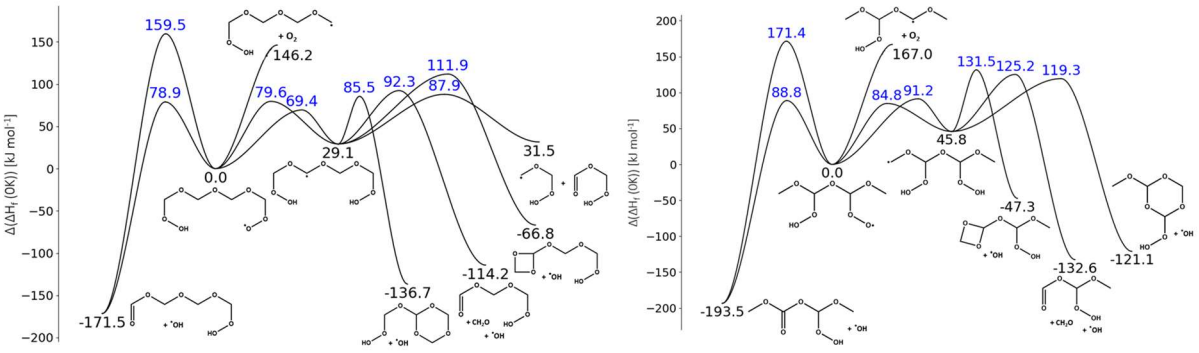

Figure IV.30. Schematic potential energy surface for ȮOOH addition to molecular oxygen. The values are CBS-QB3 calculated enthalpies of formation at 0 K relative to the sum of enthalpy of formation of both ȮOOH radicals (primary or secondary carbon site)

IV.3.4. Conclusions on OME-2 combustion in cool flames

This final section on the combustion of ethers in cool flames was dedicated to OME-2, $CH_3OCH_2OCH_2OCH_3$, in order to shed some light on its low-temperature oxidation kinetics.

To this end, two cool flames were stabilized, in the following conditions: i) $\phi = 0.3$, $x_{O3} = 2.0\%$, 5% OME-2/95% DME and ii) $\phi = 0.5$, $x_{O3} = 1.6\%$, 2.5%OME-2/97.5% DME. Temperature profiles and species mole fraction profiles were measured in both flames. The experimental results were then compared to the simulation using a recently developed model by De Ras and co-workers [248].

Comparison of the experimental and simulated temperature profiles shows a close agreement of the kinetic model regarding the maximum cool flame temperature. The positions of the simulated cool flames are however slightly shifted towards the heated plate, illustrating a lower reactivity of the simulated cool flames. With regards to the species mole fraction profiles that were measured as a function of the height above the burner, it was observed that OME-2 was partially converted in the cool flame, its conversion being however slightly higher than for dimethyl ether. The only exclusive product coming from OME-2 measured in the cool flames was methoxymethyl formate, which formation was underpredicted in both conditions by the kinetic model. The most sensitive reactions on the first-stage ignition delay of OME-2 are H-atom abstraction on the fuel molecule by Ö and ȮH, which represent almost 100% of the fuel conversion in the studied conditions as the temperature is not high enough to permit β-scission reactions to be competitive.

Finally, a rate of production analysis was performed in the cool flame to determine the different fuel consumption pathways. The H-atom abstraction takes place preferentially on the secondary carbons of the fuel molecule, possibly as a consequence of the presence of adjacent oxygen atoms. The Ṙ radical then undergoes either β-scission to form smaller molecules, especially when the temperature in the cool flame increases, or adds to O_2 to form ROȮ. The latter mainly undergoes H-atom internal migration to form ȮOOH, which tends to decompose in different smaller species, especially methyl formate. The second addition of ȮOOH to molecular oxygen is absent of the reaction pathway analysis as it was not included in the current model.

IV.4. General conclusion

In this chapter, three different ethers were studied in the newly developed stagnation plate burner: dimethyl ether (DME), diethyl ether (DEE) and oxymethylene ether-2 (OME-2). By a conjunction of different techniques, namely CH_2O-PLIF, CH_2O*-chemiluminescence, temperature measurements by thermocouple and species sampling and analysis with micro-gas chromatography, gas chromatography and mass spectrometry, the chemical structure of these flames was extensively studied for the first time.

The main interests here were to study i) the low-temperature combustion kinetics of these molecules inside stabilized cool flames, and ii) the influence of ozone on the reactivity and products distribution.

A significant effect of ozone was observed on both cool flame temperature and propagation speed, illustrated by their position displacement in the stagnation plate burner as ozone concentration in the mixture increases. As ozone decomposition before the flame front produces O-atoms, its main effect on the cool flame kinetics is the modification of the fate of the ROȮ radical. In non-ozone assisted conditions, the low-temperature oxidation chemistry is controlled by the formation and decomposition of ketohydroperoxides (KHP), which is supported by the formation of two ȮH radicals, responsible for the increase of the reactivity in the low-temperature domain. However, in the presence of ozone, as its decomposition generates an important pool of radicals, the influence of the KHP formation is weakened and alternative reactions become influent.

In the case of dimethyl ether, the increased importance of the biradical ROȮ + ROȮ reaction, yielding two RȮ radicals and molecular oxygen, explained the important production of methyl formate in the cool flame, that was initially significantly underpredicted by the AramcoMech 1.3 kinetic model. Modifications brought to the initial kinetic model allowed to better predict the species distribution downstream the cool flame.

For diethyl ether, the same reaction is also a significant reaction pathway. Direct comparison between ozone-seeded cool flames and a spontaneous cool flame, i.e., without ozone addition, confirmed the major role of ozone on this branching ratio. Moreover, ethyl acetate was experimentally measured in the ozone-seeded cool flame while it was not detected in the spontaneous cool flame, which supports the importance of RȮ radical related reactions, enhanced in the presence of ozone.

Finally, the low-temperature oxidation of OME-2 was experimentally and numerically studied in DME/OME-2 cool flames. The used model, under current development at the LCT, fairly well predicts the OME-2 conversion inside the cool flame. The formation of specific products of the low-temperature oxidation of OME-2 is however underestimated by the current model, stressing for further ameliorations, especially regarding the second addition of ȮOOH to molecular oxygen. In this precise case, the ROȮ + ROȮ reaction is not as significant as for the previous ethers, mainly due to the fact that in DME/OME-2 cool flames the fuel mole fraction is very low, which limits bimolecular reactions.

As a final comment on these three studies, one can note that if kinetic models are able, in most of the cases, to accurately predict global parameters concerning the cool flame (for example its temperature or its position), these models generally fail in precisely describing the chemical structure of cool flames. This reinforces the use of this newly developed experimental setup that constitutes an efficient tool for kinetic study of cool flames.

Chapter V. Laminar burning velocity of cool flames

V.Laminar burning velocity of cool flames

Previous laminar cool flame speed measurements from the literature were addressed in Section I.3.3, their scarcity being highlighted. The only available data for DME/O_2/O_3 cool flame Laminar Burning Velocities (LBVs) were measured by Hajilou and co-workers using the Hencken burner facility [49]. The authors reported a laminar burning velocity equal to 48.7 cm·s^{-1} for a ϕ = 0.6 cool flame, with an ozone concentration in the oxidizer stream of 6.1% and at low pressure, P = 7.3 kPa. Laminar flame speeds of DME/O_2/O_3 mixtures were also reported for equivalence ratios varying between 0.4 and 1.4, showing a significant monotonic decrease of the laminar burning velocity between ϕ = 0.6 and ϕ = 1.4. The lack of experimental data on laminar burning velocities of cool flames motivated the use of PIV to perform LBV measurements.

This final chapter presents the first (to the best of our knowledge) measurements of cool flame laminar burning velocities under atmospheric pressure. The second objective of this study is to assess the ozone-submechanism impact on the cool flame LBVs simulation, using newly acquired measurements as validation targets. Given the short duration of the experimental PIV campaign (2 weeks), these measurements were only realized in DME/O_2/O_3 cool flames.

V.1. Particle Image Velocimetry in reactive flow

V.1.1. Axial velocity profiles

The PIV setup, including particles generation and measurement, as well as the image post-process, were described in Section II.7. As an example, the axial velocity profile measured for a strained DME/O_2/O_3 cool flame at ϕ = 0.5, x_{O3} = 1.5% is pictured for five different inlet velocities u_{in} in Figure V.1. Compared to axial velocity profiles generally obtained in hot flames, the increase of velocity upstream the flame front is much less pronounced since the heat release of cool flames is significantly lower. The entire velocity profile is well defined in each condition, supporting the use of silicon oil droplets (Section II.7), as well as the selected image processing. As the inlet velocity increases, the flame moves towards the stagnation plate and the acceleration observed in the flame front is reduced in accordance with a decrease of the maximum flame temperature.

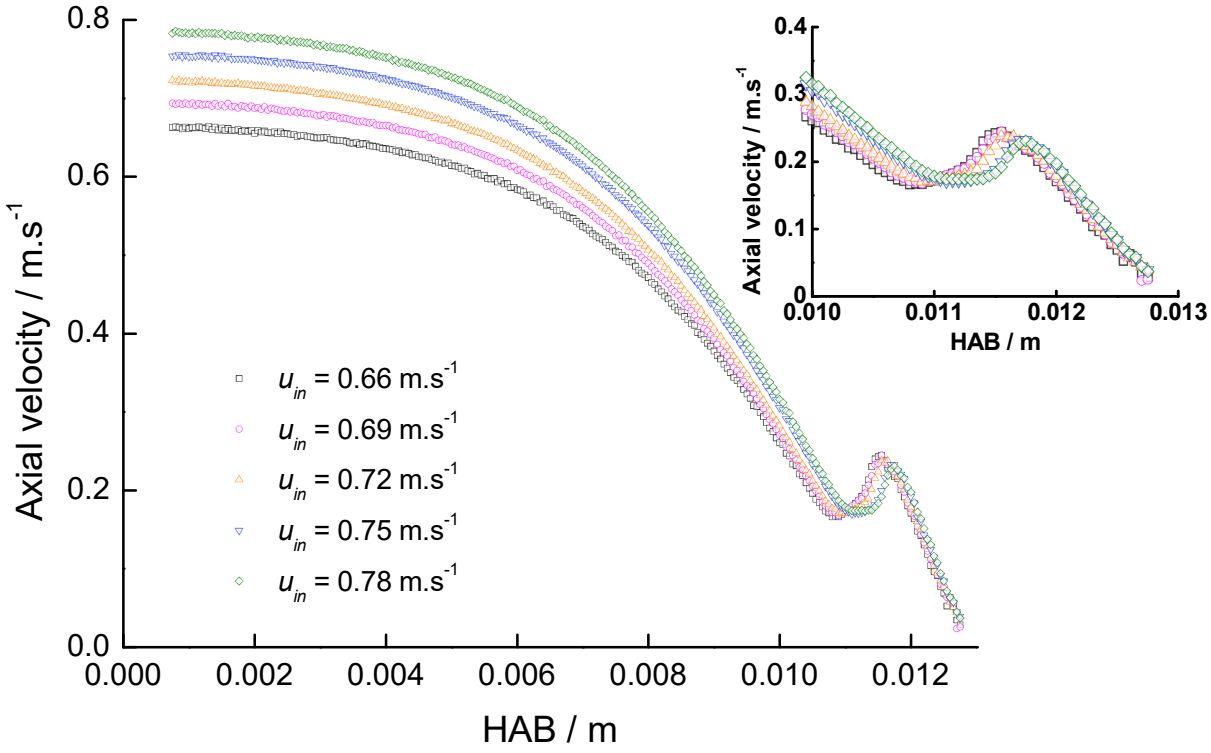

Figure V.1. Axial velocity profiles as a function of HAB of a DME/O_2/O_3 cool flame at ϕ = 0.5, x_{O3} = 1.5% at five different inlet velocities u_{in}.

V.1.2. Strain rate and flame speed determination

Two different data can be inferred from the axial velocity profile. The minimum velocity point in the axial profile is conventionally considered as the reference velocity, $S_{u,ref}$ [249]. Furthermore, the conventional definition of the strain rate, K, is based on the axial velocity gradient, as pictured in Figure V.2, which represents the principle of determination of the couple ($S_{u,ref}$; K). In the present case, it was chosen to determine the value of K at a fixed distance of 2 mm before the reference velocity position. To ensure reproducible determination of K, the experimental axial velocity profile was fitted using a 2nd-order polynomial function beforehand. The procedure is illustrated in Appendix V.A1. For a condition at which the strain is varied while the equivalence ratio and ozone concentration are kept constant, it is possible to measure several ($S_{u,ref}$; K) couples. The unstrained laminar burning velocity $S_{u,0}$ is then extracted from an extrapolation at K = 0. The extrapolation procedure will be discussed later in this chapter. It can furthermore be observed that at the position at which the minimum velocity is reached, the flame temperature roughly equals 400 K, which is below the vaporization temperature of the silicon oil droplets.

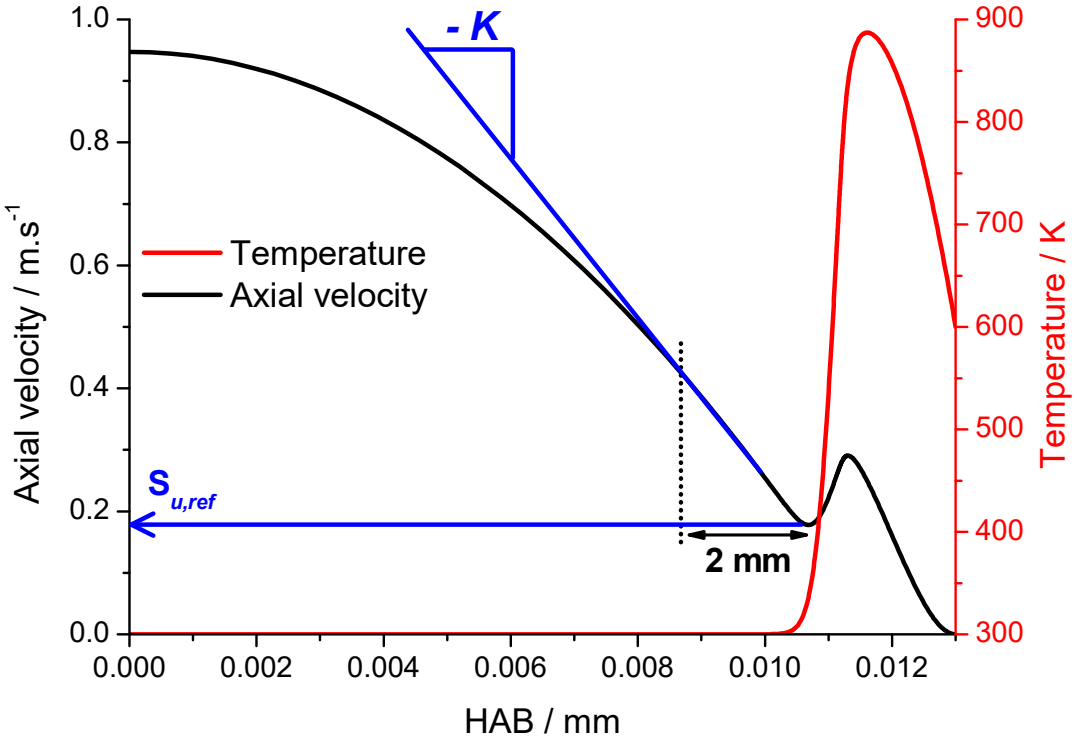

Figure V.2. Simulated axial velocity (black) and temperature (red) profiles of a cool flame. Determination of the couple ($S_{u,ref}$; K) is also shown.

V.2. Laminar burning velocity simulation

V.2.1. Kinetic models

In Chapter IV it was decided to use the ozone submechanism recently published by Jian and co-workers ('Jian model') [233] over previously published mechanisms, respectively by Zhao and co-workers ('Zhao model') [63] and Halter and co-workers ('Halter model') [219]. This choice is justified in the present chapter, as these three ozone-submechanisms were compared against flame speed measurements in different conditions. A summary of the different reactions and their associated Arrhenius rate constants is given in Appendix V.A2. Finally, concerning the dimethyl ether submechanism, it was chosen to use the modified version of the AramcoMech 1.3 model, i.e., the 'current model' used in Section IV.1.

Two different methods were tested within this work to simulate cool flames LBVs. The first method reproduces the experimental method, i.e., $S_{u,0}$ is determined from $S_{u,ref}$ = f(K) plots, using simulated cool flames in the stagnation flow configuration. With the other method, LBVs are simulated using the freely-propagating flame module of Chemkin-Pro. Advantages & drawbacks of both methods are discussed hereafter.

V.2.2. Stagnation flow flames simulation

The axial velocity profile for each flame condition was simulated with multicomponent transport using the Pre-Mixed Burner Stagnation Flame module of Chemkin-Pro 2021 [216]. The GRAD and CURV parameters were fixed at 0.03 each, resulting in ~ 450 points per simulation, which is sufficient to ensure accurate simulations of the reference axial velocity $S_{u,ref}$ within a 1% uncertainty, as demonstrated in Appendix V.A3. The Soret effect option was disabled for the axial velocity profiles simulations as it did not significantly modify the reference axial velocity while allowing a drastic reduction of the computational time, as shown in Appendix III.A4.

The modelling methodology of the stagnation plate burner was previously described in Section III.2. It was however slightly modified in the present case. An experimental axial velocity profile of a cool flame at $\phi = 0.5$, $x_{O3} = 1.5\%$ is pictured in Figure V.3, along with the simulated profiles considering different domain sizes. When modelling the axial velocity profile on the full burner/plate height, i.e., 13 mm, an important discrepancy between the experimental and simulated axial velocity profiles can be observed. It is consistent with previous studies that showed that 1-D approaches typically fail in providing accurate prediction of the corresponding velocity profile [250] and that the experimental outer flow field is neither a perfect plug nor potential flow [251]. Furthermore, effects such as gravity, thermophoresis or particles inertia, that are not considered in this work, could play a role in the discrepancy between the experimental and simulated velocity profile [252]. In order to circumvent this problematic, simulations were performed with intermediate flow boundaries, the size of the computational domain varying between $l = 0.0032$ m (3.2 mm) and $l = 0.013$ m (13 mm). For each domain size, the inlet conditions, respectively the inlet velocity and the radial strain rate, were inferred from the experimental velocity profile. Simulations better matches the experimental PIV profile when the size of the computational domain is reduced, as seen in Figure V.3. The insert in Figure V.3. presents the evolution of the standard deviation on the simulation of $S_{u,ref}$ depending on the size of the simulation domain, using the simulated $S_{u,ref}$ at $l = 0.0032$ m as reference (the closest from experimental measurement). As one can see, for domain sizes below $l = 0.0082$ m (8.2 mm), the simulated reference velocity does not significantly vary and remains within 1% of error when compared to the reference simulated velocity at $l = 0.0032$ m. However, when the computational domain size increases above $l = 0.0082$ m (8.2 mm), the simulated reference velocity deviates significantly. In this work, the inlet position of the simulation domain was fixed two millimetres before the minimum velocity upstream the flame front position. The computational domain length therefore lies between 3.05 and 4.45 mm, depending on the flame conditions. This methodology was already proposed elsewhere [93,253,254], allowing to better evaluate the kinetic model predictions against experimental data.

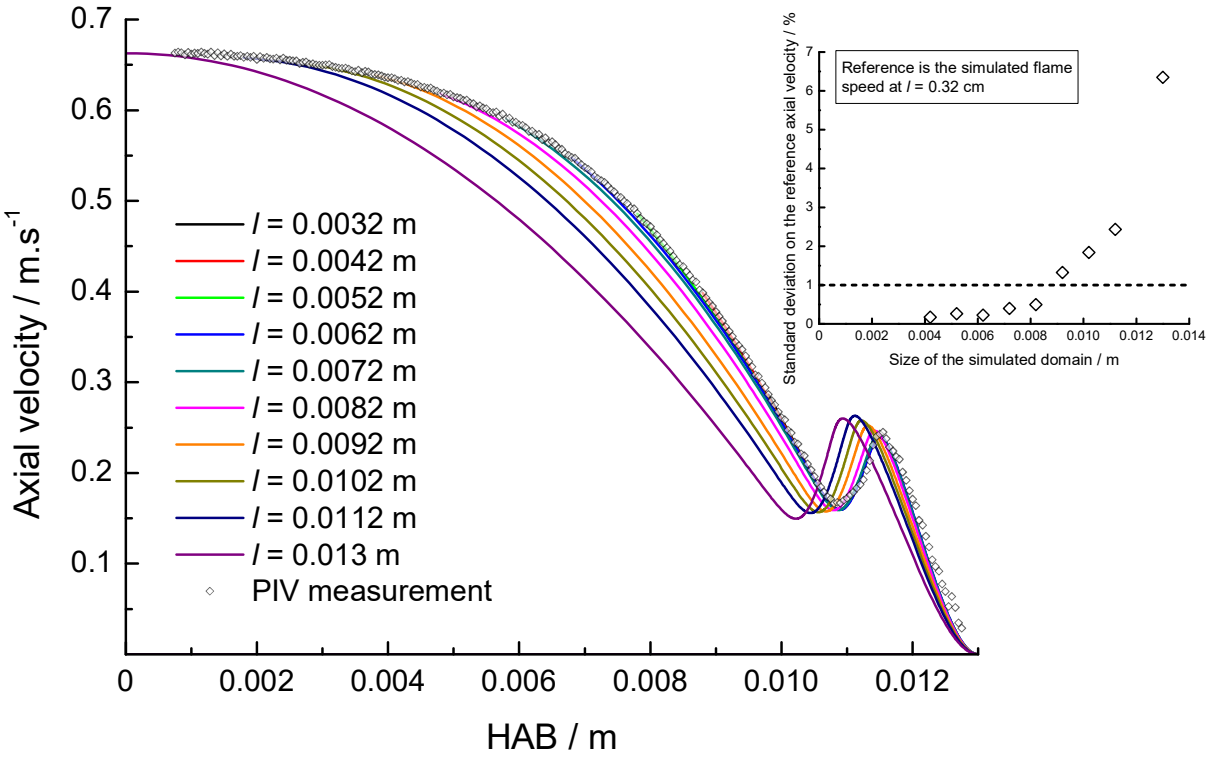

Figure V.3. Experimental (◊) PIV measurement of the axial velocity profile for the ϕ = 0.5, x_{O3} = 1.5% cool flame, and simulated (continuous line) profiles with different domain sizes. Simulations are performed with the O_3-submechanism from Jian and co-workers [233].

The influence of the computational domain size on one species mole fraction profile, CH_2O, and on the temperature profile of the ϕ = 0.5, x_{O3} = 1.5% cool flame was verified, and is provided in Appendix V.A4. While the influence of the computational domain size is negligible on the CH_2O mole fraction profile, one can observe that the simulated temperature profile is slightly more impacted. This stresses the need for further investigation, out of the scope of this work, on the 1-D simulation of the cool flames on the entire burner/plate height distance.

V.2.3. Freely-propagating flames simulation

Laminar, unstrained cool flame LBVs were also calculated using the Premixed Flame-Speed module of Chemkin-Pro 2021. The GRAD and CURV parameters were fixed at 0.04 each, ensuring ~ 330 points per simulation. Simulations were conducted using multicomponent transport data, and the Soret effect was considered as it slightly impacted the laminar burning velocity prediction. Few precautions were however necessary to avoid convergence towards a hot flame. In their work on propane [50] and *n*-heptane [52,56], Hajilou and co-workers faced the following problem: when simulating cool flames using the Premixed Flame-Speed module of Chemkin-Pro with a full detailed kinetic model covering both low- and high-temperature combustion domains, the simulation converged systematically towards a hot flame and not a cool flame. To avoid this problem, two solutions were proposed: i)

restricting the simulation domain size in order to avoid convergence towards a hot flame, or ii) reducing the kinetic model to withdraw the high-temperature part. In the present work, the first solution was chosen to model freely-propagating cool flames. To force the convergence of the solution to a cool flame, a temperature of T = 700 K is fixed at a location within the simulation domain, and the size of the domain is progressively reduced until a cool flame is obtained. It was verified that both the position and the fixed temperature did not significantly influence the LBV of the simulated cool flame as long as a 0-velocity gradient upstream the flame front was ensured. The LBV in then deduced from the initial flow rate in the unburnt mixture.

To illustrate this problematic, the simulated temperature profile of a freely-propagating flame at $\phi = 0.5$, $x_{O3} = 1.5\%$ is pictured in Figure V.4 for three different domain sizes, respectively $l_1 = 0.0115$ m, $l_2 = 0.013$ m and $l_3 = 0.0135$ m. In each of these cases, a temperature T = 700 K is fixed at l = 0.0095 m in order to facilitate the cool flame stabilization. A cool flame is successfully stabilized for the first domain size, $l_1 = 0.0115$ m, with a maximal temperature equal to $T_1 \sim 920$ K. The temperature after the flame front is almost constant, nearly forming a plateau. When the size of the domain is slightly increased to $l_2 = 0.013$ m, the profile shape is overall similar, its temperature however monotonically increases after the flame front until the end of the computational domain, leading to a final temperature equal to $T_2 \sim 1010$ K. Finally, when the size of the domain is increased up to $l_3 = 0.0135$ m, the simulation converges towards a hot flame, its temperature being constant and equal to $T_3 = 2870$ K. Situations corresponding to hot flame (l_3) and cool flame transitioning into a hot flame (l_2) were avoided by carefully selecting the computational domain size.

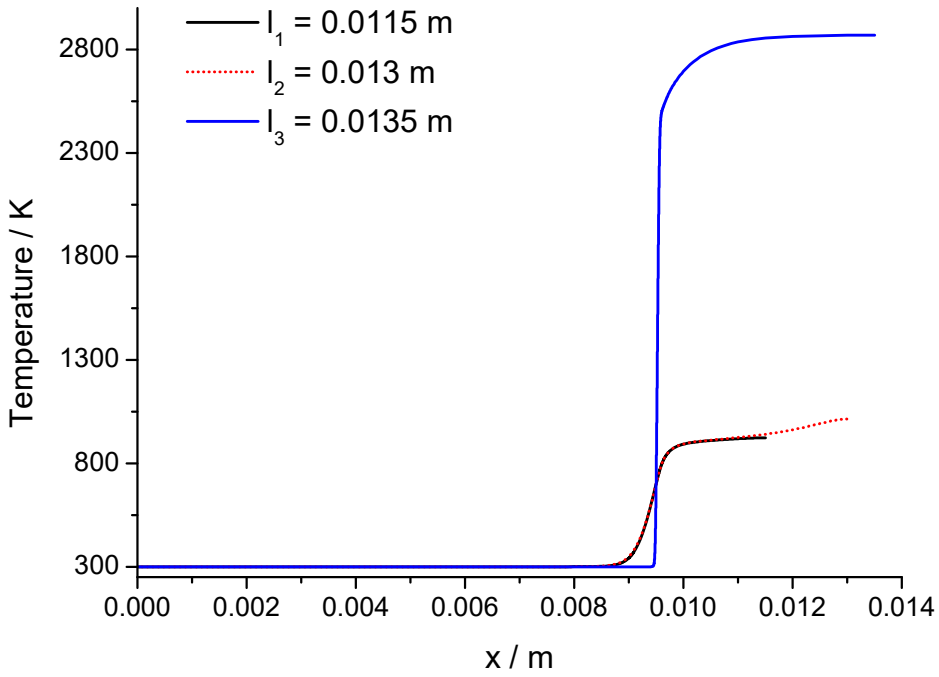

Figure V.4. Temperature profiles of simulated flames in the freely-propagating configuration, with different sizes of computational domain. Flame condition is $\phi = 0.5$, $x_{O3} = 1.5\%$.

V.3. Experimental determination of the laminar burning velocity

Five stable cool flame conditions were selected for the measurement of LBVs, and are summarized in Table V.1. Detailed conditions are presented in Appendix V.A5. Note that the inlet velocity (u_{in}) range is constrained by the stability domain of the cool flames. Furthermore, the cool flames tend to stabilize closer to the stagnation plate at high inlet velocities, leading to difficulties in resolving the entire velocity profile by PIV. On the contrary, the particle seeding is not sufficient at low velocities to provide accurate measurement of the velocity field in the burner.

Table V.1. Experimental conditions for the investigated DME/O_2/O_3 cool flames.

ϕ	x_{O3} / %	u_{in} / cm·s^{-1}
0.5	1.5	65 – 80
0.45	1.7	75 – 110
0.4	1.7	65 – 85
0.4	1.9	75 – 110
0.3	2.0	65 – 95

The first step in determining LBVs of DME/O_2/O_3 cool flames was to select the ozone-submechanism leading to the best prediction of the experimental results.

V.3.1. Comparison between experimental and simulated axial velocity profiles

The simulated axial velocity profiles using the three aforementioned ozone-submechanisms [63,219,233] were compared to the experiments. Two flame conditions at ϕ = 0.5, x_{O3} = 1.5% and ϕ = 0.3, x_{O3} = 2.0% are presented in Figure V.5 and Figure V.6 respectively. For the sake of brevity, the same comparisons for other flame conditions are presented in Appendix V.A6. Comparing the three O_3-submechanisms, large variations in the prediction of the velocity profiles can be observed between the Halter model and the two other models, with an important underprediction of $S_{u,ref}$ for the Halter model. It should be noticed that in the case ϕ = 0.3, x_{O3} = 2.0% (Figure V.6), the Halter model predicts almost no minimum velocity for the higher strain rates, but only an inflection of the axial velocity curve upstream the flame front. Predictions from the Jian model and Zhao model are comparable, as both models describe the overall velocity profile, however a slight discrepancy on the position of $S_{u,ref}$ is observed between the experiments and simulations. The observed discrepancy on the axial velocity profiles can also be observed when simulating the experimental temperature profiles with these three ozone submechanisms, which are provided in Appendix V.A7. The Halter model predicts in each case a lower cool flame temperature, which is consistent with a lower flame speed.

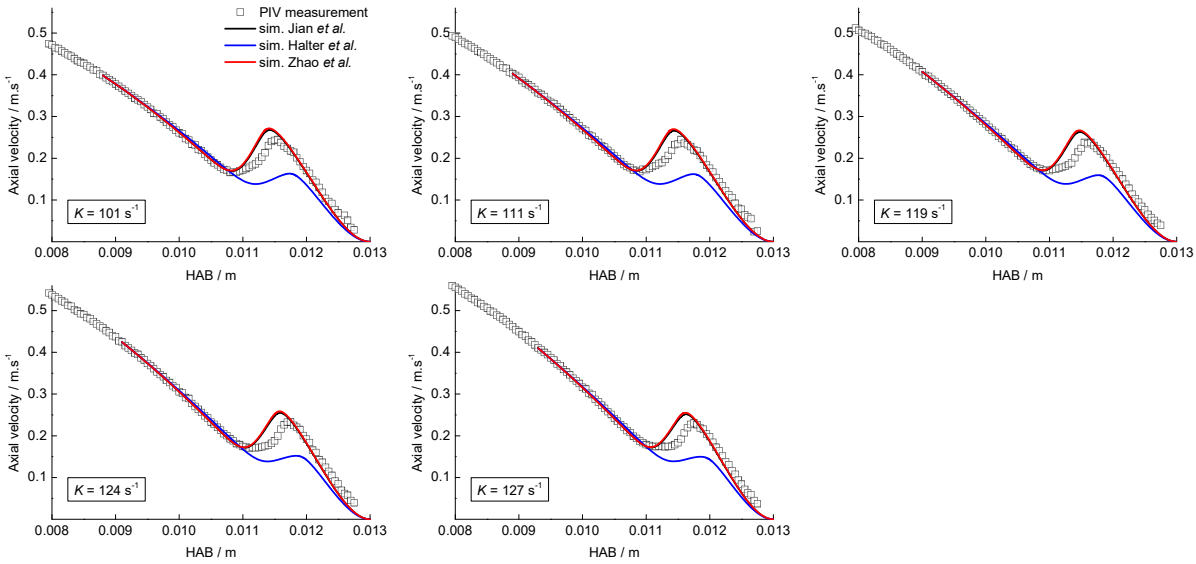

Figure V.5. Comparison between experimental axial velocity profiles measured by PIV (□) and simulated with the different O_3 submechanisms, for the cool flame at $\phi = 0.5$, $x_{O3} = 1.5\%$, at different strain rates.

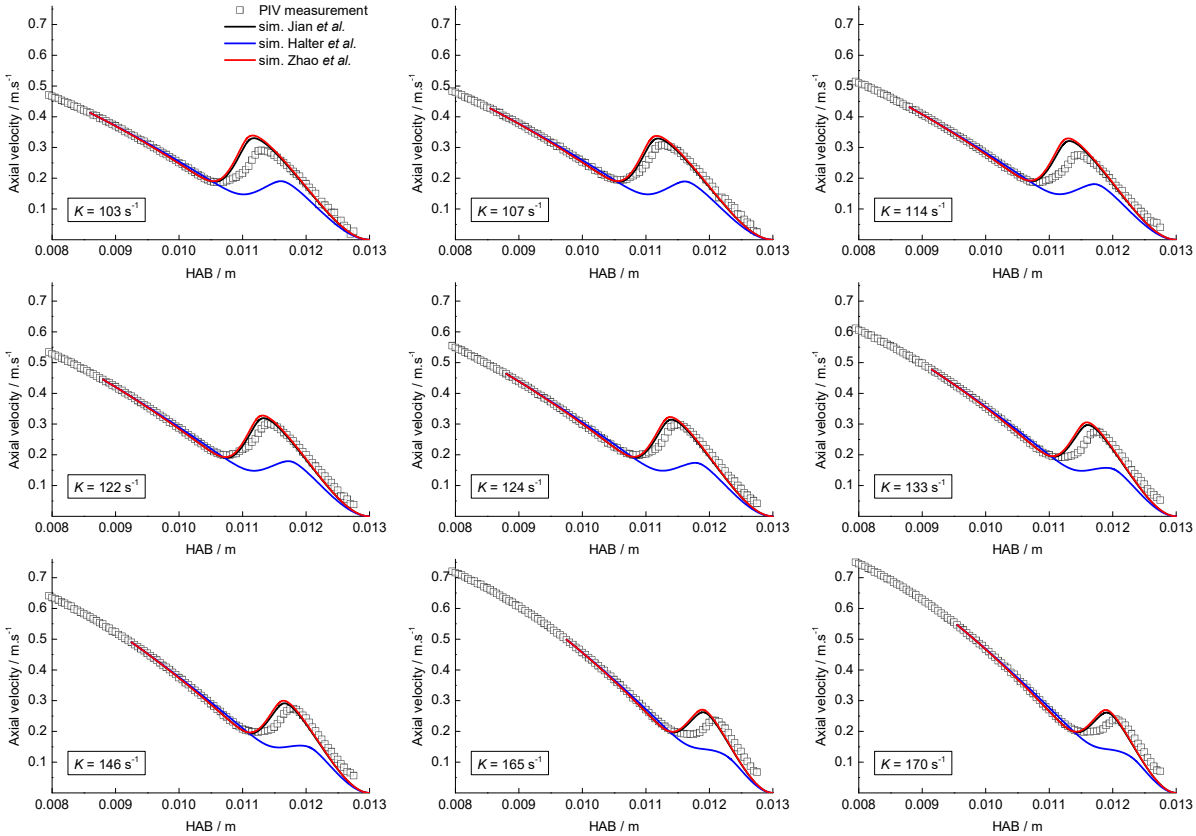

Figure V.6. Comparison between experimental axial velocity profiles measured by PIV (□) and simulated with the different O_3 submechanisms, for the cool flame at $\phi = 0.3$, $x_{O3} = 2.0\%$, at different strain rates.

In order to evaluate the capabilities of these models to predict LBVs, the Root-Mean Square Error (RMSE) between experimental and simulated $S_{u,ref}$ was calculated for the five cool flame conditions. For each flame, the strain rate K is varied within the flame stability domain, and the RMSE is determined as follows, n corresponding to the number of strain rate conditions:

$$RMSE = \sqrt{\frac{1}{n} \cdot \sum \left(S_{u,ref}^{exp} - S_{u,ref}^{sim} \right)^2}$$

The RMSE data are summed up in Table V.2. for each O_3-submechanism. One can see that the Halter model submechanism constantly exhibits the highest discrepancy on the value of $S_{u,ref}$, while the two other models yield similar performance.

Table V.2. Root-Mean Square Error (RMSE) calculated for each flame condition with the different ozone-submechanisms.

Condition	Root-Mean Square Error (RMSE)		
	Jian model	Halter model	Zhao model
ϕ = 0.5, x_{O3} = 1.5%	0.2	3.1	0.2
ϕ = 0.45, x_{O3} = 1.7%	0.2	4.5	0.4
ϕ = 0.4, x_{O3} = 1.7%	0.2	3.8	0.3
ϕ = 0.4, x_{O3} = 1.9%	1.2	5.9	0.7
ϕ = 0.3, x_{O3} = 2.0%	0.5	4.7	0.2

As previously suggested by the comparison of the axial velocity profiles, the Jian and Zhao models yield an excellent agreement with the experimental data, while the Halter model leads to an overall larger discrepancy. A possible explanation for the constant underestimation of the flame speed by the Halter model is its definition of the ozone decomposition reactions. While the ozone decomposition is declared using reactions with a third-body collision in the Jian model, and the Troe formalism in the Zhao model, meaning that every species can act as a collision partner, the only molecules participating in the ozone decomposition in the Halter model are N_2 through $O_3 + N_2 \Rightarrow O_2 + \ddot{O} + N_2$, O_2 through $O_3 + O_2 \Rightarrow O_2 + \ddot{O} + O_2$, and O_3 through $O_3 + O_3 \Rightarrow O_2 + \ddot{O} + O_3$. In our experimental conditions, the fuel mole fraction lies between 10 and 15% of the mixture. The absence of DME as collision partner in the ozone decomposition reaction can therefore lead to a lowered reactivity of the Halter model.

This comparison justifies that the ozone-submechanism from Jian and co-workers, because of its good performance in predicting $S_{u,ref}$ values and its more recent rate constants data, was chosen over the two other mechanisms. It also justifies its use in Chapter IV for the simulations of ozone-seeded DME, DEE and DME/OME-2 cool flames. For the following sections, the Jian model will be used solely.

V.3.2. Determination of the laminar burning velocity $S_{u,0}$

In the literature, a well-established method [255] is usually used to derive the unstrained LBV of hot flames. As previously discussed, from the plot of $S_{u,ref} = f(K)$, the extrapolation to strain rate $K = 0$ returns the LBV $S_{u,0}$. Both linear [256] and non-linear [87] extrapolation methods have been used in the past. Vagelopoulos and co-workers [255] and Chong and Hochgreb [90] have demonstrated that for low-strain rate hot flames (~ 50 – 250 s^{-1}), the linear extrapolation method yields accurate results within a reported uncertainty of ~ 1 – 2 $cm \cdot s^{-1}$. In the case of cool flames, for which the LBV is significantly smaller, this added uncertainty might however be problematic. The issue of non-linear extrapolation was revisited by Egolfopoulos and co-workers [91,257–259] with a computational approach, where the simulated $S_{u,ref}$ at various K (using a counterflow flame code) and the simulated $S_{u,0}$ at $K = 0$ (using a freely-propagating flame code) are fitted using a 2^{nd}-order polynomial function. This computed curve is vertically translated to best fit the experimental data, and the experimental LBV is derived from this non-linear extrapolation [259]. This method however requires using a kinetic mechanism that yields an accurate value of $S_{u,0}$.

In the present work, a similar approach was applied without using $S_{u,0}$ calculated from the freely-propagating flame module. Axial velocity profiles are simulated by progressively decreasing the strain rate, from which a numerical curve $S_{u,ref} = f(K)$ was extracted, as shown in Figure V.7. The numerical curve $S_{u,ref} = f(K)$ is then fitted using a 2^{nd}-order polynomial and vertically translated to best fit the experimental results. The experimental unstrained LBV is then considered at $K = 0$. Figure V.7. shows the application of this method for the five $DME/O_2/O_3$ cool flame conditions. As observed in Figure V.7. and discussed in the previous section, the numerical and experimental $S_{u,ref}$, and consequently $S_{u,0}$, lie very close to each other. Those values are given in Table V.3. for the five flames studied, and are compared with the calculated LBV considering a freely-propagating cool flame. While the agreement between the experimental $S_{u,0}$ and their simulations using the non-linear extrapolation is overall good, a difference of about 2 $cm \cdot s^{-1}$ is observed when comparing these values with the ones obtained using freely-propagating flames, the latter being systematically lower. This discrepancy in the predicted LBVs can be attributed to the non-adiabaticity of simulated cool flames using the freely-propagating option, as demonstrated by the non–completely horizontal asymptote observed downstream the flame front in Figure V.4 for the smallest computational domain. As the fuel conversion in only partial in the cool flame, burnt gases are not at the thermochemical equilibrium, causing non-zero temperature and velocity gradients. Thus, the freely-propagating simulation is expected to underestimate the LBV, and the numerical assisted non-linear extrapolation should be preferred.

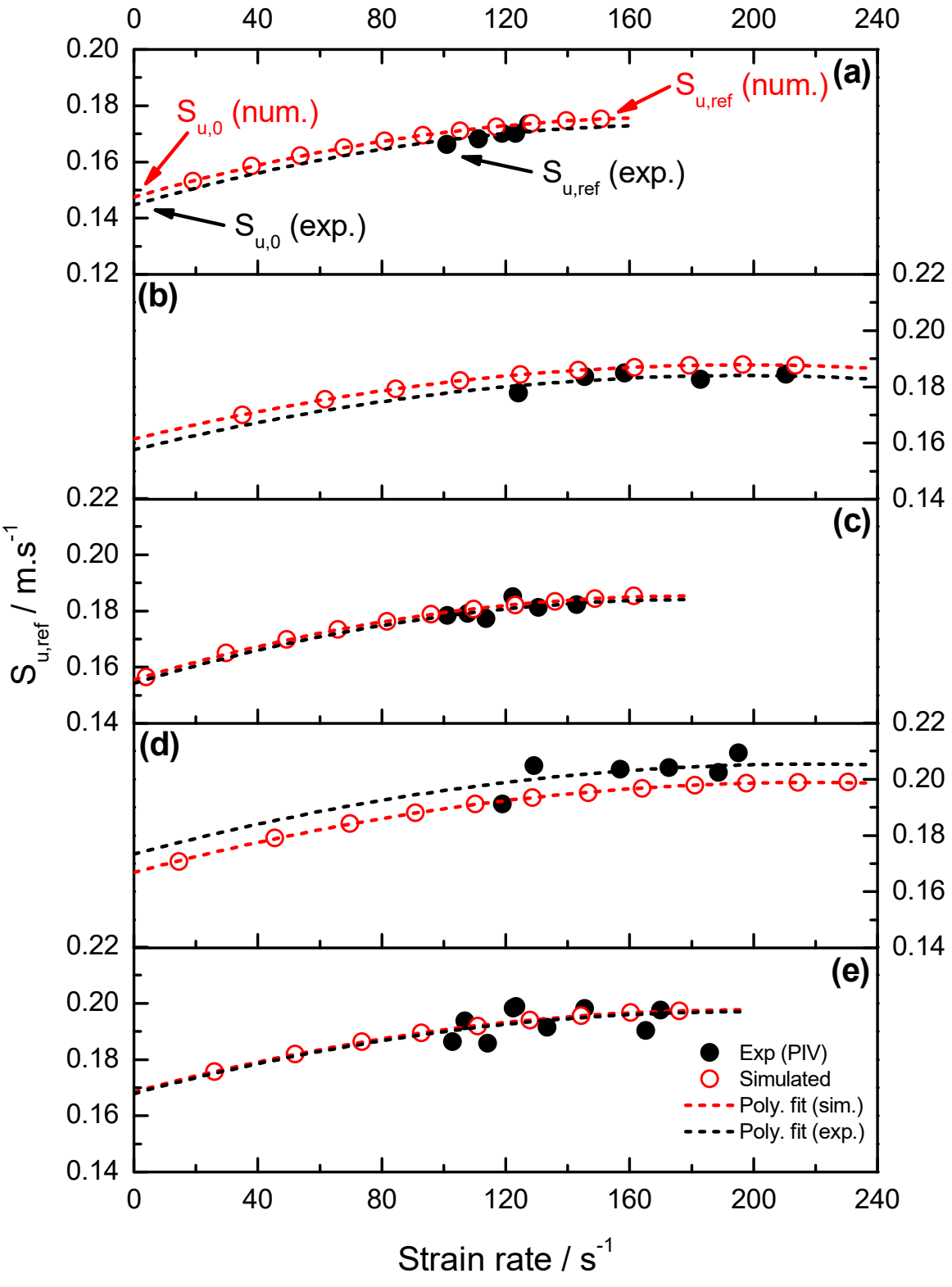

Figure V.7. Variation of $S_{u,ref}$ with K and determination of $S_{u,0}$ using a numerical assisted non-linear extrapolation. Flames conditions are: a) $\phi = 0.5$, $x_{O3} = 1.5\%$; b) $\phi = 0.45$, $x_{O3} = 1.7\%$; c) $\phi = 0.4$, $x_{O3} = 1.7\%$; d) $\phi = 0.4$, $x_{O3} = 1.9\%$; e) $\phi = 0.3$, $x_{O3} = 2.0\%$.

Table V.3. Experimental and simulated LBVs for each cool flame condition.

Flame condition	$S_{u,0}$ / cm·s^{-1}		
	Experimental from non-linear extrapolation	Simulated from non-linear extrapolation	Simulated from freely-propagating flame
$\phi = 0.5$, $x_{O3} = 1.5\%$	14.5 ± 1 cm·s^{-1}	14.7	12.8
$\phi = 0.45$, $x_{O3} = 1.7\%$	15.8	16.1	13.7
$\phi = 0.4$, $x_{O3} = 1.7\%$	15.4	15.6	13.6
$\phi = 0.4$, $x_{O3} = 1.9\%$	17.3	16.7	14.6
$\phi = 0.3$, $x_{O3} = 2.0\%$	16.8	16.9	14.7

By comparing both cool flames at x_{O3} = 1.7%, one can see that the cool flame LBV increases moderately as the equivalence ratio increases from 0.4 to 0.45. This effect is captured by both simulation procedures, but to a larger extent in the non-linear extrapolation case. A comparison of both flames at $\phi = 0.4$, respectively seeded with x_{O3} = 1.7% and x_{O3} = 1.9%, demonstrates the important effect of ozone addition on the cool flame LBV, which experimentally increases by about 2 cm·s^{-1} when the ozone mole fraction increases from 1.7% to 1.9%. Both simulation procedures however underestimate this effect.

V.4. Kinetic analysis

Sensitivity analyses were performed on the cool flame LBVs using the Chemkin-Pro PREMIX inbuilt utility. A positive sensitivity coefficient means that increasing the reaction rate constant of the associated reaction increases the cool flame LBV, and vice-versa. Two conditions were selected for the sensitivity analyses, respectively the flame at $\phi = 0.3$, x_{O3} = 2.0%, which contains the highest ozone mole fraction in this study, and the flame at $\phi = 0.5$, x_{O3} = 1.5%, which contains the lowest. The results are displayed for the 12 reactions with the highest absolute sensitivity coefficients in Figure V.8. As one can see, the most sensitive reactions on the laminar burning velocity are fuel-specific, and not coming from the O_3-submechanism. The most sensitive reaction on the LBV is the ȮOOH addition to oxygen to form a ȮOQOOH radical. ȮOOH can also undergo chain propagating reaction by β-scission. ȮOQOOH promotes the LBV by leading to the indirect chain-branching reaction sequence. The latter decomposes into an aldohydroperoxide, hydroperoxymethylformate $OCHOCH_2O_2H$, and a hydroxyl radical. The decomposition of hydroperoxymethylformate yields another ȮH radical, thus promoting the fuel consumption. To the contrary, ȮOOH decomposition forming ȮH and two CH_2O molecules is the reaction that inhibits the most the LBV. Other reactions involved into the indirect chain-branching reaction sequence, namely Ṙ addition to oxygen and further internal H-atom migration to the ROȮ radical forming ȮOOH, exhibit a positive sensitive coefficient regarding the cool flame LBV. By rapidly producing oxygen atoms, ozone decomposition promotes the combustion and increases the LBV. O-atoms and DME then react by H-atom abstraction producing hydroxyl radicals, which are also known

to participate in the conversion of the fuel by H-atom abstraction, which is the second most sensitive reaction in the present case. Thereby, ozone decomposition can lead to two successive H-atom abstraction reactions, as previously stressed in Chapter IV. One can observe that the sensitivity coefficient of the ozone decomposition reaction is higher in the $\phi = 0.3$ case, as the ozone mole fraction is higher in this case. On the other hand, in this condition most of the other sensitivity coefficients are smaller in comparison to the $\phi = 0.5$ case. This emphasizes the increasing influence of ozone as its concentration increases. Reactions inhibiting the LBV are also representative of the transition from the low- to the intermediate-temperature regime responsible for the Negative Temperature Coefficient such as the fuel radical β-scission.

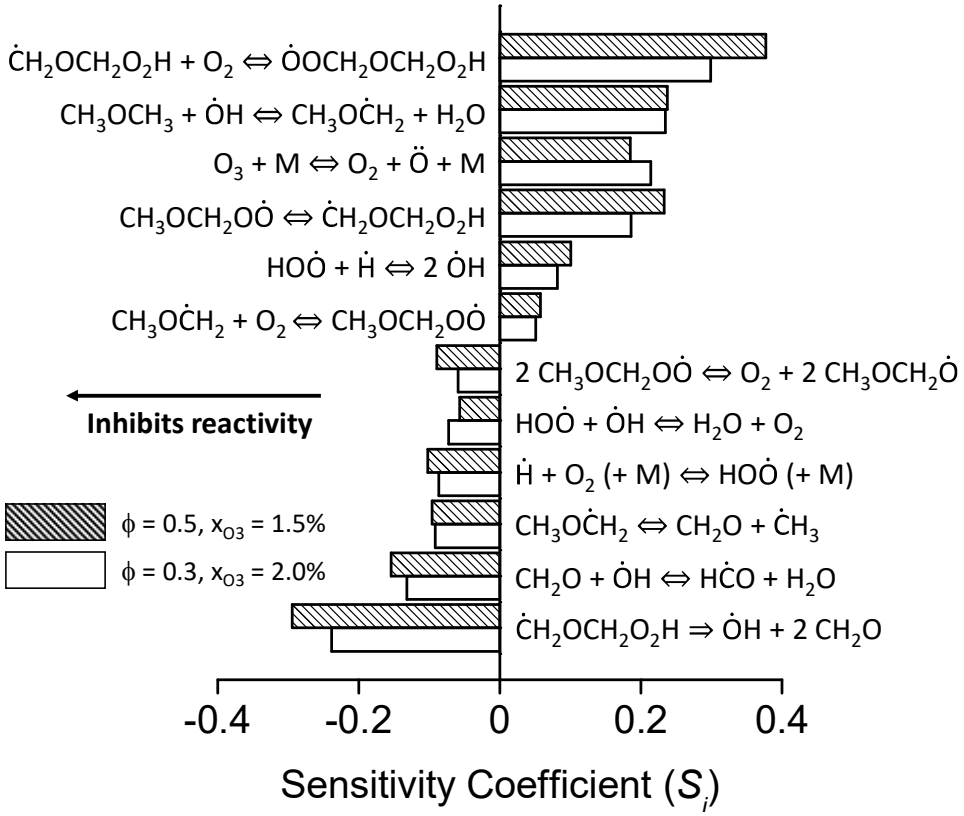

Figure V.8. Brute-force sensitivity analysis performed on the cool flame LBV, at $\phi = 0.5$, $x_{O3} = 1.5\%$ (dashed bar) and $\phi = 0.3$, $x_{O3} = 2.0\%$ (empty bar).

V.5. General conclusions

The last chapter of this manuscript introduced the measurement of cool flames laminar burning velocities, which was successfully achieved in the stagnation plate burner for the first time. The PIV technique was used to measure 2-D velocity profiles, from which axial velocity profiles were inferred to measure the cool flames LBVs. Five flame conditions, with equivalence ratios varying from 0.3 to 0.5 and ozone mole fractions varying from 1.5 to 2.0% were used to compare experimental results with kinetic modelling. To do so, the previously modified DME submechanism was used (Chapter IV.1),

coupled with three different ozone submechanisms, respectively from Jian and co-workers [233], Zhao and co-workers [63] and Halter and co-workers [219].

The comparison between experimental and simulated axial velocity profiles emphasized the importance of the ozone-submechanism on the flame speed simulation in our conditions. The Jian mechanism was selected among the others because of its good predictive ability of axial velocity profiles, and used to determine the unstrained laminar burning velocity $S_{u,0}$ for each tested condition. Two approaches towards the determination of $S_{u,0}$ were evaluated, the first one being based on a numerical assisted non-linear extrapolation method, and the second one on calculations of $S_{u,0}$ from freely-propagating cool flames simulations. The former method demonstrated better predictive ability and is recommended, when applicable, for the determination of $S_{u,0}$. However, for the purpose of kinetic mechanism validation, the direct comparison with the experimental axial velocity profiles should be preferred as it requires no numerical assisted method. Sensitivity analyses performed in two flame conditions demonstrated the particular importance of the low-temperature chain-branching reactions, and also the influence of ozone decomposition reactions, on the cool flames LBV. Even if ozone-addition significantly influences the laminar burning velocity of cool flames, fuel-specific reactions are still the most influent. It confirms the relevance of using ozone-seeded cool flames for LBV measurements in our experimental conditions.

Conclusions & outlook

This work aims at presenting a newly developed stagnation plate burner dedicated to the study of low-temperature combustion kinetics of various fuels. This burner, complementary to other experimental platforms such as JSRs or RCMs, offers a novel opportunity to investigate the structure of stabilized cool flames. The obtained experimental results were then compared to the simulation using detailed kinetic mechanisms, allowing to highlight the chemistry behind such flames.

The first chapter of this manuscript was dedicated to an overview of the work performed in the past on cool flames and low-temperature combustion kinetics of some ethers of interest. While cool flames were discovered a long time ago, little is known about them and much is to be discovered. It was notably highlighted that while low-temperature combustion kinetics of fuels are routinely studied under diluted conditions in reactors or in RCMs, kinetic studies were needed in flame conditions, allowing to couple kinetics, heat release and transport properties. While recent cool flames studies, mainly operated with ozone-adjunction to facilitate cool flames stabilization, allowed to better capture the kinetics of ignition and extinction of these flames, the literature lacks in data concerning their chemical structure. Furthermore, laminar burning velocities data of cool flames are almost inexistent in the literature, whereas it constitutes an important data regarding kinetic modelling. This assessment motivated the development of a new experimental platform, potentially offering the possibility to fill this gap.

The second chapter aimed at describing the stagnation plate burner, along with the different experimental techniques that were coupled to it in order to study the structure of cool flames. The burner configuration was first presented, including the gas supply and ozone production from oxygen. The optical diagnostics, respectively CH_2O*-chemiluminescence and CH_2O-PLIF, were then described. The objective of using these two diagnostics was to measure the flame front position of the cool flame in the burner. Their comparison showed that both techniques allowed to precisely locate the flame front, although the chemiluminescence technique led to a greater uncertainty, mainly due to the low-light emission from the cool flame and the need for a mathematical post-processing step of the raw-signal. Temperature measurements using a thin thermocouple were then presented. A number of tests were performed in order to qualify the interferences, or not, from heat losses or catalytic activity of the end flame temperature. The obtained results suggested that thermocouple measurements in cool flames could be performed without further corrections. It is mainly due to their lower temperature, compared to more common hot flames where radiative heat losses cannot be neglected. Species mole fraction measurement methodology was also presented. Coupling a variety of analytical techniques, respectively GC, µGC and QMS, allowed the detection and quantification of many intermediates resulting from the low-temperature combustion of the studied fuels. Finally, PIV measurements in the stagnation plate burner were also presented, motivated by i) the characterization of the velocity field in the burner in different reactive and non-reactive conditions, and ii) the measurement of laminar burning velocities of cool flames at atmospheric pressure. The difficulties in obtaining a sufficient particles density in the flow in

our experimental configuration required a specific data treatment that was presented, permitting to obtain an excellent spatial resolution.

In the third chapter was firstly presented the experimental stabilization procedure of cool flames in the stagnation plate burner. Cool flames were successfully obtained in a wide range of experimental conditions (strain rate, ozone concentration in the mixture, equivalence ratio) showing the convenience of such experimental configuration to study cool flames. The simulation of the stagnation plate burner was then addressed. The feasibility of simulating cool flames in a stagnation plate burner using a one-dimensional code was discussed regarding the different effects that could intervene in the experiments, while not being considered in the simulation. It was especially the case of buoyancy effect that could greatly affect the cool flame at low strain rates, i.e., low exit gas velocity. The influence of the nitrogen co-flow was also investigated in order to find experimental conditions where it did not significantly impact the cool flame. Finally, the simulation of species mole fraction profiles regarding the ozone decomposition in the burner was discussed, showing that perturbations in the measurement caused by the sampling capillary could be explained, and neglected to a certain extent.

The fourth chapter was dedicated to the low-temperature combustion kinetics studies of three different ethers, namely dimethyl ether, diethyl ether and oxymethylene ether-2. By a conjunction of different techniques presented in the second chapter, the chemical structure of these flames was extensively studied for the first time. The main interests behind these studies were i) to study the low-temperature combustion kinetics of these ethers inside stabilized cool flames and ii) to investigate the influence of ozone on the reactivity and products distribution. First of all, a significant effect of ozone was observed on both cool flame temperature and propagation speed, the latter being illustrated by its position in the stagnation plate burner. Concerning its influence on the cool flame kinetics, its main observed effect was the modification of the fate of the ROȮ radical. In non-ozone assisted conditions, the low-temperature oxidation chemistry is controlled by the formation and decomposition of ketohydroperoxides, which is supported by the formation of two ȮH radicals, responsible for the increase of the reactivity in the low-temperature domain. In the presence of ozone, as its decomposition generates an important pool of radicals, the influence of KHP formation is reduced and alternative reactions become influent. This behaviour was illustrated in the different studies using DME, DEE or OME-2 as fuels, and the main outcomes are listed below.

- In the case of dimethyl ether, the increased importance of the biradical ROȮ + ROȮ reaction, yielding two RȮ radicals and molecular oxygen, explained the important production of methyl formate in the cool flame, which mainly originated from the methoxymethoxy radical decomposition. Modifications brought to the initial kinetic model (AramcoMech 1.3) allowed to better predict the species distribution downstream the cool flame.

- For diethyl ether, the same reaction was also a significant reaction pathway. Direct comparison between ozone-seeded and spontaneous, i.e., without ozone addition, cool flames confirmed the major role of ozone on the branching ratio between the ROȮ radical isomerization and its self-reaction. Moreover, the formation of ethyl acetate was experimentally detected in the ozone-seeded cool flame while it was not detected in the spontaneous cool flame, which supports the importance of RȮ radical related reactions, enhanced in the presence of ozone.

- Finally, the study of the low-temperature oxidation of oxymethylene ether-2 was conducted by stabilizing ozone-seeded OME-2/DME cool flames. In the present case, the ROȮ + ROȮ reaction was not as significant as for the previous ethers, mainly due to the fact that the OME-2 mole fraction inside these cool flames was low, therefore limiting such biradical reaction. The formation of specific products of the low-temperature oxidation of OME-2 was however slightly underestimated by the developed model, stressing for further ameliorations, especially regarding the second addition of ȮOOH to molecular oxygen.

The final chapter of this manuscript consisted in the measurement of laminar burning velocities, which was successfully achieved in the stagnation plate burner configuration for the first time. Ozone-seeded dimethyl ether cool flames were selected for these measurements. The Particle Image Velocimetry technique was used to measure 2-dimensional velocity fields, from which axial velocity profiles were inferred to measure the cool flames laminar burning velocities. Cool flames stabilized at different equivalence ratios and ozone mole fractions were used to compare experimental results with kinetic modelling. These results notably highlighted the importance of a thoughtful choice of the ozone-submechanism, which greatly affected the predicted laminar burning velocity of cool flames. The obtained experimental results showed that the laminar burning velocities of lean, ozone-seeded, dimethyl ether cool flames lied between 14 and 18 $cm \cdot s^{-1}$, which is significantly lower than hot flames LBVs in similar conditions. While ozone-addition significantly influenced the LBVs of cool flames, kinetic analysis showed that the most influent reactions were fuel-specific and not related to the ozone-submechanism, which confirmed the relevance of using ozone-seeded cool flames for LBVs measurements in our experimental conditions.

Through these different studies using various ethers as fuels, it was highlighted that while kinetic models were able, in most of the cases, to accurately predict global parameters concerning the cool flame, as its temperature profile along the burner axis, these models frequently failed in precisely describing the chemical structure of cool flames. This assessment reinforced the use of this newly developed experimental setup, that constitutes an efficient tool for kinetic studies of cool flames, in experimental conditions that were only scarcely approached until now.

It is now time to address a few perspectives that could be considered following the present work. The considered perspectives are divided in four different categories, that are detailed below.

As previously addressed, this stagnation plate burner offers the opportunity to study low-temperature combustion kinetics of different fuels in conditions far different from those generally met in RCMs or in JSRs, which are routinely used for LTC studies. LTC kinetics of fuels can be studied in 'pure' conditions, as it was the case for dimethyl ether and diethyl ether, or as blend, e.g., OME-2 in the present work. While this work focussed on ethers, any fuel can be used, either pure or blended, depending on its low-temperature reactivity. Furthermore, alkenes are known to directly react with ozone, through ozonolysis reactions. The study of their oxidation kinetics inside stabilized, ozone-seeded, cool flames is therefore very interesting in order to evaluate the competitivity between low-temperature combustion and ozonolysis related reactions, and its impact on the cool flame structure.

Particle Image Velocimetry measurements inside stabilized dimethyl ether cool flames showed the feasibility of using this method to infer, from axial velocity profiles, the laminar burning velocities of cool flames. This methodology can then be used for various fuels, providing important data concerning the low-temperature combustion kinetics of these species. It will especially be done in a near future inside diethyl ether cool flames, this fuel being sufficiently reactive to ensure the stabilization of a cool flame without ozone-seeding. It will thus be possible to compare the cool flame propagation speed with and without-seeding. However, when comparing the axial velocity profiles on the entire burner length against simulation results, it was highlighted that 1-D approach failed in providing accurate prediction of the velocity profiles. A methodology was proposed in order to circumvent this problematic, but it stresses for further investigation concerning the simulation of cool flames using commonly used 1-D solver developed for hot flames.

Moreover, kinetic studies presented in Chapter IV were partially based on the measurement of species mole fraction profiles inside cool flames. In the present conditions, and using the available analytical techniques, only stable low-temperature combustion intermediates could be measured. In order to build trustworthy kinetic models, information on the formation and decomposition rates of reactive intermediates, such as ketohydroperoxides, are very important. Using recently developed high-resolution mass spectrometry techniques, their detection and measurement was made possible in diluted conditions in reactors. It is believed that the measurement of such species inside cool flames using the present experimental configuration can provide important information regarding these species. These experiments will be performed at the Synchrotron SOLEIL by coupling the cool flame burner with the DESIRS beamline and imaging spectrometer DELICIOUS3, based on the i^2PEPICO technique.

Finally, the last considered perspective about this work is the replacement of the ozone generator by a plasma. While ozone decomposition upstream the cool flame offers a suitable way to produce very reactive species enabling the ignition and stabilization of cool flames in a wide range of experimental

conditions, the use of a plasma would be closer to real applications. Thus, replacing the ozone generator by a DBD (Dielectric-Barrier Discharge) between two electrodes to stabilize cool flames would be very interesting from a kinetic point of view, as the composition of the plasma is much more complex than pure ozone delivered by the ozone generator.

Few is known about cool flames, and while this work allowed to shed some light on this topic, much is still to be discovered.

References

[1] bp Statistical Review of World Energy 2021, 2021.

[2] K. Kohse-Höinghaus, Combustion in the future: The importance of chemistry, Proc. Combust. Inst. 38 (2021) 1–56.

[3] H. Davy, VIII. Some new experiments and observations on the combustion of gaseous mixtures, with an account of a method of preserving a continued light in mixtures of inflammable gases and air without flame, Philos. Trans. R. Soc. Lond. 107 (1817) 77–85.

[4] W.H. Perkin, LVII.—Some observations on the luminous incomplete combustion of ether and other organic bodies, J Chem Soc Trans. 41 (1882) 363–367.

[5] H.J. Emeléus, CCCXCIV.—The spectra of the phosphorescent flames of carbon disulphide and ether, J Chem Soc. 129 (1926) 2948–2951.

[6] H.J. Emeléus, CCXXIX.—The light emission from the phosphorescent flames of ether, acetaldehyde, propaldehyde, and hexane, J Chem Soc. 0 (1929) 1733–1739.

[7] A.R.J.P. Ubbelohde, Investigations on the combustion of hydrocarbons I-The influence of molecular structure on hydrocarbon combustion, Proc. R. Soc. Lond. Ser. - Math. Phys. Sci. 152 (1935) 354–378.

[8] S. Gradstein, Über die Fluorescenz des gasförmigen Formaldehyds, Z. Für Phys. Chem. 22B (1933) 384–394.

[9] D.T.A. Townend, M.R. Mandlekar, The influence of pressure on the spontaneous ignition of inflammable gas-air mixtures. I. Butane-air mixtures, Proc. R. Soc. Lond. Ser. Contain. Pap. Math. Phys. Character. 141 (1933) 484–493.

[10] D.T.A. Townend, M.R. Mandlekar, The influence of pressure on the spontaneous ignition of inflammable gas-air mixtures. II. Pentane-air mixtures, Proc. R. Soc. Lond. Ser. Contain. Pap. Math. Phys. Character. 143 (1933) 168–176.

[11] L. Withrow, G.M. Rassweiler, Slow Motion Shows Knocking and Non-Knocking Explosions, in: SAE Trans., 1936: pp. 297–303.

[12] R.N. Pease, Characteristics of the non-explosive oxidation of propane and the butanes, J. Am. Chem. Soc. 51 (1929) 1839–1856.

[13] D.T.A. Townend, Ignition Regions of Hydrocarbons, Proc. Symp. Combust. 1–2 (1948) 134–145.

[14] O.V. Sokolov, Yu.V. Parfenov, V.S. Arutyunov, V.Va. Basevich, V.L. Vedeneev, Study of cool-flame phenomena during self-ignition of methane-oxygen mixtures, Russ. Chem. Bull. 45 (1996) 2316–2320.

[15] H.C. Bailey, R.G.W. Norrish, The oxidation of hexane in the cool-flame region, Proc. R. Soc. Lond. Ser. Math. Phys. Sci. 212 (1952) 311–330.

[16] W.G. Agnew, J.T. Agnew, Composition profiles of the diethyl ether-air two-stage reaction stabilized in a flat-flame burner, Symp. Int. Combust. 10 (1965) 123–138.

[17] A. Fish, I.A. Read, W.S. Affleck, W.W. Haskell, The controlling role of cool flames in two-stage ignition, Combust. Flame. 13 (1969) 39–49.

[18] S. Onishi, S.H. Jo, K. Shoda, P.D. Jo, S. Kato, Active Thermo-Atmosphere Combustion (ATAC) — A New Combustion Process for Internal Combustion Engines, SAE Trans. 88 (1979) 1851–1860.

[19] M. Noguchi, Y. Tanaka, T. Tanaka, Y. Takeuchi, A Study on Gasoline Engine Combustion by Observation of Intermediate Reactive Products during Combustion, SAE Trans. 88 (1979) 2816–2828.

[20] P.M. Najt, D.E. Foster, Compression-Ignited Homogeneous Charge Combustion, SAE Trans. 92 (1983) 964–979.

[21] R.H. Thring, Homogeneous-Charge Compression-Ignition (HCCI) Engines, in: SAE Tech. Pap., 1989: pp. 1–9.
[22] S.M. Aceves, J.R. Smith, C.K. Westbrook, W.J. Pitz, Compression Ratio Effect on Methane HCCI Combustion, J. Eng. Gas Turbines Power. 121 (1999) 569–574.
[23] L. Starck, B. Lecointe, L. Forti, N. Jeuland, Impact of fuel characteristics on HCCI combustion: Performances and emissions, Fuel. 89 (2010) 3069–3077.
[24] M. Richter, J. Engström, A. Franke, M. Aldén, A. Hultqvist, B. Johansson, The Influence of Charge Inhomogeneity on the HCCI Combustion Process, in: 2000: p. In press.
[25] X. Duan, M.-C. Lai, M. Jansons, G. Guo, J. Liu, A review of controlling strategies of the ignition timing and combustion phase in homogeneous charge compression ignition (HCCI) engine, Fuel. 285 (2021) In press.
[26] H. Xie, L. Li, T. Chen, W. Yu, X. Wang, H. Zhao, Study on spark assisted compression ignition (SACI) combustion with positive valve overlap at medium–high load, Appl. Energy. 101 (2013) 622–633.
[27] C. Journé, Moteur e-Skyactiv X : Mazda garde son avance, (2021). https://fr.mazda-press.com/actualites/2021/moteur-e-skyactiv-x--mazda-garde-son-avance/ (accessed May 27, 2022).
[28] F. Zhang, H. Xu, S. Zeraati Rezaei, G. Kalghatgi, S.-J. Shuai, Combustion and Emission Characteristics of a PPCI Engine Fuelled with Dieseline, in: SAE Tech. Pap., 2012: p. In press.
[29] D. Splitter, R. Reitz, R. Hanson, High Efficiency, Low Emissions RCCI Combustion by Use of a Fuel Additive, SAE Int. J. Fuels Lubr. 3 (2010) 742–756.
[30] R.D. Reitz, G. Duraisamy, Review of high efficiency and clean reactivity controlled compression ignition (RCCI) combustion in internal combustion engines, Prog. Energy Combust. Sci. 46 (2015) 12–71.
[31] M. Giannone, An Old Theory Goes Up in Cool Flames, (2012). https://www.nasa.gov/mission_pages/station/research/news/cool_flame.html (accessed September 19, 2022).
[32] V. Nayagam, D.L. Dietrich, P.V. Ferkul, M.C. Hicks, F.A. Williams, Can cool flames support quasi-steady alkane droplet burning?, Combust. Flame. 159 (2012) 3583–3588.
[33] T.I. Farouk, F.L. Dryer, Isolated n-heptane droplet combustion in microgravity: "Cool Flames" – Two-stage combustion, Combust. Flame. 161 (2014) 565–581.
[34] V. Nayagam, D.L. Dietrich, M.C. Hicks, F.A. Williams, Cool-flame extinction during n-alkane droplet combustion in microgravity, Combust. Flame. 162 (2015) 2140–2147.
[35] E.W. Anthony, Cool Flames Created During a First for International Space Station Research, Space Stn. Res. (2021). https://www.nasa.gov/mission_pages/station/research/news/Cool_Flames_First_for_ISS (accessed May 27, 2022).
[36] O. Herbinet, G. Dayma, Jet-Stirred Reactors, in: F. Battin-Leclerc, J.M. Simmie, E. Blurock (Eds.), Clean. Combust., Springer London, London, 2013: pp. 183–210.
[37] F. Battin-Leclerc, O. Herbinet, P.-A. Glaude, R. Fournet, Z. Zhou, L. Deng, H. Guo, M. Xie, F. Qi, Experimental Confirmation of the Low-Temperature Oxidation Scheme of Alkanes, Angew. Chem. 122 (2010) 3237–3240.
[38] H. Oshibe, H. Nakamura, T. Tezuka, S. Hasegawa, K. Maruta, Stabilized three-stage oxidation of DME/air mixture in a micro flow reactor with a controlled temperature profile, Combust. Flame. 157 (2010) 1572–1580.
[39] A. Yamamoto, H. Oshibe, H. Nakamura, T. Tezuka, S. Hasegawa, K. Maruta, Stabilized three-stage oxidation of gaseous n-heptane/air mixture in a micro flow reactor with a controlled temperature profile, Proc. Combust. Inst. 33 (2011) 3259–3266.

[40] S.S. Goldsborough, S. Hochgreb, G. Vanhove, M.S. Wooldridge, H.J. Curran, C.-J. Sung, Advances in rapid compression machine studies of low- and intermediate-temperature autoignition phenomena, Prog. Energy Combust. Sci. 63 (2017) 1–78.
[41] Y. Ju, C.B. Reuter, O.R. Yehia, T.I. Farouk, S.H. Won, Dynamics of cool flames, Prog. Energy Combust. Sci. 75 (2019) In press.
[42] C.B. Reuter, S.H. Won, Y. Ju, Cool Flames Activated by Ozone Addition, in: 53rd AIAA Aerosp. Sci. Meet., American Institute of Aeronautics and Astronautics, Kissimmee, Florida, 2015.
[43] Y. Ju, C.B. Reuter, S.H. Won, Numerical simulations of premixed cool flames of dimethyl ether/oxygen mixtures, Combust. Flame. 162 (2015) 3580–3588.
[44] C.B. Reuter, S.H. Won, Y. Ju, Experimental study of the dynamics and structure of self-sustaining premixed cool flames using a counterflow burner, Combust. Flame. 166 (2016) 125–132.
[45] C.B. Reuter, S.H. Won, Y. Ju, Flame structure and ignition limit of partially premixed cool flames in a counterflow burner, Proc. Combust. Inst. 36 (2017) 1513–1522.
[46] C.B. Reuter, R. Zhang, O.R. Yehia, Y. Rezgui, Y. Ju, Counterflow flame experiments and chemical kinetic modeling of dimethyl ether/methane mixtures, Combust. Flame. 196 (2018) 1–10.
[47] P. Zhao, W. Liang, S. Deng, C.K. Law, Initiation and propagation of laminar premixed cool flames, Fuel. 166 (2016) 477–487.
[48] T. Ombrello, C. Carter, V. Katta, Burner platform for sub-atmospheric pressure flame studies, Combust. Flame. 159 (2012) 2363–2373.
[49] M. Hajilou, T. Ombrello, S.H. Won, E. Belmont, Experimental and numerical characterization of freely propagating ozone-activated dimethyl ether cool flames, Combust. Flame. 176 (2017) 326–333.
[50] M. Hajilou, E. Belmont, Characterization of ozone-enhanced propane cool flames at sub-atmospheric pressures, Combust. Flame. 196 (2018) 416–423.
[51] M. Hajilou, M.Q. Brown, M.C. Brown, E. Belmont, Investigation of the structure and propagation speeds of n-heptane cool flames, Combust. Flame. 208 (2019) 99–109.
[52] M.Q. Brown, E.L. Belmont, Effects of ozone on n-heptane low temperature chemistry and premixed cool flames, Combust. Flame. 225 (2021) 20–30.
[53] M.C. Brown, E.L. Belmont, Experimental characterization of ozone-enhanced n-decane cool flames and numerical investigation of equivalence ratio dependence, Combust. Flame. 230 (2021) In press.
[54] M. Lee, Y. Fan, C.B. Reuter, Y. Ju, Y. Suzuki, DME/Oxygen wall-stabilized premixed cool flame, Proc. Combust. Inst. 37 (2019) 1749–1756.
[55] M. Lee, Y. Fan, Y. Ju, Y. Suzuki, Ignition characteristics of premixed cool flames on a heated wall, Combust. Flame. 231 (2021) In press.
[56] O. Herbinet, B. Husson, Z. Serinyel, M. Cord, V. Warth, R. Fournet, P.-A. Glaude, B. Sirjean, F. Battin-Leclerc, Z. Wang, M. Xie, Z. Cheng, F. Qi, Experimental and modeling investigation of the low-temperature oxidation of n-heptane, Combust. Flame. 159 (2012) 3455–3471.
[57] F. Battin-Leclerc, Detailed chemical kinetic models for the low-temperature combustion of hydrocarbons with application to gasoline and diesel fuel surrogates, Prog. Energy Combust. Sci. 34 (2008) 440–498.
[58] Z. Wang, S.M. Sarathy, Third O2 addition reactions promote the low-temperature auto-ignition of n-alkanes, Combust. Flame. 165 (2016) 364–372.
[59] N. Belhadj, R. Benoit, P. Dagaut, M. Lailliau, Z. Serinyel, G. Dayma, F. Khaled, B. Moreau, F. Foucher, Oxidation of di-n-butyl ether: Experimental characterization of low-temperature products in JSR and RCM, Combust. Flame. 222 (2020) 133–144.

[60] Z. Wang, O. Herbinet, N. Hansen, F. Battin-Leclerc, Exploring hydroperoxides in combustion: History, recent advances and perspectives, Prog. Energy Combust. Sci. 73 (2019) 132–181.
[61] S.M. Starikovskaya, N.L. Aleksandrov, I.N. Kosarev, S.V. Kindysheva, A.Yu. Starikovskii, Ignition with low-temperature plasma: Kinetic mechanism and experimental verification, High Energy Chem. 43 (2009) 213–218.
[62] Y. Ju, W. Sun, Plasma assisted combustion: Dynamics and chemistry, Prog. Energy Combust. Sci. 48 (2015) 21–83.
[63] H. Zhao, X. Yang, Y. Ju, Kinetic studies of ozone assisted low temperature oxidation of dimethyl ether in a flow reactor using molecular-beam mass spectrometry, Combust. Flame. 173 (2016) 187–194.
[64] H. Zhao, L. Wu, C. Patrick, Z. Zhang, Y. Rezgui, X. Yang, G. Wysocki, Y. Ju, Studies of low temperature oxidation of n-pentane with nitric oxide addition in a jet stirred reactor, Combust. Flame. 197 (2018) 78–87.
[65] A. Nishiyama, Y. Ikeda, Improvement of Lean Limit and Fuel Consumption Using Microwave Plasma Ignition Technology, in: SAE Tech. Pap., 2012: p. In press.
[66] T. Shiraishi, A. Kakuho, T. Urushihara, C. Cathey, T. Tang, M. Gundersen, A Study of Volumetric Ignition Using High-Speed Plasma for Improving Lean Combustion Performance in Internal Combustion Engines, SAE Int. J. Engines. 1 (2009) 399–408.
[67] G. Vanhove, M.-A. Boumehdi, S. Shcherbanev, Y. Fenard, P. Desgroux, S.M. Starikovskaia, A comparative experimental kinetic study of spontaneous and plasma-assisted cool flames in a rapid compression machine, Proc. Combust. Inst. 36 (2017) 4137–4143.
[68] M. Castela, B. Fiorina, A. Coussement, O. Gicquel, N. Darabiha, C.O. Laux, Modelling the impact of non-equilibrium discharges on reactive mixtures for simulations of plasma-assisted ignition in turbulent flows, Combust. Flame. 166 (2016) 133–147.
[69] T. Batakliev, V. Georgiev, M. Anachkov, S. Rakovsky, S. Rakovsky, Ozone decomposition, Interdiscip. Toxicol. 7 (2014) 47–59.
[70] R. Criegee, Mechanism of Ozonolysis, Angew. Chem. Int. Ed. Engl. 14 (1975) 745–752.
[71] A.C. Rousso, N. Hansen, A.W. Jasper, Y. Ju, Low-Temperature Oxidation of Ethylene by Ozone in a Jet-Stirred Reactor, J. Phys. Chem. A. 122 (2018) 8674–8685.
[72] J. Morrissey, C.C. Schubert, The Reactions of Ozone with Propane and Ethane, Combust. Flame. 7 (1963) 263–268.
[73] K.H. Becker, U. Schurath, H. Seitz, Ozone-olefin reactions in the gas phase 1. Rate constants and activation energies, Int. J. Chem. Kinet. 6 (1974) 725–739.
[74] H. Nishida, T. Tachibana, Homogeneous Charge Compression Ignition of Natural Gas/Air Mixture with Ozone Addition, J. Propuls. Power. 22 (2006) 151–157.
[75] F. Foucher, P. Higelin, C. Mounaïm-Rousselle, P. Dagaut, Influence of ozone on the combustion of n-heptane in a HCCI engine, Proc. Combust. Inst. 34 (2013) 3005–3012.
[76] H. Yamada, M. Yoshii, A. Tezaki, Chemical mechanistic analysis of additive effects in homogeneous charge compression ignition of dimethyl ether, Proc. Combust. Inst. 30 (2005) 2773–2780.
[77] J.-B. Masurier, F. Foucher, G. Dayma, P. Dagaut, Investigation of iso-octane combustion in a homogeneous charge compression ignition engine seeded by ozone, nitric oxide and nitrogen dioxide, Proc. Combust. Inst. 35 (2015) 3125–3132.
[78] N. Seignour, J. Masurier, B. Johansson, G. Dayma, P. Dagaut, F. Foucher, Ozone-assisted combustion of hydrogen: A comparison with isooctane, Int. J. Hydrog. Energy. 44 (2019) 13953–13963.

[79] H. Liao, S. Kang, N. Hansen, F. Zhang, B. Yang, Influence of ozone addition on the low-temperature oxidation of dimethyl ether in a jet-stirred reactor, Combust. Flame. 214 (2020) 277–286.
[80] R. Minetti, C. Corre, J.-F. Pauwels, P. Devolder, L.-R. Sochet, On the reactivity of hydroperoxy radicals and hydrogen peroxide in a two-stage butane-air flame, Combust. Flame. 85 (1991) 263–270.
[81] B. Galmiche, Caractérisation expérimentale des flammes laminaires et turbulentes en expansion, 2014.
[82] T. Poinsot, T. Echekki, M.G. Mungal, A Study of the Laminar Flame Tip and Implications for Premixed Turbulent Combustion, Combust. Sci. Technol. 81 (1992) 45–73.
[83] A. Trouvé, T. Poinsot, The evolution equation for the flame surface density in turbulent premixed combustion, J. Fluid Mech. 278 (1994) 1–31.
[84] T. Poinsot, D. Veynante, Theoretical and numerical combustion, Edwards, Philadelphia, PA, 2001.
[85] N. Bouvet, Experimental and Numerical Studies of the Fundamental Flame Speeds of Methane/Air and Syngas (H2/CO)/Air Mixtures, Theses, Université d'Orléans, 2009.
[86] K.K. Kuo, Principles of combustion, 2nd ed, John Wiley, Hoboken, NJ, 2005.
[87] J.H. Tien, M. Matalon, On the burning velocity of stretched flames, Combust. Flame. 84 (1991) 238–248.
[88] J. Jayachandran, R. Zhao, F.N. Egolfopoulos, Determination of laminar flame speeds using stagnation and spherically expanding flames: Molecular transport and radiation effects, Combust. Flame. 161 (2014) 2305–2316.
[89] N. Bouvet, C. Chauveau, I. Gökalp, F. Halter, Experimental studies of the fundamental flame speeds of syngas (H2/CO)/air mixtures, Proc. Combust. Inst. 33 (2011) 913–920.
[90] C.T. Chong, S. Hochgreb, Measurements of laminar flame speeds of acetone/methane/air mixtures, Combust. Flame. 158 (2011) 490–500.
[91] F.N. Egolfopoulos, N. Hansen, Y. Ju, K. Kohse-Höinghaus, C.K. Law, F. Qi, Advances and challenges in laminar flame experiments and implications for combustion chemistry, Prog. Energy Combust. Sci. 43 (2014) 36–67.
[92] W. Han, P. Dai, X. Gou, Z. Chen, A review of laminar flame speeds of hydrogen and syngas measured from propagating spherical flames, Appl. Energy Combust. Sci. 1–4 (2020) In press.
[93] A. Durocher, M. Meulemans, G. Bourque, J.M. Bergthorson, Measurements of the laminar flame speed of premixed, hydrogen-air-argon stagnation flames, Appl. Energy Combust. Sci. 7 (2021) In press.
[94] J.P. Botha, D.B. Spalding, The laminar flame speed of propane/air mixtures with heat extraction from the flame, Proc. R. Soc. Lond. Ser. Math. Phys. Sci. 225 (1954) 71–96.
[95] L.P.H. De Goey, A. Van Maaren, R.M. Quax, Stabilization of Adiabatic Premixed Laminar Flames on a Flat Flame Burner, Combust. Sci. Technol. 92 (1993) 201–207.
[96] A. Van Maaren, L.P.H. De Goey, Laser Doppler Thermometry in Flat Flames, Combust. Sci. Technol. 99 (1994) 105–118.
[97] E. Eteng, G.S.S. Ludford, M. Matalon, Displacement effect of a flame in a stagnation-point flow, Phys. Fluids. 29 (1986) 2172–2180.
[98] C.K. Law, C.J. Sung, Structure, aerodynamics, and geometry of premixed flamelets, Prog. Energy Combust. Sci. 26 (2000) 459–505.
[99] J.M. Bergthorson, S.D. Salusbury, P.E. Dimotakis, Experiments and modelling of premixed laminar stagnation flame hydrodynamics, J. Fluid Mech. 681 (2011) 340–369.

[100] N. Lamoureux, N. Djebaïli-Chaumeix, C.-E. Paillard, Laminar flame velocity determination for H2–air–He–CO2 mixtures using the spherical bomb method, Exp. Therm. Fluid Sci. 27 (2003) 385–393.
[101] E.F. Fiock, C.F. Marvin, The Measurement of Flame Speeds., Chem. Rev. 21 (1937) 367–387.
[102] F. Halter, G. Dayma, Z. Serinyel, P. Dagaut, C. Chauveau, Laminar flame speed determination at high pressure and temperature conditions for kinetic schemes assessment, Proc. Combust. Inst. 38 (2021) 2449–2457.
[103] G. Yin, J. Li, M. Zhou, J. Li, C. Wang, E. Hu, Z. Huang, Experimental and kinetic study on laminar flame speeds of ammonia/dimethyl ether/air under high temperature and elevated pressure, Combust. Flame. 238 (2022) 1–12.
[104] P.G. Lignola, E. Reverchon, Cool flames, Prog. Energy Combust. Sci. 13 (1987) 75–96.
[105] H. Pearlman, Low-temperature oxidation reactions and cool flames at earth and reduced gravity, Combust. Flame. 121 (2000) 390–393.
[106] H. Pearlman, Multiple cool flames in static, unstirred reactors under reduced-gravity and terrestrial conditions, Combust. Flame. 148 (2007) 280–284.
[107] M. Foster, H. Pearlman, Cool flames at terrestrial, partial, and near-zero gravity, Combust. Flame. 147 (2006) 108–117.
[108] M. Foster, H. Pearlman, Cool Flame Propagation Speeds, Combust. Sci. Technol. 179 (2007) 1349–1360.
[109] Y. Ju, W. Sun, M.P. Burke, X. Gou, Z. Chen, Multi-timescale modeling of ignition and flame regimes of n-heptane-air mixtures near spark assisted homogeneous charge compression ignition conditions, Proc. Combust. Inst. 33 (2011) 1245–1251.
[110] Y. Ju, On the propagation limits and speeds of premixed cool flames at elevated pressures, Combust. Flame. 178 (2017) 61–69.
[111] W. Zhang, M. Faqih, X. Gou, Z. Chen, Numerical study on the transient evolution of a premixed cool flame, Combust. Flame. 187 (2018) 129–136.
[112] E. Belmont, T. Ombrello, M. Brown, C. Carter, J. Ellzey, Experimental and numerical investigation of freely propagating flames stabilized on a Hencken Burner, Combust. Flame. 162 (2015) 2679–2685.
[113] A. Rodriguez, Étude de la combustion de composés organiques grâce au couplage d'un réacteur parfaitement agité avec des méthodes analytiques spectroscopiques et spectrométriques : application à la détection des hydroperoxydes, Theses, Université de Lorraine, 2016.
[114] H.J. Curran, S.L. Fischer, F.L. Dryer, The reaction kinetics of dimethyl ether. II: Low-temperature oxidation in flow reactors, Int. J. Chem. Kinet. 32 (2000) 741–759.
[115] U. Pfahl, K. Fieweger, G. Adomeit, Self-ignition of diesel-relevant hydrocarbon-air mixtures under engine conditions, Symp. Int. Combust. 26 (1996) 781–789.
[116] P. Dagaut, C. Daly, J.M. Simmie, M. Cathonnet, The oxidation and ignition of dimethylether from low to high temperature (500–1600 K): Experiments and kinetic modeling, Symp. Int. Combust. 27 (1998) 361–369.
[117] H. Niki, P.D. Maker, C.M. Savage, L.P. Breitenbach, An Fourier transform infrared study of the kinetics and mechanism for the reaction of hydroxyl radical with formaldehyde, J. Phys. Chem. 88 (1984) 5342–5344.
[118] H. Guo, W. Sun, F.M. Haas, T. Farouk, F.L. Dryer, Y. Ju, Measurements of H2O2 in low temperature dimethyl ether oxidation, Proc. Combust. Inst. 34 (2013) 573–581.
[119] N. Kurimoto, B. Brumfield, X. Yang, T. Wada, P. Diévart, G. Wysocki, Y. Ju, Quantitative measurements of HO_2/H_2O_2 and intermediate species in low and intermediate temperature oxidation of dimethyl ether, Proc. Combust. Inst. 35 (2015) 457–464.

[120] A. Rodriguez, O. Frottier, O. Herbinet, R. Fournet, R. Bounaceur, C. Fittschen, F. Battin-Leclerc, Experimental and Modeling Investigation of the Low-Temperature Oxidation of Dimethyl Ether, J. Phys. Chem. A. 119 (2015) 7905–7923.
[121] P. Dagaut, J.-C. Boettner, M. Cathonnet, Chemical kinetic study of dimethylether oxidation in a jet stirred reactor from 1 to 10 ATM: Experiments and kinetic modeling, Symp. Int. Combust. 26 (1996) 627–632.
[122] F. Herrmann, P. Oßwald, K. Kohse-Höinghaus, Mass spectrometric investigation of the low-temperature dimethyl ether oxidation in an atmospheric pressure laminar flow reactor, Proc. Combust. Inst. 34 (2013) 771–778.
[123] F. Herrmann, B. Jochim, P. Oßwald, L. Cai, H. Pitsch, K. Kohse-Höinghaus, Experimental and numerical low-temperature oxidation study of ethanol and dimethyl ether, Combust. Flame. 161 (2014) 384–397.
[124] Z. Wang, X. Zhang, L. Xing, L. Zhang, F. Herrmann, K. Moshammer, F. Qi, K. Kohse-Höinghaus, Experimental and kinetic modeling study of the low- and intermediate-temperature oxidation of dimethyl ether, Combust. Flame. 162 (2015) 1113–1125.
[125] N.L. Le Tan, M. Djehiche, C.D. Jain, P. Dagaut, G. Dayma, Quantification of HO2 and other products of dimethyl ether oxidation (H2O2, H2O, and CH2O) in a jet-stirred reactor at elevated temperatures by low-pressure sampling and continuous-wave cavity ring-down spectroscopy, Fuel. 158 (2015) 248–252.
[126] K. Moshammer, A.W. Jasper, D.M. Popolan-Vaida, A. Lucassen, P. Diévart, H. Selim, A.J. Eskola, C.A. Taatjes, S.R. Leone, S.M. Sarathy, Y. Ju, P. Dagaut, K. Kohse-Höinghaus, N. Hansen, Detection and Identification of the Keto-Hydroperoxide (HOOCH $_2$ OCHO) and Other Intermediates during Low-Temperature Oxidation of Dimethyl Ether, J. Phys. Chem. A. 119 (2015) 7361–7374.
[127] K. Moshammer, A.W. Jasper, D.M. Popolan-Vaida, Z. Wang, V.S. Bhavani Shankar, L. Ruwe, C.A. Taatjes, P. Dagaut, N. Hansen, Quantification of the Keto-Hydroperoxide ($HOOCH_2OCHO$) and Other Elusive Intermediates during Low-Temperature Oxidation of Dimethyl Ether, J. Phys. Chem. A. 120 (2016) 7890–7901.
[128] J. Gao, Y. Nakamura, Low-temperature ignition of dimethyl ether: transition from cool flame to hot flame promoted by decomposition of HPMF (HO2CH2OCHO), Combust. Flame. 165 (2016) 68–82.
[129] G. Mittal, M. Chaos, C.-J. Sung, F.L. Dryer, Dimethyl ether autoignition in a rapid compression machine: Experiments and chemical kinetic modeling, Fuel Process. Technol. 89 (2008) 1244–1254.
[130] E.W. Kaiser, T.J. Wallington, M.D. Hurley, J. Platz, H.J. Curran, W.J. Pitz, C.K. Westbrook, Experimental and Modeling Study of Premixed Atmospheric-Pressure Dimethyl Ether−Air Flames, J. Phys. Chem. A. 104 (2000) 8194–8206.
[131] Z. Zhao, A. Kazakov, F.L. Dryer, Measurements of dimethyl ether/air mixture burning velocities by using particle image velocimetry, Combust. Flame. 139 (2004) 52–60.
[132] D. Liu, J. Santner, C. Togbé, D. Felsmann, J. Koppmann, A. Lackner, X. Yang, X. Shen, Y. Ju, K. Kohse-Höinghaus, Flame structure and kinetic studies of carbon dioxide-diluted dimethyl ether flames at reduced and elevated pressures, Combust. Flame. 160 (2013) 2654–2668.
[133] Y.L. Wang, A.T. Holley, C. Ji, F.N. Egolfopoulos, T.T. Tsotsis, H.J. Curran, Propagation and extinction of premixed dimethyl-ether/air flames, Proc. Combust. Inst. 32 (2009) 1035–1042.
[134] C.A. Daly, J.M. Simmie, J. Würmel, N. DjebaÏli, C. Paillard, Burning velocities of dimethyl ether and air, Combust. Flame. 125 (2001) 1329–1340.
[135] X. Qin, Y. Ju, Measurements of burning velocities of dimethyl ether and air premixed flames at elevated pressures, Proc. Combust. Inst. 30 (2005) 233–240.

[136] Z. Huang, Q. Wang, J. Yu, Y. Zhang, K. Zeng, H. Miao, D. Jiang, Measurement of laminar burning velocity of dimethyl ether–air premixed mixtures, Fuel. 86 (2007) 2360–2366.
[137] Z. Chen, L. Wei, Z. Huang, H. Miao, X. Wang, D. Jiang, Measurement of Laminar Burning Velocities of Dimethyl Ether−Air Premixed Mixtures with N_2 and CO_2 Dilution, Energy Fuels. 23 (2009) 735–739.
[138] J. de Vries, W.B. Lowry, Z. Serinyel, H.J. Curran, E.L. Petersen, Laminar flame speed measurements of dimethyl ether in air at pressures up to 10atm, Fuel. 90 (2011) 331–338.
[139] R. Zhang, H. Liao, J. Yang, B. Yang, Exploring chemical kinetics of plasma assisted oxidation of dimethyl ether (DME), Combust. Flame. 225 (2021) 388–394.
[140] H.J. Curran, W.J. Pitz, C.K. Westbrook, P. Dagaut, J.-C. Boettner, M. Cathonnet, A wide range modeling study of dimethyl ether oxidation, Int. J. Chem. Kinet. 30 (1998) 229–241.
[141] H.J. Curran, P. Gaffuri, W.J. Pitz, C.K. Westbrook, A Comprehensive Modeling Study of n-Heptane Oxidation, Combust. Flame. 114 (1998) 149–177.
[142] S.L. Fischer, F.L. Dryer, H.J. Curran, The reaction kinetics of dimethyl ether. I: High-temperature pyrolysis and oxidation in flow reactors, Int. J. Chem. Kinet. 32 (2000) 713–740.
[143] Z. Zhao, M. Chaos, A. Kazakov, F.L. Dryer, Thermal decomposition reaction and a comprehensive kinetic model of dimethyl ether, Int. J. Chem. Kinet. 40 (2008) 1–18.
[144] U. Burke, K.P. Somers, P. O'Toole, C.M. Zinner, N. Marquet, G. Bourque, E.L. Petersen, W.K. Metcalfe, Z. Serinyel, H.J. Curran, An ignition delay and kinetic modeling study of methane, dimethyl ether, and their mixtures at high pressures, Combust. Flame. 162 (2015) 315–330.
[145] E.E. Dames, A.S. Rosen, B.W. Weber, C.W. Gao, C.-J. Sung, W.H. Green, A detailed combined experimental and theoretical study on dimethyl ether/propane blended oxidation, Combust. Flame. 168 (2016) 310–330.
[146] W.K. Metcalfe, S.M. Burke, S.S. Ahmed, H.J. Curran, A Hierarchical and Comparative Kinetic Modeling Study of $C_1 - C_2$ Hydrocarbon and Oxygenated Fuels, Int. J. Chem. Kinet. 45 (2013) 638–675.
[147] Y. Li, C.-W. Zhou, K.P. Somers, K. Zhang, H.J. Curran, The oxidation of 2-butene: A high pressure ignition delay, kinetic modeling study and reactivity comparison with isobutene and 1-butene, Proc. Combust. Inst. 36 (2017) 403–411.
[148] C.-W. Zhou, Y. Li, U. Burke, C. Banyon, K.P. Somers, S. Ding, S. Khan, J.W. Hargis, T. Sikes, O. Mathieu, E.L. Petersen, M. AlAbbad, A. Farooq, Y. Pan, Y. Zhang, Z. Huang, J. Lopez, Z. Loparo, S.S. Vasu, H.J. Curran, An experimental and chemical kinetic modeling study of 1,3-butadiene combustion: Ignition delay time and laminar flame speed measurements, Combust. Flame. 197 (2018) 423–438.
[149] Y. Wu, S. Panigrahy, A.B. Sahu, C. Bariki, J. Beeckmann, J. Liang, A.A.E. Mohamed, S. Dong, C. Tang, H. Pitsch, Z. Huang, H.J. Curran, Understanding the antagonistic effect of methanol as a component in surrogate fuel models: A case study of methanol/n-heptane mixtures, Combust. Flame. 226 (2021) 229–242.
[150] D.C. Rakopoulos, C.D. Rakopoulos, E.G. Giakoumis, A.M. Dimaratos, Characteristics of performance and emissions in high-speed direct injection diesel engine fueled with diethyl ether/diesel fuel blends, Energy. 43 (2012) 214–224.
[151] K. Sudheesh, J.M. Mallikarjuna, Diethyl ether as an ignition improver for biogas homogeneous charge compression ignition (HCCI) operation - An experimental investigation, Energy. 35 (2010) 3614–3622.

[152] S. Polat, An experimental study on combustion, engine performance and exhaust emissions in a HCCI engine fuelled with diethyl ether–ethanol fuel blends, Fuel Process. Technol. 143 (2016) 140–150.
[153] M. Zeng, J. Wullenkord, I. Graf, K. Kohse-Höinghaus, Influence of dimethyl ether and diethyl ether addition on the flame structure and pollutant formation in premixed iso-octane flames, Combust. Flame. 184 (2017) 41–54.
[154] K. Yasunaga, F. Gillespie, J.M. Simmie, H.J. Curran, Y. Kuraguchi, H. Hoshikawa, M. Yamane, Y. Hidaka, A Multiple Shock Tube and Chemical Kinetic Modeling Study of Diethyl Ether Pyrolysis and Oxidation, J. Phys. Chem. A. 114 (2010) 9098–9109.
[155] M. Werler, L.R. Cancino, R. Schiessl, U. Maas, C. Schulz, M. Fikri, Ignition delay times of diethyl ether measured in a high-pressure shock tube and a rapid compression machine, Proc. Combust. Inst. 35 (2015) 259–266.
[156] L.-S. Tran, J. Pieper, H.-H. Carstensen, H. Zhao, I. Graf, Y. Ju, F. Qi, K. Kohse-Höinghaus, Experimental and kinetic modeling study of diethyl ether flames, Proc. Combust. Inst. 36 (2017) 1165–1173.
[157] F. Gillespie, W.K. Metcalfe, P. Dirrenberger, O. Herbinet, P.-A. Glaude, F. Battin-Leclerc, H.J. Curran, Measurements of flat-flame velocities of diethyl ether in air, Energy. 43 (2012) 140–145.
[158] N. Vin, O. Herbinet, F. Battin-Leclerc, Diethyl ether pyrolysis study in a jet-stirred reactor, J. Anal. Appl. Pyrolysis. 121 (2016) 173–176.
[159] J. Hashimoto, K. Tanoue, N. Taide, Y. Nouno, Extinction limits and flame structures of 1-butanol and Diethyl Ether non-premixed flames, Proc. Combust. Inst. 35 (2015) 973–980.
[160] K.C. Salooja, Mechanism of combustion of diethyl ether. Comparative studies of diethyl ether, pentane and acetaldehyde, Combust. Flame. 9 (1965) 33–41.
[161] J.F. Griffiths, T. Inomata, Oscillatory cool flames in the combustion of diethyl ether, J. Chem. Soc. Faraday Trans. 88 (1992) 3153–3158.
[162] S. Di Tommaso, P. Rotureau, O. Crescenzi, C. Adamo, Oxidation mechanism of diethyl ether: a complex process for a simple molecule, Phys. Chem. Chem. Phys. 13 (2011) In press.
[163] M. Naito, C. Radcliffe, Y. Wada, T. Hoshino, X. Liu, M. Arai, M. Tamura, A comparative study on the autoxidation of dimethyl ether (DME) comparison with diethyl ether (DEE) and diisopropyl ether (DIPE), J. Loss Prev. Process Ind. 18 (2005) 469–473.
[164] T. Inomata, J.F. Griffiths, A.J. Pappin, The role of additives as sensitizers for the spontaneous ignition of hydrocarbons, Symp. Int. Combust. 23 (1991) 1759–1766.
[165] Y. Uygun, Ignition studies of undiluted diethyl ether in a high-pressure shock tube, Combust. Flame. 194 (2018) 396–409.
[166] Z. Serinyel, M. Lailliau, S. Thion, G. Dayma, P. Dagaut, An experimental chemical kinetic study of the oxidation of diethyl ether in a jet-stirred reactor and comprehensive modeling, Combust. Flame. 193 (2018) 453–462.
[167] L.-S. Tran, O. Herbinet, Y. Li, J. Wullenkord, M. Zeng, E. Bräuer, F. Qi, K. Kohse-Höinghaus, F. Battin-Leclerc, Low-temperature gas-phase oxidation of diethyl ether: Fuel reactivity and fuel-specific products, Proc. Combust. Inst. 37 (2019) 511–519.
[168] S. Thion, C. Togbé, Z. Serinyel, G. Dayma, P. Dagaut, A chemical kinetic study of the oxidation of dibutyl-ether in a jet-stirred reactor, Combust. Flame. 185 (2017) 4–15.
[169] L.-S. Tran, J. Wullenkord, Y. Li, O. Herbinet, M. Zeng, F. Qi, K. Kohse-Höinghaus, F. Battin-Leclerc, Probing the low-temperature chemistry of di-n-butyl ether: Detection of previously unobserved intermediates, Combust. Flame. 210 (2019) 9–24.

[170] N. Belhadj, R. Benoit, M. Lailliau, V. Glasziou, P. Dagaut, Oxidation of diethyl ether: Extensive characterization of products formed at low temperature using high resolution mass spectrometry, Combust. Flame. 228 (2021) 340–350.
[171] J. Eble, J. Kiecherer, M. Olzmann, Low-Temperature Autoignition of Diethyl Ether/O_2 Mixtures: Mechanistic Considerations and Kinetic Modeling, Z. Für Phys. Chem. 231 (2017) 1603–1623.
[172] Z. Tang, L. Zhang, X. Chen, G. Tang, Improved Kinetic Mechanism for Diethyl Ether Oxidation with a Reduced Model, Energy Fuels. 31 (2017) 2803–2813.
[173] Y. Sakai, J. Herzler, M. Werler, C. Schulz, M. Fikri, A quantum chemical and kinetics modeling study on the autoignition mechanism of diethyl ether, Proc. Combust. Inst. 36 (2017) 195–202.
[174] Y. Sakai, H. Ando, H.K. Chakravarty, H. Pitsch, R.X. Fernandes, A computational study on the kinetics of unimolecular reactions of ethoxyethylperoxy radicals employing CTST and VTST, Proc. Combust. Inst. 35 (2015) 161–169.
[175] E. Hu, Y. Chen, Z. Zhang, J.-Y. Chen, Z. Huang, Ab initio calculation and kinetic modeling study of diethyl ether ignition with application toward a skeletal mechanism for CI engine modeling, Fuel. 209 (2017) 509–520.
[176] A.D. Danilack, S.J. Klippenstein, Y. Georgievskii, C.F. Goldsmith, Low-temperature oxidation of diethyl ether: Reactions of hot radicals across coupled potential energy surfaces, Proc. Combust. Inst. 38 (2021) 671–679.
[177] C.R. Mulvihill, A.D. Danilack, C.F. Goldsmith, M. Demireva, L. Sheps, Y. Georgievskii, S.N. Elliott, S.J. Klippenstein, Non-Boltzmann Effects in Chain Branching and Pathway Branching for Diethyl Ether Oxidation, Energy Fuels. 35 (2021) 17890–17908.
[178] L. Cai, S. Jacobs, R. Langer, F. vom Lehn, K.A. Heufer, H. Pitsch, Auto-ignition of oxymethylene ethers (OMEn, n = 2–4) as promising synthetic e-fuels from renewable electricity: shock tube experiments and automatic mechanism generation, Fuel. 264 (2020) In press.
[179] S. Drost, R. Schießl, M. Werler, J. Sommerer, U. Maas, Ignition delay times of polyoxymethylene dimethyl ether fuels (OME 2 and OME 3) and air: Measurements in a rapid compression machine, Fuel. 258 (2019) In press.
[180] N. Gaiser, T. Bierkandt, P. Oßwald, J. Zinsmeister, T. Kathrotia, S. Shaqiri, P. Hemberger, T. Kasper, M. Aigner, M. Köhler, Oxidation of oxymethylene ether (OME0−5): An experimental systematic study by mass spectrometry and photoelectron photoion coincidence spectroscopy, Fuel. 313 (2022) In press.
[181] J.M. Ngugi, S. Richter, M. Braun-Unkhoff, C. Naumann, M. Köhler, U. Riedel, A Study on Fundamental Combustion Properties of Oxymethylene Ether-2, J. Eng. Gas Turbines Power. 144 (2022) In press.
[182] J.M. Ngugi, S. Richter, M. Braun-Unkhoff, C. Naumann, U. Riedel, A study on fundamental combustion properties of oxymethylene ether-1, the primary reference fuel 90, and their blend: Experiments and modeling, Combust. Flame. 238 (2022) In press.
[183] K. De Ras, M. Kusenberg, G. Vanhove, Y. Fenard, A. Eschenbacher, R.J. Varghese, J. Aerssens, R. Van de Vijver, L.-S. Tran, J.W. Thybaut, K.M. Van Geem, A detailed experimental and kinetic modeling study on pyrolysis and oxidation of oxymethylene ether-2 (OME-2), Combust. Flame. 238 (2022) In press.
[184] Y. Fenard, G. Vanhove, A Mini-Review on the Advances in the Kinetic Understanding of the Combustion of Linear and Cyclic Oxymethylene Ethers, Energy Fuels. 35 (2021) 14325–14342.
[185] J.C. Rolon, Etude théorique et expérimentale de la flamme de diffusion à contre-courant, Université Paris-Saclay, 1988.

[186] V. Gorshelev, A. Serdyuchenko, M. Weber, W. Chehade, J.P. Burrows, High spectral resolution ozone absorption cross-sections – Part 1: Measurements, data analysis and comparison with previous measurements around 293 K, Atmospheric Meas. Tech. 7 (2014) 609–624.
[187] R.S. Sheinson, F.W. Williams, Chemiluminescence spectra from cool and blue flames: Electronically excited formaldehyde, Combust. Flame. 21 (1973) 221–230.
[188] D.I. Shin, T. Dreier, J. Wolfrum, Spatially resolved absolute concentration and fluorescence-lifetime determination of H2CO in atmospheric-pressure CH4/air flames, Appl. Phys. B. 72 (2001) 257–261.
[189] B. Bäuerle, F. Hoffmann, F. Behrendt, J. Warnatz, Detection of hot spots in the end gas of an internal combustion engine using two-dimensional lif of formaldehyde, Symp. Int. Combust. 25 (1994) 135–141.
[190] B. Bäuerle, J. Warnat, F. Behrendt, Time-resolved investigation of hot spots in the end gas of an S. I. engine by means of 2-D double-pulse lif of formaldehyde, Symp. Int. Combust. 26 (1996) 2619–2626.
[191] M. Barret, S. Houdier, F. Domine, Thermodynamics of the Formaldehyde−Water and Formaldehyde−Ice Systems for Atmospheric Applications, J. Phys. Chem. A. 115 (2011) 307–317.
[192] E.C. Eckbreth, Laser diagnostics for combustion temperature and species, 2nd Ed., Gordon and Breach Publishers, Amsterdam, 1996.
[193] I.A. Mulla, A. Dowlut, T. Hussain, Z.M. Nikolaou, S.R. Chakravarthy, N. Swaminathan, R. Balachandran, Heat release rate estimation in laminar premixed flames using laser-induced fluorescence of CH2O and H-atom, Combust. Flame. 165 (2016) 373–383.
[194] B.O. Ayoola, R. Balachandran, J.H. Frank, E. Mastorakos, C.F. Kaminski, Spatially resolved heat release rate measurements in turbulent premixed flames, Combust. Flame. 144 (2006) 1–16.
[195] D.C. Kyritsis, V.S. Santoro, A. Gomez, The effect of temperature correction on the measured thickness of formaldehyde zones in diffusion flames for 355 nm excitation, Exp. Fluids. 37 (2004) 769–772.
[196] D.J. Clouthier, D.A. Ramsay, The Spectroscopy of Formaldehyde and Thioformaldehyde, Annu. Rev. Phys. Chem. 34 (1983) 31–58.
[197] M.V. Heitor, A.L.N. Moreira, Thermocouples and sample probes for combustion studies, Prog. Energy Combust. Sci. 19 (1993) 259–278.
[198] W.G. Bessler, C. Schulz, Quantitative multi-line NO-LIF temperature imaging, Appl. Phys. B Lasers Opt. 78 (2004) 519–533.
[199] K.K. Foo, N. Lamoureux, A. Cessou, C. Lacour, P. Desgroux, The accuracy and precision of multi-line NO-LIF thermometry in a wide range of pressures and temperatures, J. Quant. Spectrosc. Radiat. Transf. 255 (2020) In press.
[200] R.P. Lucht, R.E. Teets, R.M. Green, R.E. Palmer, C.R. Ferguson, Unburned Gas Temperatures in an Internal Combustion Engine. I:Cars Temperature Measurements, Combust. Sci. Technol. 55 (1987) 41–61.
[201] M. Cafiero, V. Dias, S. Iavarone, A. Coussement, H. Jeanmart, A. Parente, Investigation of temperature correction methods for fine wire thermocouple losses in low-pressure flat premixed laminar flames, Combust. Flame. 244 (2022) In press.
[202] D. Bradley, K.J. Matthews, Measurement of High Gas Temperatures with Fine Wire Thermocouples, J. Mech. Eng. Sci. 10 (1968) 299–305.
[203] R. Lemaire, S. Menanteau, Assessment of radiation correction methods for bare bead thermocouples in a combustion environment, Int. J. Therm. Sci. 122 (2017) 186–200.
[204] T. Holm, Aspects of the mechanism of the flame ionization detector, J. Chromatogr. A. 842 (1999) 221–227.

[205] K. Schofield, The enigmatic mechanism of the flame ionization detector: Its overlooked implications for fossil fuel combustion modeling, Prog. Energy Combust. Sci. 34 (2008) 330–350.
[206] J.T. Scanlon, D.E. Willis, Calculation of Flame Ionization Detector Relative Response Factors Using the Effective Carbon Number Concept, J. Chromatogr. Sci. 23 (1985) 333–340.
[207] L. Giarracca, Impact of lignocellulosic biofuels on NOx formation in premixed laminar flames, Theses, Université de Lille, 2018.
[208] S. Hochgreb, F.L. Dryer, Decomposition of 1,3,5-trioxane at 700-800 K, J. Phys. Chem. 96 (1992) 295–297.
[209] A. Melling, Tracer particles and seeding for particle image velocimetry, Meas. Sci. Technol. 8 (1997) 1406–1416.
[210] I. Grant, Particle image velocimetry: A review, Proc. Inst. Mech. Eng. Part C J. Mech. Eng. Sci. 211 (1997) 55–76.
[211] R.J. Adrian, Twenty years of particle image velocimetry, Exp. Fluids. 39 (2005) 159–169.
[212] R.J. Adrian, J. Westerweel, Particle Image Velocimetry, Cambridge University Press, 2011.
[213] C. Kähler, B. Sammler, J. Kompenhans, Generation and control of tracer particles for optical flow investigations in air, Exp. Fluids. 33 (2002) 736–742.
[214] B. Lecordier, D. Demare, L.M.J. Vervisch, J. Réveillon, M. Trinite, Estimation of the accuracy of PIV treatments for turbulent flow studies by direct numerical simulation of multi-phase flow, Meas. Sci. Technol. 12 (2001) 1382–1391.
[215] D. Goodwin, H. Moffat, R. Speth, Cantera: An Object-oriented Software Toolkit for Chemical Kinetics, Thermodynamics, and Transport Processes, 2015.
[216] Ansys Chemkin Pro, Release 2021 R1, (2021). https://www.ansys.com/products/fluids/ansys-chemkin-pro (accessed December 24, 2021).
[217] R.J. Kee, M.E. Coltrin, P. Glarborg, H. Zhu, Chemically Reacting Flow: Theory and Practice, 2d Edition, John Wiley and Sons, 2017.
[218] H.K. Chelliah, C.K. Law, T. Ueda, M.D. Smooke, F.A. Williams, An experimental and theoretical investigation of the dilution, pressure and flow-field effects on the extinction condition of methane-air-nitrogen diffusion flames, Symp. Int. Combust. 23 (1991) 503–511.
[219] F. Halter, P. Higelin, P. Dagaut, Experimental and Detailed Kinetic Modeling Study of the Effect of Ozone on the Combustion of Methane, Energy Fuels. 25 (2011) 2909–2916.
[220] W. Pejpichestakul, A. Cuoci, A. Frassoldati, M. Pelucchi, A. Parente, T. Faravelli, Buoyancy effect in sooting laminar premixed ethylene flame, Combust. Flame. 205 (2019) 135–146.
[221] W. Wißdorf, D. Müller, Y. Brachthäuser, M. Langner, V. Derpmann, S. Klopotowski, C. Polaczek, H. Kersten, K. Brockmann, T. Benter, Gas Flow Dynamics in Inlet Capillaries: Evidence for non Laminar Conditions, J. Am. Soc. Mass Spectrom. 27 (2016) 1550–1563.
[222] M. Wutz, H. Adam, W. Walcher, Theorie und Praxis der Vakuumtechnik, Vieweg+Teubner Verlag, Wiesbaden, 1988.
[223] T. Panaget, N. Mokrani, S. Batut, A. Lahccen, Y. Fenard, L. Pillier, G. Vanhove, Insight into the Ozone-Assisted Low-Temperature Combustion of Dimethyl Ether by Means of Stabilized Cool Flames, J. Phys. Chem. A. 125 (2021) 9167–9179.

[224] L.B. Harding, S.J. Klippenstein, Y. Georgievskii, Reactions of oxygen atoms with hydrocarbon radicals: a priori kinetic predictions for the CH3+O, C2H5+O, and C2H3+O reactions, Proc. Combust. Inst. 30 (2005) 985–993.
[225] X. Song, H. Hou, B. Wang, Mechanistic and kinetic study of the O + CH3OCH2 reaction and the unimolecular decomposition of CH3OCH2O, Phys. Chem. Chem. Phys. 7 (2005) 3980–3988.
[226] M. Döntgen, Y. Fenard, K.A. Heufer, Atomic Partial Charges as Descriptors for Barrier Heights, J. Chem. Inf. Model. 60 (2020) 5928–5931.
[227] K. Yasunaga, F. Gillespie, J.M. Simmie, H.J. Curran, Y. Kuraguchi, H. Hoshikawa, M. Yamane, Y. Hidaka, A Multiple Shock Tube and Chemical Kinetic Modeling Study of Diethyl Ether Pyrolysis and Oxidation, J. Phys. Chem. A. 114 (2010) 9098–9109.
[228] M. Keiffer, A.J. Miscampbell, M.J. Pilling, A global technique for analysing multiple decay curves. Application to the CH3 + O2 system, J. Chem. Soc. Faraday Trans. 2. 84 (1988) 505–514.
[229] F.H. Vermeire, H.-H. Carstensen, O. Herbinet, F. Battin-Leclerc, G.B. Marin, K.M. Van Geem, Experimental and modeling study of the pyrolysis and combustion of dimethoxymethane, Combust. Flame. 190 (2018) 270–283.
[230] A.A. Konnov, E.J.K. Nilsson, M. Christensen, C.-W. Zhou, Combustion chemistry of methoxymethanol. Part II: Laminar flames of methanol+formaldehyde fuel mixtures, Combust. Flame. 229 (2021) In press.
[231] H. Minwegen, M. Döntgen, C. Hemken, R.D. Büttgen, K. Leonhard, K.A. Heufer, Experimental and theoretical investigations of methyl formate oxidation including hot β-scission, Proc. Combust. Inst. 37 (2019) 307–314.
[232] C.M. Rosado-Reyes, J.S. Francisco, J.J. Szente, M.M. Maricq, L. Frøsig Østergaard, Dimethyl Ether Oxidation at Elevated Temperatures (295−600 K), J. Phys. Chem. A. 109 (2005) 10940–10953.
[233] J. Jian, H. Hashemi, H. Wu, A.W. Jasper, P. Glarborg, A reaction mechanism for ozone dissociation and reaction with hydrogen at elevated temperature, Fuel. 322 (2022) In press.
[234] J. Vandooren, J. Peeters, P.J.V. Tiggelen, Rate constant of the elementary reaction of carbon monoxide with hydroxyl radical, Symp. Int. Combust. 15 (1975) 745–753.
[235] W. Tsang, Chemical Kinetic Data Base for Combustion Chemistry. Part 2. Methanol, J. Phys. Chem. Ref. Data. 16 (1987) 471–508.
[236] Z. Wang, H. Zhao, C. Yan, Y. Lin, A.D. Lele, W. Xu, B. Rotavera, A.W. Jasper, S.J. Klippenstein, Y. Ju, Methanol oxidation up to 100 atm in a supercritical pressure jet-stirred reactor, Proc. Combust. Inst. (2022) In press.
[237] H. Zhao, C. Yan, G. Song, Z. Wang, Y. Ju, Studies of Low and Intermediate Temperature Oxidation of Propane up to 100 Atm in a Supercritical-Pressure Jet-Stirred Reactor, Proc. Combust. Inst. (2022) In press.
[238] T. Panaget, K. Potier, S. Batut, A. Lahccen, Y. Fenard, L. Pillier, G. Vanhove, How ozone affects the product distribution inside cool flames of diethyl ether, Proc. Combust. Inst. 39 (2022) In press.
[239] Y. Murakami, C.B. Reuter, O.R. Yehia, Y. Ju, Studies of autoignition-assisted nonpremixed cool flames, Proc. Combust. Inst. 38 (2021) 2333–2340.
[240] W. Sun, Z. Chen, X. Gou, Y. Ju, A path flux analysis method for the reduction of detailed chemical kinetic mechanisms, Combust. Flame. 157 (2010) 1298–1307.
[241] T.J. Wallington, S.M. Japar, Atmospheric chemistry of diethyl ether and ethyl tert-butyl ether, Environ. Sci. Technol. 25 (1991) 410–415.

[242] J. Eberhard, C. MüLler, D.W. Stocker, J.A. Kerr, The photo-oxidation of diethyl ether in smog chamber experiments simulating tropospheric conditions: Product studies and proposed mechanism, Int. J. Chem. Kinet. 25 (1993) 639–649.
[243] S.A. Cheema, K.A. Holbrook, G.A. Oldershaw, D.P. Starkey, R.W. Walker, The effect of oxygen pressure on the tropospheric oxidation of diethyl ether, H-atom elimination from the 1-ethoxyethoxy radical, Phys. Chem. Chem. Phys. 1 (1999) 3243–3245.
[244] J.J. Orlando, The atmospheric oxidation of diethyl ether: chemistry of the C2H5–O–CH(O˙)CH3 radical between 218 and 335 K, Phys. Chem. Chem. Phys. 9 (2007) 4189–4199.
[245] K. De Ras, M. Kusenberg, J.W. Thybaut, K.M. Van Geem, Unraveling the carbene chemistry of oxymethylene ethers: Experimental investigation and kinetic modeling of the high-temperature pyrolysis of OME-2, Proc. Combust. Inst. (2022) In press.
[246] N.M. Vandewiele, K.M. Van Geem, M.-F. Reyniers, G.B. Marin, Genesys: Kinetic model construction using chemo-informatics, Chem. Eng. J. 207–208 (2012) 526–538.
[247] K. Takahashi, O. Yamamoto, T. Inomata, M. Kogoma, Shock-tube studies on the reactions of dimethyl ether with oxygen and hydrogen atoms, Int. J. Chem. Kinet. 39 (2007) 97–108.
[248] K. De Ras, M. Kusenberg, G. Vanhove, Y. Fenard, A. Eschenbacher, R.J. Varghese, J. Aerssens, R. Van de Vijver, L.-S. Tran, J.W. Thybaut, K.M. Van Geem, A detailed experimental and kinetic modeling study on pyrolysis and oxidation of oxymethylene ether-2 (OME-2), Combust. Flame. 238 (2022) In press.
[249] T. Hirasawa, C.J. Sung, A. Joshi, Z. Yang, H. Wang, C.K. Law, Determination of laminar flame speeds using digital particle image velocimetry: Binary Fuel blends of ethylene, n-Butane, and toluene, Proc. Combust. Inst. 29 (2002) 1427–1434.
[250] N. Bouvet, D. Davidenko, C. Chauveau, L. Pillier, Y. Yoon, On the simulation of laminar strained flames in stagnation flows: 1D and 2D approaches versus experiments, Combust. Flame. 161 (2014) 438–452.
[251] C.J. Sung, J.S. Kistler, M. Nishioka, C.K. Law, Further studies on effects of thermophoresis on seeding particles in LDV measurements of strained flames, Combust. Flame. 105 (1996) 189–201.
[252] C.J. Sung, C.K. Law, R. L Axelbaum, Thermophoretic Effects on Seeding Particles in LDV Measurements of Flames, Combust. Sci. Technol. 99 (1994) 119–132.
[253] J.M. Bergthorson, S.D. Salusbury, P.E. Dimotakis, Experiments and modelling of premixed laminar stagnation flame hydrodynamics, J. Fluid Mech. 681 (2011) 340–369.
[254] J.D. Munzar, B. Akih-Kumgeh, B.M. Denman, A. Zia, J.M. Bergthorson, An experimental and reduced modeling study of the laminar flame speed of jet fuel surrogate components, Fuel. 113 (2013) 586–597.
[255] C.M. Vagelopoulos, F.N. Egolfopoulos, Direct experimental determination of laminar flame speeds, Symp. Int. Combust. 27 (1998) 513–519.
[256] S.G. Davis, C.K. Law, Determination of and Fuel Structure Effects on Laminar Flame Speeds of C_1 to C_8 Hydrocarbons, Combust. Sci. Technol. 140 (1998) 427–449.
[257] P.S. Veloo, Y.L. Wang, F.N. Egolfopoulos, C.K. Westbrook, A comparative experimental and computational study of methanol, ethanol, and n-butanol flames, Combust. Flame. 157 (2010) 1989–2004.
[258] C. Ji, E. Dames, Y.L. Wang, H. Wang, F.N. Egolfopoulos, Propagation and extinction of premixed C5–C12 n-alkane flames, Combust. Flame. 157 (2010) 277–287.
[259] Y.L. Wang, A.T. Holley, C. Ji, F.N. Egolfopoulos, T.T. Tsotsis, H.J. Curran, Propagation and extinction of premixed dimethyl-ether/air flames, Proc. Combust. Inst. 32 (2009) 1035–1042.

[260] S. Gordon, B. McBride, Computer Program for Calculation of Complex Chemical Equilibrium Composition and Applications, Comput. Sci. (1971).
[261] U. Pfahl, K. Fieweger, G. Adomeit, Self-ignition of diesel-relevant hydrocarbon-air mixtures under engine conditions, Symp. Int. Combust. 26 (1996) 781–789.
[262] U. Burke, K.P. Somers, P. O'Toole, C.M. Zinner, N. Marquet, G. Bourque, E.L. Petersen, W.K. Metcalfe, Z. Serinyel, H.J. Curran, An ignition delay and kinetic modeling study of methane, dimethyl ether, and their mixtures at high pressures, Combust. Flame. 162 (2015) 315–330.
[263] X. Qin, Y. Ju, Measurements of burning velocities of dimethyl ether and air premixed flames at elevated pressures, Proc. Combust. Inst. 30 (2005) 233–240.
[264] Z. Zhao, A. Kazakov, F.L. Dryer, Measurements of dimethyl ether/air mixture burning velocities by using particle image velocimetry, Combust. Flame. 139 (2004) 52–60.

Appendices

Appendix II.A1. Purities of the used chemicals.

Compound	Purity	Provider
N_2	≥ 99.995%	Air Liquide
O_2	≥ 99.995%	Air Liquide
DME (CH_3OCH_3)	100%	Messer
DEE ($C_2H_5OC_2H_5$)	≥ 99.8%	Sigma-Aldrich
OME-2 ($CH_3OCH_2OCH_2OCH_3$)	≥ 98.5%	ASG Analytik-Service

Appendix II.A2. O_3 production as a function of the inlet oxygen flow with the 803N and 802N ozone generators (the O_3 percentage is expressed in the oxygen flow).

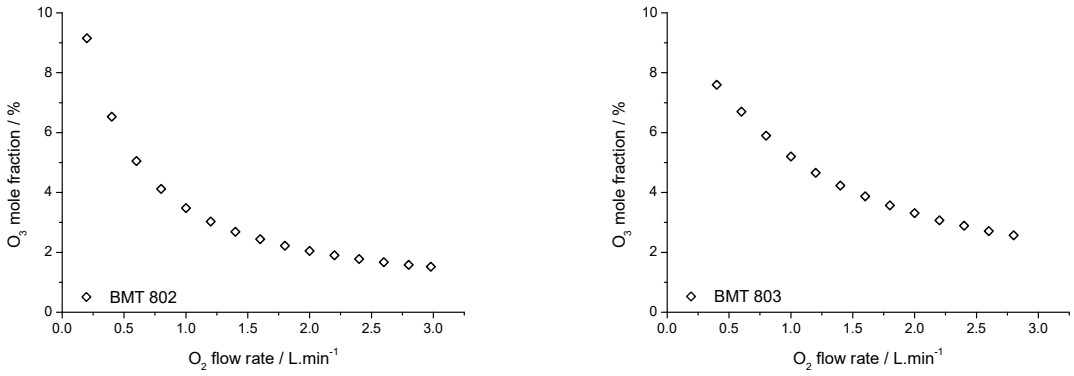

Appendix II.A3. Calculation of the inlet flow rates and ozone mole fraction in O_2 using the equivalence ratio, the inlet velocity and the ozone mole fraction in the Fuel/O_2 mixture as inputs. $\dot{F}$ refers to a molar flux, $\dot{Q}$ to a volumetric flux, x to a mole fraction and ξ the extent of reaction.

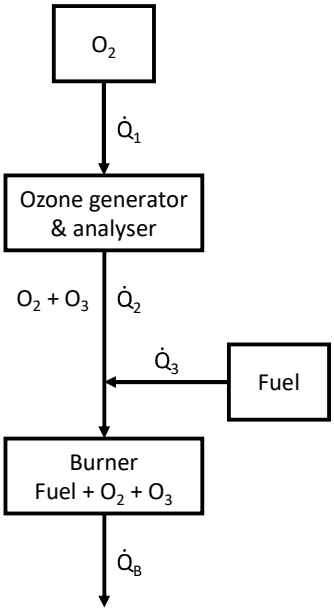

Firstly, each flux is defined as follow:

· **O_2** $\dot{F}_{1,O_2} - \xi = \dot{F}_{B,O_2}$ (1)

· **O_3** $\frac{2}{3}\xi = \dot{F}_{B,O_3}$, considering $O_2 \Leftrightarrow \frac{2}{3} O_3$. As $\dot{F}_{B,O_3} = \dot{F}_B \cdot x_{B,O_3}$, it comes $\xi = \frac{3}{2}\dot{F}_B \cdot x_{O_3}$ (2)

· **Fuel** $\dot{F}_{3,F} = \dot{F}_{3,B}$ (3)

· **Stoichiometry** $\varphi = \frac{\left(\frac{\dot{F}_{3,F}}{\dot{F}_{1,O_2}}\right)}{\left(\frac{\upsilon_F}{\upsilon_{O_2}}\right)} \Leftrightarrow \dot{F}_{3,F} = \left(\frac{\upsilon_F}{\upsilon_{O_2}}\right) \cdot \varphi \cdot \dot{F}_{1,O_2}$,

$\dot{F}_3 \cdot x_{3,F} = \left(\frac{\upsilon_F}{\upsilon_{O_2}}\right) \cdot \varphi \cdot \dot{F}_1 \cdot x_{3,O_2}$ (4)

The molar flow at the burner exit, $\dot{F}_B$, can be expressed as follow:

$$\dot{F}_B = \dot{F}_{1,O_2} - \frac{1}{3}\xi + \dot{F}_{3,F} \qquad (5)$$

The ozone mole fraction at the burner exit can thus be expressed, following (2) and (5)

$$x_{B,O_3} = \frac{\frac{2}{3}\xi}{\dot{F}_{1,O_2} - \frac{1}{3}\xi + \dot{F}_{3,F}} \qquad (6)$$

$$\Leftrightarrow x_{B,O_3} = \frac{\dot{F}_B \cdot x_{B,O_3}}{\dot{F}_1 + \left(\frac{\upsilon_F}{\upsilon_{O_2}}\right)\cdot\varphi\cdot\dot{F}_1\cdot\left(\frac{x_{3,O_2}}{x_{3,F}}\right) - \frac{1}{2}\dot{F}_B\cdot x_{B,O_3}}$$

$$\Leftrightarrow \dot{F}_1 + \left(\frac{\upsilon_F}{\upsilon_{O_2}}\right)\cdot\varphi\cdot\dot{F}_1\cdot\left(\frac{x_{3,O_2}}{x_{3,F}}\right) - \frac{1}{2}\dot{F}_B\cdot x_{B,O_3} = \dot{F}_B$$

$$\Leftrightarrow \dot{F}_1\cdot\left(1 + \left(\frac{\upsilon_F}{\upsilon_{O_2}}\right)\cdot\varphi\cdot\left(\frac{x_{3,O_2}}{x_{3,F}}\right)\right) = \dot{F}_B\left(1 + \frac{1}{2}x_{B,O_3}\right)$$

$$\Leftrightarrow \dot{F}_1 = \dot{F}_B\frac{\left(1+\frac{1}{2}x_{B,O_3}\right)}{\left(1+\left(\frac{\upsilon_F}{\upsilon_{O_2}}\right)\cdot\varphi\cdot\left(\frac{x_{3,O_2}}{x_{3,F}}\right)\right)}$$

$$\Leftrightarrow \dot{Q}_1 = \dot{Q}_B\frac{\left(1+\frac{1}{2}x_{B,O_3}\right)}{\left(1+\left(\frac{\upsilon_F}{\upsilon_{O_2}}\right)\cdot\varphi\cdot\left(\frac{x_{3,O_2}}{x_{3,F}}\right)\right)}, \text{ and } \dot{Q}_3 = \left(\frac{\upsilon_F}{\upsilon_{O_2}}\right)\cdot\varphi\cdot\dot{Q}_1\cdot\frac{x_{3,O_2}}{x_{3,F}}$$

Finally,

$$x_{2,O_3} = \frac{F_{2,O_3}}{F_2} = \frac{\dot{F}_B\cdot x_{B,O_3}}{\dot{F}_1 - \frac{1}{2}\dot{F}_B\cdot x_{B,O_3}} = \frac{\dot{Q}_B\cdot x_{B,O_3}}{\dot{Q}_1 - \frac{1}{2}\dot{Q}_B\cdot x_{B,O_3}}$$

In our experimental conditions, $\dot{Q}_B$ is calculated from the strain rate (α, s^{-1}) and the inlet section of the burner. Moreover, the equivalence ratio ϕ and the ozone concentration x_{B,O_3} are used as inputs.

Appendix II.A4. Step-by-step calculation of the quenched CH_2O signal from simulated profiles.

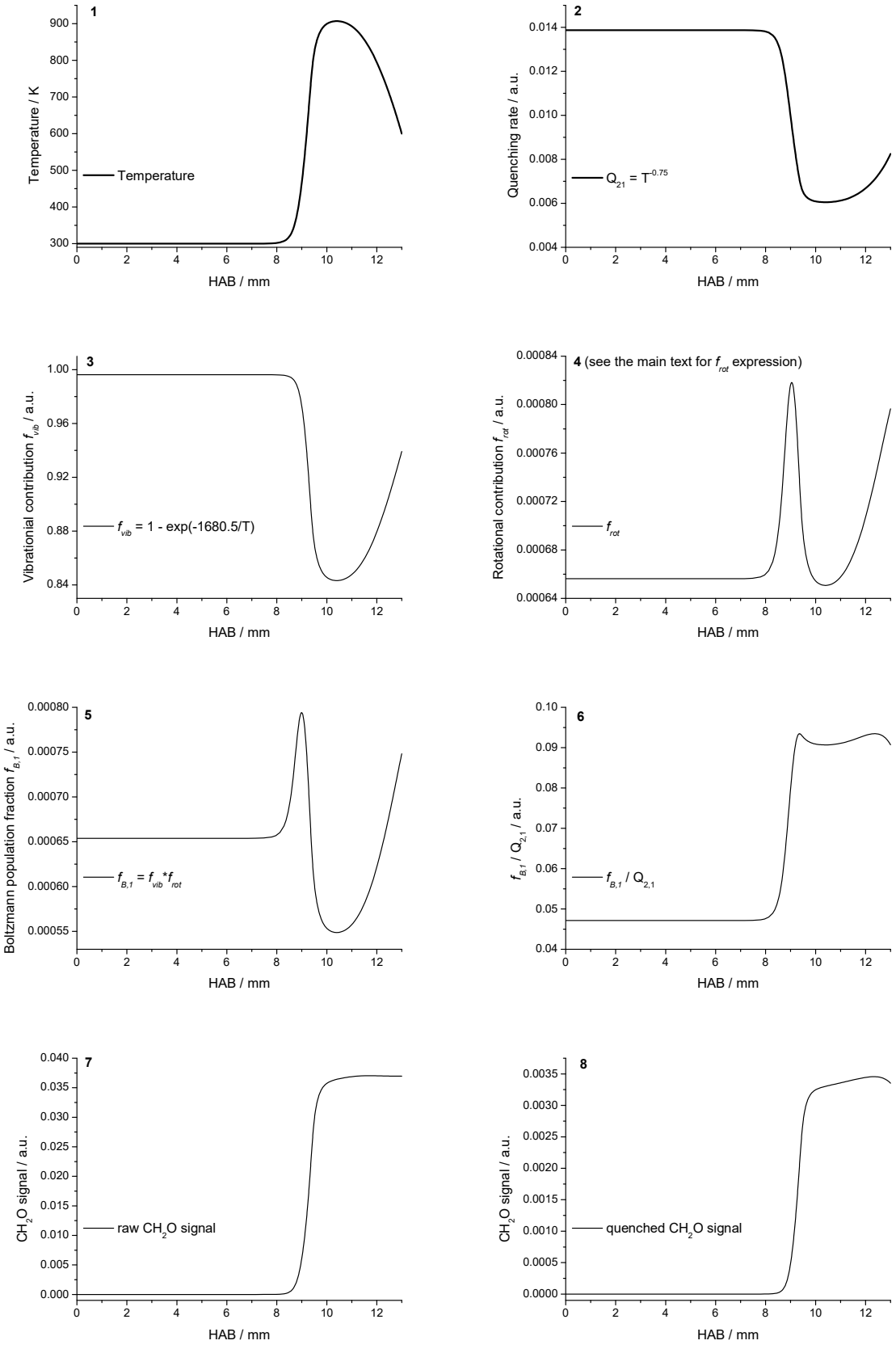

Appendix II.A5. Operating conditions of the GCs & µGCs.

- Operating conditions of the µGC

Run time	90 seconds
Injection time	100 ms
Injector temperature	50°C
Column temperature (constant)	120°C
Column pressure (constant)	150 kPa

- GCs columns temperature ramps

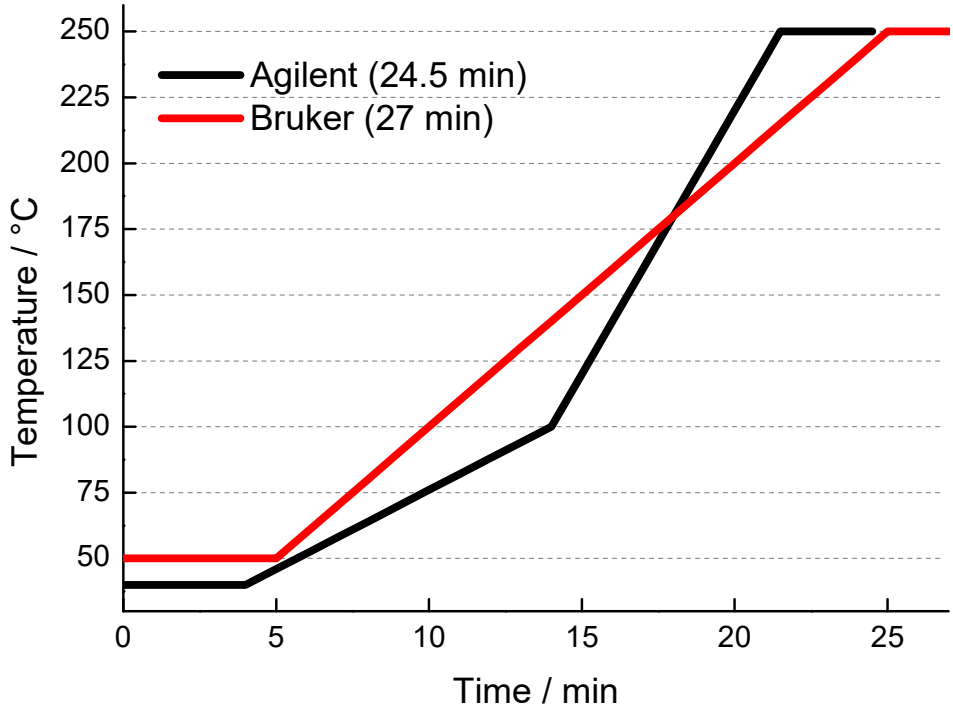

The Bruker's column temperature ramp is the same for DEE and OME-2/DME cool flame analyses.

Appendix II.A6. µGC injection procedure & protocol.

- Injection scheme & protocol

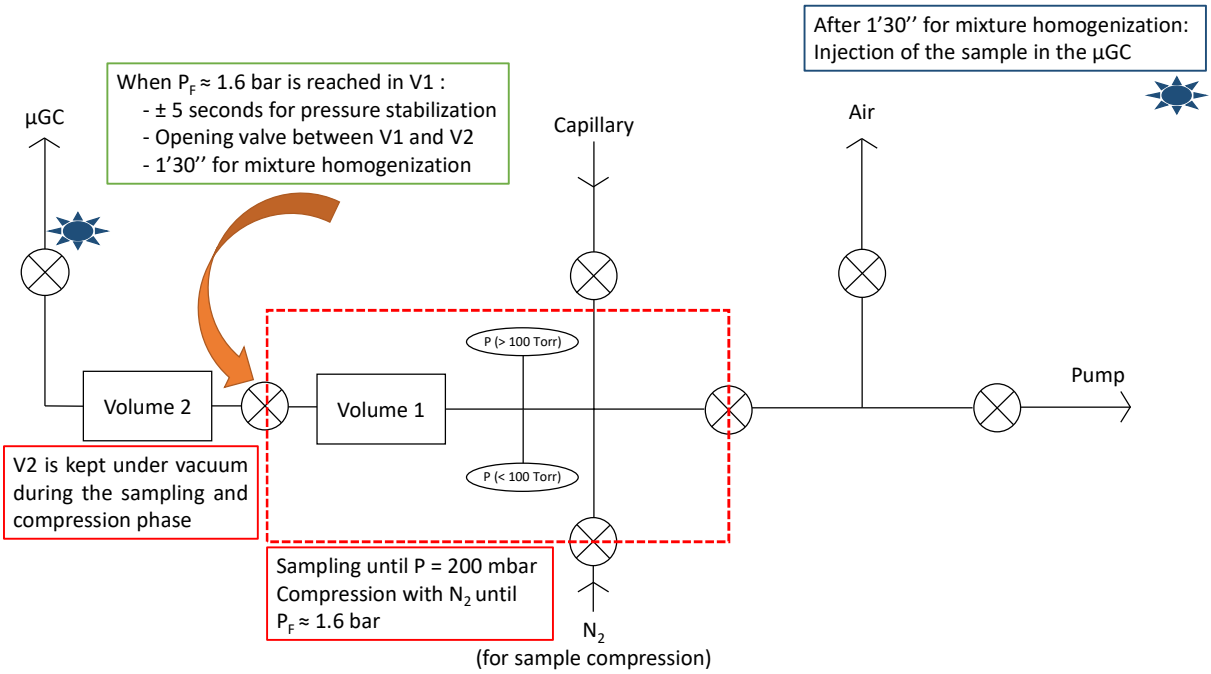

- Repeatability tests

While performing different tests ensuring that data from the µGC can be trustworthy, it was found out that the response signal from the µGC was highly dependent on the homogenization time in Volume 2 while the mole fraction of the tested species was kept constant. As observed in the figure below, the signal does not significantly vary when the homogenization time exceeds 30 seconds. To ensure a sufficient homogenization of the mixture before injection, the mixture homogenization time was set at 90 s. Gases used for these tests were CO_2 and DME.

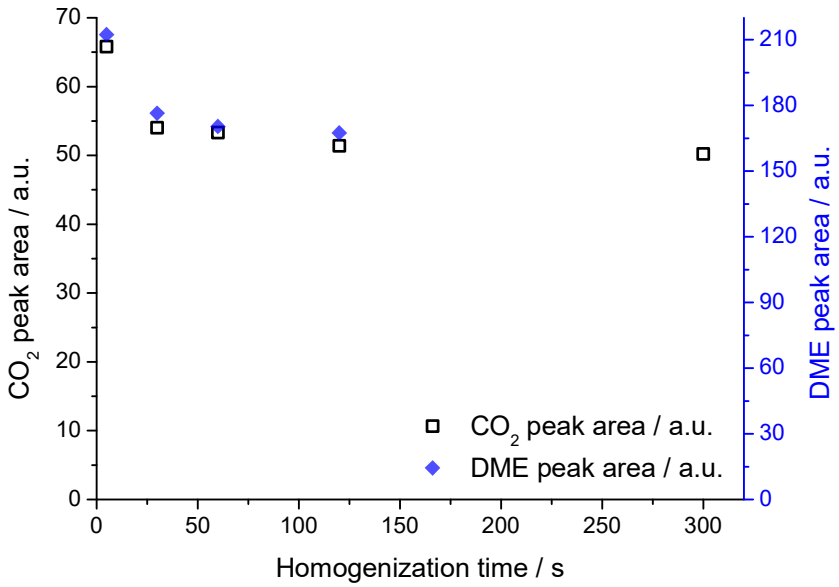

Appendix II.A7. Calibration curves for the different species measured in each cool flame.

- Calibrations for DME/O_2/O_3 cool flames

Measurements in the DME/O_2/O_3 cool flames were performed with the μGC (CH_3OCH_3, CH_3OCHO, CH_3OH, CH_2O, CO_2) and the Agilent 6890 GC (CO). In the μGC, samples were diluted in nitrogen allowing to reach an injection pressure above 1 atm. Thus, the calibration curves are presented as Signal(Species) = f(species mole fraction * dilution factor). The CO calibration was performed using a standard reference gas. Finally, for CH_2O calibration, the 1,3,5-trioxane calibration (used to correct the CH_2O mole fraction) is also shown.

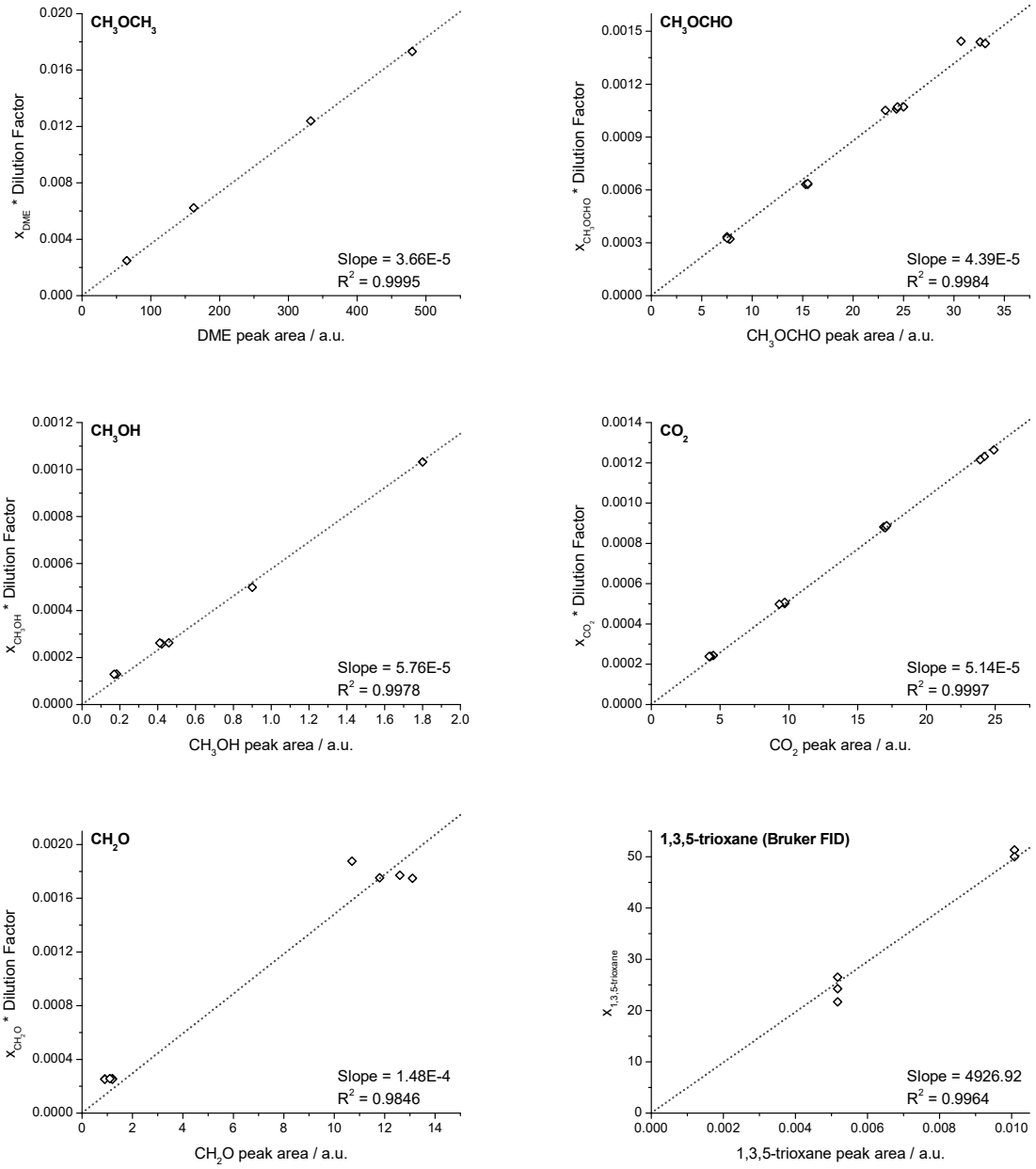

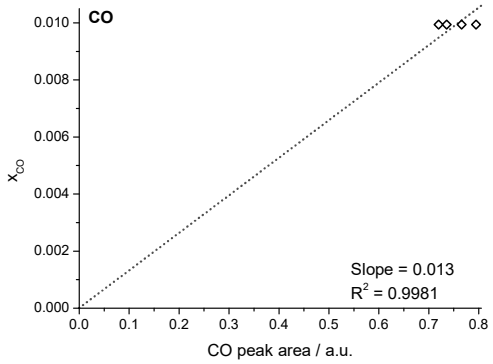

- Calibrations for $DEE/O_2/O_3$ and DEE/O_2 cool flames

Measurements in the $DEE/O_2/O_3$ and DEE/O_2 cool flames were performed with the Bruker Scion GC/MS and the Agilent 6890 GC.

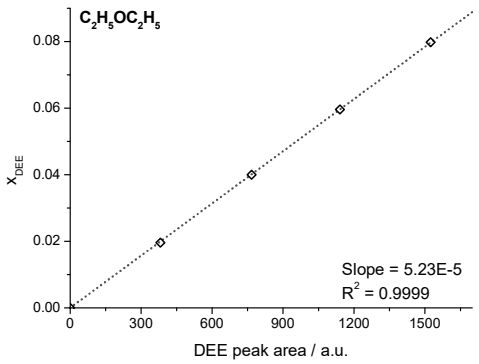

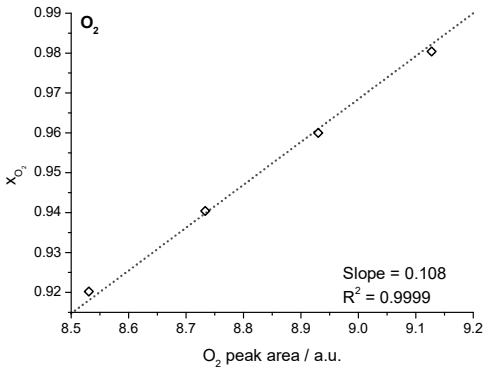

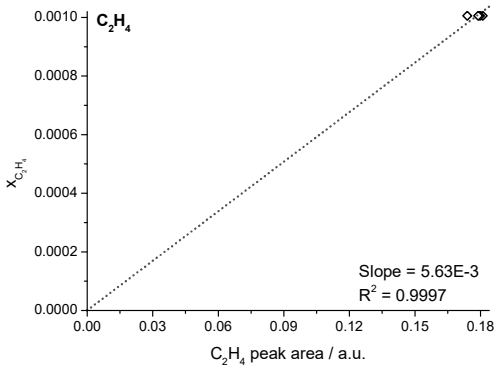

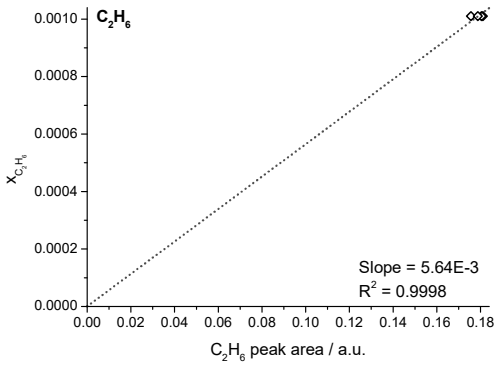

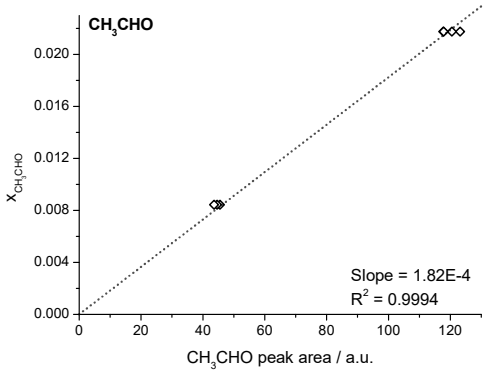
CH3CHO
Slope = 1.82E-4
R2 = 0.9994
CH3CHO peak area / a.u.

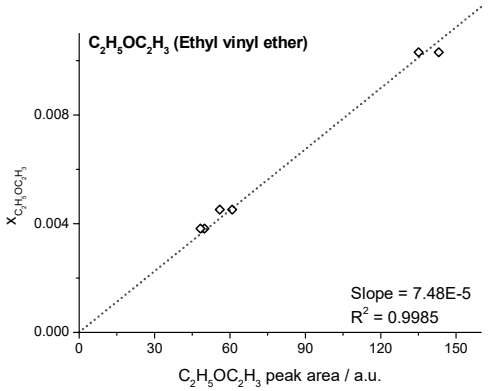
C2H5OC2H3 (Ethyl vinyl ether)
Slope = 7.48E-5
R2 = 0.9985
C2H5OC2H3 peak area / a.u.

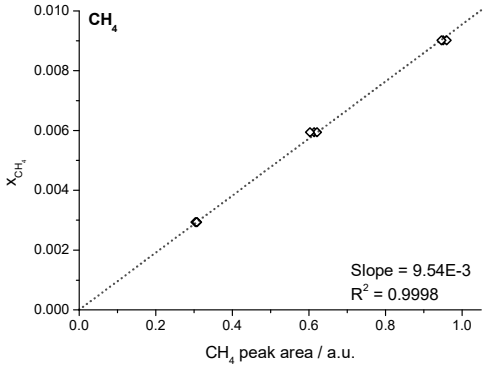
CH4
Slope = 9.54E-3
R2 = 0.9998
CH4 peak area / a.u.

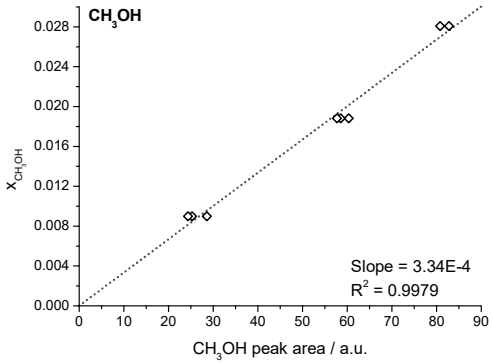
CH3OH
Slope = 3.34E-4
R2 = 0.9979
CH3OH peak area / a.u.

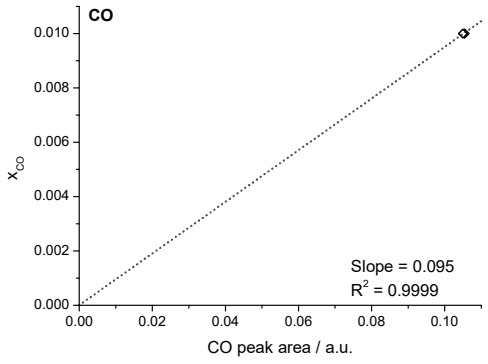
CO
Slope = 0.095
R2 = 0.9999
CO peak area / a.u.

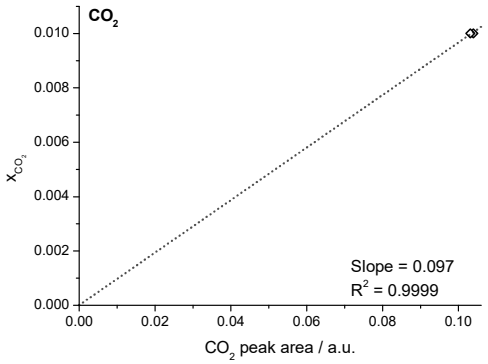
CO2
Slope = 0.097
R2 = 0.9999
CO2 peak area / a.u.

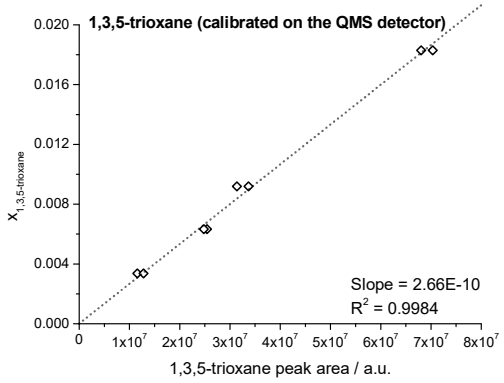
1,3,5-trioxane (calibrated on the QMS detector)
Slope = 2.66E-10
R2 = 0.9984
1,3,5-trioxane peak area / a.u.

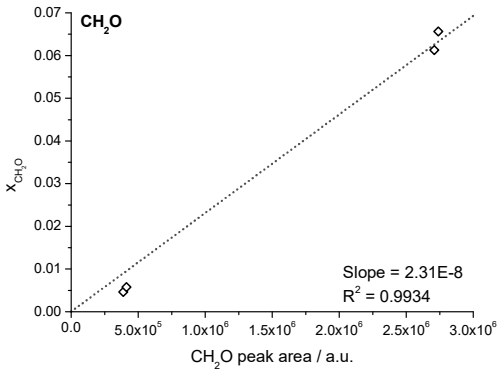
CH2O
Slope = 2.31E-8
R2 = 0.9934
CH2O peak area / a.u.

Below is presented the acid acetic calibration, performed on the QMS detector of the Bruker Scion GC. As explained in the main text, it was calibrated using methanol/acid acetic/acetaldehyde solutions. Thus, the acetic acid signal is plotted as follows:

$$\frac{Peak\ area_{acetaldehyde}}{Peak\ area_{acetic\ acid}} = f\left(\frac{n_{acetaldehyd}}{n_{acetic\ acid}}\right)$$

The acetaldehyde peak area on the QMS detector is measured at 44 m/z, and 60 m/z for acetic acid, their respective molecular ions.

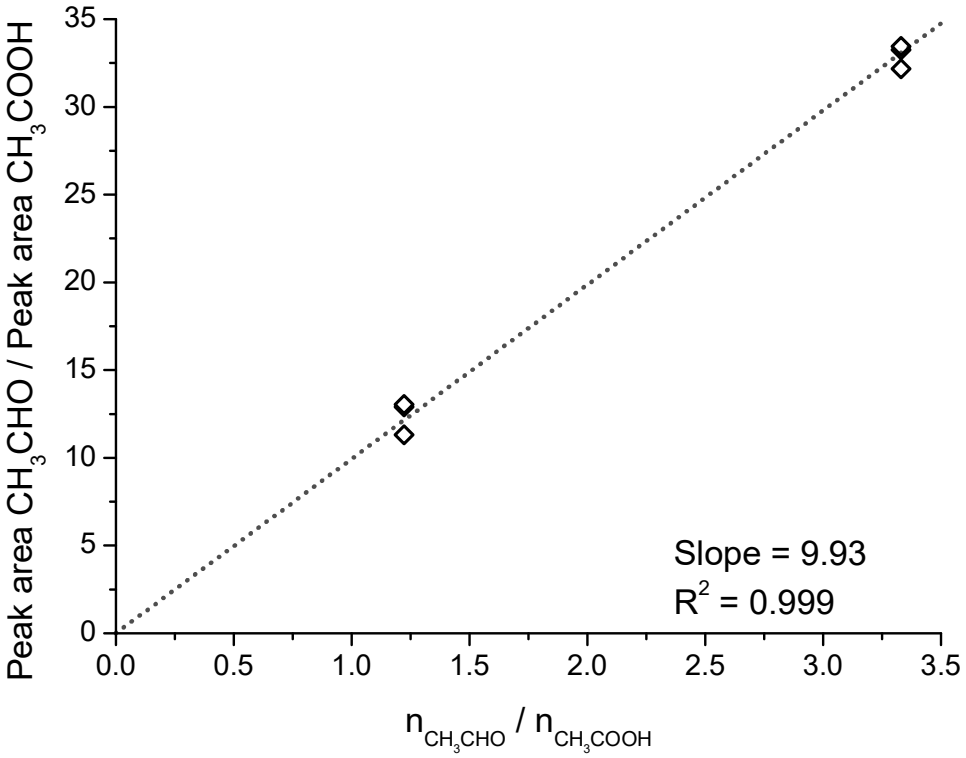

- Calibrations for the OME-2/DME/O_2/O_3 cool flames

Measurements in the OME-2/DME/O_2/O_3 cool flames were performed with the Bruker Scion GC/MS and the Agilent 6890 GC.

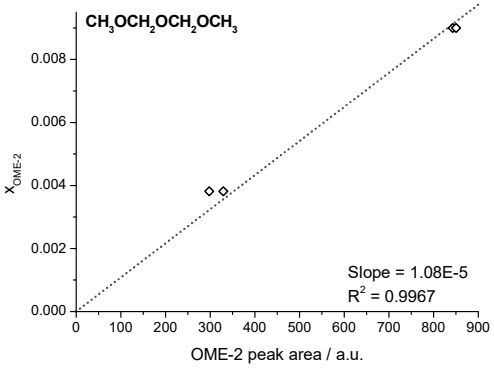

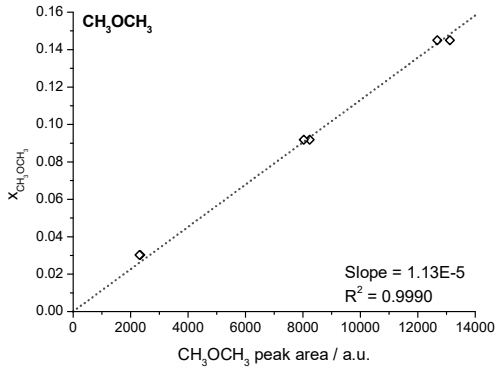

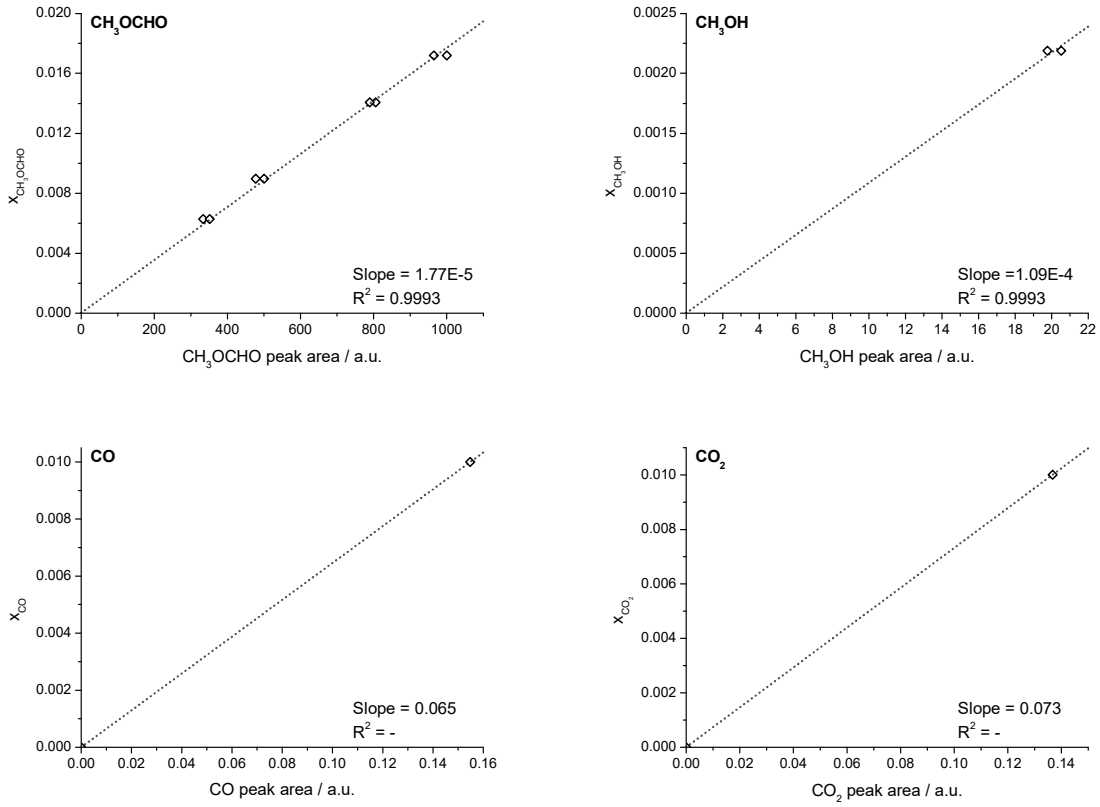

Appendix II.A8. Comparison between species mole fraction profiles obtained by i) in-house gas mixture calibration or ii) the equivalent carbon number method. Acetaldehyde and methanol mole fraction profiles in the DEE/O_2/O_3 (ϕ = 0.5) cool flame are used for illustration.

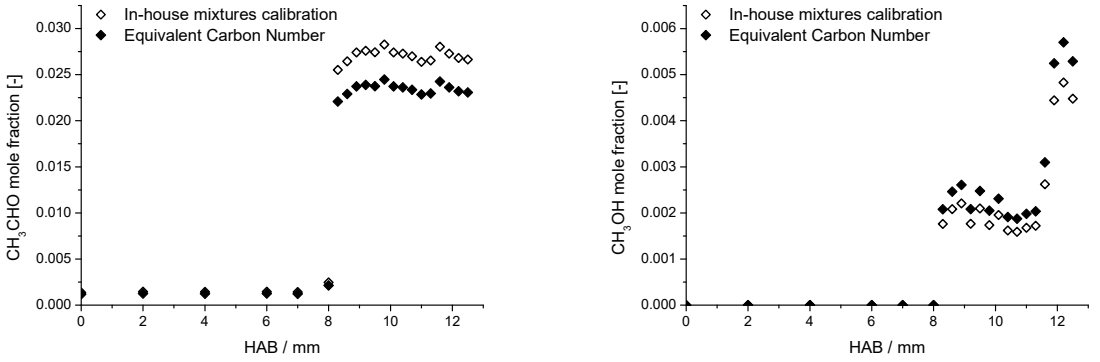

Appendix II.A9. Ozone calibrations using the Omnistar GSD 301 O2 Pfeiffer Vacuum mass spectrometer. The calibration (a) is for the DME/O_2/O_3 cool flames, (b) for the DEE/O_2/O_3 cool flame and (c) for the OME-2/DME/O_2/O_3 cool flames.

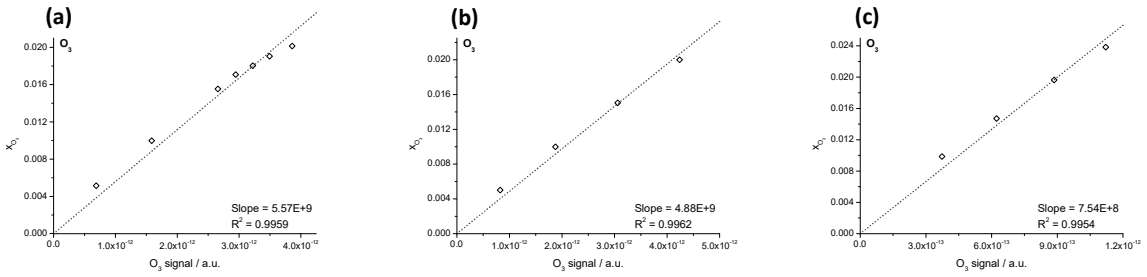

Appendix II.A10. Comparison of the ozone mole fraction upstream and downstream the burner. The flow consists of pure oxygen at different ozone concentrations (different set points on the ozone generator). The oxygen flow rate was set at 2.74 slpm.

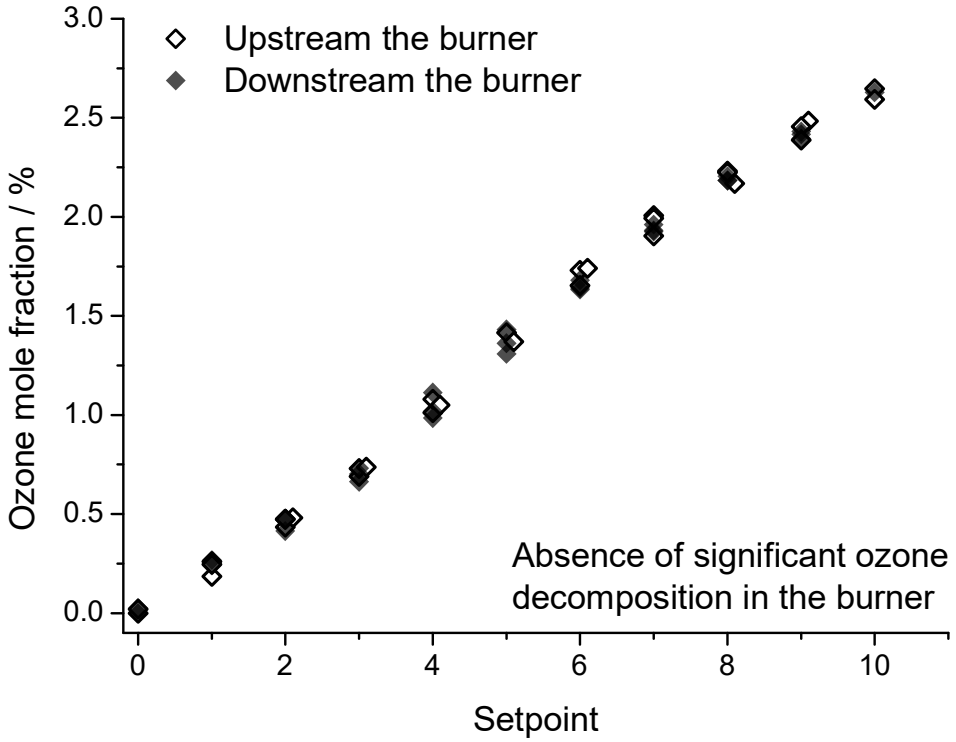

Appendix II.A11. Comparison of the two image-processing methods in reactive conditions. Both flames conditions are ϕ = 0.4, x_{O3} = 1.9%, with inlet velocities respectively equal to 0.75 m·s^{-1} (black points) and 1.10 m·s^{-1} (blue points).

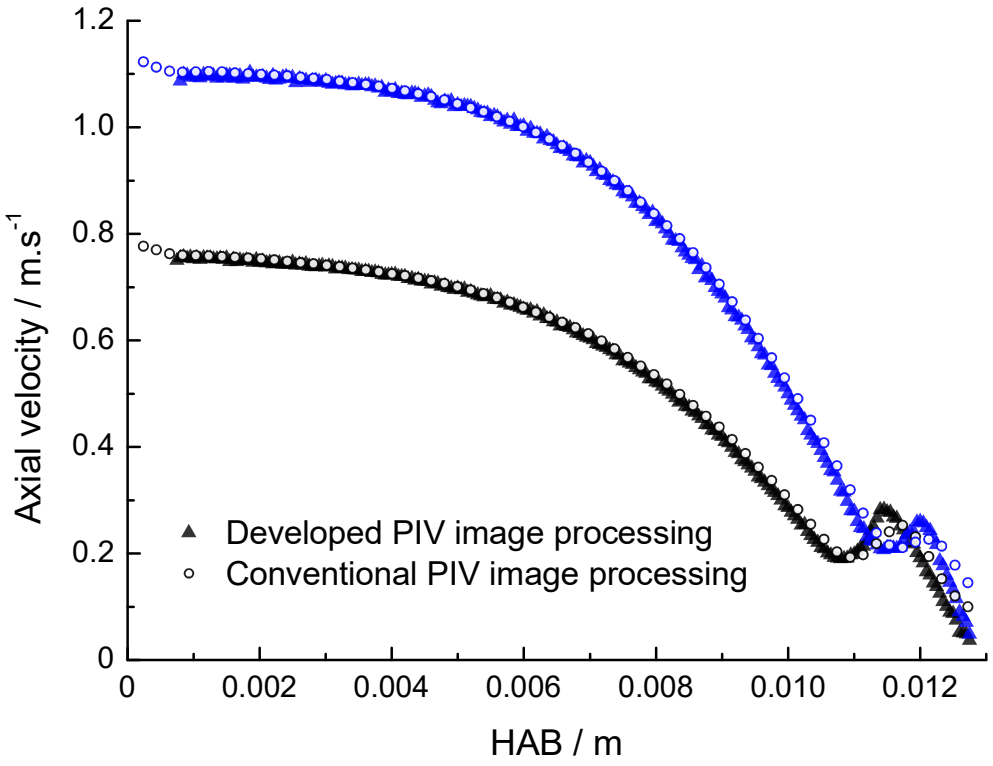

Appendix II.A12. Comparison between non-averaged and averaged axial velocity profiles on several burner radii, respectively ± 250 µm, ± 500 µm, ± 750 µm and ± 1 mm. Obtained velocity profiles are very similar whatever the averaged interval, comforting us in the choice of averaging axial velocity profiles on ± 1 mm.

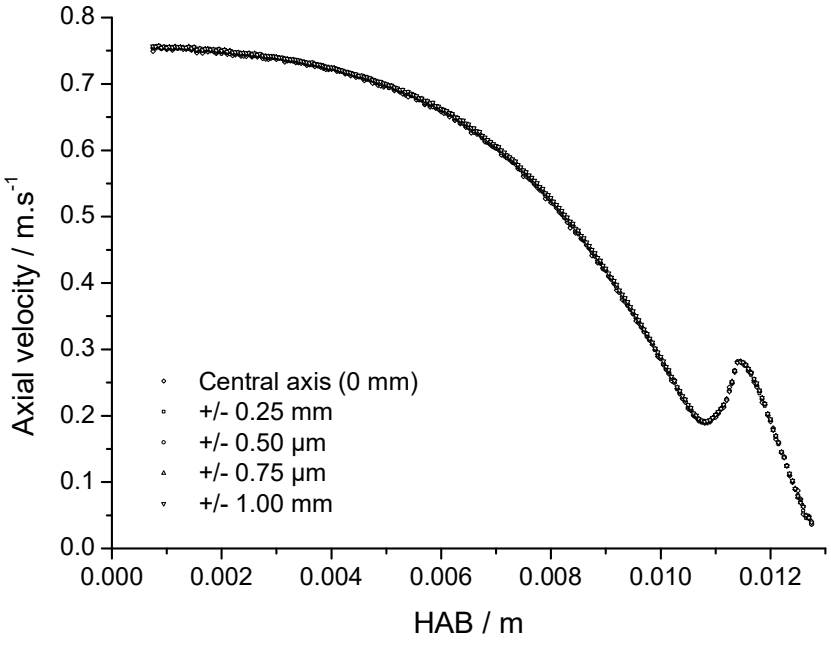

Appendix II.A13. Averaged axial velocity profile (± 1 mm) using 200 post-processed images and 1000 post-process images. The obtained axial velocity profile using 1000 images is slightly less scattered compared to the one resulting from 200 images.

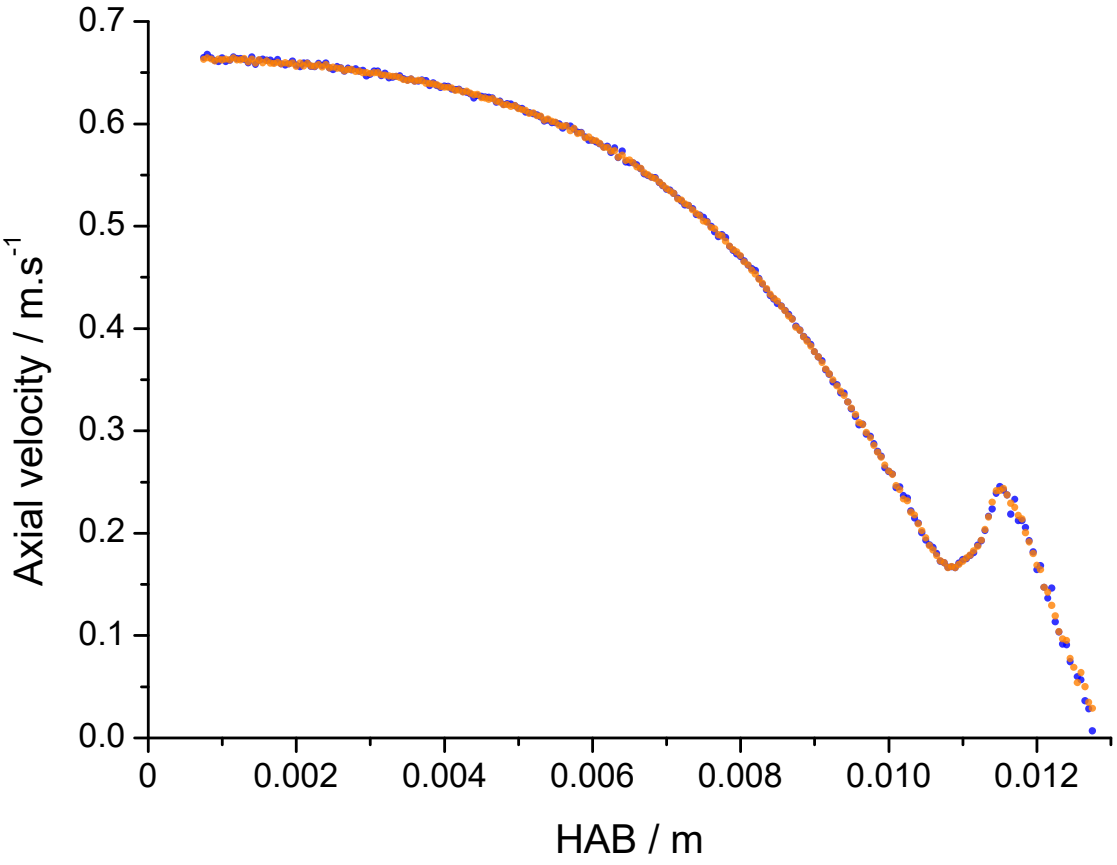

Appendix III.A1. Impact of ozone on the flame front position at different equivalence ratios and at different strain rates, respectively: (a) $\alpha = 10\ s^{-1}$, (b) $\alpha = 15\ s^{-1}$, (c) $\alpha = 20\ s^{-1}$, (d) $\alpha = 25\ s^{-1}$, (e) $\alpha = 40\ s^{-1}$, (f) $\alpha = 50\ s^{-1}$.

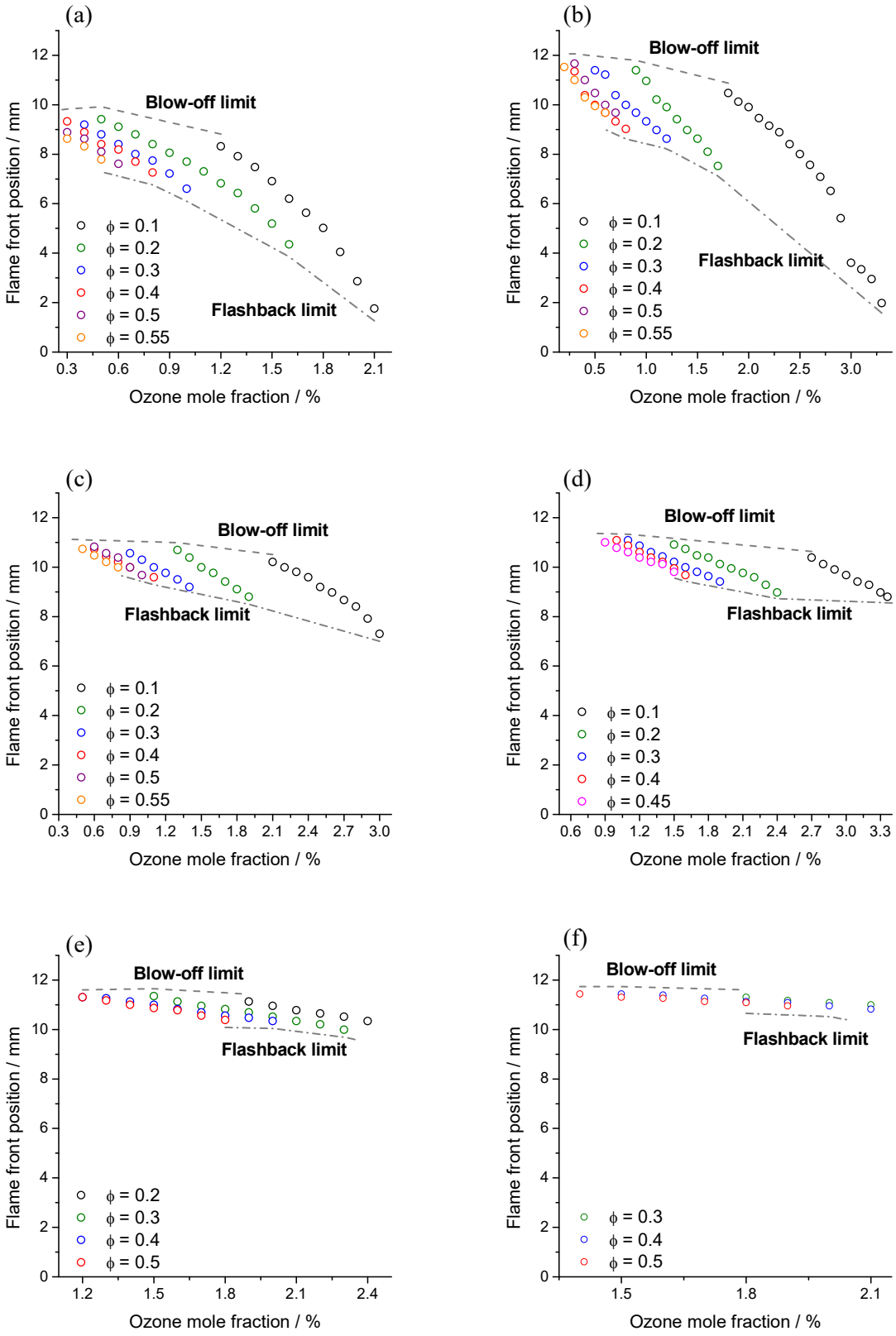

Appendix III.A2. DME, O_2 and N_2 flow rates corresponding to the experimental conditions shown in Appendix II.A1.

Condition	$\dot{Q}_{O2}$ / L·min^{-1}	$\dot{Q}_{N2}$ / L·min^{-1}	$\dot{Q}_{DME}$ / mL·min^{-1}
$\alpha = 10$ s^{-1} $\phi = 0.1 \rightarrow 0.55$ $x_{O3} = 0.3 \rightarrow 2.1\%$	0.51 – 0.60	0.68	20.0 – 95.9
$\alpha = 15$ s^{-1} $\phi = 0.1 \rightarrow 0.55$ $x_{O3} = 0.2 \rightarrow 3.3\%$	0.78 – 0.90	1.03	30.0 – 143.9
$\alpha = 20$ s^{-1} $\phi = 0.1 \rightarrow 0.55$ $x_{O3} = 0.5 \rightarrow 3.0\%$	1.04 – 1.20	1.37	39.9 – 191.8
$\alpha = 25$ s^{-1} $\phi = 0.1 \rightarrow 0.45$ $x_{O3} = 0.9 \rightarrow 3.3\%$	1.35 – 1.50	1.71	49.9 – 201.9
$\alpha = 40$ s^{-1} $\phi = 0.2 \rightarrow 0.5$ $x_{O3} = 1.2 \rightarrow 2.4\%$	2.12 – 2.32	1.37	154.8 – 353.7
$\alpha = 50$ s^{-1} $\phi = 0.3 \rightarrow 0.5$ $x_{O3} = 1.4 \rightarrow 2.1\%$	2.65 – 2.81	1.71	281.4 – 442.2

Appendix III.A3. Ozone mole fraction influence on the flame front position.

■ Variation of the ozone mole fraction at $\alpha = 10\ s^{-1}$ for different equivalence ratios, respectively a) $\phi = 0.1$, b) $\phi = 0.2$, c) $\phi = 0.3$, d) $\phi = 0.4$, e) $\phi = 0.5$, g) $\phi = 0.55$.

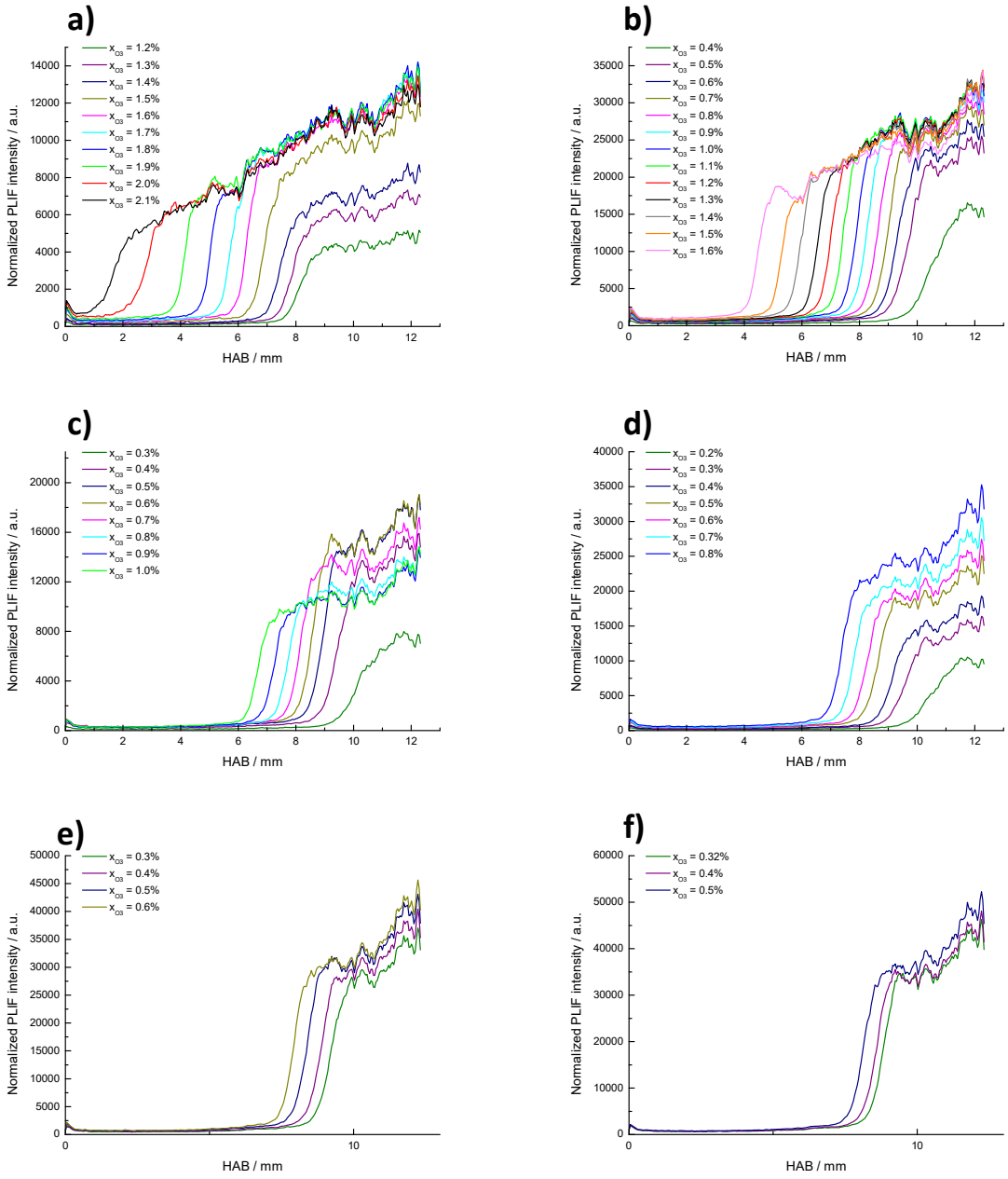

■ Variation of the ozone mole fraction at $\alpha = 15\ s^{-1}$ for different equivalence ratios, respectively a) $\phi = 0.1$, b) $\phi = 0.2$, c) $\phi = 0.3$, d) $\phi = 0.4$, e) $\phi = 0.5$, g) $\phi = 0.55$.

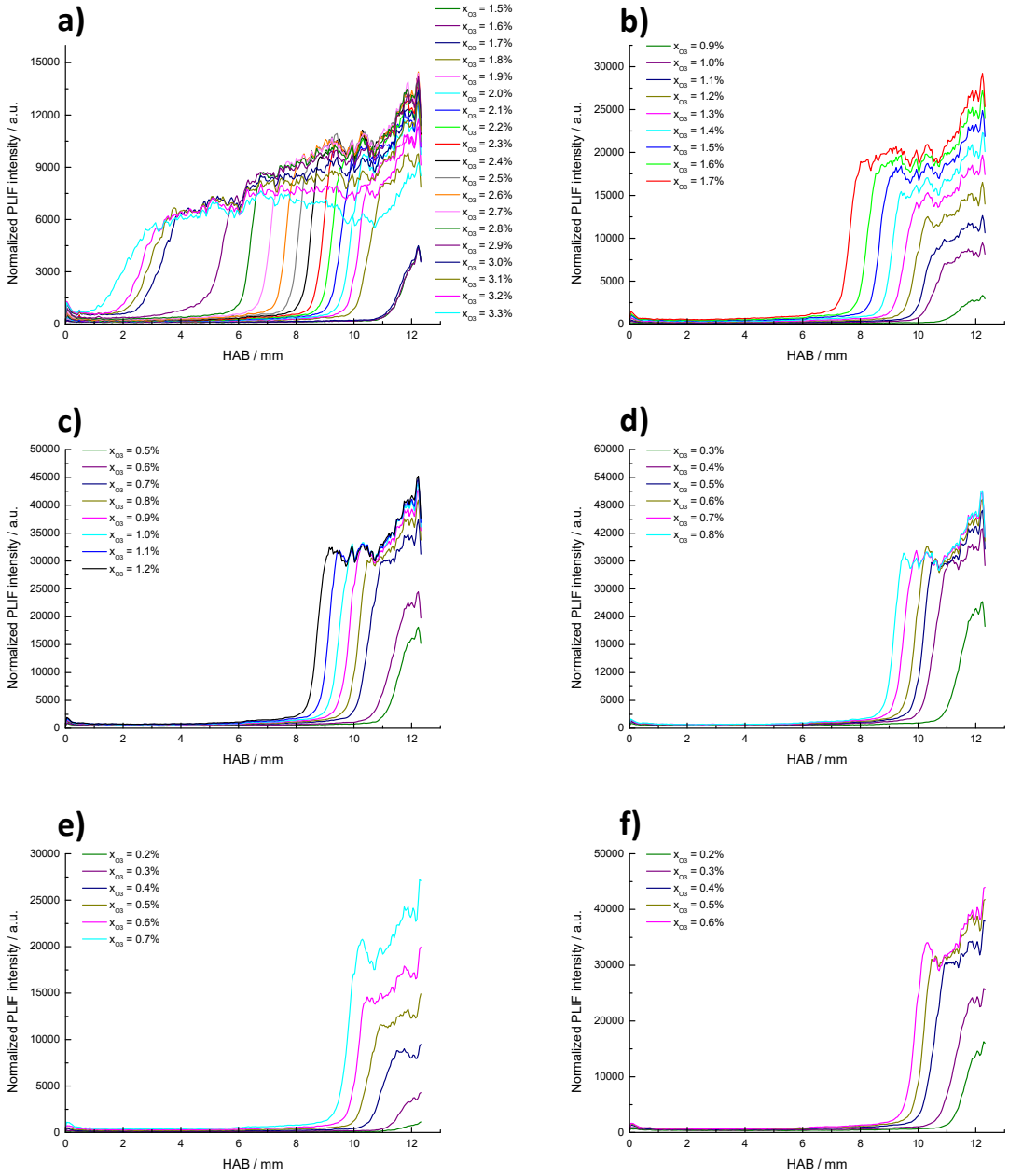

■ Variation of the ozone mole fraction at $\alpha = 20\ s^{-1}$ for different equivalence ratios, respectively a) $\phi = 0.1$, b) $\phi = 0.2$, c) $\phi = 0.3$, d) $\phi = 0.4$, e) $\phi = 0.5$, g) $\phi = 0.55$.

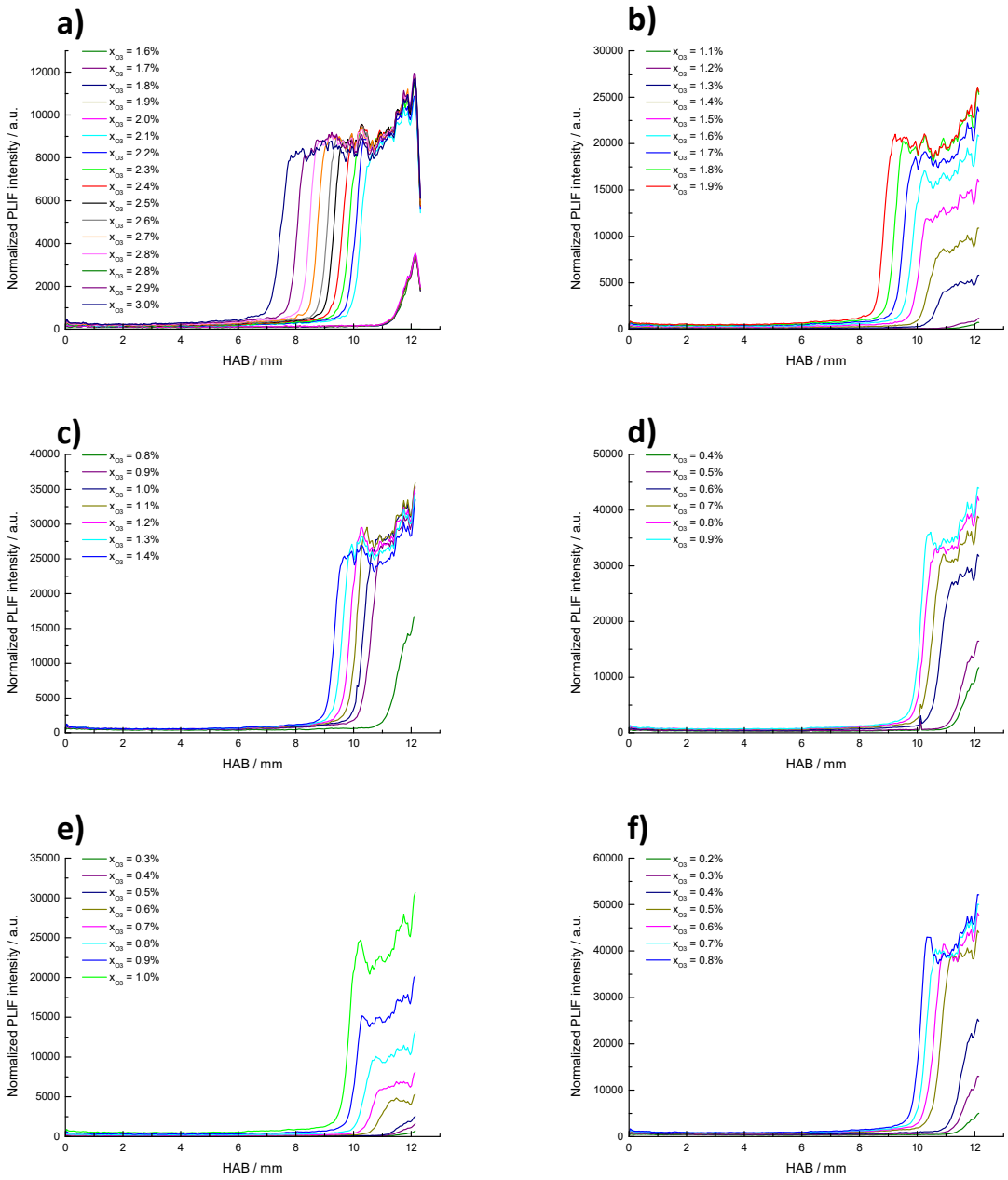

■ Variation of the ozone mole fraction at $\alpha = 25\ s^{-1}$ for different equivalence ratios, respectively a) $\phi = 0.1$, b) $\phi = 0.2$, c) $\phi = 0.3$, d) $\phi = 0.4$, e) $\phi = 0.45$.

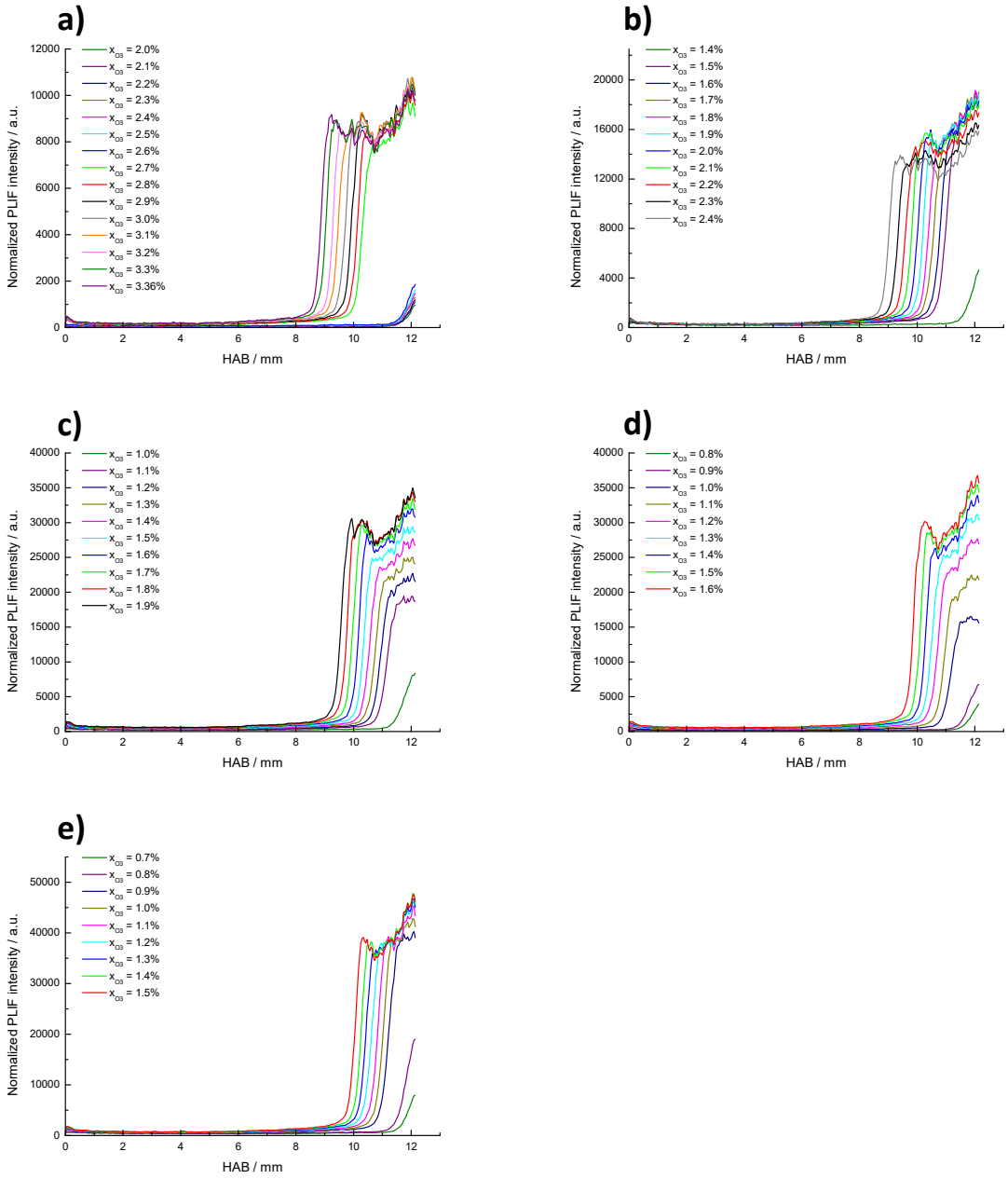

■ Variation of the ozone mole fraction at $\alpha = 40\ s^{-1}$ for different equivalence ratios, respectively a) $\phi = 0.2$, b) $\phi = 0.3$, c) $\phi = 0.4$, d) $\phi = 0.5$.

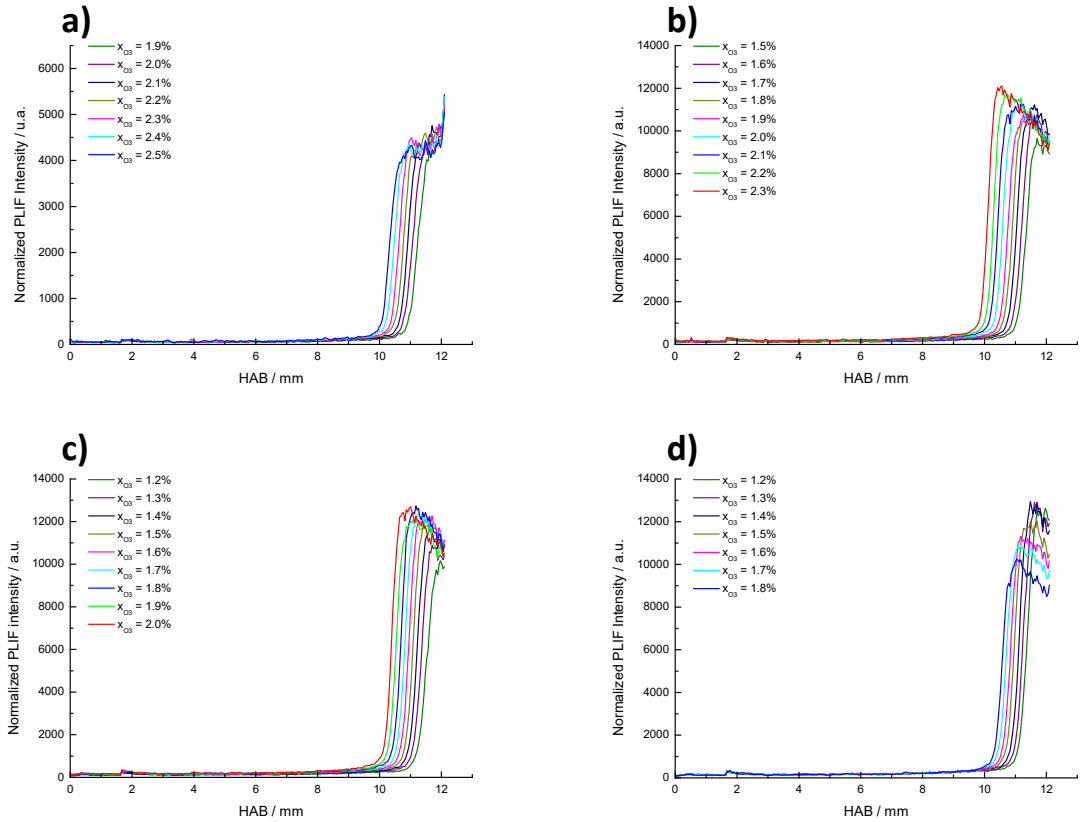

■ Variation of the ozone mole fraction at $\alpha = 50\ s^{-1}$ for different equivalence ratios, respectively a) $\phi = 0.3$, b) $\phi = 0.4$, c) $\phi = 0.5$.

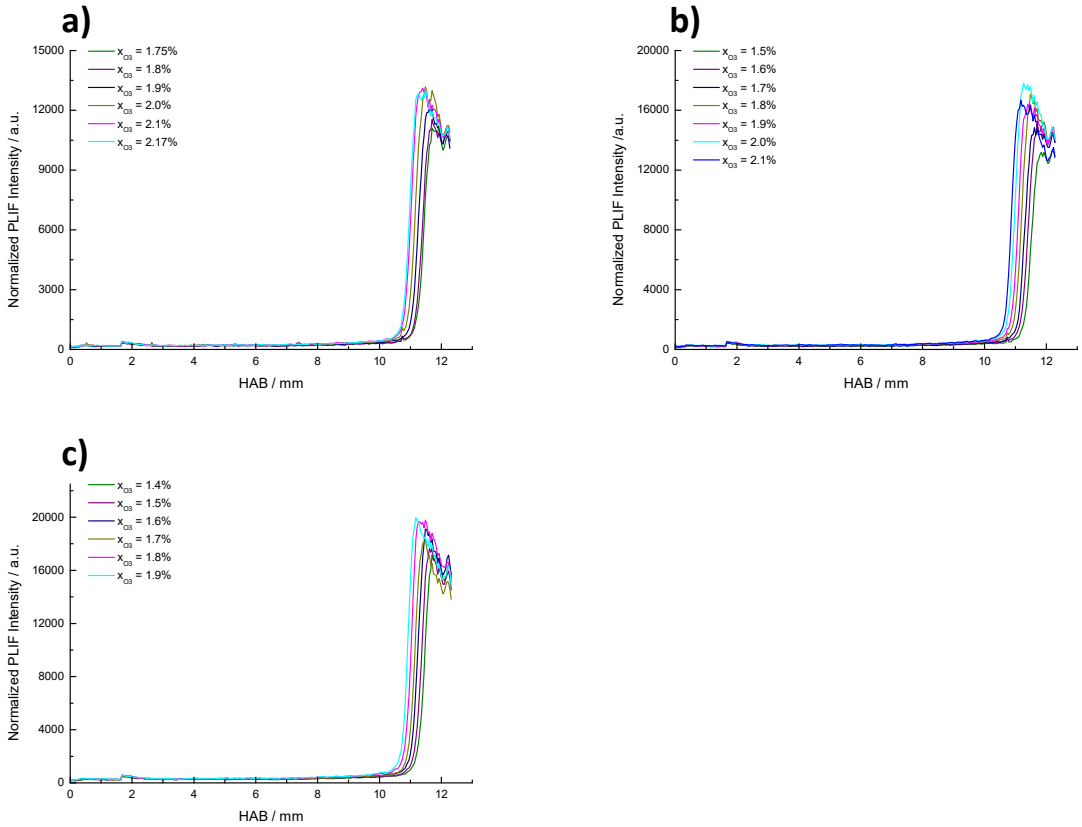

Appendix III.A4. Generalities on kinetic modelling and kinetic model structure.

Each elementary reaction is defined by a reaction rate, which represents the consumption rate of the reactants and the formation rate of the products. Considering a reaction written as aA + bB ↔ cC + dD, the consumption rate of A and B can be expressed as:

$$\frac{1}{a}\cdot\frac{d[A]}{dt}=\frac{1}{b}\cdot\frac{d[B]}{dt}=-k_{forward}\cdot[A]^{a}\cdot[B]^{b}+k_{backward}[C]^{C}\cdot[D]^{D}$$

where $[A]$ and $[B]$ represent the molar concentration of each reactant, a and b the stoichiometric coefficients, t the time and k the forward reaction rate constant. Using the Arrhenius formalism, the rate constant k can be expressed as follows:

$$k=A\cdot e^{-\frac{E_A}{RT}}$$

where A is the so-called pre-exponential factor, E_A the activation energy of the reaction, R the universal constant of the ideal gas law, and T the temperature. Due to a non-linear evolution of ln(k) as a function of 1/T in some conditions, a modified version of the Arrhenius formalism was introduced, as is expressed as follows:

$$k=A\cdot T^{n}\cdot e^{-\frac{E_A}{RT}}$$

where n is a constant which introduces the non-linear temperature dependence of ln(k) regarding 1/T.

Finally, the last notion that needs to be introduced is the thermal equilibrium K_c. In the case of reversible reactions, the thermal equilibrium can be expressed as follows -using the molar concentrations-:

$$K_c=\frac{k_{forward}}{k_{reverse}}=\frac{[C]^{c}\cdot[D]^{d}}{[A]^{a}\cdot[B]^{b}}$$

Parameters defined in the kinetic model allow to calculate the value of the rate constant k of each elementary reaction present in the model at the needed temperature and pressure. Each reaction is defined by three parameters, respectively A, n and E_a, allowing in each case to calculate the reaction rate k following the modified Arrhenius law. An example of reaction definition in a kinetic file (generally .inp for the Chemkin-Pro format) is presented below, the unit for the activation energy being generally in cal·mol^{-1}.

Reaction	**A**	**n**	**Ea**
CH3OCH3 + OH ↔ CH3OCH2 + H2O	9.3500e+05	2.29	-780.7

These three parameters permit to calculate the forward rate constant when the latter is defined as reversible (symbol: ↔). In this case, the reverse rate constant is calculated using the previously defined equilibrium constant K. Calculation of the equilibrium constant is realized in Chemkin-Pro and Cantera through the use of the thermodynamic data. Firstly, the equilibrium rate constant K_c is re-calculated in pressure units as follow:

$$K_c = K_p \cdot \left(\frac{P_{atm}}{R \cdot T}\right)^{\sum \nu_{ki}}$$

The equilibrium constant K_p is obtained with the following relationship:

$$K_p = e^{\left(\frac{\Delta S_i^0}{R} - \frac{\Delta H_i^0}{RT}\right)}$$

where ΔS and ΔH refer to variation of entropy and enthalpy when passing completely from reactants to products in the i^{th} reaction. Finally, S_i^0, $H_i^0$and $C_{p,i}^0$, respectively the entropy, the enthalpy and the heat capacity of the species *i*, can be calculated from the thermodynamic data which are defined by the NASA polynomial formalism [260]:

Heat capacity: $\frac{C_p^0}{R} = a_1 + a_2 T + a_3 T^2 + a_4 T^3 + a_5 T^4$

Enthalpy: $\frac{H^0(T)}{RT} = a_1 + \frac{a_2}{2} T + \frac{a_3}{3} T^2 + \frac{a_4}{4} T^3 + \frac{a_5}{5} T^4 + a_6 \frac{1}{T}$

Entropy: $\frac{S^0}{R} = a_1 \ln(T) + a_2 T + \frac{a_3}{2} T^2 + \frac{a_4}{3} T^3 + \frac{a_5}{4} T^4 + a_7$

where the coefficients a_n ($1 \leq n \leq 7$) are declared in the thermodynamic file for two different temperature domains: the first one at low temperatures, frequently defined between 300 and 1000 K, and the second one at higher temperatures, frequently between 1000 and 5000 K. An example is shown below, where the 7 first coefficients are the coefficients a_1 to a_7 of the high temperature domain, and the 7 last coefficients are the coefficients a_1 to a_7 of the low temperature domain.

```
CH3OCH3                                                                 1
6.032E+00       1.561E-02       5.507E-06       8.76E-10        -5.17E-14  2
-2.53E+04       -8.26E+00       2.056E+00       2.07E-02        -5.00E-06  3
-1.62E-09       6.843E-13       -2.35E+04       1.45E+01                   4
```

Finally, the last important data are the transport data. These data are not necessary for 0-D simulations such as homogeneous reactors, but are mandatory for 1-D simulations. They allow to consider for molecular diffusion of species. They are especially sensitive for small species such as atoms or small radicals.

Brute-force sensitivity analysis:

Brute-force sensitivity analyses are performed on the cool flame delay, i.e., the first stage ignition delay in a constant volume reactor. This analysis allows to highlight the influent reactions on the calculated parameter, here the first stage ignition delay time. The sensitivity coefficient on the reaction *i*, S_i, was calculated as follows:

$$S_i = \frac{\ln\left(\frac{\tau_i^+}{\tau_i^-}\right)}{\ln\left(\frac{2}{0.5}\right)}$$

where τ_i^+ represents the first-stage ignition delay time when the pre-exponential factor of the ith reaction is multiplied by a factor of 2, and τ_i^- the first-stage ignition delay when the pre-exponential factor of the ith reaction is divided by a factor of 2.

Rate of production analysis (ROP):

The rate of production analysis allows to determine the formation and consumption channels of a species i at a precise position in the cool flame, which corresponds to a fixed flame temperature. The formation rate, $R_{f,i}$, and the consumption rate, $R_{c,i}$, can be expressed as the sum of each reaction rate, ν_k, in which the species is involved:

$$R_{f,i} = \sum_i \nu_{f,k,i} \qquad R_{c,i} = \sum_i \nu_{c,k,i}$$

Then, the contribution of the kth reaction on the rate of production ($ROP_{i,k}$) and rate of consumption ($ROC_{i,k}$) can be deduced:

$$ROP_{i,k} = \frac{\nu_{f,k,i}}{R_{f,i}} \qquad ROC_{i,k} = \frac{\nu_{c,k,i}}{R_{c,i}}$$

Appendix III.A5. Influence of the mixture-averaged transport, multicomponent transport data and thermal diffusion (Soret effect) on the simulated temperature, formaldehyde and dimethyl ether mole fraction profiles. The flame condition is a DME/O_2/O_3 cool flame at ϕ = 0.3, α = 50 s^{-1}, x_{O3} = 2.0%.

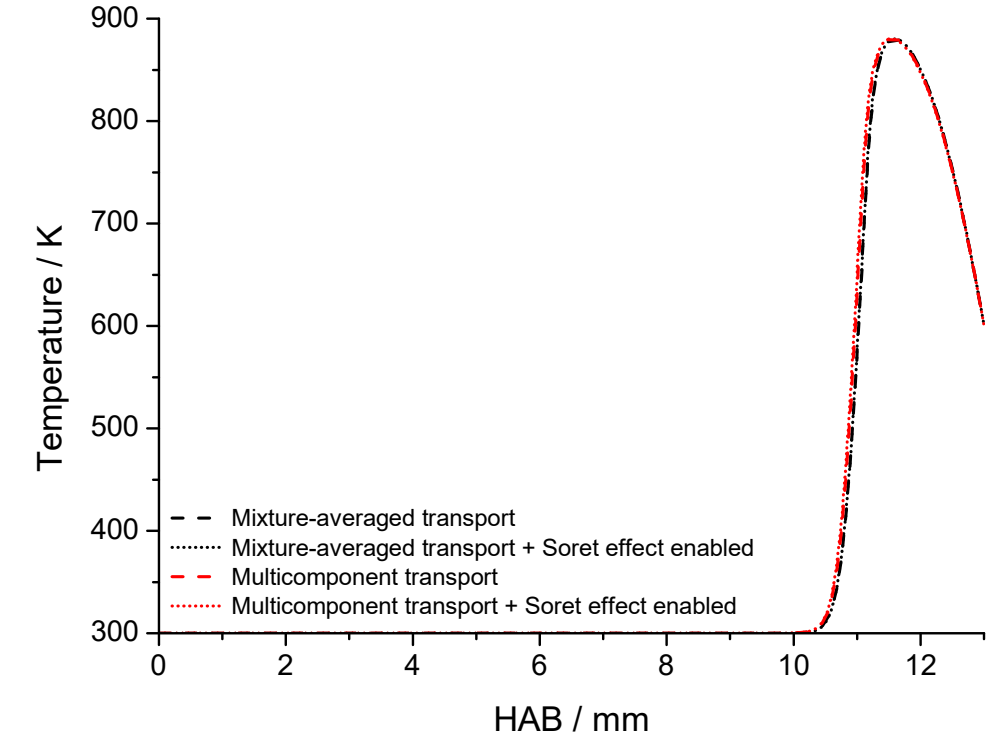

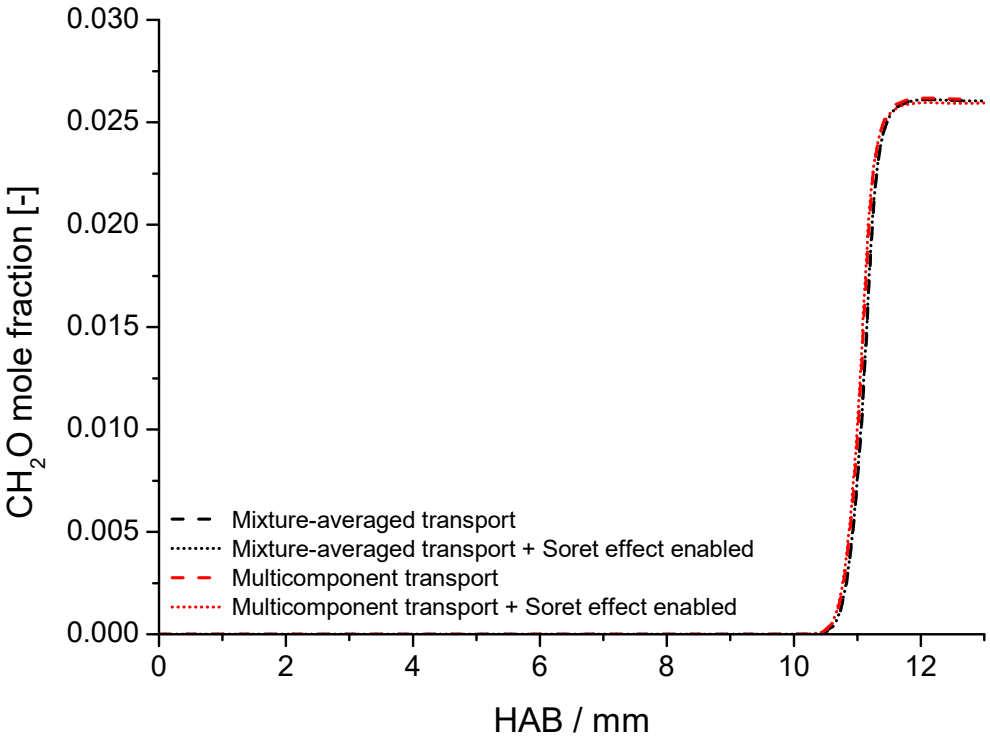

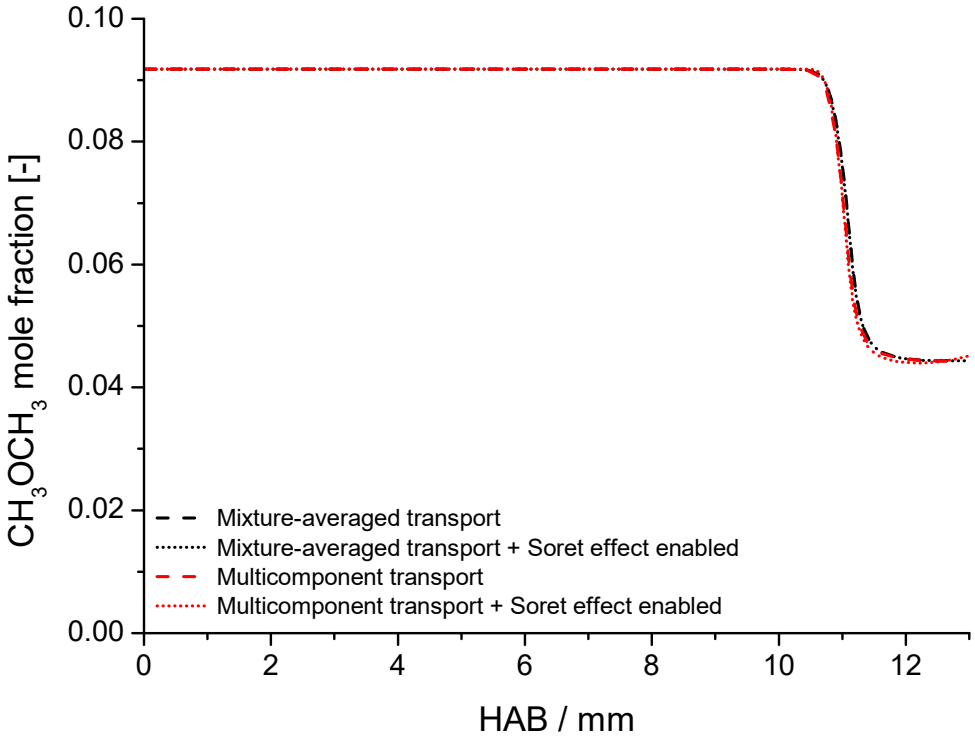
0.10
0.08
0.06
0.04
0.02
0.00
CH_3OCH_3 mole fraction [-]
0
2
4
6
8
10
12
HAB / mm
Mixture-averaged transport
Mixture-averaged transport + Soret effect enabled
Multicomponent transport
Multicomponent transport + Soret effect enabled

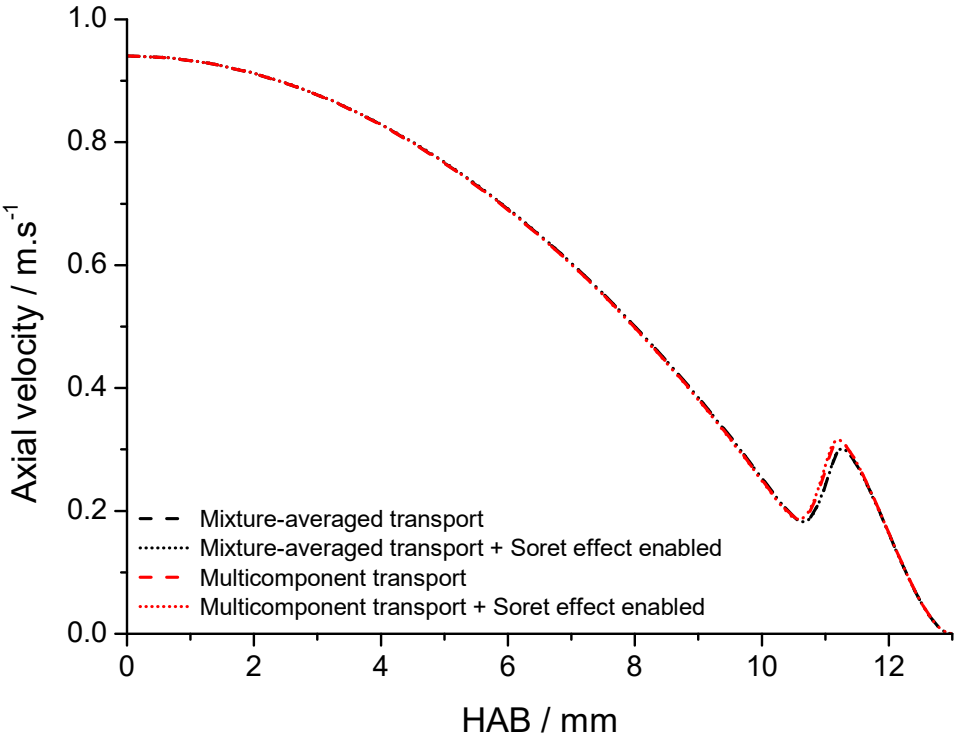
1.0
0.8
0.6
0.4
0.2
0.0
Axial velocity / $m.s^{-1}$
0
2
4
6
8
10
12
HAB / mm
Mixture-averaged transport
Mixture-averaged transport + Soret effect enabled
Multicomponent transport
Multicomponent transport + Soret effect enabled

In the Table below are reported the maximal temperature of the cool flame, along with the post-flame CH_2O and CH_3OCH_3 mole fraction, in each simulated condition. It demonstrates that using mixture-averaged or multicomponent transport data, as well as enabling or not the Soret effect, does not significantly influence the final results on the targeted values except for $S_{u,ref}$ when using mixture-averaged transport data.

Condition	Maximal temperature / K	Post-flame CH_2O mole fraction [-]	Post-flame CH_3OCH_3 mole fraction [-]	$S_{u,ref}$ / $m.s^{-1}$
Mixture-averaged transport	880	0.026	0.044	0.183
Mixture-averaged transport + Soret effect	880	0.026	0.044	0.182
Multicomponent transport	881	0.026	0.044	0.186
Multicomponent transport + Soret effect	880	0.026	0.045	0.186

Appendix III.A6. Influence of the plate temperature on the flame front position at different conditions, $\alpha = 20\ s^{-1}$ (left) and $\alpha = 40$ & $50\ s^{-1}$ (right).

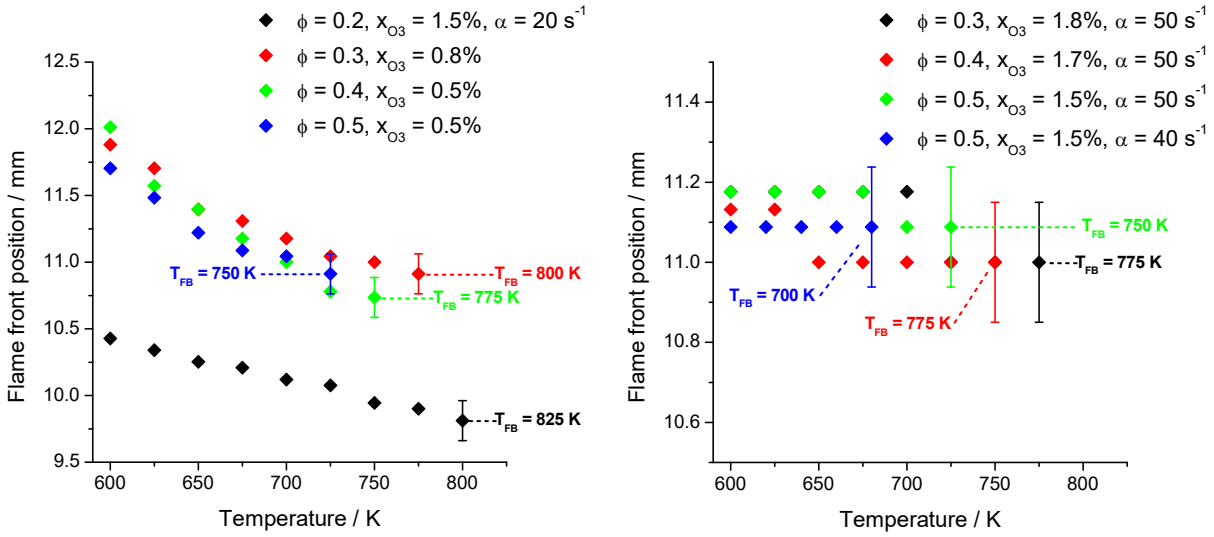

From an initial value of 600 K, the plate temperature was progressively increased by steps of 25 K until the cool flame underwent a flashback, i.e., turned itself into a hot flame. The flashback temperature, T_{FB}, is given for each condition.

Appendix III.A7. Calculated and measured velocities at the burner exit in reactive conditions.

Condition	Inlet velocity / $m \cdot s^{-1}$	
	'Calculated velocity'	'Measured velocity'
$\phi = 0.5$, $x_{O3} = 1.5\%$	0.442	0.663
	0.468	0.694
	0.494	0.723
	0.52	0.753
	0.546	0.783
$\phi = 0.4$, $x_{O3} = 1.7\%$	0.442	0.684
	0.468	0.693
	0.494	0.731
	0.52	0.753
	0.546	0.787
	0.572	0.831
$\phi = 0.3$, $x_{O3} = 2.0\%$	0.442	0.665
	0.468	0.690
	0.494	0.728
	0.52	0.760
	0.546	0.785
	0.572	0.823
	0.598	0.861
	0.624	0.916
	0.65	0.949
$\phi = 0.4$, $x_{O3} = 1.9\%$	0.52	0.757
	0.572	0.821
	0.624	0.920
	0.676	0.990
	0.78	1.100
	0.52	0.763
$\phi = 0.45$, $x_{O3} = 1.7\%$	0.572	0.835
	0.624	0.914
	0.78	1.108
	0.442	0.663

Appendix III.A8. DME, O_2 and N_2 flow rates corresponding to the experimental conditions shown in Figure III.8. 100% co-flow rate corresponds to the case in which its velocity is equal to the inlet velocity of the DME/O_2/O_3 mixture.

Condition	$\dot{Q}_{O2}$ / L·min^{-1}	$\dot{Q}_{DME}$ / mL·min^{-1}	%N_2 investigated	$\dot{Q}_{N2}$ / L·min^{-1}
α = 20 s^{-1}, ϕ = 0.25, x_{O3} = 1.7%	1.14	95.05	10 → 100%	0.34 → 3.42
α = 20 s^{-1}, ϕ = 0.30, x_{O3} = 1.7%	1.12	112.33	10 → 100%	0.34 → 3.42
α = 20 s^{-1}, ϕ = 0.35, x_{O3} = 1.7%	1.11	129.10	10 → 100%	0.34 → 3.42
α = 20 s^{-1}, ϕ = 0.40, x_{O3} = 1.2%	1.09	145.00	10 → 100%	0.34 → 3.42
α = 20 s^{-1}, ϕ = 0.45, x_{O3} = 1.2%	1.07	160.77	10 → 100%	0.34 → 3.42
α = 20 s^{-1}, ϕ = 0.50, x_{O3} = 1.2%	1.06	176.08	10 → 100%	0.34 → 3.42
α = 10 s^{-1}, ϕ = 0.07, x_{O3} = 3.0%	0.61	14.18	10 → 100%	0.17 → 1.71
α = 15 s^{-1}, ϕ = 0.10, x_{O3} = 3.0%	0.90	30.09	10 → 100%	0.26 → 2.56
α = 20 s^{-1}, ϕ = 0.14, x_{O3} = 3.0%	1.19	55.45	10 → 100%	0.34 → 3.42
α = 25 s^{-1}, ϕ = 0.19, x_{O3} = 3.0%	1.46	92.59	10 → 100%	0.43 → 4.27
α = 40 s^{-1}, ϕ = 0.50, x_{O3} = 1.6%	2.12	352.86	5 → 40%	0.34 → 2.73
α = 50 s^{-1}, ϕ = 0.50, x_{O3} = 1.8%	2.65	441.52	5 → 40%	0.43 → 3.42

Appendix III.A9. CH_2O-PLIF profiles corresponding to the experimental conditions shown in Figure III.8, and used for the flame front position determination.

■ Influence of the co-flow for different conditions, a) $\alpha = 10\ s^{-1}$, $\phi = 0.07$, $x_{O3} = 3\%$; b) $\alpha = 15\ s^{-1}$, $\phi = 0.1$, $x_{O3} = 3\%$; c) $\alpha = 20\ s^{-1}$, $\phi = 0.14$, $x_{O3} = 3\%$; d) $\alpha = 25\ s^{-1}$, $\phi = 0.19$, $x_{O3} = 3\%$.

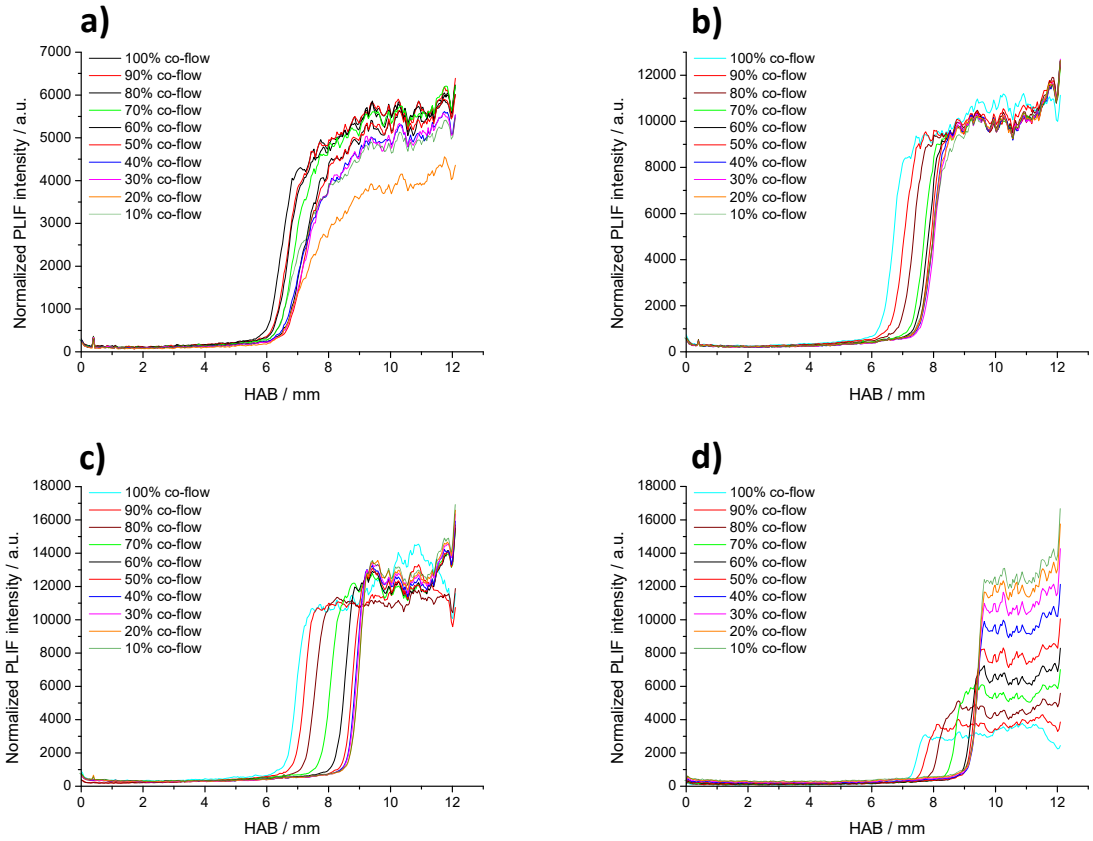

■ Influence of the co-flow for different conditions, a) $\alpha = 20\ s^{-1}$, $\phi = 0.25$, $x_{O3} = 1.7\%$; b) $\alpha = 20\ s^{-1}$, $\phi = 0.30$, $x_{O3} = 1.7\%$; c) $\alpha = 20\ s^{-1}$, $\phi = 0.35$, $x_{O3} = 1.7\%$; d) $\alpha = 20\ s^{-1}$, $\phi = 0.4$, $x_{O3} = 1.2\%$; e) $\alpha = 20\ s^{-1}$, $\phi = 0.45$, $x_{O3} = 1.2\%$; f) $\alpha = 20\ s^{-1}$, $\phi = 0.50$, $x_{O3} = 1.2\%$; g) $\alpha = 20\ s^{-1}$, $\phi = 0.55$, $x_{O3} = 1.2\%$.

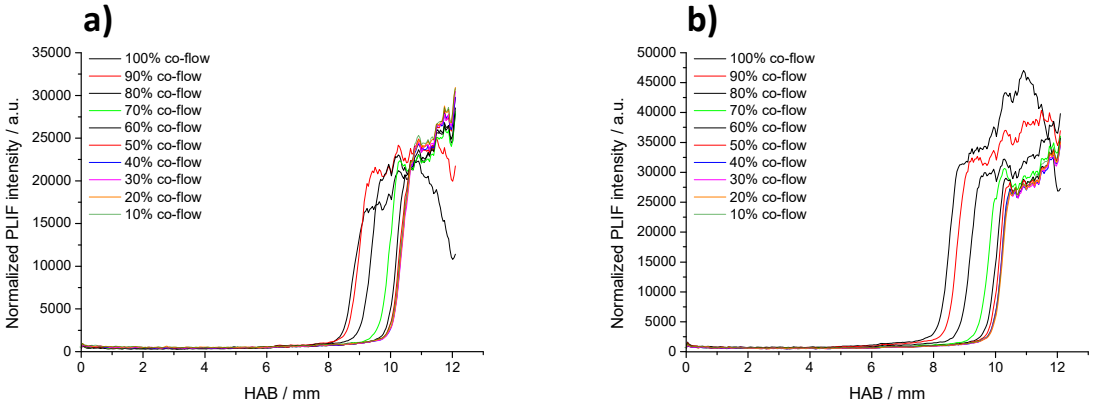

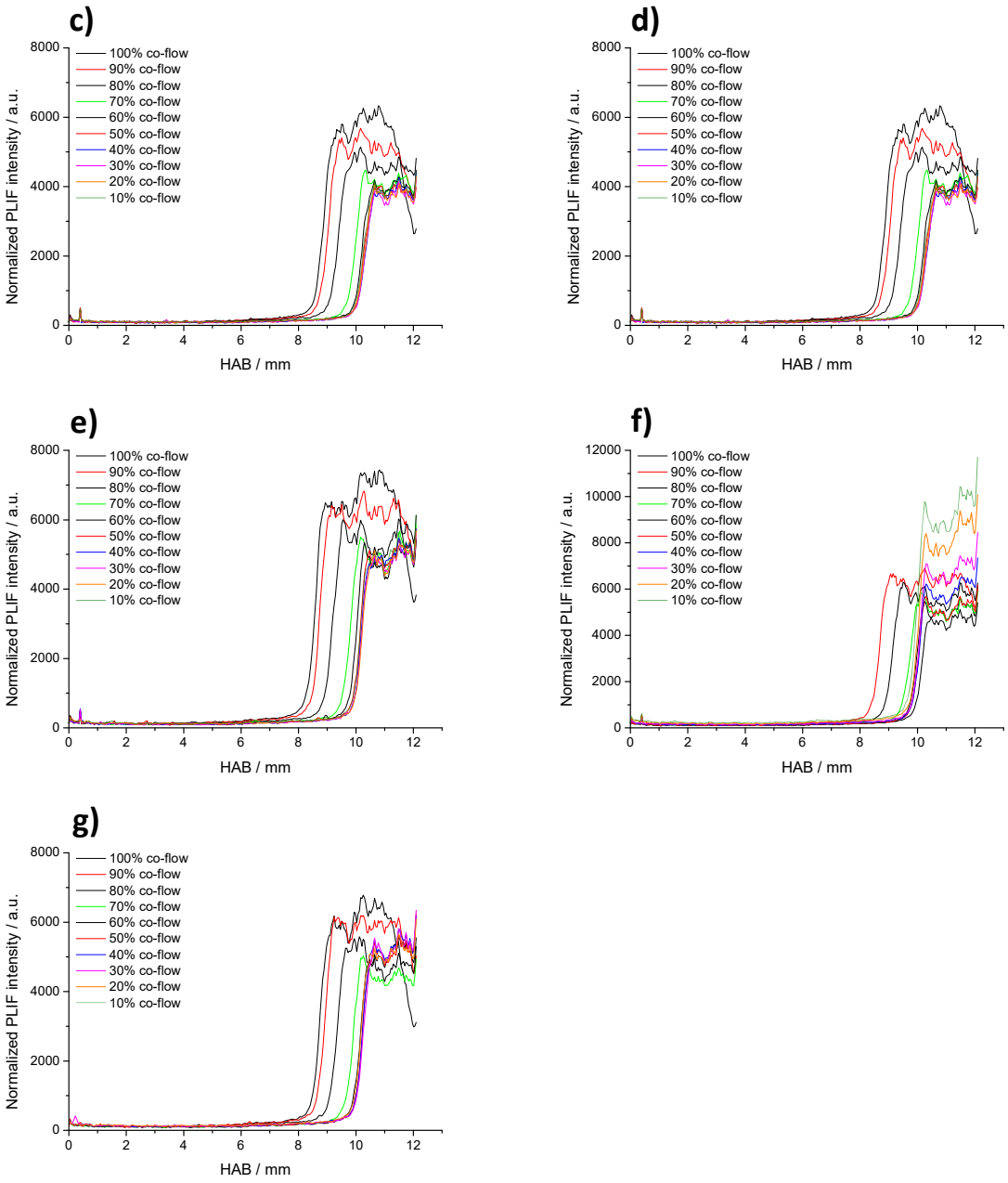
c)
d)
e)
f)
g)
100% co-flow
90% co-flow
80% co-flow
70% co-flow
60% co-flow
50% co-flow
40% co-flow
30% co-flow
20% co-flow
10% co-flow
Normalized PLIF intensity / a.u.
HAB / mm

Appendix IV.A1. Cool flame, hot flame or no flame occurrence of DME/O_2/O_3 reactive mixtures using different models from the literature, respectively AramcoMech 1.3 [1], AramcoMech 3.0 [2], Wang model [3] and HP-mech v3.3 [4] (mechanisms references in the main text, Section IV.1.1.1, the number attributed in each case corresponds to the Table below). The O_3-submechanism from Halter and co-workers was added for every model except HP-mech v3.3. Green case indicates that the simulation converged towards a cool flame, red for a hot flame and grey for no flame. Simulations that did not converge are indicated (-). The AramcoMech 1.3 + Halter and co-workers model converged towards a cool flame in every experimental condition, and can thus be used as a reference.

x_{O3} / %	α = 40 s^{-1}															
	ϕ = 0.2				ϕ = 0.3				ϕ = 0.4				ϕ = 0.5			
	[1]	[2]	[3]	[4]	[1]	[2]	[3]	[4]	[1]	[2]	[3]	[4]	[1]	[2]	[3]	[4]
1.2																
1.3																
1.4																
1.5																
1.6																
1.7																
1.8														-		
1.9											-					
2																
2.1																
2.2																
2.3																
2.4																
x_{O3} / %	α = 50 s^{-1}															
	ϕ = 0.2				ϕ = 0.3				ϕ = 0.4				ϕ = 0.5			
	[1]	[2]	[3]	[4]	[1]	[2]	[3]	[4]	[1]	[2]	[3]	[4]	[1]	[2]	[3]	[4]
1.4																
1.5																
1.6																
1.7																
1.8																
1.9																
2																
2.1																

[1] AramcoMech 1.3 [2] AramcoMech 3.0 [3] HP-Mech v3.3 [4] Wang

In the case of the AramcoMech 1.3 model (+ Halter and co-workers model), the simulations converged towards a cool flame in every condition. The other models failed in simulating a cool flame in many of the tested conditions, the simulation resulting either in a hot flame or no flame.

Appendix IV.A2. Deviation from the carbon balance in both DME/O_2/O_3 studied cool flames.

	Deviation from the carbon balance / %	
HAB / mm	ϕ = 0.3, x_{O3} = 2.0%	ϕ = 0.5, x_{O3} = 1.7%
0	-	-
1	0.44	0.53
2	0.58	0.01
3	0.37	0.16
4	0.68	0.17
5	0.87	0.04
6	0.85	0.33
7	0.79	0.06
8	0.57	0.27
8.3	0.68	0.69
8.6	0.12	0.66
8.9	0.01	1.65
9.2	4.49	1.59
9.5	3.11	0.29
9.8	2.14	0.36
10.1	0.44	1.66
10.4	0.37	1.43
10.7	1.69	2.50
11	4.66	4.69
11.3	6.07	5.29
11.6	4.16	6.48
11.9	1.94	3.31
12.2	0.08	4.09
12.5	1.13	2.79
12.7	0.89	2.68

The carbon balances indicate a maximal deviation of + 6% in the flame front area, and + 3% in the burnt gas area.

Appendix IV.A3. Comparison of sensitivity analyses performed using the first-stage ignition delay time at 450 and 650 K (a) or the inlet flow rate (b) and the temperature (c) of a freely-propagating flame.

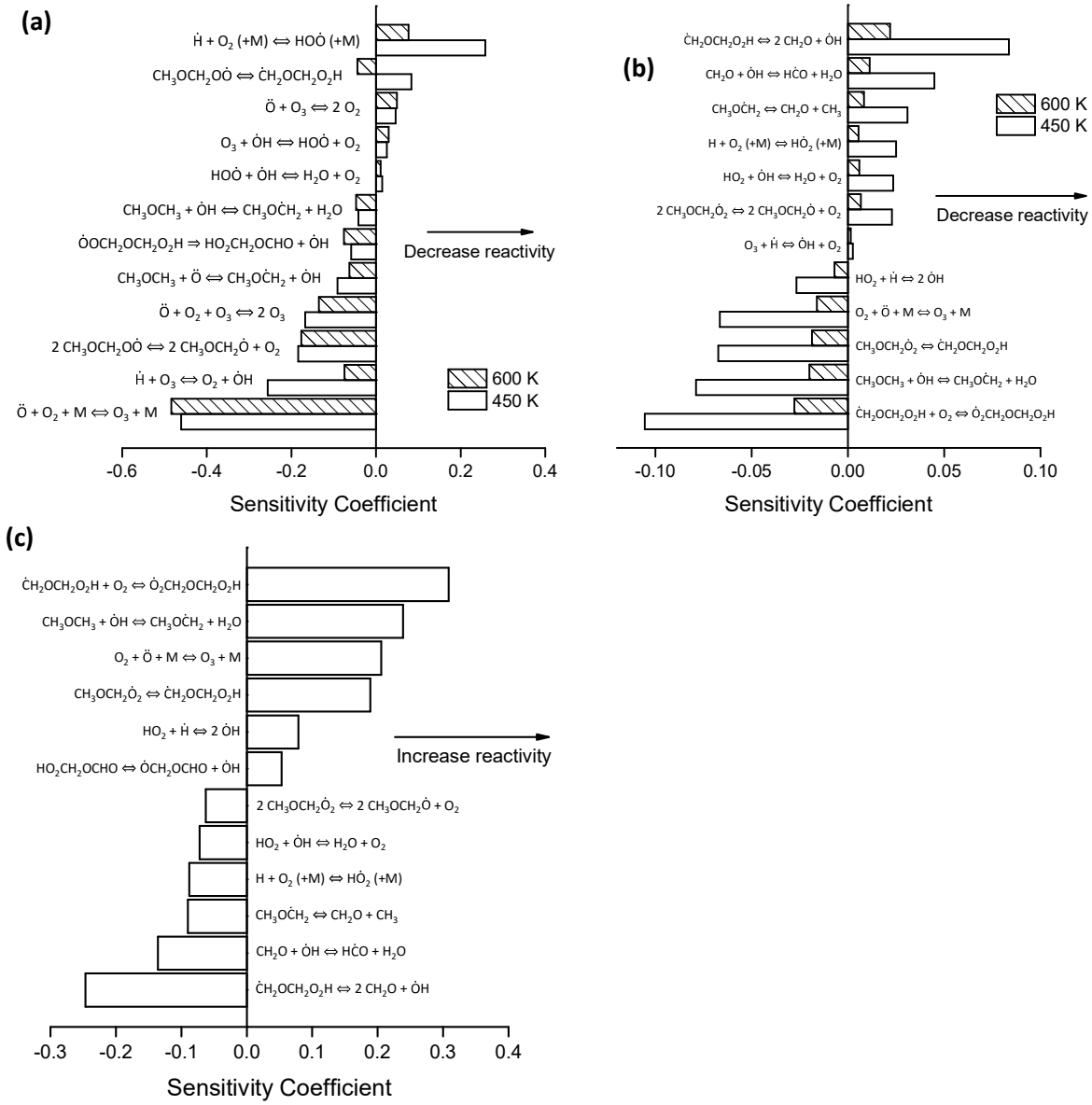

Appendix IV.A4. Comparison of the current model and AramcoMech 1.3 against experimental data from the literature.

- Comparison of the AramcoMech 1.3 model with the current model used in this study, against delays of stoichiometric DME/Air mixtures from the literature (Pfahl *et al*., 1996 [261]). IDT = Ignition Delay Time, FSIDT = First Stage Ignition Delay Time.

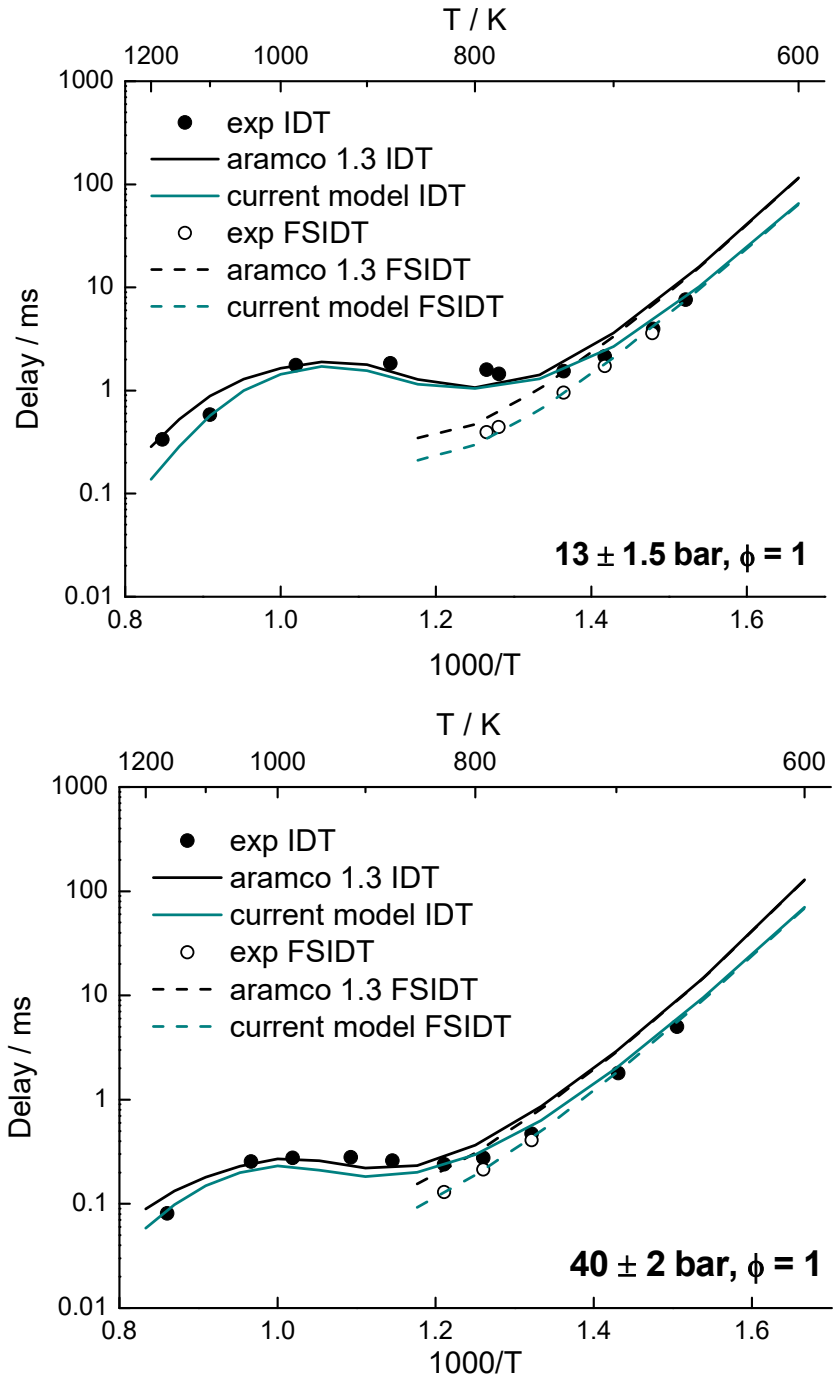

- Comparison of the Aramco 1.3 model with the current model used in this study, against delays of stoichiometric DME/Air mixtures from the literature (Burke *et al*., 2015 [262]). IDT = Ignition Delay Time.

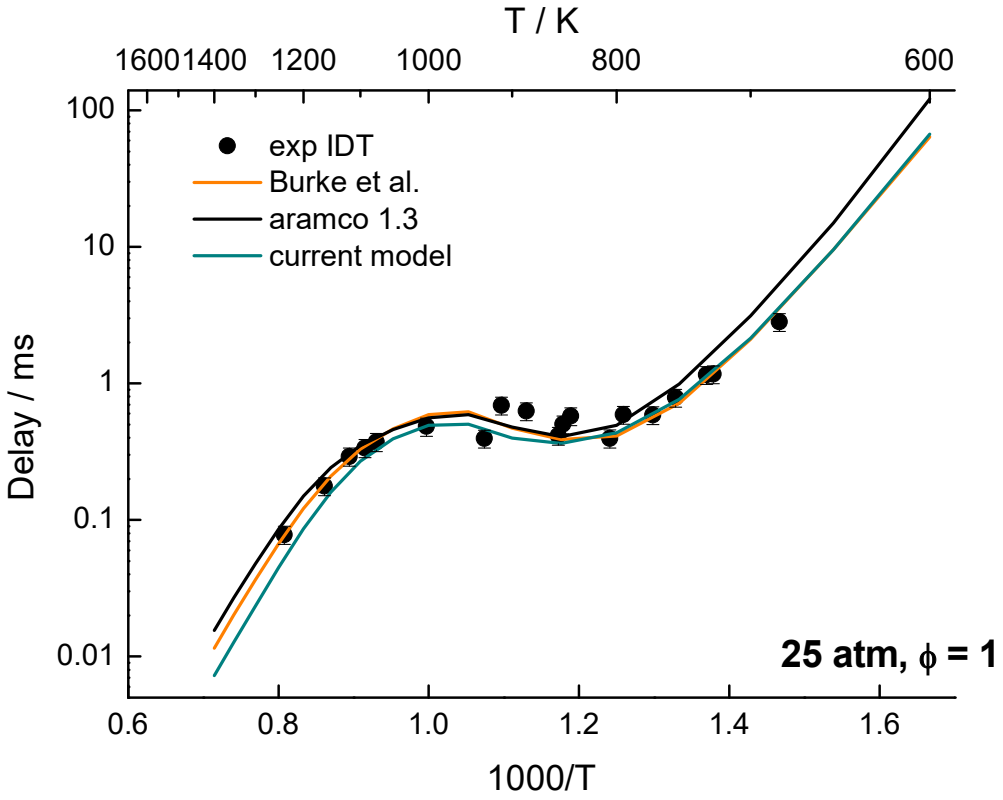

Comparison of the Aramco 1.3 model with the current model used in this study, against hot flame laminar burning velocity of DME/Air mixtures from the literature [134,263,264].

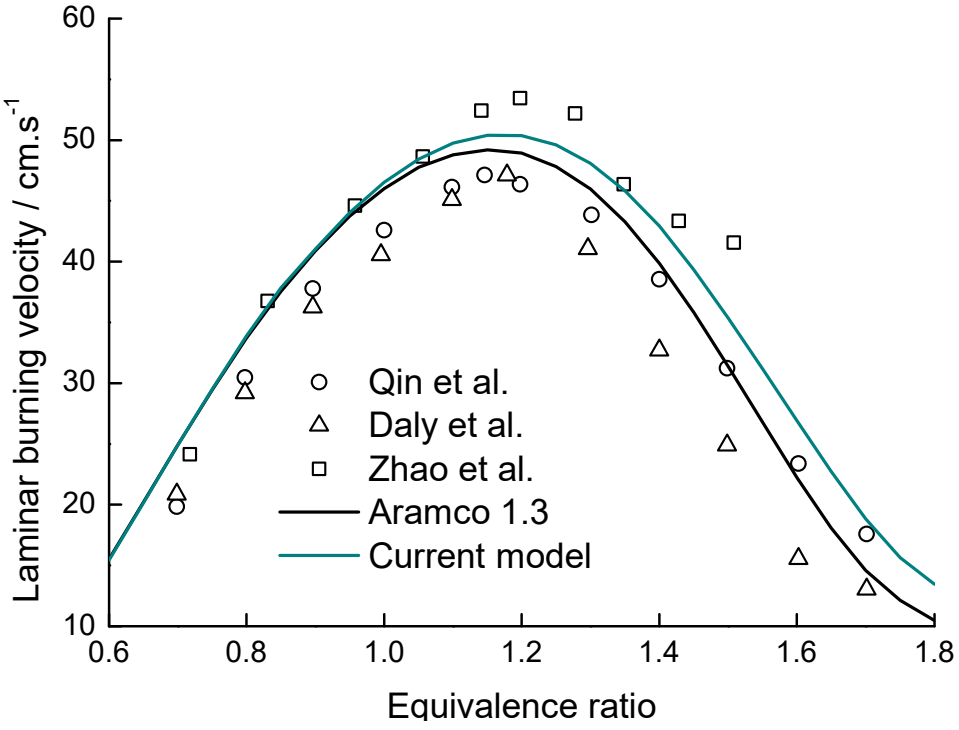

Appendix IV.A5. Temperature profiles of the ϕ = 0.5, α = 50 s^{-1}, x_{O3} = 1.4% cool flame measured in both directions, ensuring the absence of catalytic effect at the surface of the thermocouple.

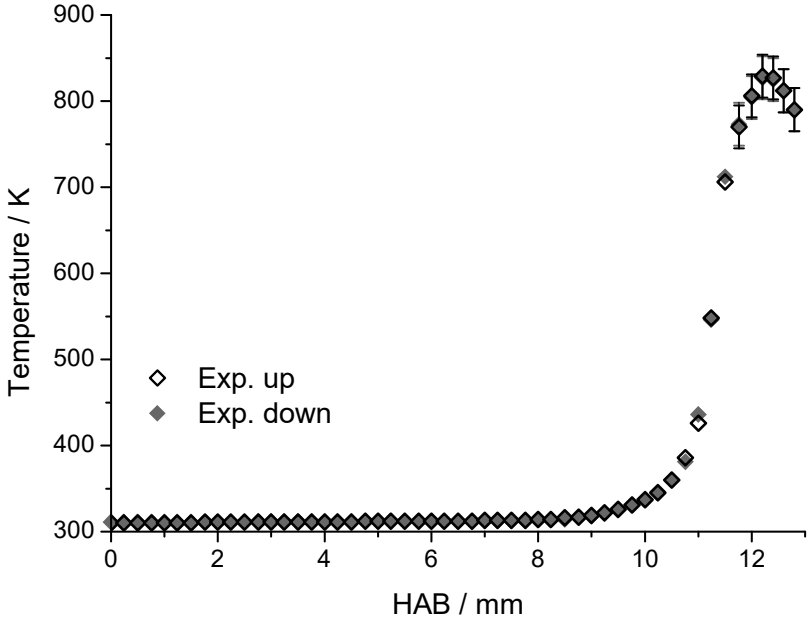

Appendix IV.A6. Deviation from the carbon balance in the DEE/O_2 and DEE/O_2/O_3 cool flames.

Deviation from the carbon balance / %			
ϕ = 0.5, x_{O3} = 1.4%		ϕ = 1.0, x_{O3} = 0%	
HAB / mm	-	HAB / mm	-
0	-	0	-
2	2.07	3	0.09
4	2.42	6	0.45
6	2.08	9	1.01
7	2.98	11	1.03
8	0.96	11.4	1.16
8.3	5.26	11.6	0.70
8.6	2.91	11.8	0.06
8.9	4.43	12	3.23
9.2	2.47	12.2	4.22
9.5	1.73	12.4	4.29
9.8	2.82	12.6	3.29
10.1	0.11	12.7	2.84
10.4	0.33		
10.7	0.61		
11	2.03		
11.3	0.15		
11.6	2.52		
11.9	3.31		
12.2	10.79		
12.5	12.76		

Appendix IV.A7. Species mole fraction profiles in the OME-2/DME/O_2/O_3 cool flames.

- ϕ = 0.3, x_{O3} = 2.0%, 5% OME-2/95% DME

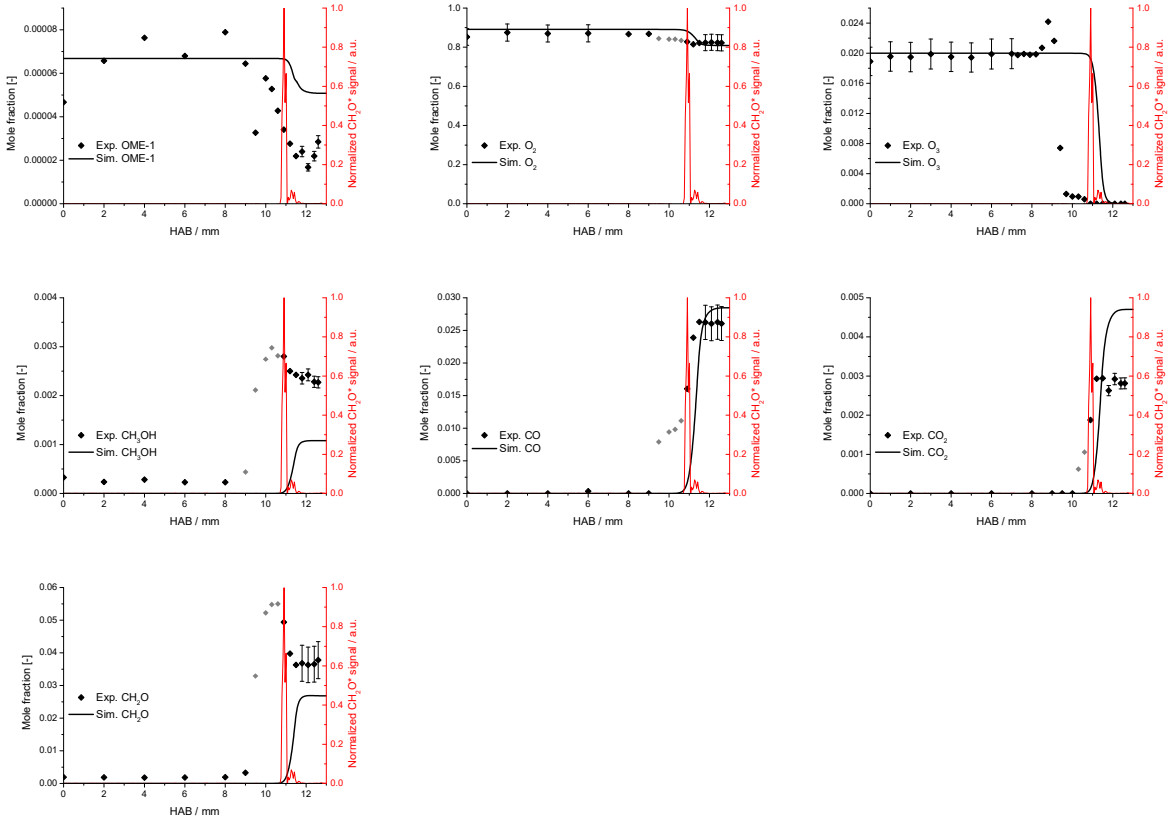

- ϕ = 0.5, x_{O3} = 1.6%, 2.5% OME-2/97.5% DME

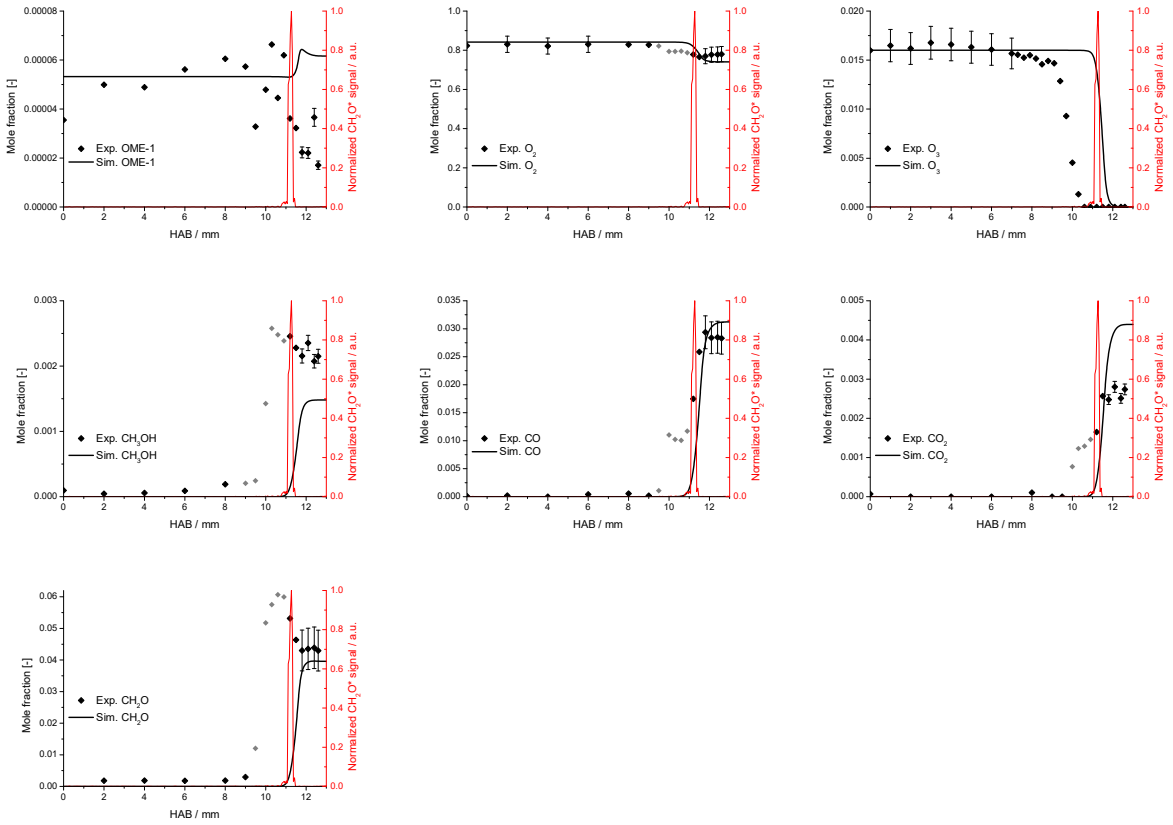

Associated deviation from the carbon balance:

	Deviation from the carbon balance / %	
HAB / mm	ϕ = 0.3, x_{O3} = 2.0%, 5% OME-2	ϕ = 0.5, x_{O3} = 1.6%, 2.5%OME-2
0	-	-
2	1.352380357	0.97300333
4	2.656428545	0.294699131
6	2.093796819	0.531528271
8	0.795878937	0.019401765
9	0.771115152	0.276556525
9.5	0.854555741	0.838998515
10	11.03723768	2.297912193
10.3	12.80689153	5.344006914
10.6	13.18774804	6.69977134
10.9	9.921062369	7.076426918
11.2	0.168019631	4.430108032
11.5	2.763186294	0.311321135
11.8	4.120841695	2.714394619
12.1	4.41895281	4.482164322
12.4	4.296084986	3.977620311
12.6	3.702137926	4.453499903

Appendix V.A1. Fitting procedure for the determination of the axial strain rate, K. The experimental condition is $\phi = 0.5$, $x_{O3} = 1.7\%$.

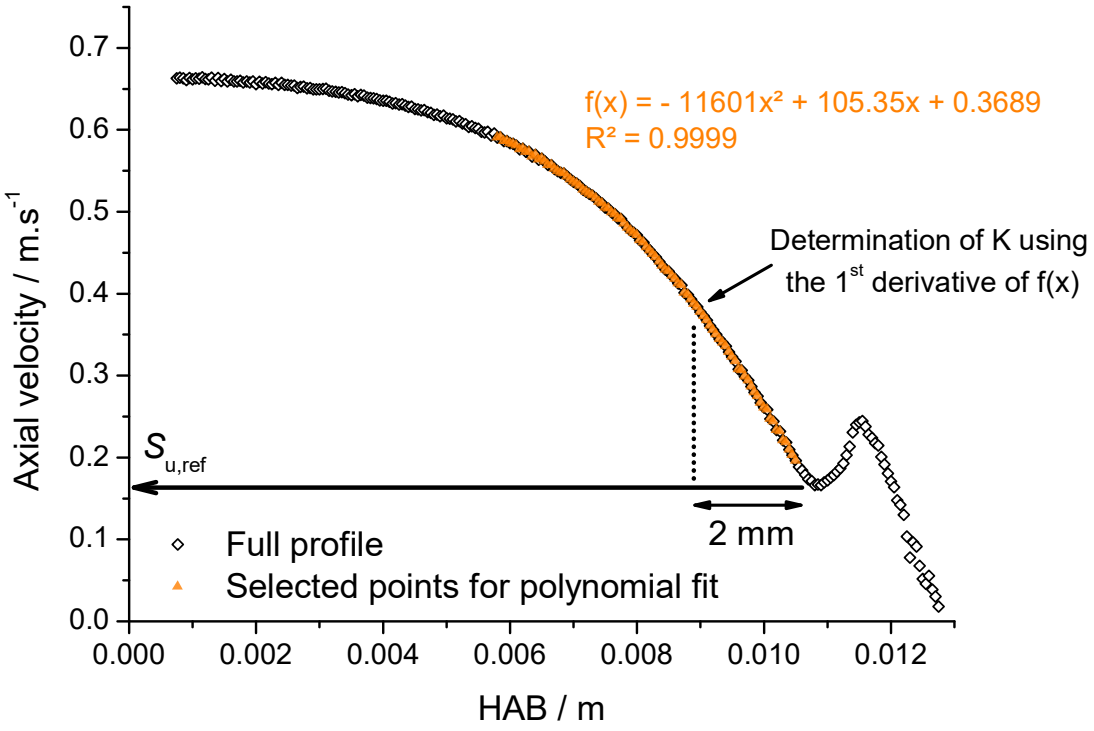

Appendix V.A2. Reactions and associated rate constant parameters for the three O_3-submechanisms used in the current study

Units: cm^3, mole, s, cal

Reaction	A	n	E_a
Halter model			
$O_3 + N_2 \rightarrow O_2 + O + N_2$	4.00E+14	0	22667
$O_2 + O + N_2 \rightarrow O_3 + N_2$	1.60E+14	-0.4	-1391
$O_3 + O_2 \rightarrow O_2 + O_2 + O$	1.54E+14	0	23064
$O_2 + O_2 + O \rightarrow O_3 + O_2$	3.26E+19	-2.1	0
$O_3 + O_3 \rightarrow O_2 + O_3 + O$	4.40E+14	0	23064
$O_2 + O_3 + O \rightarrow O_3 + O_3$	1.67E+15	-0.5	-1391
$O_3 + H \Leftrightarrow O_2 + OH$	8.43E+13	0	934
$O_3 + O \Leftrightarrow O_2 + O_2$	4.82E+12	0	4094
$O_3 + OH \Leftrightarrow O_2 + HO_2$	1.85E+11	0	831
$O_3 + HO_2 \Leftrightarrow O_2 + OH + O_2$	6.02E+09	0	938
$O_3 + H_2O \Leftrightarrow O_2 + H_2O_2$	6.62E+01	0	0
$O_3 + CH_3 \Leftrightarrow O_2 + CH_3O$	3.07E+12	0	417
$O_3 + H \Leftrightarrow O + HO_2$	4.52E+11	0	0
$O_3 + H_2 \Leftrightarrow OH + HO_2$	6.00E+10	0	19840
$O_3 + CH_4 \Leftrightarrow CH_3O + HO_2$	8.13E+10	0	15280
Jian model			
$O_2 + O + M \Leftrightarrow O_3 + M$	1.00E+19	-2	0
$N_2 = 1.3$; $O_2 = 1.2$; Kr = 1 ; Ar = 1 ; $O_3 = 0$			
$O_2 + O + O_3 \Leftrightarrow O_3 + O_3$	1.00E+23	-3	0
$O_3 + O \Leftrightarrow O_2 + O_2$	1.10E+13	0	4300
$O_3 + H \Leftrightarrow OH + O_2$	8.43E+13	0	934
$O_3 + HO_2 \Leftrightarrow O_2 + O_2 + OH$	5.80E-04	4.57	-1377
$O_3 + OH \Leftrightarrow HO_2 + O_2$	1.20E+05	2.5	800
Zhao model			
O_3 (+M) $\Leftrightarrow O_2 + O$ (+M)			
Low-Pressure	2.23E+28	-4.37	27297
High-Pressure	1.37E+15	-0.67	25990
Troe Parameters (0.6417 3.91E-04 8680.74 6060.75)			
Ar = 1 ; He = 1.2 ; $N_2 = 1.5$; $H_2 = 3$; $O_2 = 1.5$; $O_3 = 3.75$; O = 6			
$O_3 + O \Leftrightarrow O_2 + O_2$	4.82E+12	0	4094
$O_3 + O \Leftrightarrow O_2$ (sing) + O_2	1.44E+11	0	4094
$O_3 + O \Leftrightarrow O_2 + OH$	8.43E+13	0	934
$O_3 + H \Leftrightarrow O + HO_2$	4.52E+11	0	0
$O_3 + OH \Leftrightarrow O_2 + HO_2$	1.85E+11	0	831
$O_3 + H_2O \Leftrightarrow O_2 + H_2O_2$	6.62E+01	0	0
$O_3 + HO_2 \Leftrightarrow OH + O_2 + O_2$	6.62E+09	0	994
$O_3 + CO \Leftrightarrow O_2 + CO_2$	6.02E+02	0	0
$O_3 + HCO \Leftrightarrow O_2 + H + CO_2$	5.00E+11	0	0
$O_3 + CH_3 \Leftrightarrow CH_3O + O_2$	5.83E+11	0	0

Appendix V.A3. Evolution of the standard deviation on the simulated reference axial velocity as a function of the number of grid points used for the simulation. The reference value was simulated with a grid containing 1637 points.

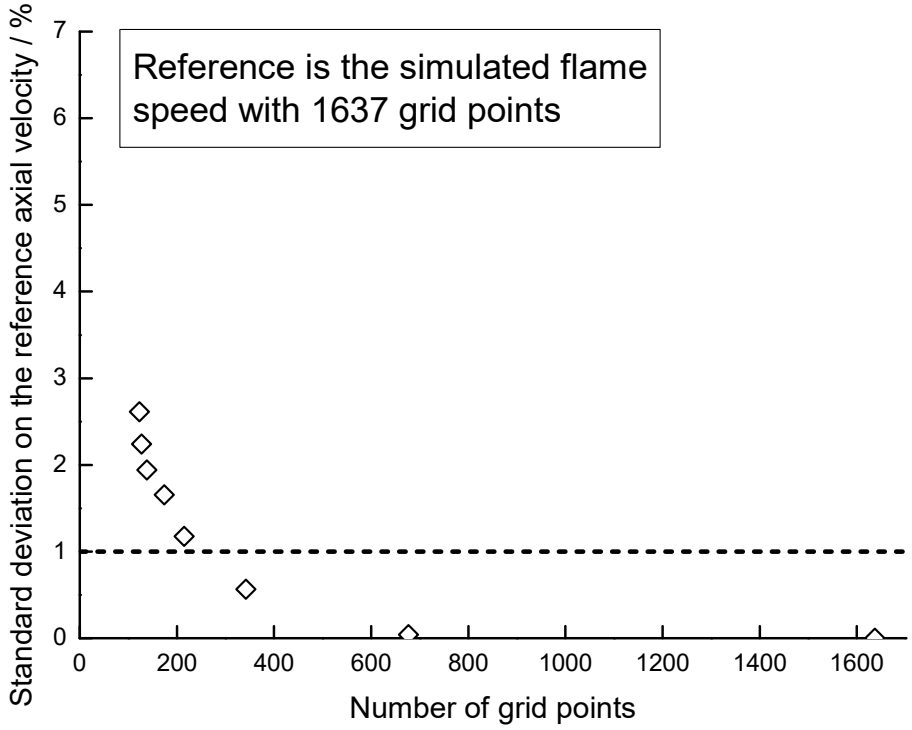

Appendix V.A4. Influence of the size of the simulated domain on i) the simulated formaldehyde mole fraction profile and ii) the simulated temperature profile. Condition: $\phi = 0.5$, $x_{O3} = 1.5\%$.

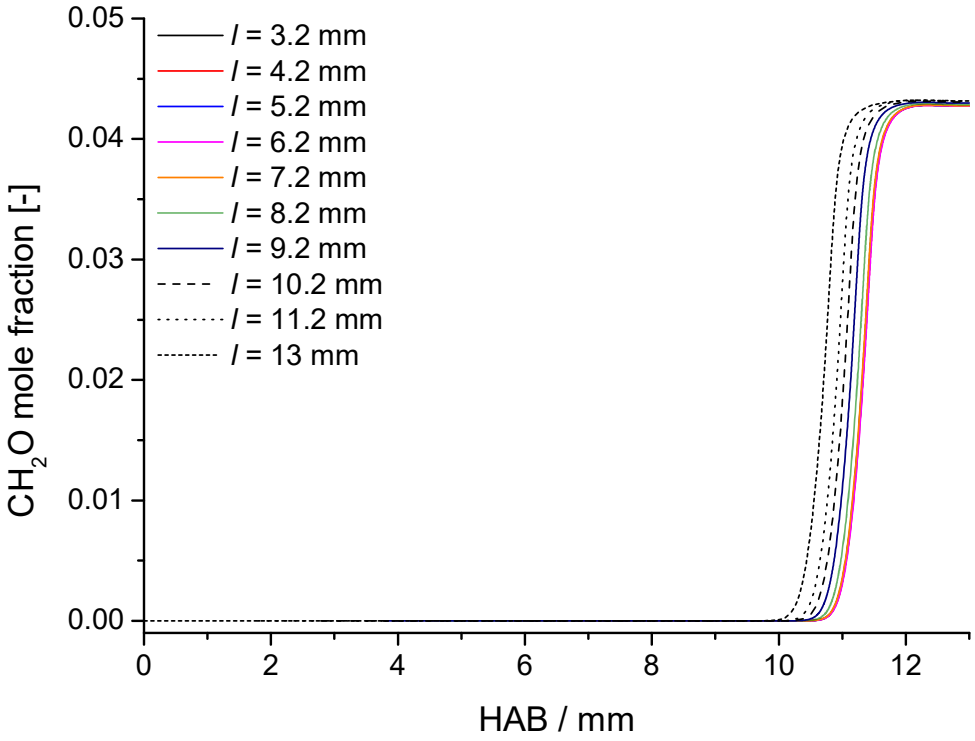

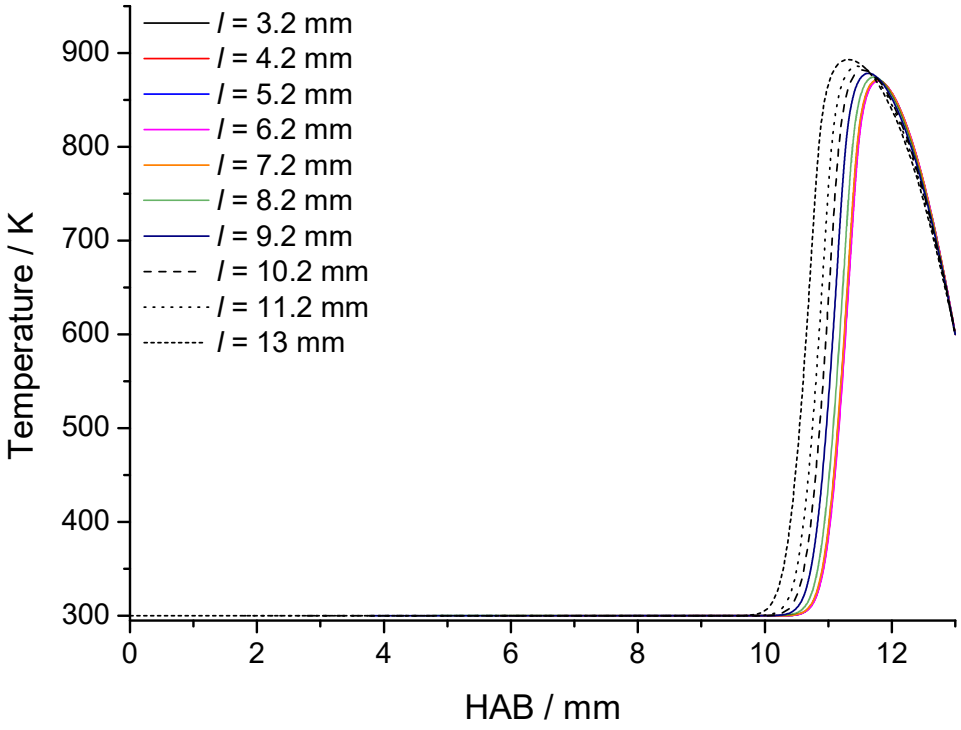
l = 3.2 mm
l = 4.2 mm
l = 5.2 mm
l = 6.2 mm
l = 7.2 mm
l = 8.2 mm
l = 9.2 mm
l = 10.2 mm
l = 11.2 mm
l = 13 mm
Temperature / K
HAB / mm
300
400
500
600
700
800
900
0
2
4
6
8
10
12

Appendix V.A5. Cool flames conditions for LBV determination

Conditions	**Size of the domain for the axial velocity profiles simulation** (Pre-Mixed Burner Stagnation Flame module) **/ cm**	**Inlet velocity / cm·s^{-1}**	**Imposed radial strain rate / s^{-1}**	**Measured* LBV / cm·s^{-1}**
ϕ = 0.5 x_{O3} = 1.5% (x_{DME} = 0.144 x_{O2} = 0.841 x_{O3} = 0.015)	0.42	39.9	50.5	16.6
	0.41	40.3	55.6	16.8
	0.4	40.8	59.4	17.0
	0.39	42.5	61.6	17.0
	0.37	41.0	63.7	17.3
ϕ = 0.4 x_{O3} = 1.7% (x_{DME} = 0.119 x_{O2} = 0.864 x_{O3} = 0.017)	0.40	41.3	50.6	17.8
	0.42	41.3	53.9	17.9
	0.41	43.0	56.8	17.7
	0.41	43.2	61.2	18.5
	0.375	42.6	65.3	18.1
	0.365	45.9	71.5	18.2
ϕ = 0.3 x_{O3} = 2.0% (x_{DME} = 0.092 x_{O2} = 0.881 x_{O3} = 0.02)	0.44	41.3	51.5	18.6
	0.445	42.7	53.4	19.4
	0.42	43.1	57.1	18.6
	0.42	44.5	61.2	19.8
	0.42	46.4	61.7	19.9
	0.385	47.7	66.7	19.1
	0.375	49.0	72.8	19.8
	0.325	49.9	82.6	19.0
	0.345	54.7	85.0	19.7
ϕ = 0.4 x_{O3} = 1.9% (x_{DME} = 0.119 x_{O2} = 0.862 x_{O3} = 0.019)	0.42	44.6	59.5	19.1
	0.41	48.9	64.6	20.5
	0.365	54.1	78.5	20.4
	0.34	54.8	86.4	20.4
	0.335	54.0	94.3	20.2
	0.35	59.9	97.6	20.9
ϕ = 0.45 x_{O3} = 1.7% (x_{DME} = 0.132 x_{O2} = 0.851 x_{O3} = 0.017)	0.40	43.2	62.1	17.8
	0.365	46.8	72.8	18.4
	0.36	51.8	79.2	18.5
	0.305	51.1	91.4	18.3
	0.305	54.0	105.3	18.4

*Measured using the numerically assisted non-linear extrapolation method

Appendix V.A6. Comparison between experimental axial velocity profiles measured by PIV (□) and simulated ones with the different O_3 submechanisms, at different strain rates for the following conditions:

- $\phi = 0.45$, $x_{O3} = 1.7\%$

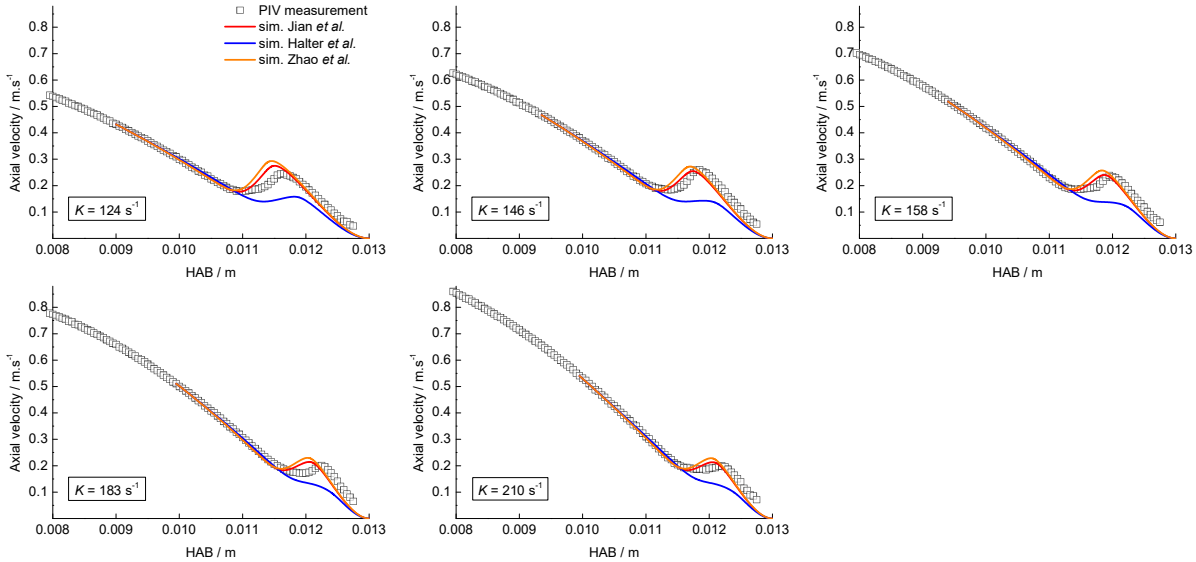

- $\phi = 0.4$, $x_{O3} = 1.7\%$

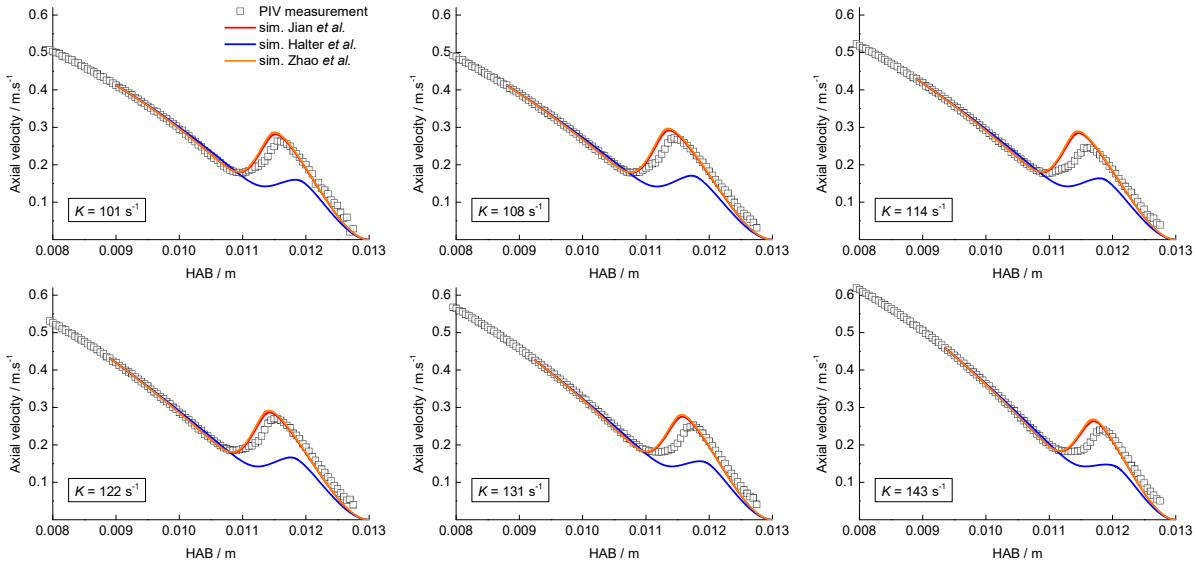

- $\phi = 0.4$, $x_{O3} = 1.9\%$

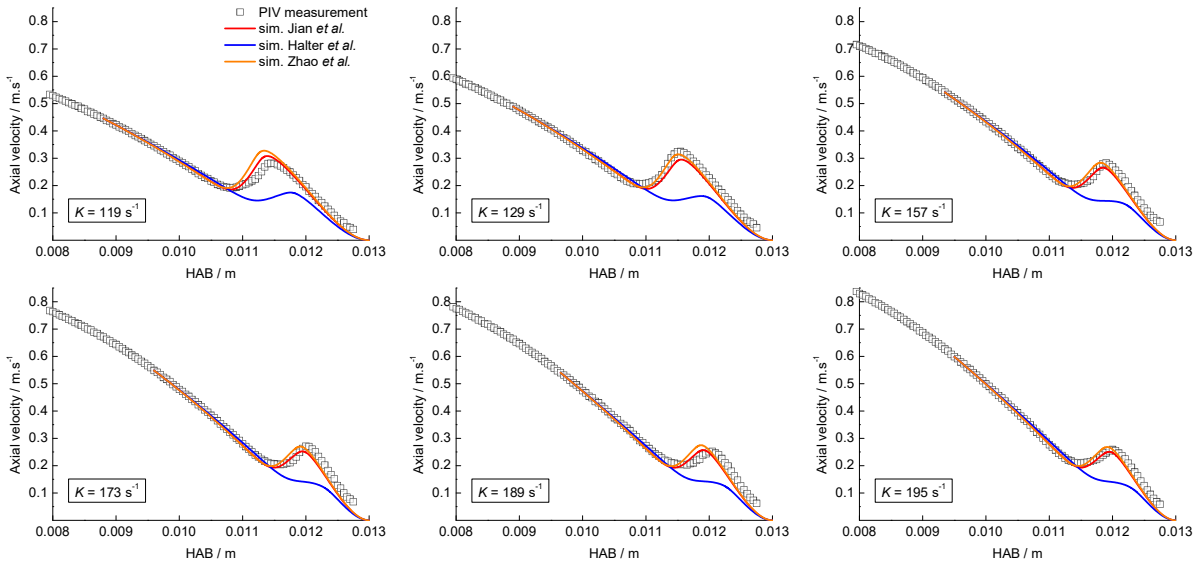

Appendix V.A7. Experimental and simulated temperature profiles of DME/O_2/O_3 cool flames, respectively with the submechanisms from Zhao and co-workers, Jian and co-workers, Halter and co-workers. The DME submechanism is the modified version of AramcoMech 1.3, introduced in Chapter IV.1.

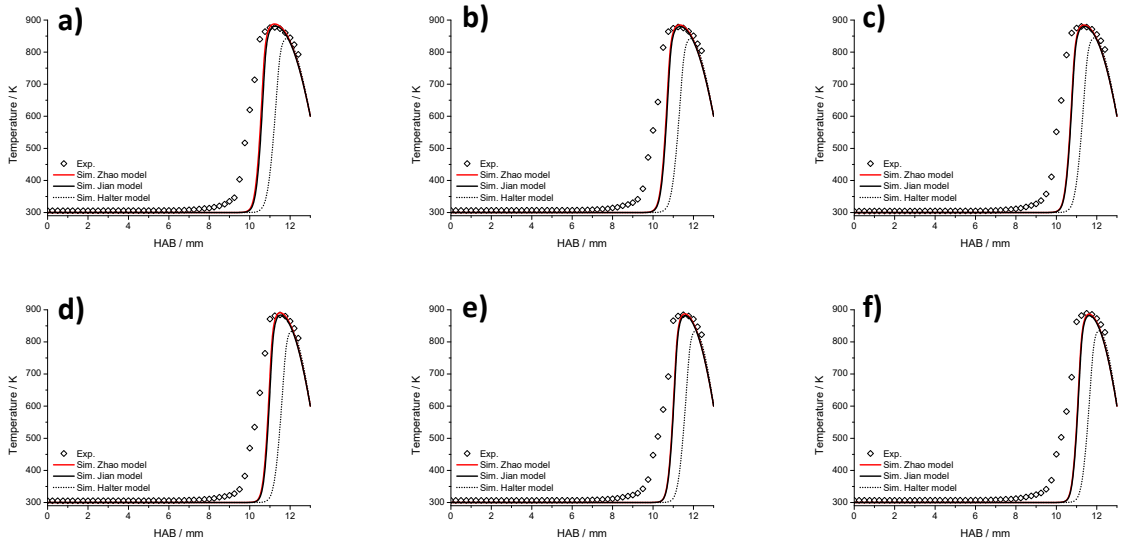

Experimental conditions: **a)** $\phi = 0.3$, a = 40 s^{-1}, $x_{O3} = 1.8\%$, **b)** $\phi = 0.4$, a = 40 s^{-1}, $x_{O3} = 1.6\%$, **c)** $\phi = 0.5$, a = 40 s^{-1}, $x_{O3} = 1.5\%$, **d)** $\phi = 0.3$, a = 50 s^{-1}, $x_{O3} = 2.0\%$, **e)** $\phi = 0.4$, a = 50 s^{-1}, $x_{O3} = 1.8\%$, **f)** $\phi = 0.5$, a = 50 s^{-1}, $x_{O3} = 1.7\%$.

Résumé

L'avenir des processus de combustion est tributaire d'une réduction significative des émissions polluantes, ainsi que de l'augmentation des rendements énergétiques. Le contrôle de l'initiation de la combustion est une étape critique dans cette direction, et ce dans de nombreuses configurations. Quelle qu'en soit l'application, l'initiation reproductible de la phase de combustion est recherchée. Cependant, l'initiation de l'inflammation des carburants est largement dépendante des mécanismes chimiques de basses températures, dits LTC (Low-Temperature Combustion), responsables de la formation de flammes froides. Ces mécanismes impliquent la formation et décomposition de composés hautement oxygénés instables, des peroxydes, dont la structure reflète celle du carburant initial. Celle-ci conditionne donc fortement sa réactivité. De plus, la généralisation de carburants biosourcés ou de synthèse nécessite une compréhension fine de leurs chemins réactionnels, ceux-ci pouvant être spécifiques aux fonctions chimiques absentes des carburants fossiles. Enfin, les récentes démonstrations de la facilitation de l'initiation d'une flamme froide par interaction avec un plasma froid ou par ensemencement d'ozone souligne le besoin d'études fondamentales de ces mécanismes chimiques de combustion de basses températures. Dans le cadre de cette thèse effectuée au laboratoire PC2A, un brûleur à plan de stagnation dédié à l'étude de la cinétique des flammes froides a été conçu et caractérisé.

La structure chimique détaillée de flammes froides est obtenue par la mise en commun de différentes techniques analytiques et optiques, respectivement la fluorescence induite par plan laser du formaldéhyde, la chimiluminescence du formaldéhyde excité, la mesure de température par thermocouple, l'analyse chimique par (micro-)chromatographie en phase gaz et spectrométrie de masse. Trois carburants ont été sélectionnés, respectivement le diméthyl éther (DME), le diéthyl éther (DEE) et l'oxyméthylène éther-2 (OME-2). Les flammes froides étudiées sont généralement stabilisées à basse richesse ($0.2 < E.R. < 0.5$) à l'aide d'ajout d'ozone (variant entre 1 et 2% mol. du prémélange), à l'exception du diéthyl éther, où une flamme froide a été stabilisée à la stœchiométrie sans ozone. L'établissement de structures détaillées de ces flammes froides a notamment permis, lorsque comparées aux prédictions de divers modèles cinétiques, de constater les manques de certains de ces modèles quant à la prédiction de la réactivité dans ces conditions spécifiques. De plus, l'influence de l'ozone comme générateur de radicaux in-situ a été étudié. Bien que son utilisation n'affecte que marginalement la composition chimique après la flamme froide, son influence est importante sur certains branchements de réactions primordiaux à basses températures, favorisant les réactions de propagation par rapport à celles de branchement.

Finalement, l'utilisation de la Vélocimétrie par Imagerie de Particules (PIV – Particle Image Velocimetry) dans le brûleur à plan de stagnation a permis, pour la première fois, la mesure de la vitesse de propagation de flammes froides à pression atmosphérique. Cette donnée, intrinsèque au carburant étudié, dépendant des composition, température et pression du mélange initial, est particulièrement importante pour la modélisation cinétique de systèmes réactifs. L'utilisation de flammes froides de DME ensemencées à l'ozone a permis sa mesure à basse richesse, les vitesses de propagation mesurées variant entre 14 et 18 $cm \cdot s^{-1}$. Cette étude a notamment permis de mettre en lumière les réactions les plus importantes pour la prédiction d'une telle grandeur.

Les nouvelles données expérimentales obtenues dans le cadre de ces travaux de thèse constituent les fondations de travaux plus larges sur l'influence de l'ozone sur la chimie de basses températures, dans des conditions expérimentales originales et complémentaires de celles généralement étudiées en laboratoire.

Abstract

The future of combustion processes lies on a significant reduction of pollutant emissions, as well as increased efficiencies. The control of the ignition phase is a critical step towards this goal, in many different configurations. Whatever the application, reproductible initiation of the combustion phase is sought. It is well known that the fuel ignition is largely dependent on low-temperature combustion (LTC) mechanisms, responsible for the occurrence of cool flames. These mechanisms involve the formation and decomposition of highly reactive intermediates, peroxides, whose structure reflect the initial fuel structure. Therefore, the fuel structure strongly influences its reactivity. Furthermore, the widespread use of bio-based or synthetic fuels requires a detailed understanding of their reaction pathway in this temperature domain, which may differ from those of fossil fuels. Finally, following the recent demonstration of easier cool flame ignition through the use of dielectric barrier plasma discharge or ozone-seeding stresses the need for fundamental studies on these low-temperature combustion kinetics. Within this work performed at the PC2A laboratory, a stagnation plate burner dedicated to the low-temperature combustion kinetics studies of fuels inside stabilized cool flames was developed and characterized.

The detailed chemical structures of cool flames were established by coupling different analytic and optical techniques, namely formaldehyde Planar Laser Induced Fluorescence (CH_2O-PLIF), excited formaldehyde chemiluminescence, temperature measurements by thermocouple, (micro-) gas chromatography and mass spectrometry. Three different fuels were selected in this work: dimethyl ether (DME), diethyl ether (DEE) and oxymethylene ether-2 (OME-2). Cool flames were generally stabilized under lean conditions (varying between 0.2 and 0.5) by means of ozone-seeding (varying between 1 and 2% mol. of the mixture), except for diethyl ether, for which a stoichiometric self-sustaining cool flame was investigated without ozone-addition. Comparing measured and simulated cool flames chemical structures, using various detailed kinetic mechanisms from the literature, allowed to assess the performance of these models in these specific conditions. Furthermore, the ozone influence as in-situ radical provider was investigated. While its use only slightly affects the products distribution downstream of the cool flame, this species highly impacts some reaction pathways in the cool flame, promoting chain-propagating over chain-branching reactions.

Finally, Particle Image Velocimetry (PIV) technique was used in the stagnation plate burner configuration, allowing the measurement of cool flames laminar burning velocities (LBVs) at atmospheric pressure for the first time. The LBV is an intrinsic data of the fuel, depending on the initial mixture composition, temperature and pression. This data is particularly valuable for kinetic studies, but was almost never investigated in the case of cool flames. Its measurement was successfully achieved inside lean, ozone-seeded dimethyl ether cool flames, the experimental propagation speeds varying between 14 and 18 $cm \cdot s^{-1}$. This study notably allowed to highlight the most important reactions for the prediction of cool flames LBVs.

The newly acquired data in this work constitute a strong foundation to further work on the low-temperature combustion mechanisms in the presence of ozone, in novel experimental conditions complementary to those met in typical kinetic reactors.